
Dual-species apparatus for
creating a dipolar quantum gas
of $^{23}\text{Na}^{40}\text{K}$ molecules



Dual-species apparatus for
creating a dipolar quantum gas
of $^{23}\text{Na}^{40}\text{K}$ molecules

Dissertation an der Fakultät für Physik
der Ludwig-Maximilians-Universität München

vorgelegt von

Nikolaus Walter Buchheim

aus Starnberg

2015

Tag der mündlichen Prüfung: 23. November 2015

Erstgutachter: Prof. Immanuel Bloch

Zweitgutachter: Prof. Florian Schreck

Zusammenfassung

In dieser Arbeit wird der Aufbau eines neuartigen, atomphysikalischen Experiments beschrieben, das zum Ziel hat, stark wechselwirkende Vielteilchensysteme bestehend aus polaren $^{23}\text{Na}^{40}\text{K}$ Molekülen zu erzeugen und zu studieren. Die anisotrope und langreichweitige Dipol-Dipol Wechselwirkung zwischen den Molekülen sollte es möglich machen, bisher nicht beobachtete Quanten-Vielteilchenzustände zu beobachten und prototypische Gittermodelle der Festkörperphysik zu simulieren, die zur Beschreibung von Quantenmagnetismus und Hochtemperatursupraleitern verwendet werden. Das $^{23}\text{Na}^{40}\text{K}$ Molekül ist für diesen Zweck besonders gut geeignet, da es in einer zwei-Körper Kollision chemisch stabil ist, fermionischer Quantenstatistik unterliegt und ein starkes Dipol Moment aufweist.

Die experimentelle Prozedur zur Erzeugung eines ultrakalten Quantengases aus heteronuklearen Molekülen erfordert es, zuerst die elementaren Bestandteile des Moleküls durch Laser- und Verdampfungskühlen in den Zustand der simultanen Quantenentartung zu überführen. Die Wechselwirkung zwischen den bosonischen ^{23}Na und den fermionischen ^{40}K Atomen lässt sich durch Ausnutzen einer Feshbach Streuresonanz mit einem externen Magnetfeld kontrollieren. In der Nähe einer solchen *Feshbach Resonanz* werden schwach gebundene $^{23}\text{Na}^{40}\text{K}$ Moleküle durch Radiofrequenzassoziation erzeugt.

In einem weiteren Schritt sollen diese *Feshbach Moleküle* durch eine *stimulierte Raman adiabatische Passage* (STIRAP) in den rovibronischen und Hyperfein-Grundzustand des Moleküls überführt werden. Die Differenz der Bindungsenergie wird hierbei nicht spontan frei, was unweigerlich die Aufhebung der Quantenentartung des Molekül-gases zur Folge hätte, sondern wird durch stimulierte Emission kontrolliert abgeführt. Die Kombination beider Methoden, der Feshbach Assoziation und der STIRAP, erlaubt es den Prozess der Molekülbindung auf fundamentaler, quantenmechanischer Ebene zu steuern.

Um die STIRAP zu implementieren ist es notwendig, ein geeignetes molekulares Zwischenniveau in einem elektronisch angeregten Zustand zu identifizieren, über welches das Feshbach Molekül mit dem rovibronischen Grundzustand in einen zwei-Photonen Übergang gekoppelt wird. Ein solches Zwischenniveau konnte durch hochauflösende Molekülspektroskopie im elektronisch angeregten $d^3\Pi$ Zustand identifiziert werden. Dieser Vibrationszustand (${}^3\Pi_{\Omega=1} \nu = 5$) ist durch molekulare Spin-Orbit Wechselwirkung an einen nah-resonanten Vibrationszustand im $D^1\Pi$ Zustand gekoppelt. Erst durch die Beimischung dieses Spin-Singulett Zustands ist es möglich den rovibronischen Grundzustand (ebenfalls Spin-Singulett) zu adressieren. Die zugehörige Übergangsfrequenz konnte durch kohärente Zwei-Photonen Spektroskopie bestimmt werden. Durch *elektromagnetisch induzierte Transparenz* wurden die Rabifrequenzen beider STIRAP Übergänge bestimmt und die Kohärenzeigenschaften des *Dunkelzustandes* untersucht.

Bis zum heutigen Zeitpunkt ist es nicht möglich den identifizierten Zwischenzustand zu

benutzen um $^{23}\text{Na}^{40}\text{K}$ Moleküle in den rovibronischen Grundzustand zu überführen. Das Phasenrauschen der zum Einsatz kommenden Halbleiter-Laser konnte als limitierender Faktor identifiziert werden. Darüberhinaus führt die spektroskopisch nicht auflösbare molekulare Hyperfeinstruktur des $|^3\Pi_{\Omega=1} \nu = 5\rangle$ Zustands zu einer Konfiguration in der kein echter Dunkelzustand existiert, der für die STIRAP benutzt werden kann. Aus diesen Gründen erscheint es unwahrscheinlich, dass das gegenwärtige STIRAP Schema (Halbleit-erlaser, $|^3\Pi_{\Omega=1} \nu = 5\rangle$ Zwischenniveau, resonante STIRAP) Grundzustandsmoleküle mit hoher Effizienz erzeugen wird. Dieses Schema kann jedoch durch ein anderes ersetzt werden, das erst kürzlich erfolgreich für den Grundzustands-Transfer von $^{23}\text{Na}^{40}\text{K}$ verwendet wurde. Die günstigen Eigenschaften des $^{23}\text{Na}^{40}\text{K}$ Moleküls in Kombination mit dem hier präsentierten Experimentaufbau sollten es daher in Zukunft möglich machen, dipolare Vielteilchensysteme zu erzeugen und zu studieren.

Abstract

This thesis report describes the construction of a novel atomic physics experiment, that should enable the study of quantum many-body system consisting of polar $^{23}\text{Na}^{40}\text{K}$ molecules. The anisotropy and the long-range character of the dipole-dipole interaction between these molecules should make it possible to observe novel quantum many-body states and to simulate prototypical lattice models of solid state physics that are used to describe quantum magnetism and the microscopic origin of high temperature superconductivity. For this purpose the $^{23}\text{Na}^{40}\text{K}$ molecule is particularly well suited, since it is chemically stable in two-body collisions, features a fairly large dipole moment and obeys fermionic quantum statistics.

In order to create an ultracold quantum gas of heteronuclear molecules it is necessary to first prepare the constituent atoms in a state of simultaneous quantum degeneracy by consecutive laser and evaporative cooling. The effective low temperature interaction in this mixture of bosonic ^{23}Na and fermionic ^{40}K atoms can be controlled with an external magnetic field by exploiting a Feshbach scattering resonance. In the vicinity of a *Feshbach resonance* weakly bound $^{23}\text{Na}^{40}\text{K}$ molecules are created by radio frequency association. In a next step these *Feshbach molecules* should be transferred to the rovibronic and hyperfine groundstate of the molecule via *stimulated Raman adiabatic passage* (STIRAP). In this process the difference in binding energy is not released spontaneously but is removed in a controlled manner by stimulated emission. Both techniques combined - Feshbach association and STIRAP - constitute a way to fundamentally control chemical bond formation on the quantum level.

In order to implement STIRAP it is necessary to identify a suitable molecular intermediate level belonging to an electronically excited molecular state that facilitates a two-photon coupling between the Feshbach molecule and the rovibronic groundstate. To this end we have performed high resolution molecular spectroscopy and have identified a suitable intermediate level in the electronic $d^3\Pi$ state. This vibrational level ($|^3\Pi_{\Omega=1} \nu = 5\rangle$) is coupled to a near-resonant vibrational level in the $D^1\Pi$ state. It is only the admixture of this spin-singlet level that allows to address the equally spin-singlet rovibronic groundstate. By using a narrow linewidth Raman laser system we have measured the binding energy of the rovibronic groundstate in coherent dark state spectroscopy. In addition, the observation of *electromagnetically induced transparency* (EIT) enabled us to determine the Rabi frequencies of both STIRAP transitions and to characterize the coherence properties of the dark state.

Up to date it has not been possible to populate the rovibronic groundstate by using the identified intermediate state. The phase noise performance of the semiconductor lasers that are employed in the Raman laser setup has been identified as the limiting parameter. Moreover, the spectroscopically not resolved molecular hyperfine structure of the

$|\ ^3\Pi_{\Omega=1} \nu = 5 \rangle$ level results in a near degenerate multi-level STIRAP configuration that does not feature a true dark state which can be used for adiabatic transfer. For these reasons it appears improbable that the current STIRAP scheme (semiconductor lasers, $|\ ^3\Pi_{\Omega=1} \nu = 5 \rangle$ intermediate level, resonant STIRAP) will result in groundstate transfer with high efficiency. However, the current STIRAP scheme could easily be changed to an alternative one that very recently has been proven to work for groundstate transfer of $^{23}\text{Na}^{40}\text{K}$. The unique properties of the $^{23}\text{Na}^{40}\text{K}$ molecule in combination with the experimental setup design that is presented in this report should make it possible to realize and study dipolar many-body systems in near-future experiments.

Contents

Zusammenfassung	v
Abstract	vii
1 Introduction and Motivation	1
1.1 Dipolar many-body physics with ultracold molecules	4
1.1.1 Weakly interacting dipolar Fermi gas	6
1.1.2 Anisotropic Fermi liquid state	9
1.1.3 BCS pairing and superfluidity	10
1.1.4 Dipolar many-body physics in 2D	11
1.1.5 Lattice models and quantum magnetism	14
2 The experimental setup	17
2.1 Design considerations	18
2.2 Overview	19
2.3 Ultra high vacuum system	20
2.4 $^{23}\text{Na}^{40}\text{K}$ Bose-Fermi mixture - overview of the experimental sequence	21
2.5 Laser cooling	24
2.5.1 Laser system and Zeeman slower for ^{23}Na	25
2.5.2 Laser system and 2D-MOT for ^{40}K	35
2.5.3 Dual-species MOT	36
2.6 Magnetic Trap and evaporative cooling	37
2.7 Optical dipole trap	40
2.8 Attaining dual species degeneracy	46
2.8.1 Feshbach optimized sympathetic cooling	48
2.9 Summary	53
3 Feshbach molecules	55
3.1 Theoretical background: Feshbach resonances and molecule association	56
3.2 RF association of $^{23}\text{Na}^{40}\text{K}$ Feshbach molecules	61
3.2.1 Improved Feshbach association starting from a deeply degenerate Bose-Fermi mixture	67
3.3 Summary and discussion	69
4 Molecular spectroscopy	71
4.1 Overview	71
4.2 Background: Molecular structure of $^{23}\text{Na}^{40}\text{K}$	74
4.2.1 The Born-Oppenheimer approximation	75

4.2.2	Basis functions and perturbations	76
4.2.3	Fine structure model for the $d^3\Pi/D^1\Pi$ complex	78
4.3	Photoassociation spectroscopy	80
4.3.1	Spin Character and wave function of the initial state	81
4.3.2	Vibrational structure of the $d^3\Pi/D^1\Pi$ complex	81
4.3.3	Molecular fine structure of the $d^3\Pi/D^1\Pi$ complex	82
4.4	High resolution molecular spectroscopy	84
4.4.1	Wave function and spin-character of the initial state	86
4.4.2	Hyperfine and Zeeman substructure of the candidate level	88
4.4.3	Origin of the non-resolved hyperfine structure of the $\Omega = 1, J = 1$ component	91
4.5	Groundstate spectroscopy	93
4.5.1	Coherent population trapping, STIRAP and EIT	93
4.5.2	Results of EIT spectroscopy	100
4.5.3	Characterization of the $d^3\Pi/D^1\Pi$ - STIRAP scheme	103
4.6	Numerical model for groundstate transfer via the $d^3\Pi/D^1\Pi$ complex	106
4.6.1	Hyperfine structure of the rovibronic groundstate	107
4.6.2	Conclusions	115
5	Summary and outlook	117
5.1	Outlook	118
	References	119
	Danksagung	127

Introduction and Motivation

The realization of Bose-Einstein condensation and the observation of Fermi degeneracy in dilute gases of ultracold atoms has significantly advanced our understanding of collective quantum phenomena. In these systems the de Broglie wavelength associated with the movement of the atoms becomes larger than the inter-particle separation, the atoms become indistinguishable and quantum statistics governs system behavior. Well described effects from low temperature condensed matter physics such as superfluidity and the Bardeen-Cooper-Schrieffer (BCS) mechanism of superconductivity have been readily observed with trapped ultracold atoms [1, 2]. During the last decade new experimental techniques have been developed that considerably increase the scope of physical phenomena that can be investigated with ultracold gases. First, magnetic field controlled scattering resonances (*Feshbach resonances*) allow to tune the strength of the effective low temperature interaction in a quantum gas. In fermionic systems, which are stabilized by quantum statistics against three-body molecule formation the elastic scattering cross-section can approach the *unitarity limit*. In this situation all particles in a gas are correlated and the system is said to be *strongly interacting* in contrast to *weakly interacting* systems that only exhibit pairwise correlations. In addition, Feshbach resonances can be used to associate weakly bound molecules in single or two component systems. In a two component Fermi gas Feshbach resonances allow to investigate the *BCS-BEC crossover* region [3] where a BCS superfluid of Cooper pairs that are correlated in momentum space can be converted to a BEC of Feshbach molecules.

The second key development, trapping of ultracold atoms in periodic optical potentials started a completely new branch of AMO physics: the quest to engineer prototype lattice-models of solid-state physics using neutral atoms that move and interact in an optical lattice in order to simulate the behavior of electrons in a crystal lattice. By controlling the ratio between on-site interaction and the kinetic energy in an optical lattice a quantum phase-transition from a superfluid many-body state to a strongly-correlated Mott insulator state has been observed [4]. A review article from 2008 [5] gives an extensive overview on how both techniques (Feshbach resonances and optical lattices) can be used to study strongly correlated many-body phenomena. Recent developments include the engineering of artificial gauge potentials in optical lattices [6, 7], as well as single-site and single atom detection [8] and manipulation techniques [9].

Common to all these techniques is the fact that the van der Waals interaction between neutral atoms reduces to an isotropic contact interaction in the low temperature limit. As

a consequence, atoms only interact with each other when they occupy the same lattice site. For this reason, lattice spin-models such as the Heisenberg and t-J model, which are used to describe quantum magnetism and high T_C superconductivity will be difficult to investigate. To make this statement more concrete, consider that the formation of a Mott-insulator in an optical lattice requires the on-site interaction U to be much larger than the absolute value of the hopping matrix element t of the Bose-Hubbard model [5]. It is only in this configuration, where the many-body dynamics include the spin-exchange interaction $J = \frac{4t^2}{U}$ that is believed to be at the heart of high T_C superconductivity in the cuprates [10]. However, the Mott insulator requirement that $U \gg t$ most certainly excludes to enter a regime where strong competition between spin exchange J that favors an ordered state and particle hopping t is present. Note that it is commonly assumed that high T_C superconductivity in the cuprates appears in a parameter regime where $\frac{J}{t} \simeq \frac{1}{3}$ [10]. Moreover, magnetic ordering is predicted to appear in atomic Mott insulators only at extremely low temperature that have not yet been achieved experimentally [5].

For this reason, as well as for many others (see review article [11]), considerable efforts have been made to achieve quantum degeneracy and to enter the strongly correlated regime for samples of ultracold polar molecules. In contrast to the van der Waals interaction, the dipole-dipole interaction between polar molecules is of long-range character [12], it is anisotropic with changing polarity and (similar to the scattering length in the vicinity of a Feshbach resonance) can easily be tuned by external electric fields. Combined, the intriguing properties of the dipole-dipole interaction should make it possible to explore much richer and much more complex many-body phenomena as compared to ultracold gases of neutral atoms.

To date, direct cooling techniques allow to study samples of chemically inert polar molecules in the mK range. The attainable phase-space density however is still orders of magnitude too small for reaching quantum degeneracy. In a complementary approach weakly bound diatomic molecules are associated starting from samples of ultracold atoms by using the strong coupling between unbound colliding atoms and a molecular bound-state in the vicinity of a Feshbach resonance [13]. In a second step these so called Feshbach molecules can be transferred to the rovibronic groundstate of the molecular potential by stimulated Raman adiabatic passage (STIRAP) [14]. Controlling chemical bond formation in this way, has been successfully applied to homonuclear $^{133}\text{Cs}_2$ [15] and the alkaline-earth element $^{84}\text{Sr}_2$ [16, 17] as well as heteronuclear $^{40}\text{K}^{87}\text{Rb}$ [18], $^{87}\text{Rb}^{133}\text{Cs}$ [19, 20], $^{23}\text{N}^{40}\text{K}$ [21] molecules.

Recently $^{40}\text{K}^{87}\text{Rb}$ molecules have been trapped in an optical lattice and dipolar spin-exchange interaction could be realized for deeply confined molecules in absence of particle tunneling [22]. In this experiment the spin-degree of freedom is encoded in two rotational states of the groundstate molecule. As proposed in [23] spin-exchange is mediated by the dipole-dipole interaction between the molecules. For the $^{40}\text{K}^{87}\text{Rb}$ molecule however it seems to be quite difficult to achieve a higher lattice filling fraction and to allow for tunneling of molecules between the lattice sites. Experiments that studied the collision properties of ultracold $^{40}\text{K}^{87}\text{Rb}$ molecules revealed an exothermic exchange reaction



that prevents increasing phase-space density via evaporative cooling of molecules [24]. For certain molecules however this process is predicted to be endothermic [25] and therefore strongly suppressed at low temperatures. Table 1.1 lists the dipole moment of all alkali-alkali molecules in SI units (i.e. $1D = 3.335 \cdot C \cdot m = 0.3935 \cdot e^- \cdot a_0$). Entries that are highlighted in bold script are predicted to be chemically stable.

	Na	K	Rb	Cs
Li	0.566	3.565	4.165	5.529
Na		2.759	3.306	4.607
K			0.615	1.837
Rb				1.237

Table 1.1 – Groundstate dipole moments in Debye for all possible alkali-alkali molecules. Molecules that are predicted to be chemically stable (see [25]) are highlighted in bold script. Fermionic molecules involve either ${}^6\text{Li}$ or ${}^{40}\text{K}$.

The lifetime of $\tau > 2s$ that has been recently observed for ${}^{87}\text{Rb}{}^{133}\text{Cs}$ and ${}^{23}\text{Na}{}^{40}\text{K}$ molecules in the rovibronic (and hyperfine) groundstate indeed shows evidence for the absence of this two-body loss channel [19, 21].

The ${}^{23}\text{Na}{}^{40}\text{K}$ molecule is a particularly promising candidate to realize a dipolar quantum gas of molecules. Since all molecules that involve the fermionic isotope of lithium ${}^6\text{Li}$ are chemically unstable, ${}^{23}\text{Na}{}^{40}\text{K}$ is the fermionic molecule with the largest dipole moment among all alkali-alkali combinations. The dipole-moment of $2.7D$ is $\simeq 4.5$ times larger than that of ${}^{40}\text{K}{}^{87}\text{Rb}$, for which dipolar effects were clearly observable in experiments. Since the dipole-dipole interaction scales quadratically with the dipole moment of the molecule, ${}^{23}\text{Na}{}^{40}\text{K}$ offers a factor of $\simeq 20$ increase in interaction energy compared to ${}^{40}\text{K}{}^{87}\text{Rb}$. In addition, the significant mass imbalance between bosonic ${}^{87}\text{Rb}$ and fermionic ${}^{40}\text{K}$ results in a unfavorable situation for molecule formation by Feshbach association. When a ${}^{40}\text{K}{}^{87}\text{Rb}$ mixture is cooled to quantum degeneracy in a far detuned optical dipole trap, the density overlap between both species decreases drastically due to Fermi pressure when the degeneracy region is entered. For this reason Feshbach association is performed just above the condensation temperature of ${}^{87}\text{Rb}$ when ${}^{40}\text{K}$ is still above the Fermi temperature where quantum statistics does not significantly affect the density distribution. For the ${}^{23}\text{Na}{}^{40}\text{K}$ mixture the situation is reversed and molecules association can be performed at much higher phase-space density. For these reasons we decided to construct a novel experimental apparatus that aims to realize quantum degeneracy for groundstate ${}^{23}\text{Na}{}^{40}\text{K}$ molecules and should make it possible to enter the strongly correlated regime. The next section presents in more detail which dipolar many-body phenomena can be studied with groundstate polar molecules. I analyze the required physical parameter regime by reference to the ${}^{23}\text{Na}{}^{40}\text{K}$ molecule and our current experimental setup.

Polar molecules oriented by an electric field

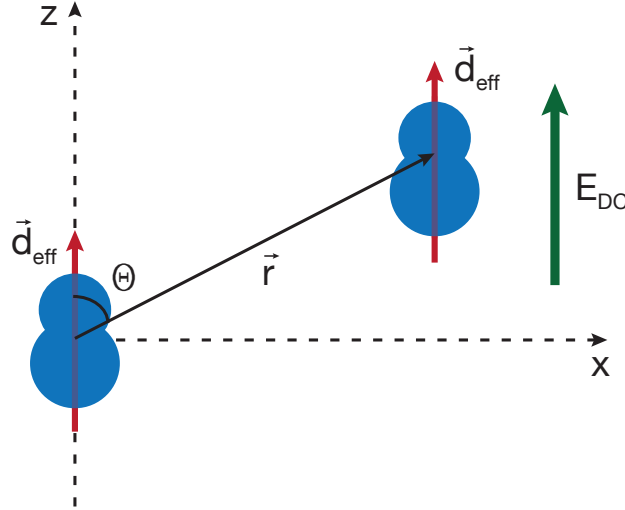


Figure 1.1 – Geometry for two interacting dipoles that have been aligned by an external electric field.

1.1 Dipolar many-body physics with ultracold molecules

Due to their large intrinsic electric dipole moment, heteronuclear molecules are promising candidates for creating dipolar interacting quantum matter. Once prepared in the rovibronic groundstate external electric fields can be used to orient the permanent dipole moment of the molecules along an arbitrary direction in space. Rotational symmetry is broken and the groundstate acquires a non-vanishing dipole moment. By this mechanism tunable and anisotropic dipole forces can be induced between the molecules in a gas. At low temperatures the internal structure of the molecules is decoupled from the many-body dynamics of the system and the gas can be regarded as consisting of point particles interacting via dipole-dipole and van der Waals interaction. A recent review article [26] summarizes theoretical work on the physics of dipolar quantum gases. The many-body phenomena that are presented all rely on the assumption that the constituent particles of a quantum many-body system can effectively be regarded as point particles with no internal structure interacting via dipole-dipole interaction:

$$V_{dd}(\mathbf{r}_1 - \mathbf{r}_2) = \frac{\mathbf{d}_1 \cdot \mathbf{d}_2 - 3(\mathbf{d}_1 \cdot \hat{\mathbf{r}}_1)(\mathbf{d}_2 \cdot \hat{\mathbf{r}}_2)}{4\pi\epsilon_0(r_1 - r_2)^3}. \quad (1.1)$$

This formula can be derived [27] by calculating the potential energy of two electric dipoles far apart from each other $r \gg d$. The description of point-like particles breaks down at short inter particle distance where the internal structure of the molecules becomes relevant. In a dilute, ultracold and weakly correlated gas the effect of the short range potential can be parametrized by an effective contact interaction [26]. For polar molecules that have been oriented by an external electric field (see Fig. 1.1) the combined effective

interaction potential is then given by

$$V(r, \theta) = \frac{2\pi\hbar^2 a(d_{\text{eff}}^2)}{m} \delta(r) + \frac{d_{\text{eff}}^2(E)}{4\pi\epsilon_0 r^3} (1 - 3\cos^2 \theta). \quad (1.2)$$

The short range part of the interaction is parametrized by a s-wave scattering length that now depends on the strength of the induced dipole moment d_{eff} . For fermionic molecules the contact part of the interaction potential vanishes at low temperatures due to quantum statistics. Therefore the potential for ultracold and polarized $^{23}\text{Na}^{40}\text{K}$ molecules reduces to

$$V_{dd}(r, \theta) = \frac{d_{\text{eff}}^2(E)}{4\pi\epsilon_0 r^3} (1 - 3\cos^2 \theta). \quad (1.3)$$

The strength of the induced dipole-dipole interaction is conventionally expressed in terms of the *dipolar length* a_{dd} :

$$a_{dd}(E) = \frac{m d_{\text{eff}}^2(E)}{4\pi\epsilon_0 \hbar^2} \quad (1.4)$$

This definition allows to relate the dipole-dipole interaction with the average inter-particle distance in a trapped gas or the Fermi wave-vector k_F of a Fermi gas at $T = 0$.

The effective dipole moment at a given electric field $d_{\text{eff}}(E)$ can be estimated by numerical diagonalization of the following Hamiltonian that describes a polar molecule in the rovibronic groundstate in presence of an external electric field:

$$H = B_0 \cdot J(J + 1) + \hat{d} \cdot \mathbf{E}. \quad (1.5)$$

Here B_0 is the rotational constant of the rovibronic groundstate, \hat{d} the dipole operator and \mathbf{E} the external electric field. From the eigenvalues $\epsilon(E)$ of the diagonalized Hamiltonian

$$H = \sum_{\epsilon} \epsilon(E) |\epsilon\rangle \langle \epsilon| \quad (1.6)$$

the induced dipole moment $d_{\text{eff}}(E)$ in state $|\epsilon\rangle$ at a given field E_0 is obtained by

$$d_{\text{eff}}(E) = \left. \frac{d\epsilon(E)}{dE} \right|_{E=E_0} \quad (1.7)$$

The first thing to note is, that the expectation value of the dipole operator in any eigenstate of the rotation operator vanishes

$$d = \langle Jm_J | \hat{d} | Jm_J \rangle = 0 \quad (1.8)$$

due to parity symmetry. Therefore, in absence of an external electric field, groundstate molecules interact only via van der Waals forces. However, the dipole operator is non-diagonal in the rotational basis $\{J = 0, 1, 2, \dots, m_J = -J, \dots, J\}$ and mixes states of opposite parity. Since the rotational states become mixed by the linear Stark effect and the energy splitting between states of opposite parity is given by the rotational constant B_0 which for alkali-alkali molecules is on the order of 1 – 10GHz, the DC stark shift for polar molecules is orders of magnitudes larger than for atoms. As a consequence the dressed molecular groundstate in presence of an electric field $|\epsilon = 0\rangle$ can acquire a dipole moment that

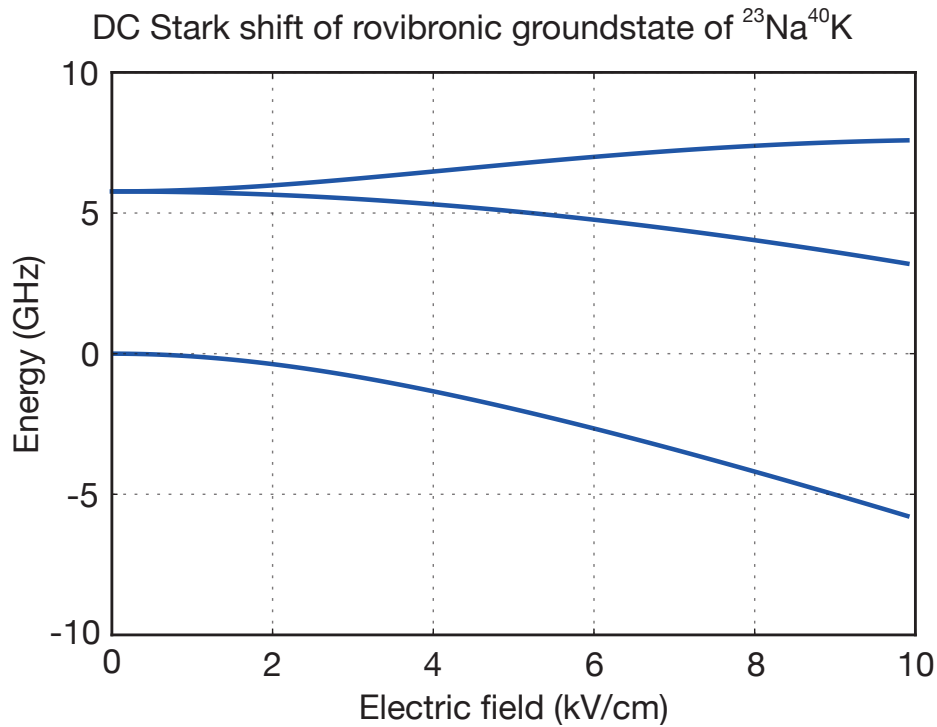


Figure 1.2 – Energy of the three lowest rotational states of the vibronic groundstate as a function of the applied electric field.

approaches the value of the intrinsic dipole moment. In order to estimate the effective dipole moment that can realistically be induced for groundstate $^{23}\text{Na}^{40}\text{K}$ molecules, we diagonalize the Hamiltonian from equation 1.5 on a truncated basis set with $J \leq 5$ where the maximal value of J is chosen such that the dipole moment does not change by less than 1% when we include the next rotational state to the diagonalization procedure. Fig. 1.2 and Fig. 1.3 display the eigenenergies of the three lowest lying rotational states and the dipole moment of the groundstate as a function of magnetic field

In order to make the induced dipole moment as large as possible we decided to install the required electric field electrodes inside the vacuum chamber in which our experiments take place. In its current configuration we can safely apply $\approx 5\text{kV/cm}$ resulting in a maximal induced dipole moment of $d_{\text{eff}} \approx 1.3D$. We will use this value to estimate the range of weakly and strongly interacting many-body effects that we can expect to observe with $^{23}\text{Na}^{40}\text{K}$.

1.1.1 Weakly interacting dipolar Fermi gas

Identical fermionic polar molecules cannot be in the same quantum state. As a result contact interaction is suppressed and the scattering potential is only given by the dipole-dipole interaction of equation 1.3. For the same reason the many-body wavefunction of a single component Fermi gas has to be completely anti-symmetric with respect to particle exchange. The Hamiltonian of a trapped, weakly interacting ($k_F a_{dd} \ll 1$), dipolar Fermi gas is then given by [26]:

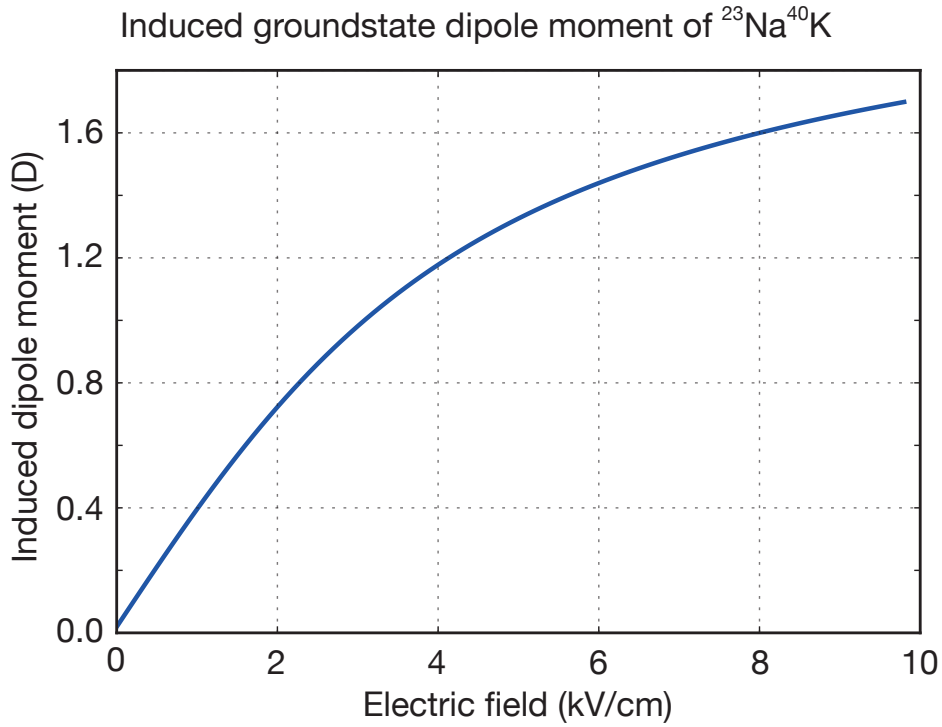


Figure 1.3 – Induced dipole moment of the absolute groundstate $|J = 0, m_J = 0\rangle$ as a function of magnetic field.

$$\hat{H} = \int d\mathbf{r} \hat{\Psi}^\dagger(\mathbf{r}) \left[\frac{-\hbar^2}{2m} \nabla^2 + V_{tr}(\mathbf{r}) \right] \hat{\Psi}(\mathbf{r}) + \frac{1}{2} \int d\mathbf{r} d\mathbf{r}' \hat{\Psi}^\dagger(\mathbf{r}) \hat{\Psi}^\dagger(\mathbf{r}') [V_{dd}(\mathbf{r} - \mathbf{r}')] \hat{\Psi}(\mathbf{r}) \hat{\Psi}(\mathbf{r}')$$

Here V_{dd} the dipole-dipole interaction of equation 1.3 and V_{tr} the external trapping potential typically created by an optical dipole trap. This trapping potential is approximated by a cylindrical harmonic trap:

$$V_{tr}(r, z, \phi) = -V_0 + \frac{1}{2} m (\omega_r^2 r^2 + \omega_z^2 z^2), \quad (1.9)$$

with radial and axial trap frequencies ω_r and ω_z . The field operators $\hat{\Psi}(\mathbf{r})$ fulfill fermionic anti-commutation relations:

$$\{\hat{\Psi}(\mathbf{r}), \hat{\Psi}^\dagger(\mathbf{r}')\} = \delta(\mathbf{r} - \mathbf{r}') \\ \{\hat{\Psi}(\mathbf{r}), \hat{\Psi}(\mathbf{r}')\} = \{\hat{\Psi}^\dagger(\mathbf{r}), \hat{\Psi}^\dagger(\mathbf{r}')\} = 0.$$

The Fermi-Dirac distribution for the average occupation of a quantum state with energy ϵ_i is given by:

$$n_{FD}(\epsilon_i) = \frac{1}{\exp[(\epsilon_i - \mu)/k_B T] + 1}, \quad (1.10)$$

where the temperature dependent chemical potential $\mu(T)$ ensures that the Fermi-Dirac distribution is properly normalized, i.e.

$$\sum_i n_{FD}(\epsilon_i) = N, \quad (1.11)$$

where N is the total number of trapped fermions. The Fermi-Dirac distribution results in a completely filled Fermi sphere for all levels with energy $\epsilon_i \leq \frac{p_F(\mathbf{r})^2}{2m}$ as $T \rightarrow 0$. If the chemical potential at $T = 0$ (also called the Fermi energy ϵ_F) is much larger than the level spacing in the harmonic trap (which is given by the average trap frequency $\hbar(\omega_z \omega_r^2)^{1/3}$), the position dependent Fermi momentum $p_F(\mathbf{r})$ is given by the *local density approximation* (LDA)

$$p_F(\mathbf{r}) = \sqrt{2m[\mu - V_{tr}(\mathbf{r})]} \quad (1.12)$$

Since the Fermi energy for a trapped gas is given by

$$\epsilon_F = \mu(T = 0) = \hbar(\omega_z \omega_r^2)^{1/3} \cdot (6N^{1/3}) \quad (1.13)$$

the LDA is valid for particle numbers $N \gtrsim 1000$. Since the particle density $n(\mathbf{r})$ is related to the Fermi momentum via

$$n(\mathbf{r}) = \frac{p_F(\mathbf{r})^3}{6\pi^2 \hbar^3} \quad (1.14)$$

we can relate the density distribution in a harmonic trap directly to the total number of particles and the trap geometry by using equation 1.12:

$$n(\mathbf{r}) = n_0 \left[1 - \frac{r^2}{R_r^2} - \frac{z^2}{R_z^2} \right]^{3/2}. \quad (1.15)$$

Here the central density n_0 of the Fermi gas is given by

$$n_0 = \frac{(2m\epsilon_F)^{3/2}}{6\pi^2 \hbar^3} \quad (1.16)$$

and the *Thomas Fermi radii* $R_{r/z}$ by:

$$R_{r/z} = \left(\frac{2\epsilon_F}{m\omega_{r/z}^2} \right)^{1/2} \quad (1.17)$$

For a dipolar Fermi gas the weakly interacting regime is characterized by a configuration where the kinetic energy due to the Pauli pressure is much larger than the strength of the dipole-dipole interaction. In terms of the dipolar length $a_{dd}(E)$ this condition is expressed as:

$$\frac{p_F(\mathbf{r}) \cdot a_{dd}(E)}{\hbar} = k_F(\mathbf{r}) \cdot a_{dd}(E) \ll 1 \quad (1.18)$$

In this case the Pauli pressure stabilizes a dipolar Fermi gas against collapse due to the attractive part of the dipole-dipole interaction. For a trapped gas the system will become unstable and undergo collapse when

$$\frac{p_F(0) \cdot a_{dd}(E)}{\hbar} \simeq 1. \quad (1.19)$$

By solving for d_{eff} we arrive at a relation between central density n_0 and the induced dipole moment at which collapse is expected:

$$d_{\text{max}} = \sqrt{\frac{4\pi\epsilon_0\hbar^2}{(6\pi^2n_0)^{1/3}}}. \quad (1.20)$$

1.1.2 Anisotropic Fermi liquid state

A Fermi gas of polar molecules with an induced dipole moment $d_{\text{eff}}(E)$ and a temperature above the BCS transition (see section 1.1.3) would constitute a single component realization of a Fermi liquid [28] with anisotropic inter-particle interaction. Following the arguments in [28] an interacting Fermi gas at low temperatures ($T < T_F$) is described in terms of *dressed fermionic quasi-particles*. For a single-component Fermi gas the momentum distribution function $n(\mathbf{p})$ of the quasi-particles is defined by the following implicit expression:

$$n(\mathbf{p}) = \frac{1}{\exp((\epsilon[n(\mathbf{p})] - \mu(T))/T k_b) + 1}, \quad (1.21)$$

where the energy of the quasi-particles is defined by the functional derivative of the total energy functional $E[n(\mathbf{p})]$ with respect to the distribution function:

$$\delta E[n(\mathbf{p})]/V = \int \frac{d\mathbf{p}}{(2\pi\hbar)^3} \epsilon[n(\mathbf{p})] \delta n(\mathbf{p}), \quad (1.22)$$

where V is the volume occupied by the system. Note that due to the interaction between the fermions in the gas the energy of the quasi-particles depends on the distribution of all particles in the Fermi gas and is itself a functional of the distribution function $n(\mathbf{p})$. Including pairwise interactions between the quasi-particles the total change in energy of the system in response to an infinitesimal change $\delta n(\mathbf{p})$ in the distribution function is given by:

$$\begin{aligned} \delta E/V &= \int \frac{d\mathbf{p}}{(2\pi\hbar)^3} \epsilon(\mathbf{p}) \delta n(\mathbf{p}) \\ &+ \frac{1}{2} \int \frac{d\mathbf{p}}{(2\pi\hbar)^3} \int \frac{d\mathbf{p}'}{(2\pi\hbar)^3} f(\mathbf{p}, \mathbf{p}') \delta n(\mathbf{p}) \delta n(\mathbf{p}'). \end{aligned} \quad (1.23)$$

Comparing equation 1.22 to 1.23 the energy functional of the quasi-particles appearing in the distribution function 1.21 is identified with:

$$\epsilon[n(\mathbf{p})] = \epsilon(\mathbf{p}) + \frac{1}{2} \int \frac{d\mathbf{p}'}{(2\pi\hbar)^3} f(\mathbf{p}, \mathbf{p}') \delta n(\mathbf{p}'), \quad (1.24)$$

where the bare quasi-particle energy $\epsilon(\mathbf{p})$ is given by [26]:

$$\epsilon(\mathbf{p}) = \left. \frac{\delta E}{\delta n(\mathbf{p})} \right|_{\delta n(\mathbf{p})=0} \quad (1.25)$$

and the *Landau interaction function* $f(\mathbf{p}, \mathbf{p}')$ by:

$$f(\mathbf{p}, \mathbf{p}') = \left. \frac{\delta^2 E}{\delta n(\mathbf{p}) \delta n(\mathbf{p}')} \right|_{\delta n(\mathbf{p})=0}. \quad (1.26)$$

For quasi-particles that exist close to the Fermi surface the quasi-particle dispersion relation can be approximated by

$$\epsilon(\mathbf{p}) \simeq \frac{p_F}{m^*} (p - p_F), \quad (1.27)$$

where p_F is the Fermi momentum and m^* the *effective mass* which, for an anisotropic interaction potential in general is a tensorial quantity.

For a weakly interacting (i.e. $k_F a_{dd}(E) \ll 1$) dipolar Fermi liquid with a homogeneous density $n(\mathbf{r}) = n$ a Hatree-Fock approximation for the total energy is justified:

$$\begin{aligned} \frac{E}{V} = & \int \frac{d\mathbf{p}}{(2\pi\hbar)^3} \frac{p^2}{2m} n(\mathbf{p})_\alpha \\ & + \frac{1}{2} \int \frac{d\mathbf{p}}{(2\pi\hbar)^3} \int \frac{d\mathbf{p}'}{(2\pi\hbar)^3} n(\mathbf{p})_\alpha V_{dd}(\mathbf{p} - \mathbf{p}') n(\mathbf{p}')_\alpha. \end{aligned} \quad (1.28)$$

Using the variational Ansatz [26]

$$n(\mathbf{p})_\alpha = \theta \left[p_F^2 - \frac{1}{\alpha} p_r^2 - \alpha^2 p_z^2 \right] \quad (1.29)$$

for the momentum distribution function and minimizing the total energy with respect to α results in a deformed Fermi surface - a spheroid that is stretched in the direction of the external electric field ($\alpha < 1$). In this configuration the quasi-particle dispersion relation is given by:

$$\epsilon(\mathbf{p}) = \frac{p^2}{2m} - \int \frac{d\mathbf{p}'}{(2\pi\hbar)^3} V_{dd}(\mathbf{p} - \mathbf{p}') n(\mathbf{p}')_\alpha. \quad (1.30)$$

In principle it should be possible to measure the quasi-particle dispersion relation with *Bragg-spectroscopy* in an experiment analogous to [29]. Moreover, anisotropic Landau *zero sound* [28, 26, 30] could be observable.

1.1.3 BCS pairing and superfluidity

Due to the attractive part or the dipole interaction (see equation 1.3) the groundstate of a dipolar Fermi gas as $T \rightarrow 0$ is given by a superfluid of Cooper pairs. In the weakly interacting regime the critical temperature for superfluidity is much smaller than the Fermi temperature. The system is a BCS superfluid if

$$T < T_C \ll T_F \quad (1.31)$$

and a dipolar Fermi liquid if

$$T_C < T < T_F. \quad (1.32)$$

Due to the anisotropic character of the dipole-dipole interaction the pairing mechanism in a single component dipolar Fermi gas differs from the attractive s-wave pairing [2] in a two-component Fermi gas of neutral atoms. Negative matrix elements of the dipole-dipole interaction only exist for collision channels with an odd value for the angular momentum of collision L . At ultracold temperatures the p -wave channel dominates and the only negative valued matrix element of V_{dd} in is due to:

$$\langle L = 1 m_L = 0 | 1 - 3 \cos^2 \theta | L = 1 m_L = 0 \rangle = -\frac{4\pi}{5}. \quad (1.33)$$

BCS pairing corresponds to a non-zero value of the BCS order parameter defined by [26]:

$$\Delta(\mathbf{r}_1 - \mathbf{r}_1) = V_{dd}(\mathbf{r}_1 - \mathbf{r}_1) \langle MBS | \hat{\Psi}(\mathbf{r}_1) \hat{\Psi}(\mathbf{r}_2) | MBS \rangle, \quad (1.34)$$

where $\hat{\Psi}(\mathbf{r}_i)$ is a fermionic *particle destruction operator*. The order parameter is zero if the many-body state $|MBS\rangle$ of the system is the Fermi liquid state. It is non zero in the BCS groundstate $|BCS\rangle$ that is approximately given by [2]:

$$|BCS\rangle = N' \left(\sum_{\mathbf{p}} c_{\mathbf{p}} a_{\mathbf{p}}^{\dagger} a_{-\mathbf{p}}^{\dagger} \right)^{N/2} |VAC\rangle, \quad (1.35)$$

where the momentum dependent coefficients $c_{\mathbf{p}}$ fulfill $c_{\mathbf{p}} = c_{-\mathbf{p}}$. Note that for the non-interacting Fermi gas $c_{\mathbf{p}} = \theta(p_F - p)$ at $T = 0$. In the BCS groundstate the order parameter can be regarded as the wave function of the Cooper pairs.

For a homogeneous dipolar Fermi gas the critical temperature for BCS superfluidity can be derived [26]:

$$k_B T_C(n, d_{eff}, m) = 1.44 \epsilon_F \exp\left(-\frac{\pi \epsilon_F}{12 n d_{eff}^2 \cdot 4 \pi \epsilon_0}\right), \quad (1.36)$$

where the Fermi energy is related to the mass m of the molecule and the density n via:

$$\epsilon_F = \frac{(6\pi^2 \hbar^3 n)^{2/3}}{2m}. \quad (1.37)$$

We can now estimate the BCS transition temperature for $^{23}\text{Na}^{40}\text{K}$ molecules as function of the induced dipole moment $d_{eff}(E)$. Fig. 1.4 shows T_C as function of $d_{eff}(E)$ for realistic but optimistic values of the particle density n . The red arrows indicate the value of d_{eff} at which the system will undergo collapse (i.e. $k_F(\mathbf{r}) \cdot a_{dd}(E) = 1$). Since the required temperature are an order of magnitude smaller than the coldest temperatures that have been observed even for atomic Fermi gases [29] it will be very challenging to observe dipolar BCS superfluidity with our current experimental setup. In fact, by just substituting $d_{max}^2 = \frac{\hbar^3}{m \cdot p_F}$ into equation 1.36 one arrives at a general upper bound for the critical temperature of BCS superfluidity in terms of the Fermi temperature:

$$T_C = 6.19 \cdot 10^{-4} T_F. \quad (1.38)$$

These considerations immediately motivate the use of strong confinement in the direction of the external electric field in order to stabilize the system against collapse due to the attractive part of the dipole-dipole interaction.

1.1.4 Dipolar many-body physics in 2D

The regime of strong interactions is entered when the strength of the interaction becomes comparable or larger than the kinetic energy of the particles. In a 3D system however the attractive part of the dipole-dipole interaction will result in a many-body instability and ultimately in particle loss by chemical reactions when the induced dipole moment is increased. Strongly interacting many-body states can realistically only be observed with polar molecules if attractive head-to-tail collisions are suppressed by confining the molecules

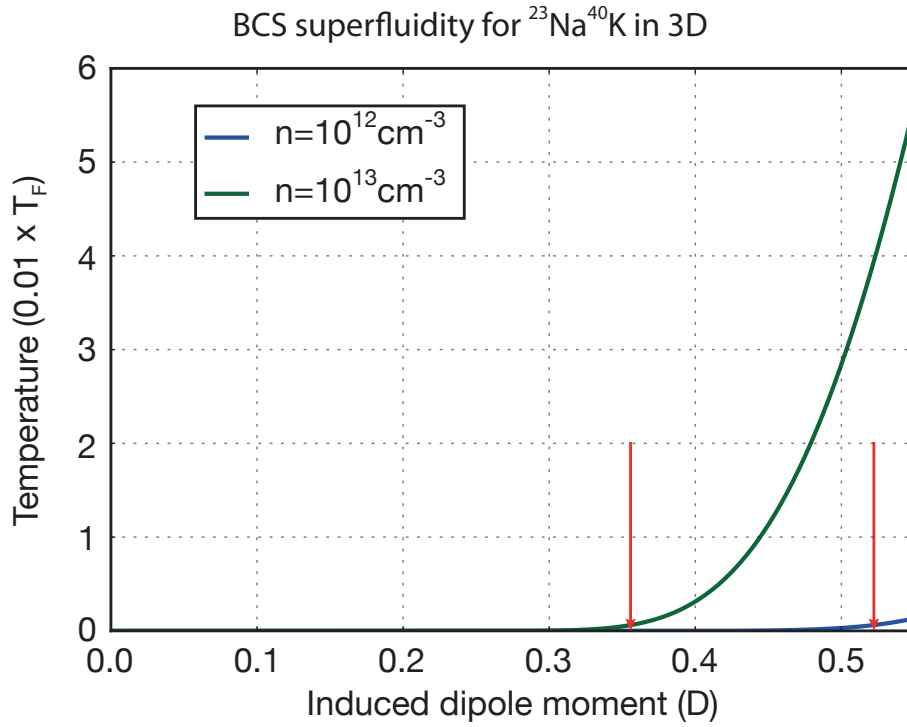


Figure 1.4 – BCS transition temperature for a homogeneous sample of $^{23}\text{Na}^{40}\text{K}$ molecules as function of the induced dipole moment for optimistic values of the particle density calculated by equation 1.36. The red arrows indicate the value of the dipole moment where the system will undergo collapse ($k_F(\mathbf{r}) \cdot a_{dd}(E) = 1$) due to the attractive part of the dipole-dipole interaction.

in periodic optical potentials (2D confinement or optical lattice). A strong 2D confinement can be realized by an optical standing wave along the direction of the external electric field that is required to polarize the molecules. This situation has been analyzed in detail in [31, 32] with an emphasis on chemically unstable molecular species such as $^{40}\text{K}^{87}\text{Rb}$ that exhibit *universal* (i.e. species independent) inelastic collision rates at short inter-molecular distances. Fig. 1 from [31] shows the proposed experimental configuration. The trapping potential is given by [33]:

$$V_{tr} = -V_0 \cdot \exp\left(-\frac{2r^2}{w^2(z)}\right) \cdot \sin^2(kz), \quad (1.39)$$

where $w(z)$ is the beam radius and $k = 2\pi/\lambda$ the wave vector of the Gaussian laser beam that is used to generate the periodic potential. V_0 designates the depth of the trapping potential. For low kinetic energy the trapping potential is approximately harmonic

$$V_{tr}(r, z, \phi) = -V_0 + \frac{1}{2}m(\omega_r^2 r^2 + \omega_z^2 z^2) \quad (1.40)$$

The trapping frequency ω_z along the direction of the electric field can be as large as $\omega_z \simeq 150\text{kHz}$ whereas $\omega_r \simeq 0.1 - 1\text{kHz}$. The harmonic oscillator length associated with the strong confinement along the z -direction is defined as

$$a_{ho} = \sqrt{\frac{\hbar}{m\omega_z}} \quad (1.41)$$

The long-range potential $V(\rho, z)$ in this quasi-2D geometry for two polar molecules with induced dipole moment d_{eff} is given by [32]:

$$V(\rho, z) = \frac{1}{2}\mu\omega_z^2 z^2 + \frac{\hbar^2(m^2 - 1/4)}{2\mu\rho^2} - \frac{C_6}{r^6} + \frac{d_{\text{eff}}^2}{r^3} \left(1 - \frac{3z^2}{r^2}\right). \quad (1.42)$$

Here $\mathbf{r} = (\rho, \phi, z)$ is the distance between the two molecules, μ the reduced mass, C_6 the van der Waals coefficient and m the projection of the angular momentum of collision. For chemically reactive molecules two-body loss will occur with unit probability at a typical interaction distance of $a_{\text{ch}} \lesssim 1\text{nm}$ [32]. The combination of low collision energies, a strong confinement in the z -direction and the repulsive part of the dipole-dipole interaction can result in repulsive potential barrier (see Fig. 1 of [32]) that prevents the molecules from entering the molecular *core region* where the chemical reaction takes place. Since fermionic molecules in the same internal state can only collide in p-wave collisions $|m| = 1$ an additional centrifugal barrier further stabilizes the system. For chemically stable molecules (e.g. $^{23}\text{Na}^{40}\text{K}$) two-body loss is absent and the dominant loss channel will be three-body loss. In contrast to the reactive species, that do not exhibit scattering resonances, the three-body loss rate could be drastically increased by the existence of near threshold bound states [32]. Since the magnitude of the three-body loss coefficient has not been estimated, it seems reasonable to treat the $^{23}\text{Na}^{40}\text{K}$ molecule in a quasi-2D geometry in the same way as a reactive molecule and obtain a worst case scenario when considering collisional stability.

I will now follow the discussion in [31, 26, 34] and estimate whether it could be possible to observe a quantum phase transition from a Fermi liquid to a dipolar crystal in a quasi-2D geometry with $^{23}\text{Na}^{40}\text{K}$ using our current experimental setup. To this end the following quantities have to be determined:

1. The critical 2D density at which a dipolar crystal is energetically favorable for a given effective dipole moment d_{eff} at $T = 0$.
2. The melting temperature at which the crystal will be destroyed by thermal fluctuations.
3. The critical 2D density at which the system will become unstable due to chemical reactions.

Note that it will be impossible to observe dipolar crystallization if the system becomes unstable before the critical density for the dipolar crystal is reached. I assume that the maximal dipole moment is given by $d_{\text{max}} = 1.35D$ (see section 1.1) and the trapping frequency in z -direction is $\omega_z = 150\text{kHz}$. According to [34] the dipolar crystallization density is reached when

$$k_F \cdot a_{dd} = \sqrt{4\pi n_{2D}} \cdot a_{dd} \simeq 25, \quad (1.43)$$

where k_F is the Fermi momentum and n_{2D} the 2D density of molecules. At the maximally attainable dipole moment of $d_{\text{max}} = 1.35D$ crystallization requires a 2D density of:

$$n_{2D} \geq 1.7 \cdot 10^9 \frac{1}{\text{cm}^2} \quad (1.44)$$

The maximal interparticle distance is given by $a_{max} \leq 245\text{nm}$. According to [26, 31] the potential barrier given by equation 1.42 stabilizes the system for interparticle distances that are larger then

$$a_{min} = \left(\frac{12d_{\text{eff}}^2}{4\pi\epsilon_0 m \omega_z^2} \right)^{1/5} \simeq 120\text{nm} \quad (1.45)$$

The first thing to note is that the system should become crystalline before it becomes unstable. The (classical) melting temperature of a dipolar crystal is related to the interparticle distance a via [26]:

$$T_{melt} \simeq \frac{0.089D^2}{4\pi\epsilon_0 a^3 k_B} \quad (1.46)$$

For the interval $a_{min} < a < a_{max}$ the melting temperature ranges from 700nK to 82nK. The exact phase diagram (in the parameter space spanned by the temperature T and the interaction strength $\sqrt{4\pi n_{2D}} \cdot a_{dd}$) is still being debated on and many open questions remain to be explored experimentally (compare the discussions in [26, 34]).

1.1.5 Lattice models and quantum magnetism

Another class of potential experimental configurations that could be realized with ultra-cold polar molecules is concerned with long-range interacting lattice spin-models. This section is mainly based on the original publications [23, 35] and motivated by the first experimental observation of dipolar spin-exchange interaction for lattice confined $^{40}\text{K}^{87}\text{Rb}$ molecules [22]. In this section I will again estimate the relevant experimental parameters for the $^{23}\text{Na}^{40}\text{K}$ molecule and our current experimental setup.

In [23] it is shown how polar molecules that are trapped in the lowest band of a 3D optical lattice can be used to simulate a generalization of the t-J model that is believed to capture the essential mechanism responsible for high temperature superconductivity [10]. This generalization is termed the t-J-V-W model. The tight-binding Hamiltonian of this model is given by:

$$H = - \sum_{\langle i,j \rangle m} t [b_{im}^\dagger b_{jm} + h.c.] + \frac{1}{2} \sum_{i \neq j} |\mathbf{r}_1 - \mathbf{r}_2|^{-3} \times \left[J_z S_i^z S_j^z + \frac{J_\perp}{2} (S_i^+ S_j^- + S_i^- S_j^+) + V n_i n_j + W (n_i S_j^z + n_j S_i^z) \right]. \quad (1.47)$$

The first term in 1.47 describes tunneling of the molecules between neighboring lattice sites. The operator c_{im}^\dagger creates a fermionic molecule at lattice site i in a dressed (by DC or MW electric fields) rotational state $|m\rangle$ with $m \in \{m_0, m_0\}$. The gain in energy is determined by the *hopping matrix element* t between adjacent sites i, j [36]:

$$t = - \int d^3 r w(\mathbf{r} - \mathbf{r}_i) \left(\frac{-\hbar^2 \nabla^2}{2m} + V_{\text{trap}}(\mathbf{r}) \right) w(\mathbf{r} - \mathbf{r}_j), \quad (1.48)$$

where the *Wannier functions* $w(\mathbf{r} - \mathbf{r}_i)$ are related to the lowest band *Bloch function* $\psi_{0\mathbf{k}}(\mathbf{r})$ of the optical lattice via a discrete Fourier transform [37]:

$$\psi_{0\mathbf{k}}(\mathbf{r}) = \sum_i w(\mathbf{r} - \mathbf{r}_i) \exp(i\mathbf{r}_i \cdot \mathbf{k}). \quad (1.49)$$

The second term is the dipole-dipole interaction. The remaining operators that appear in 1.47 are defined as: $n_{im} = c_{im}^\dagger c_{im}$, $n_i = \sum n_{jm}$, $S_i^+ = c_{im_0}^\dagger c_{im_1}$, $S_i^z = (n_{im_0} - n_{im_1})/2$. The coupling coefficients J_z (spin-spin interaction), V (density-density interaction) and W (spin-density interaction) are related to the induced dipole moment of each dressed rotational state [35], whereas J_\perp (spin-exchange interaction) arises from the transition dipole moment between the rotational states. It is shown in detail in [23] that by using suitable electric DC and MW fields that couple and dress the six lowest lying rotational states all four coupling parameters can be controlled. In contrast to the cold atom realization of the t-J model [38] where $J \ll t$, it is possible to tune J_z and J_\perp independently from each other and from the hopping matrix element t . In [22] a next-neighbor spin exchange interaction with $J_\perp/2h \simeq 50\text{Hz}$ has been realized with $^{40}\text{K}^{87}\text{Rb}$ molecules in a 3D optical lattice ($\lambda = 1064\text{nm}$). However, the lattice filling fraction of $\simeq 10\%$ did not allow to observe strong correlations. Replacing $^{40}\text{K}^{87}\text{Rb}$ by $^{23}\text{Na}^{40}\text{K}$ would increase the next-neighbor spin-exchange interaction to $J_\perp/2h \simeq 1\text{kHz}$. In addition, the absence of the two-body loss mechanism for the $^{23}\text{Na}^{40}\text{K}$ molecule should facilitate to achieve a higher lattice filling fraction and also to allow for particle tunneling. For these reasons the observation of the competition between spin-exchange and particle tunneling in a strongly correlated many-body system seems to be feasible by using $^{23}\text{Na}^{40}\text{K}$ molecules.

The experimental setup

The main task of this PhD project was the construction of a novel experimental apparatus deliberately designed to study dipolar interactions in an ultracold sample of fermionic $^{23}\text{Na}^{40}\text{K}$ molecules. The complete project can be subdivided into sequential experimental steps:

1. Preparation of a degenerate Bose-Fermi mixture of ^{23}Na and ^{40}K atoms.
2. Identification of Feshbach resonances suitable for molecule association.
3. Association of weakly bound Feshbach molecules as a starting point for coherent groundstate transfer.
4. Identification of a suitable molecular three-level system by high-resolution molecular spectroscopy that can be used for STIRAP to the rovibronic groundstate.
5. Preparation of a high phase-space density sample of groundstate molecules by STIRAP.
6. Application of strong electric fields to induce dipole forces between the molecules.
7. Detection of dipolar many-body effects in different trap geometries (3D, 2D, optical lattice).

This chapter gives an overview of the design considerations, setup construction and the experimental implementation. The various subsystems are described and their performance is characterized. The current experimental setup is capable of creating a high density degenerate Bose-Fermi mixture of ^{23}Na and ^{40}K atoms in their lowest energy hyperfine state configuration (i.e. $F = 1, m_F = -1$ for ^{23}Na and $F = 9/2, m_F = 9/2$ for ^{40}K). The mixture can be transported in vacuum to a separate glass science cell, where quantum degeneracy is obtained for both species. The internal state configuration of the atoms can be prepared with high efficiency ($> 95\%$) by coherent RF manipulations. Precise control of an external magnetic field then enables us to address inter-species Feshbach resonances. In the vicinity of a Feshbach resonance the magnitude and sign of the low-temperature inter-particle interaction can be adjusted at will by changing the external magnetic field. Moreover the least bound vibrational state of the spin-triplet $^{23}\text{Na}^{40}\text{K}$ groundstate potential can be populated by RF association of Feshbach molecules. In addition, photo-association

spectroscopy of the near-degenerate $^{23}\text{Na}^{40}\text{K}$ mixture can be performed as well as high resolution spectroscopy of Feshbach molecules. To this end a narrow linewidth Raman laser system has been constructed, that allowed us to observe coherent population trapping in a molecular three level system formed by the Feshbach molecule, the rovibronic groundstate and an intermediate level in the spin-orbit coupled $d^3\Pi/D^1\Pi$ complex. This laser system will also be used in future STIRAP experiments. In order to realize strong dipole forces between groundstate molecules the setup features in-vacuum field electrodes that allow us to apply the electric fields of $\simeq 5\text{kV}/\text{cm}$. The attainable effective dipole moment for groundstate molecules $d_{eff} \simeq 1.3D$ would result in interaction energies that are one order of magnitude larger compared to previous experimental realizations of ultracold groundstate molecules [18]. Finally, the large optical access of the science cell facilitates the future implementation of optical lattices and a high resolution imaging system.

2.1 Design considerations

The design of our experimental setup is targeted on maximizing the effects of dipolar interactions. Therefore the key quantities that need to be considered for setup design are the strength S_{dd} of the dipole-dipole interaction between the molecules in a quantum gas with density n_0 given by (compare equation 1.3):

$$S_{dd} = \frac{d_{eff}^2}{4\pi\epsilon_0} n_0 \quad (2.1)$$

and the Fermi energy of the gas as $T \rightarrow 0$:

$$\epsilon_F = \frac{\hbar^2}{2m} (6\pi^2 n_0)^{2/3}. \quad (2.2)$$

Here d_{eff} is the induced dipole moment in presence of an external electric field. The ratio of both quantities is given by:

$$\frac{S_{dd}}{\epsilon_F} = \frac{2md_{eff}^2}{4\pi\epsilon_0\hbar^2(6\pi^2)^{2/3}} \cdot n_0^{1/3} \quad (2.3)$$

For a given type of molecule (see section 1) setup design is therefore focused on creating high density samples of groundstate molecules and on realizing strong electric fields. In addition, the implementation of a 1D or 3D optical lattice is required for observing new quantum states of matter [39] or the simulation of spin lattice models with long-range interactions [23]. Moreover, a high resolution imaging system could become imperative for observing density modulations due to dipole forces or even dipolar crystallization phenomena. This reasoning motivates the following design decisions:

1. Separate the atom sources for ^{40}K and ^{23}Na from the part of the setup where laser and evaporative cooling take place. This should ensure better vacuum quality and larger initial atom numbers.
2. Include an intermediate magnetic trap after the initial *magneto optical trap* (MOT) phase to facilitate efficient sympathetic cooling of fermionic ^{40}K by bosonic ^{23}Na .

3. Load a single beam optical dipole trap after pre-cooling in the magnetic trap and transport the mixture to a separate glass science chamber with large optical access and good vacuum quality.
4. Place electrodes for generating strong electric fields inside the vacuum system without obstructing optical access.
5. Place magnetic field coils and RF equipment around the science cell for precise magnetic field control and efficient hyperfine state manipulation.
6. Construct a versatile and frequency tuneable Raman laser system for high-resolution molecular spectroscopy and coherent groundstate spectroscopy.

The next sections describe the various subsystems of the experimental setup in detail.

2.2 Overview

The system architecture for the complete experimental setup is displayed in Fig. 2.1. Ultra-cold samples of ^{40}K and ^{23}Na atoms have to be prepared in an ultra high vacuum (UHV) environment ($p < 10^{-11}\text{mbar}$) that serves as thermal insulation and suppresses background gas collisions. The UHV system also comprises the sources for both atomic species. For laser cooling and imaging, a separate laser system is required for each chemical element. Additional laser systems have been constructed in order to trap, transport and evaporatively cool the $^{23}\text{Na}^{40}\text{K}$ mixture in optical dipole traps as well as perform high resolution molecular spectroscopy on $^{23}\text{Na}^{40}\text{K}$ molecules. Radio frequency (RF) ($\omega < 2\pi \cdot 1\text{GHz}$) and microwave ($\omega > 2\pi \cdot 1\text{GHz}$) (MW) equipment is required to perform internal state manipulations on both atomic species. Magnetic field coils and fast, high precision current controllers are used to generate various magnetic fields for atom trapping, to compensate environmental fields, to induce a Zeeman splitting between internal states of the atoms and to address magnetic field controlled scattering resonances. Finally, high voltage power supplies generate in combination with in vacuum steel electrodes static electric fields that can produce a DC Stark shift on molecular transitions and will be used to induce the dipole moment for groundstate molecules inside the vacuum chamber. All subsystems are controlled from a central real-time experiment control unit with a timing resolution of $4\mu\text{s}$. In the current configuration the control system features 32 digital to analog converters that are used for remote control of various experimental parameters (e.g. laser frequencies, laser intensities, magnetic field values, etc.) and 96 digital output channels that are used for precisely timed switching of relevant equipment. Every experimental run is finished by taking one or several absorption images of the atomic or molecular samples, that have been prepared and manipulated during the preceding experimental sequence. Image processing and data analysis is performed on a standard personal computer via custom developed software written in Python.

System architecture $^{23}\text{Na}^{40}\text{K}$ polar molecules setup

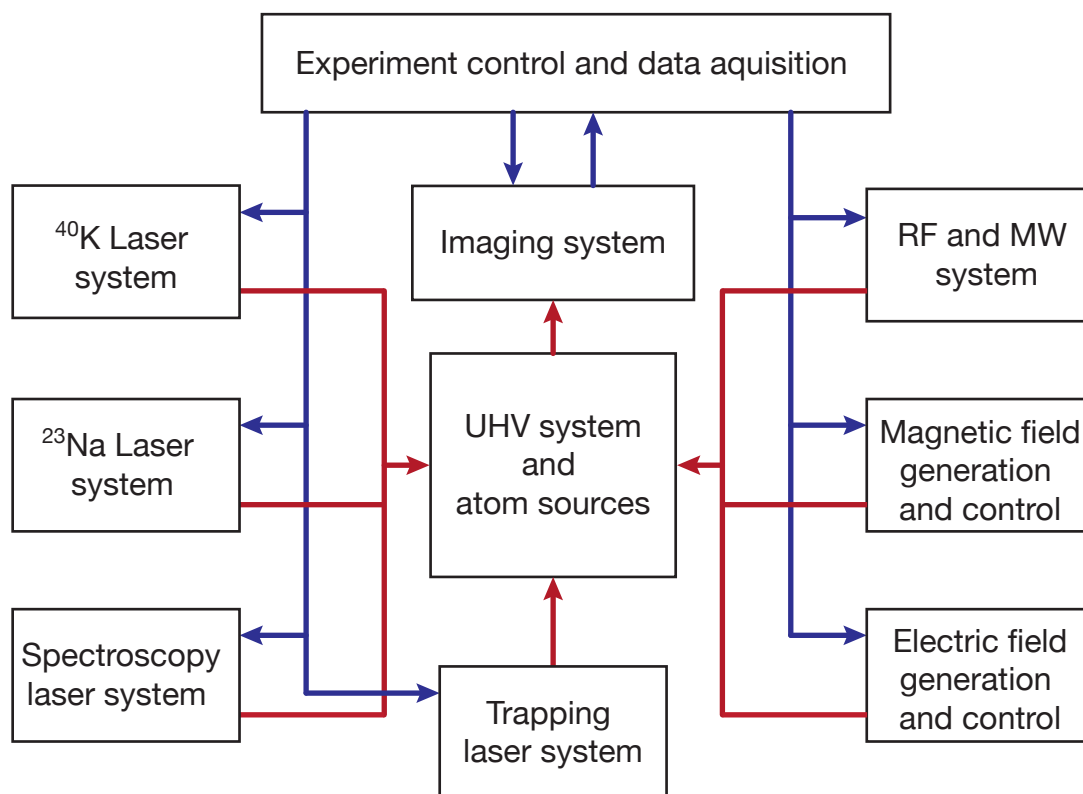


Figure 2.1 – Current system architecture of the experimental setup. Ultracold atomic and molecular samples are prepared, manipulated and imaged inside a ultra high vacuum environment. All relevant subsystems interact with the atoms and molecules via magnetic, electric, RF, MW or laser fields (red arrows). The experiment is controlled (blue arrows) via a real-time processing unit while images of the ultracold gases are processed and analyzed on a separate personal computer.

2.3 Ultra high vacuum system

The computer aided design (CAD) model shown in Fig. 2.2 displays the current vacuum system. The optical assemblies that are used for laser beam routing are constructed around the vacuum system. Together they constitute the main part of the experimental setup and are located on a separate vibration isolated optical table in the center of the laboratory. The various laser systems are held by two additional tables. Optical fibers connect them to the main setup. The enclosure of each table is temperature stabilized to $\pm 0.1^\circ\text{C}$ and equipped with air flow boxes that provide a dust free environment for the optical setups. The main features of the setup are a spin-flip Zeeman slower for ^{23}Na atoms, a 2D-MOT for ^{40}K , a steel chamber with re-entrant windows and anti-Helmholtz coils, the glass science cell with electric field electrodes and a large surface pump chamber that has been coated with a non-evaporative getter (NEG) material. The dual-species MOT and the subsequent magnetic trap are operated in the steel MOT chamber. After combined evaporation in the magnetic trap the mixture is transported to the science cell by a moving optical dipole

trap. Two different source regions for both atomic species are separated from the main experimental chamber by differential pumping sections to ensure a vacuum quality of $p < 10^{-11}$ mbar inside the MOT chamber and the glass science cell. A beam of cold ^{23}Na atoms is generated by a spin-flip Zeeman slower. ^{23}Na vapor effuses with an average axial velocity of $\simeq 900\text{m/s}$ from a custom designed recirculating atom oven kept at 330°C . The reflow tube in combination with a small aperture skimmer significantly reduces the amount of ^{23}Na that is lost during setup operation - the initial sample of 25g of purified ^{23}Na is still in use after more than 3 years of operation. The oven is followed by a pneumatic atomic beam shutter, a dual stage differential pumping section, an all-metal gate valve and the water cooled coil assembly of the Zeeman slower. A NEG pump is attached to the zero field section of the Zeeman slower. The cold beam of ^{40}K atoms is generated by a standard 2D-MOT assembly that is kept at 60°C and separated from the main experimental chamber by a single stage differential pumping section. The stainless steel MOT chamber features re-entering bucket windows that allow for a short distance between the atomic samples in the center of the chamber and the water cooled magnetic field coil assembly. The field coils are connected in Anti-Helmholtz configuration and can generate a magnetic quadrupole trap with a maximal field gradient of $\simeq 1000\text{G/cm}$ along the symmetry axis. The same coils are also used for MOT operation at a gradient of $\simeq 10\text{G/cm}$. The beams for dual species laser cooling, imaging, dipole trapping and molecular spectroscopy enter the MOT chamber through AR coated, non-magnetic vacuum viewports. A non-AR coated glass science cell is attached to the MOT chamber. Electric field electrodes are installed inside the glass cell and isolated by a Markor support structure. The electrodes are connected via a high voltage vacuum feed through. UHV is sustained by three ion pumps located at the source sections and a separate pump chamber that consists of a large surface tube that is coated by NEG material, a Titanium sublimation pump and an additional ion pump. The inside of the MOT chamber is also coated by the same NEG material. Vacuum quality is measured at the source sections and the pump chamber by Bayard-Alpert ionization gauges.

2.4 $^{23}\text{Na}^{40}\text{K}$ Bose-Fermi mixture - overview of the experimental sequence

Fig. 2.3 illustrates how degenerate Bose-Fermi mixtures of $^{23}\text{Na}^{40}\text{K}$ atoms are produced in our experimental setup. Cold beams of both species are generated by a spin-flip Zeeman slower [40] and a 2D-MOT [41]. Inside the stainless steel chamber a standard D2-line dual species MOT is simultaneously operated. Initial MOT loading is followed by a compressed MOT (C-MOT) [42] phase that increases the central density of the atomic gas by reducing the photon scattering rate. We achieve this by decreasing the repump power and increasing the detuning of the cooling laser beams.

After compression in the C-MOT is completed, the MOT lasers and field gradient are switched off and both species are optically pumped by a circularly polarized dual wavelength laser beam to the low field seeking stretched states (i.e. $|F = 2m_F = 2\rangle$) for ^{23}Na

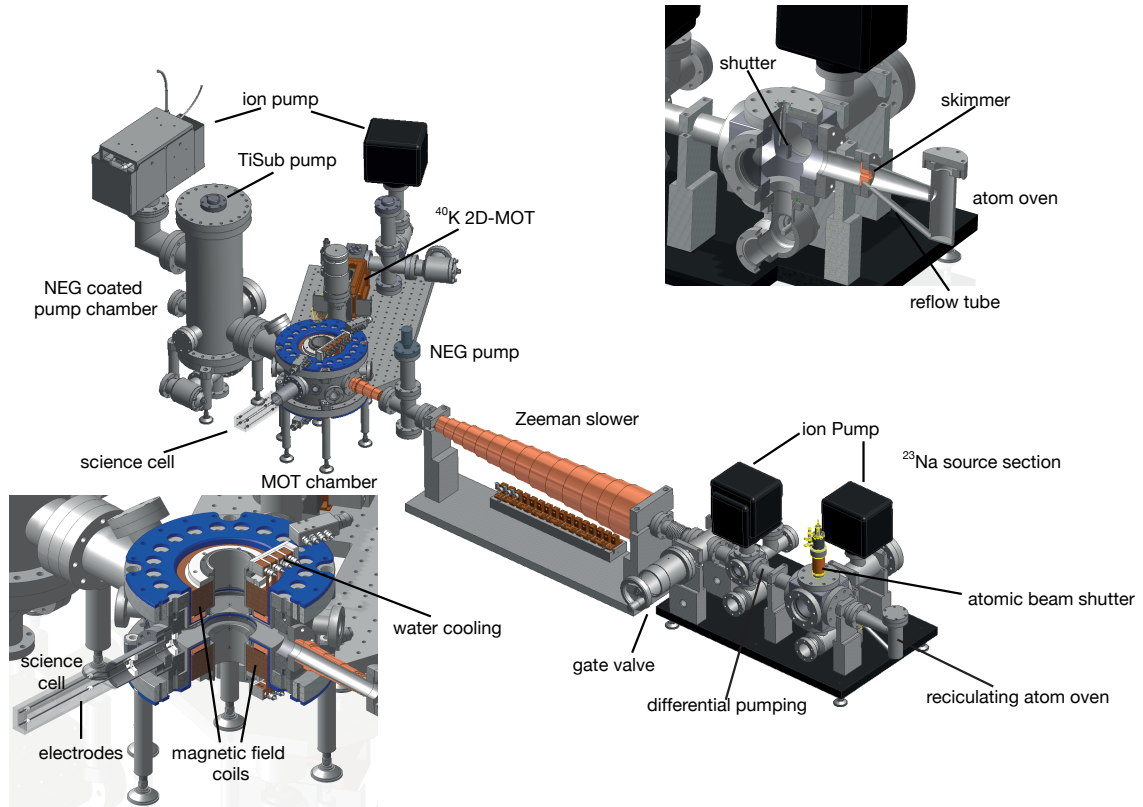


Figure 2.2 – CAD model of the current UHV system. The source regions for both atomic species are separated from the main experimental chamber. The MOT chamber features re-entering bucket windows and a water cooled magnetic field coil assembly that is used for MOT operation and a magnetic quadrupole trap. The beams for laser cooling, imaging, dipole trapping and molecular spectroscopy enter the MOT chamber through AR coated, non-magnetic vacuum viewports. A glass science cell is attached to the MOT chamber. Electric field electrodes are installed inside the glass cell. UHV is sustained by three ion pumps located at the source sections and a high yield pump chamber. Vacuum quality is measured by Bayard-Alpert ionization gauges. More details are given in the main text

and $|F = 9/2, m_F = 9/2\rangle$ for ^{40}K). We then swiftly ramp on the magnetic quadrupole trap to a gradient of 250G/cm. We use three pairs of compensation coils to ensure best overlap between the C-MOT position and the center of the magnetic trap. A *plug laser* ($\lambda = 532\text{nm}$, $P = 5\text{W}$, $w_0 = 50\mu\text{m}$) is directed to the center of the magnetic trap in order to suppress so called Majoranan losses [43] - diabatic spin-flips to high field seeking states. The field gradient is then gradually lowered to 8.25G/cm a value at which only both stretched states are still supported against gravity. This obligatory spin-purification step is necessary to suppress spin-exchange collision [1] - which do not occur for atoms in their stretched states due to conservation of angular momentum. After a spin purified sample has been obtained the field gradient is again increased to 250G/cm and the $^{23}\text{Na}^{40}\text{K}$ mixture is cooled from an initial temperature of $\simeq 2\text{mK}$ to $\simeq 6\mu\text{K}$ by forced MW evaporation on the $F = 2 \rightarrow F = 1$ hyperfine transition of ^{23}Na . The large inter-species scattering length of $\simeq -690a_0$ [44] facilitates efficient sympathetic cooling of fermionic ^{40}K atoms. In order to avoid the detrimental effects of intra-species and inter-species

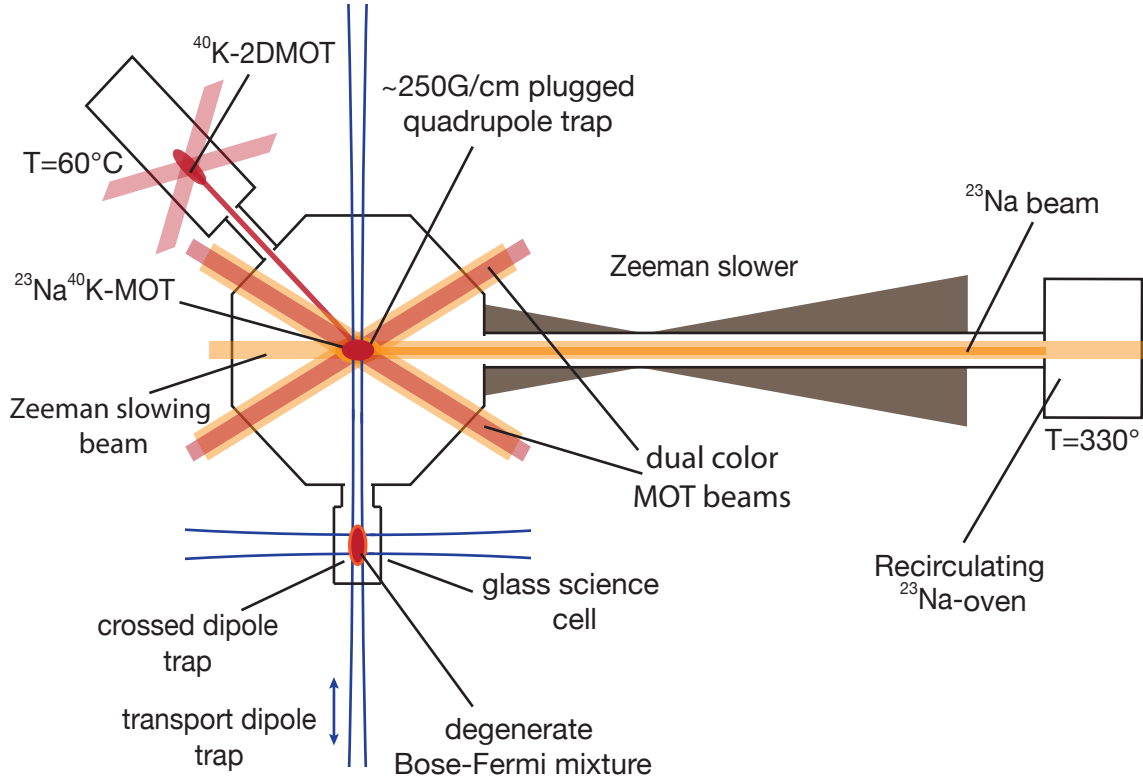
Setup for producing $^{23}\text{Na}^{40}\text{K}$ Bose-Fermi mixtures

Figure 2.3 – Schematic illustration of the experimental setup that is used to produce degenerate Bose-Fermi mixtures of $^{23}\text{Na}^{40}\text{K}$ atoms. Cold beams of ^{23}Na and ^{40}K are generated by a Zeeman slower and a 2D-MOT. The atoms are simultaneously laser cooled in a dual color MOT inside a stainless steel chamber that is isolated from the high pressure oven regions by differential pumping sections. After MOT loading is completed the mixture is evaporatively cooled to $\simeq 6\mu\text{K}$ in a plugged magnetic quadrupole trap. The mixture is then loaded to a single beam dipole trap and transported to the science cell, where quantum degeneracy is obtained by subsequent evaporation in a crossed dipole trap.

three-body loss the magnetic field gradient is gradually decreased to 40G/cm during the evaporation sequence. Since the three-body loss rate scales quadratically with the density of ^{23}Na for both loss channels whereas the thermalization coefficient only linearly, runaway evaporation defined by [45]

$$\frac{dn_{Na}/dt}{n_{Na}(t)} = -\alpha \frac{dN_{Na}/dt}{N_{Na}(t)}, \quad \text{with } \alpha > 0 \quad (2.4)$$

can be maintained during the entire evaporation sequence. Here $\frac{dN_{Na}/dt}{N_{Na}(t)}$ is the instantaneous loss rate of ^{23}Na atoms due to the evaporation process and n_{Na} is the density of ^{23}Na atoms. Runaway evaporation occurs when the density in the trap increases although the total atom number decreases by evaporation. It is termed runaway, because with increasing density also the thermalization rate increases and therefore evaporation efficiency [45]. 2.1MHz above trap floor MW evaporation is stopped and the magnetic field gradient is decreased to 0.1G/cm. Simultaneously, a single beam optical dipole trap

($\lambda = 1064\text{nm}$, $P = 7.5\text{W}$, $w_0 = 40\mu\text{m}$) that is overlapped with the potential minimum of the magnetic trap is ramped to full power. In addition, a magnetic guiding field of $\simeq 1\text{G}$ is applied along the symmetry axis of the magnetic trap. Directly after dipole trap loading we perform a Landau Zener MW sweep for ^{23}Na from $|F = 2, m_F = 2\rangle$ to $|F = 1, m_F = 1\rangle$ in order to suppress inelastic hyperfine state changing collisions [44]. The mixture is now spin polarized in the lowest energy hyperfine state combination

$$|F = 1, m_F = 1\rangle_{\text{Na}} \otimes |F = 9/2, m_F = 9/2\rangle_{\text{K}} \quad (2.5)$$

The mixture is then transported in 0.75s to the glass science cell by moving the focus position of the single beam dipole trap using an air bearing translation stage. In the science cell a 14.5G guiding field is applied along the direction of gravity. The final evaporation step to quantum degeneracy is then performed in a crossed dipole trap formed by the transport trap and an additional laser beam ($\lambda = 1550\text{nm}$, $P = 4\text{W}$, $w_0 = 100\mu\text{m}$). The relative atom number of both species can be adjusted by changing the loading time of the ^{40}K MOT from 0s to 4s while ^{23}Na is always loaded for 4s. This (near-)degenerate Bose-Fermi mixture of $^{23}\text{Na}^{40}\text{K}$ serves as the starting point for further experiments that deal with inter-species Feshbach resonances, photoassociation spectroscopy of the excited molecular level structure in the spin-orbit coupled $d^3\Pi/D^1\Pi$ complex and RF association of weakly bound Feshbach molecules. The next section presents implementation details of the laser cooling subsystem.

2.5 Laser cooling

Laser cooling of alkali atoms relies on the existence of a strong and cycling dipole transition in the atomic energy spectrum, that can be used for continuous momentum transfer by repeated absorption and consecutive spontaneous emission of resonant laser light [46]. A cycling transition is realized if resonant absorption and spontaneous emission only happen between the same two hyperfine states. For alkali atoms the natural choice is to couple the stretched hyperfine state of the $S_{1/2}$ groundstate manifold i.e. $|F = I + 1/2, m_F = F\rangle$ to the stretched hyperfine state of the $P_{3/2}$ excited state of the D2-line, i.e. $|F' = I + 3/2, m'_F = F'\rangle$ via σ_+ -polarized laser light. Since for alkali atoms the excited state hyperfine splitting is on the order of a few times the natural linewidth Γ non-resonant excitation of non-stretched hyperfine states can result in spontaneous decay to the lower hyperfine state of the groundstate manifold i.e. $|F = I - 1/2, m_F\rangle$. An additional laser that is resonant with the so called repump transition from $|F = I - 1/2, m_F\rangle$ to $|F' = I + 1/2, m'_F\rangle$ ensures that the atom is always pumped back to the cycling transition. The momentum transfer from the laser to the atom happens in direction of the laser beam and depends on the intensity of the laser and the detuning with respect to the cycling transition. The effective scattering force is given by:

$$F_{sc}(I, \Delta) = \frac{d\mathbf{p}}{dt} = \frac{\Gamma}{2} \hbar \mathbf{k} \cdot \frac{I/I_{sat}}{1 + I/I_{sat} + (2\Delta/\Gamma)^2}, \quad (2.6)$$

where I is the intensity of the laser measured in W/cm^2 , $|\hbar \mathbf{k}| = \frac{\hbar \omega_l}{c}$ is the photon momentum and $\Delta = \omega_l - \omega_0$ the detuning of the laser frequency with respect to the cycling

transition frequency. The saturation intensity I_{sat} is related to the Rabi frequency Ω via:

$$I_{sat} = \frac{I}{2} \cdot \frac{\Gamma^2}{\Omega^2} \quad (2.7)$$

In contrast to the momentum change that is caused by the absorption of photons from the laser beam the momentum change due to spontaneous emission is uncorrelated. The atom therefore undergoes a random walk in the plane perpendicular to the direction of the laser. Laser cooling now relies on the fact that the detuning Δ in equation 2.6 depends via the Doppler shift on the momentum component of the atom in direction of the laser beam. For thermal atoms that are trapped and cooled in our experiment the non-relativistic doppler shift $\Delta_D(v_z)$ is given by

$$\Delta_D(v_z) = \omega_0 \cdot \frac{v_z}{c}, \quad (2.8)$$

where ω_0 is the bare atomic transition frequency and $v_z = p_z/m$ the velocity component of the atom in direction of the laser beam. Adjusting the laser frequency such that it is red detuned with respect to the bare atomic transition frequency ensures that atoms that are counter-propagating with respect to the laser beam are shifted towards resonance by the Doppler effect; co-propagating atoms are shifted out of resonance. Therefore the average velocity of a thermal atomic sample is reduced in direction of the laser beam. The natural laser beam configuration for laser cooling then consists of six pairwise counter-propagating laser beams that are orthogonal to each other and are red detuned with respect to the D2-line cycling transition of an alkaline atom. This configuration is also called an *optical molasses* [46], since the velocity dependent three dimensional scattering force results in a friction-like behavior for atomic motion in the region where the laser beams overlap. The optical molasses configuration can be combined with a weak magnetic quadrupole field that induces a position dependent Zeeman shift between the the different m_F components of the $F = I + 1/2$ groundstate and the $F = I + 3/2$ excited state. Adjusting the laser polarization to σ_+ with respect to the magnetic field direction for all six cooling beams results in a position dependent restoring force. This extension of the optical molasses is called a *magneto optical trap* (MOT) [46]. In a MOT the scattering force F_{sc} is rendered position dependent and velocity dependent in such a way that alkali atoms are simultaneously trapped and cooled by continuous absorption-emission cycles.

2.5.1 Laser system and Zeeman slower for ^{23}Na

Fig. 2.4 shows the atomic fine and hyperfine structure of the states that form the D2-line in ^{23}Na [47]. The cycling and the repump transitions are indicated. Since the hyperfine splitting between the $F = 3$ component and the adjacent $F = 2$ component in the $3^2P_{3/2}$ state is $58.3 \simeq 6\Gamma$, the rate of unwanted non-resonant excitation is suppressed by more than two orders of magnitude (see equation 2.6). Therefore the repump beam can be much weaker than the cooling laser to ensure continuous absorption and re-emission of photons from the cooling beams. The groundstate hyperfine splitting is 1771.6MHz. The repump laser therefore has to be blue detuned with respect to the cooling laser by 1713.3MHz.

The laser cooling setup (see Fig. 2.3) for ^{23}Na consists of a standard D2-line MOT [46] operated in the main vacuum chamber and an effusive atom oven that is separated from

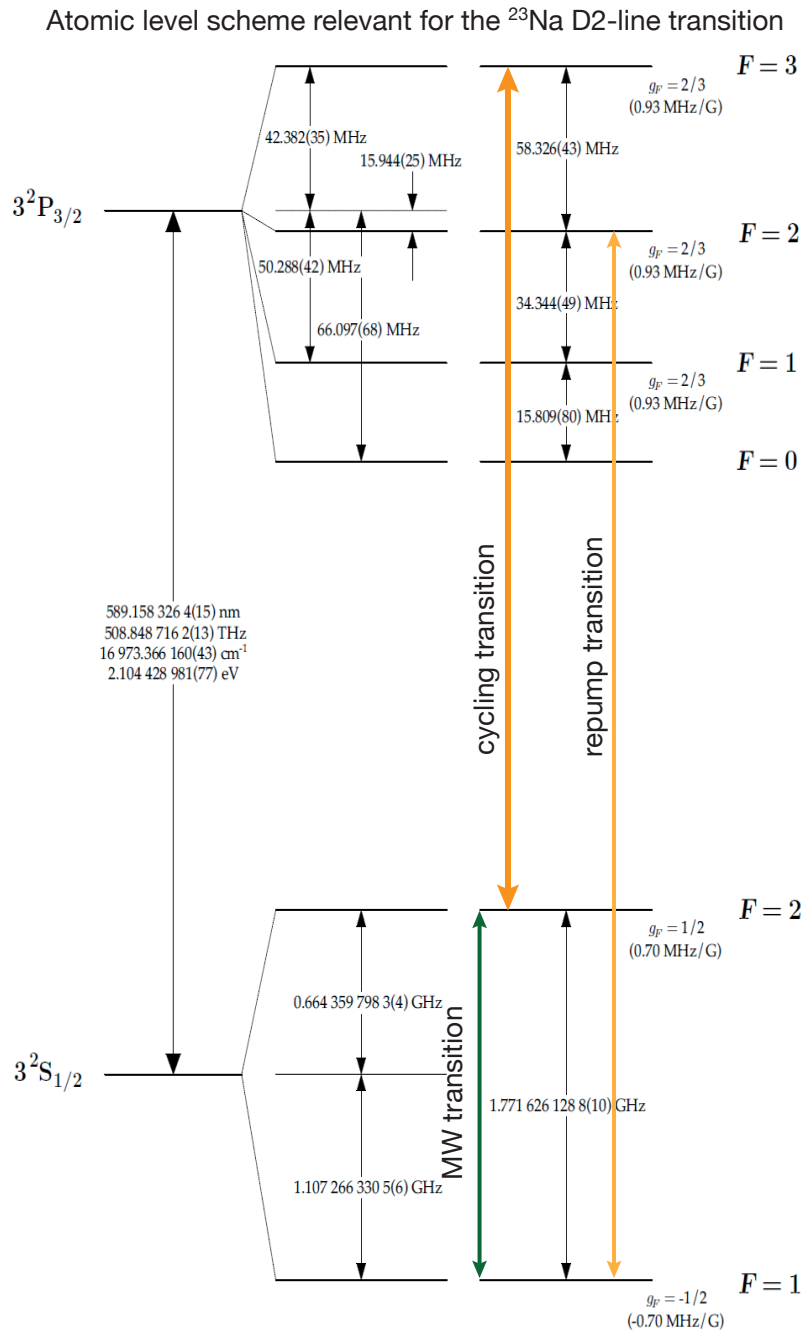


Figure 2.4 – Atomic energy spectrum of the D2-line of ^{23}Na modified from [47]. The cycling and repump transition used for laser cooling and imaging of ^{23}Na atoms are indicated. Due to the resolved excited state hyperfine splitting the repump laser can be $\simeq 100$ times less intense than the cooling laser. The groundstate hyperfine transition that is used for MW evaporation in the magnetic trap is indicated by the green line.

the main chamber by a dual stage differential pumping section. The number of atoms that can be trapped and cool in a MOT is determined by a dynamical equilibrium between the capture rate of the MOT and the sum of various decay rates. Therefore it is desirable to make the capture rate of the MOT as large as possible. The capture rate of the MOT is determined by the flux density of ^{23}Na atoms at the MOT region that have a small

enough velocity to be trapped. The capture velocity of the MOT depends on the detuning, geometry and the intensity of the MOT lasers via equation 2.6 and for typical experimental parameters is on the order of 30–50m/s. Since ^{23}Na has to be heated to obtain a significant fraction of atoms in the gas phase, loading the MOT directly from an effusive atom oven is inefficient due to a thermal velocity distribution with almost no weight below the capture velocity. The vapor pressure of ^{23}Na in the liquid phase ($T > 98^\circ\text{C}$) is calculated by [47]

$$P_{liq}(T) = 133.32 \cdot 10^{(10.86 + \frac{5619.41}{T} - 1.04 \log_{10}(T))} \frac{N}{m^2}. \quad (2.9)$$

The atomic density is then given by

$$n(T, P_{liq}) = \frac{P_{liq}(T)}{k_b T}. \quad (2.10)$$

At a temperature of $330^\circ\text{C} = 603.15\text{K}$ the vapor pressure of ^{23}Na is $\simeq 0.4\text{mbar}$ and the density is $\simeq 7.2 \cdot 10^{14} \frac{1}{\text{cm}^3}$. The kinematics of atomic and molecular beam experiments are reviewed in [48, 49]. To calculate the atom flux and the axial velocity distribution in the ^{23}Na beam one has to take into account that the skimmer functions as a transvers velocity filter for the atomic beam. Only atoms that fulfill

$$v_t < \frac{v_z \cdot r_s}{l_s} \quad (2.11)$$

can exit the oven and contribute to the flux present at the MOT region. Here v_t and v_z are the transvers and the axial velocity of the atom, l_s is the distance between the oven aperture and the skimmer and r_s the radius of the skimmer aperture. Starting from the Maxwell-Boltzmann distribution for v_t and v_z in cylindrical coordinates

$$f(v_z, v_t) = 2\pi v_t \left(\frac{m_{Na}}{2\pi k_b T} \right)^{3/2} \exp\left(-\frac{m_{Na}(v_t^2 + v_z^2)}{2k_b T} \right) \quad (2.12)$$

the axial flux j_{Na} of the collimated atom beam can be estimated by

$$j_{Na}(T) = \pi r_o^2 \cdot n(T, P_{liq}) \int_0^\infty \int_0^{\frac{r_s v_z}{l_s}} v_z \cdot f(v_z, v_t) dv_t dv_z. \quad (2.13)$$

Here r_o is the radius of the oven aperture. Taking the exact geometry of our experimental setup, we estimate a total flux of sodium atoms at the MOT region of $\simeq 2.4 \cdot 10^{11} \frac{1}{\text{cm}^2\text{s}}$. The axial velocity distribution in the collimated beam can be derived by normalizing the flux density distribution with the total atom flux $j_{Na}(T)$.

$$f_{beam}(v_z) = \frac{\pi r_o^2 \cdot n(T, P_{liq})}{j_{Na}(T)} \int_0^{\frac{r_s v_z}{l_s}} v_z \cdot f(v_z, v_t) dv_t \quad (2.14)$$

This distribution is shown in Fig. 2.5. The fraction of atoms in the collimated beam that can be captured by a MOT with capture velocity of 50m/s is only 16ppm. The flux of atoms with $v_z < 50\text{m/s}$ is estimated to be $\simeq 3.9 \cdot 10^6 \frac{1}{\text{cm}^2\text{s}}$. In order to increase the fraction of atoms with an axial velocity that is smaller than the capture velocity of the MOT we constructed a spin-flip Zeeman slower [40]. The Zeeman slower consists of two magnetic

Axial velocity distribution of the collimated Na beam

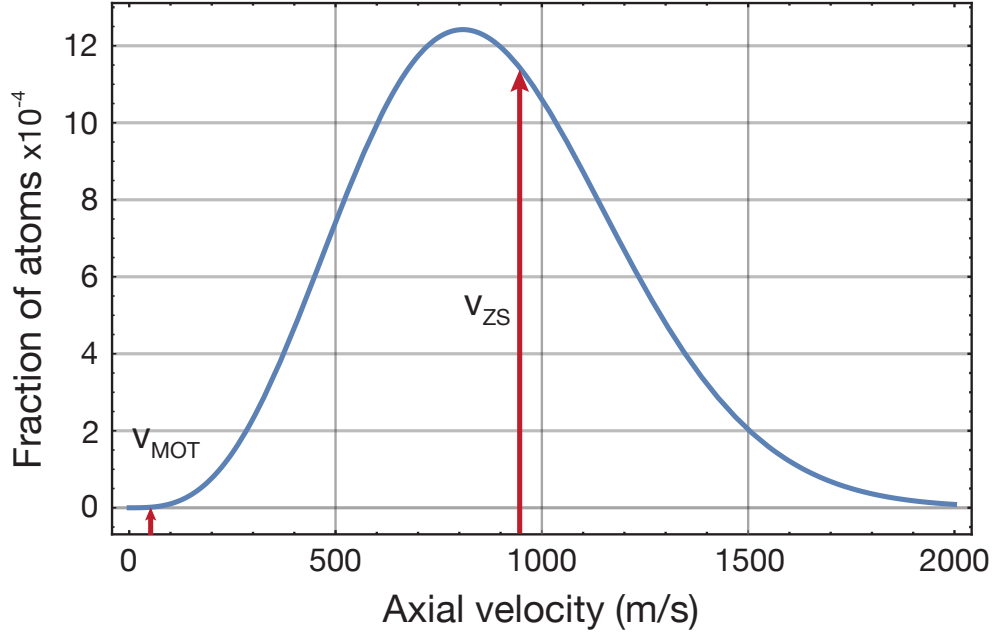


Figure 2.5 – Axial velocity distribution of a collimated ^{23}Na beam effusing from an atom oven at 330°C as calculated by equation 2.14. A working Zeeman slower increases the flux of slow atoms that can be trapped by a MOT by 4 orders of magnitude (red arrows).

field coil assemblies that are built around the vacuum tube that connects the oven section with the MOT chamber (see Fig. 2.3)

A circularly polarized laser beam is counter-propagating to the atomic beam. The laser frequency is red detuned with respect to the ^{23}Na cycling transition (see Fig.2.4). The field coils generate a position dependent axial magnetic field $B(z)$ along the atomic beam direction. Since the cycling transition involves only stretched hyperfine states, the position dependent Zeeman shift is linear for all values of the magnetic field:

$$\Delta_Z(z) = \frac{(g'_F m'_F - g_F m_F) \cdot B(z) \mu_B}{\hbar} = \frac{\delta\mu}{\hbar} \cdot B(z). \quad (2.15)$$

The total position and velocity dependent detuning of the slowing beam with respect to the cycling transition is then given by the sum of the fixed laser detuning Δ_L , the position dependent Zeeman shift $\Delta_Z(z)$ and the velocity dependent doppler shift $\Delta_D(v)$:

$$\Delta_{tot}(v_z, z) = \Delta_L + \omega_0 \cdot \frac{v_z}{c} + \frac{\delta\mu}{\hbar} \cdot B(z). \quad (2.16)$$

Here g_F is the Lande g-factor and μ_B the Bohr magneton. Note that the sign of the Zeeman shift can be changed by changing the direction of the current in the magnetic field coils. An ideal magnetic field configuration would give $\Delta_{tot}(v_z, z) = 0$ along the complete trajectory of an ^{23}Na atom with initial axial velocity v_0 . The resulting constant negative acceleration

is given by

$$a_{res} = F_{sc}(I, 0)/m_{Na} = \frac{\Gamma}{2} \frac{\hbar\omega_l}{c \cdot m_{Na}} \cdot \frac{I/I_{sat}}{1 + I/I_{sat}}, \quad (2.17)$$

For constant negative acceleration the position dependent velocity along the slowing region is given by

$$v(z) = \sqrt{v_0^2 - 2 \cdot a_{res} \cdot z}. \quad (2.18)$$

By solving the resonance condition $\Delta_{tot}(v_z, z) = 0$ for the magnetic field we arrive at an expression for $B(z)$:

$$B_z(z) = -\frac{\Delta_L \cdot \hbar}{\delta\mu} - \frac{\omega_0 \hbar}{\delta\mu} \frac{v_0}{c} \sqrt{1 - \frac{2a_{res}z}{v_0^2}} \quad (2.19)$$

A spin-flip Zeeman slower is realized for a large negative detuning Δ_L . In this configuration the magnetic field first decreases from its initial value $B_z(0)$ to zero, changes direction and then increases again to its final value given by the desired final velocity v_{end} via

$$B_{end} = B_z \left(z = \frac{v_0^2 - v_{end}^2}{2a_{res}} \right) \quad (2.20)$$

The advantage of the spin-flip configuration relies on the fact that the slower beam is far enough red detuned with respect to the bare atomic transition to not interfere with MOT operation. An ideal Zeeman slower increases the capture velocity of the MOT to the capture velocity of the Zeeman slower given by

$$v_{ZS} = -\frac{c}{\omega_0} (\Delta_L + \frac{\delta\mu}{\hbar} \cdot B_0). \quad (2.21)$$

Note that in the last equation B_0 and Δ_L are both negative. A Zeeman slower is designed on basis of three design parameters: the laser detuning Δ_L which affects only the relative length between the increasing and the decreasing field section, the capture velocity v_{ZS} which is chosen such that a major fraction of the axial velocity distribution is captured by the slower, and the laser intensity I_L which is related to the total length of the Zeeman slower. We designed our Zeeman slower according to the following parameters:

$$I_L = 2 \cdot I_{sat}, \quad \Delta_L = -2\pi \cdot 640\text{MHz}, \quad v_{ZS} = 950\text{m/s} \quad (2.22)$$

The fraction of ^{23}Na atoms with a velocity smaller than 950m/s now is 61% resulting in an increase of MOT loading rate by $\simeq 4 \cdot 10^4$. To build the Zeeman slower we approximated the the magnetic field produced by given coil configuration by the field that is generated by an array of current loops with an on axis field given by the Biot-Savart law. The field of a single current loop at position (i, j) in the array is parametrized by:

$$B_z(z, i, j) = \frac{\mu_0 \cdot I}{2(r_T + (i - 0.5)d_t)} \frac{1}{\left(1 + \frac{(z - (j - \delta_j - 0.5)d_z)^2}{(r_T + (i - 0.5)d_y)^2}\right)^{3/2}}. \quad (2.23)$$

Here μ_0 is the magnetic permeability of free space, r_T is the outer diameter of the vacuum tube to which the Zeeman slower coil is attached, d_z and d_t are the outer dimensions of the wire that is used for coil winding and δ_j is the number of current loops in z -direction that

precede the origin ($z = 0$) of the ideal magnetic field from equation 2.19. Typical arrays of current loops are illustrated in Fig. 2.6 and Fig. 2.7. The design has to include a zero field section between the decreasing and the increasing field section that allows for an adiabatic change of the quantization axis as required for optical pumping from the σ_+ to the σ_- cycling transition. Finding the correct winding pattern that best approximates the ideal magnetic field is then a numerical optimization task that includes the geometry of the vacuum system and the dimensions of the wire that is used for the magnetic field coils. Fig. 2.6 and Fig. 2.7 show the winding pattern that resulted from the numerical optimization procedure. Due to a total dissipated electric power of $\approx 300\text{W}$ the decreasing field section is made from hollow core conductor that is also used for water cooling. The whole coil assembly is connected in series such that all current loops carry the same current. The increasing section is wound on a vacuum tube with smaller outer diameter in order to decrease the maximal electric current. Here we also use two separate coils that allow for a better fine tuning of the final velocity of the slowed atomic beam. The simulated magnetic field of the Zeeman slower is shown in Fig. 2.8. A numerical integration of the equation of motion for an atom with initial velocity of 950m/s in presence of the cooling laser and the simulated magnetic field is shown in Fig. 2.9.

Zeeman slower winding pattern decreasing field section

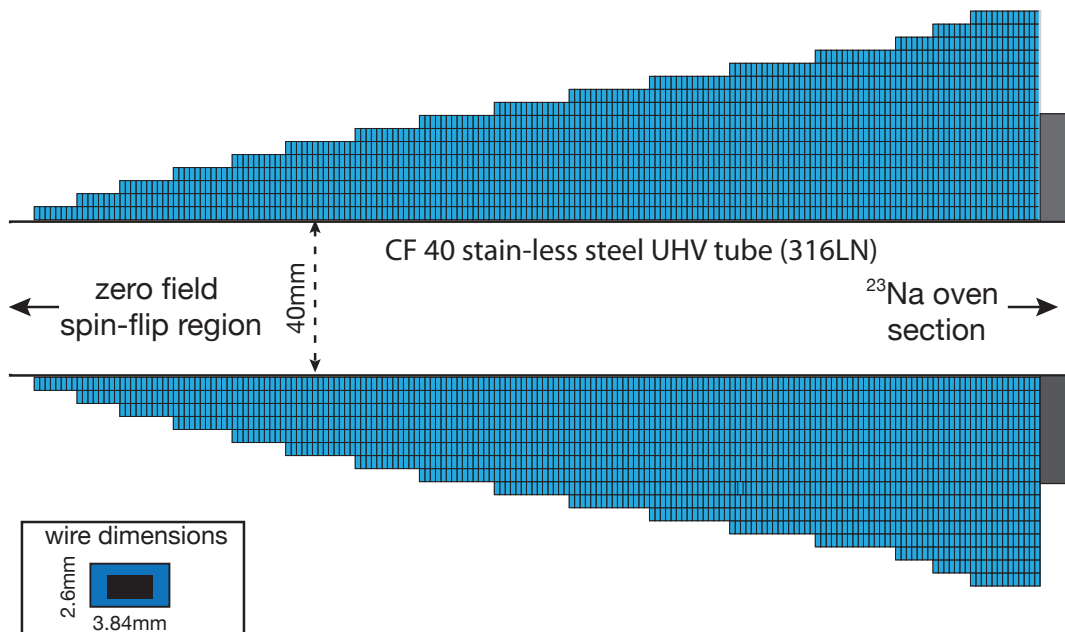


Figure 2.6 – Coil winding pattern of the decreasing field section of the Zeeman slower. For this section a hollow core wire was used to implement efficient water cooling of the coil assembly. The whole section is connected in series and is operated at a current of 18.0A

Laser setup

This section briefly describes the laser system that is used for cooling, imaging and optical pumping of ^{23}Na atoms. Fig. 2.10 displays the current laser setup. Laser light at

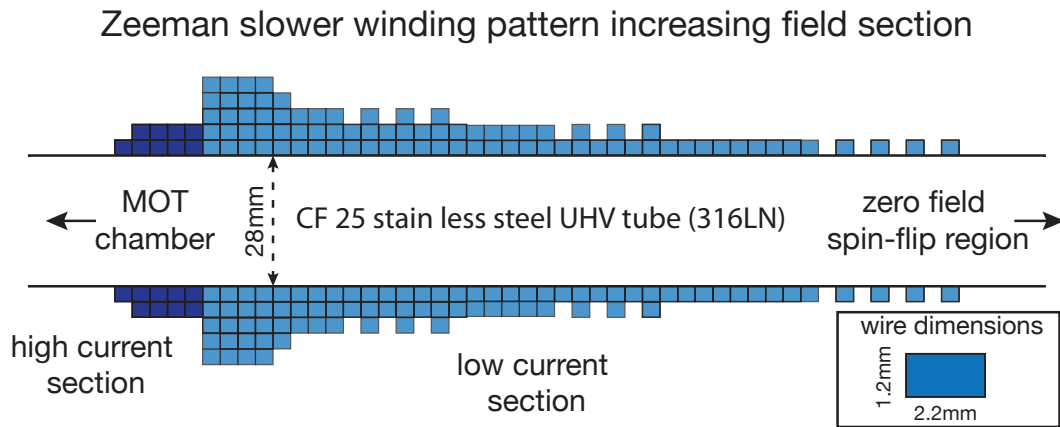


Figure 2.7 – Coil winding pattern of the increasing field section of the Zeeman slower. Two separate section that are operated at 15.2A and 62.3A allow for fine-tuning of the final velocity of the slowed atoms.

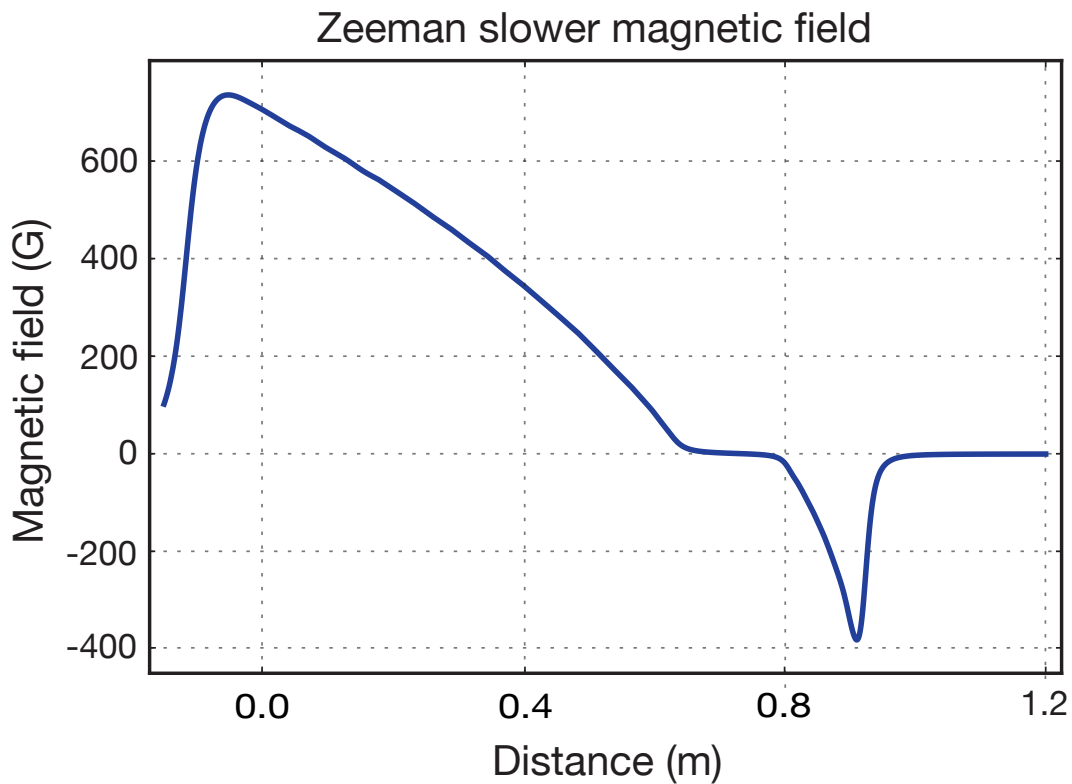


Figure 2.8 – Calculated magnetic field generated by the winding patterns shown in Fig. 2.6 and 2.7. The zero field section at $\approx 0.75\text{m}$ is required for efficient optical pumping from the σ_+ to the σ_- cycling transition.

the required wavelength of 589nm is derived from second harmonic generation modules. In order to have sufficient power for Zeeman slowing and laser cooling the main SHG modules is seeded by a commercial 10W infrared laser system (External cavity diode laser (ECDL) seed + Raman fiber amplifier). Although the SHG module is operated at 110% of the maximal specified output power (i.e. $P = 1.65\text{W}$, $P_{\text{max}} = 1.5\text{W}$) the laser system has been in operation for more than 4 years without requiring any maintenance. A second SHG unit is directly seeded by a 1178nm ECDL and delivers $\approx 3\text{mW}$ of output power for

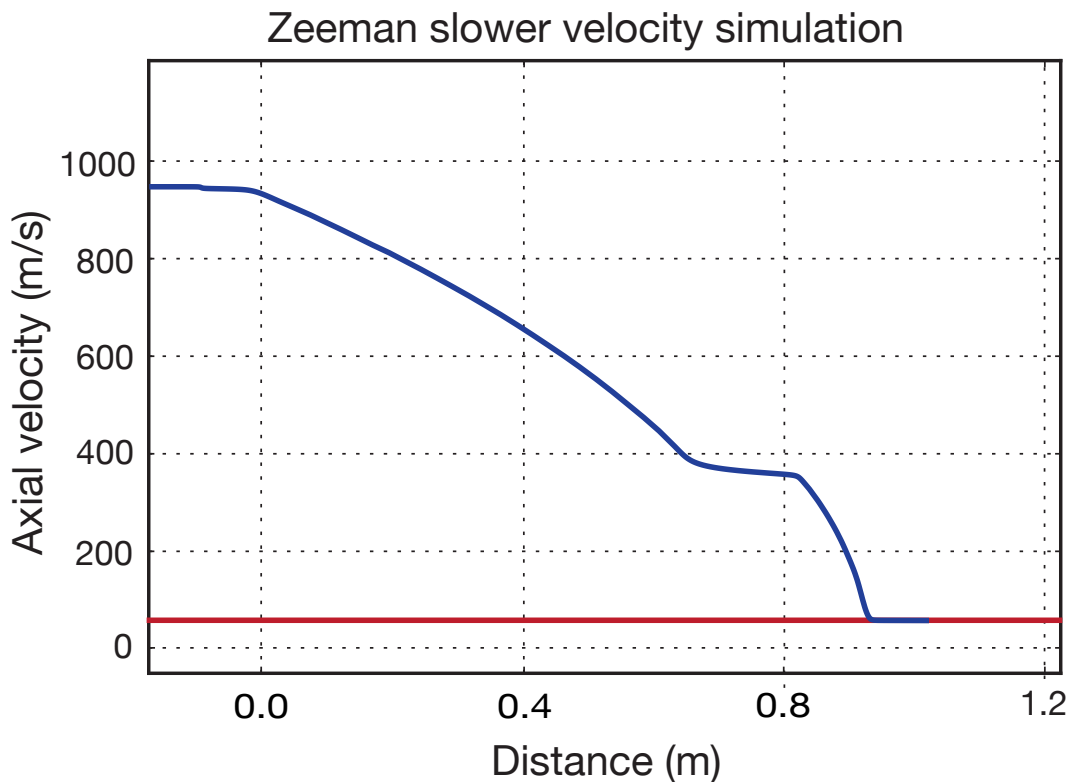


Figure 2.9 – Simulation of the velocity evolution for a single ^{23}Na atom that enters the Zeeman slower with an initial velocity of 950m/s. The red line indicates the target velocity (30m/s) of the Zeeman slower design.

imaging in the glass science cell.

Besides the auxiliary imaging laser, all other beams that are needed for cooling, optical pumping and imaging along the symmetry axis of the magnetic trap need to be derived from output of the main SHG unit. The main laser system is frequency stabilized to the $F = 2 \rightarrow F' = 3$ cycling transition via RF modulation spectroscopy. A proportional-integral (PI) feedback loop adjusts the piezo voltage and the laser diode current of the ECDL accordingly. The frequency of the beam entering the spectroscopy setup (red shaded area in Fig. 2.10) is shifted by $+2 \cdot 189\text{MHz}$ using an acousto-optical modulator (AOM) in double pass (DP) configuration. The output frequency of the SHG is therefore red detuned with respect to the cycling transition by 378MHz. Together with a single pass AOM that shifts the frequency by additional -201MHz the detuning that is needed for the Zeeman slower $\simeq -600\text{MHz}$ is achieved. 15% of the total output power is sent through a special AOM with a frequency shift of $+1713\text{MHz}$ to generate two beams that can be used for optical pumping from the $F = 1$ to the $F = 2$ hyperfine groundstate. An additional DP-AOM compensates for the initial red detuning of the laser and allows to tune the frequency of both repump beams within $\pm 20\text{MHz}$. Note that both repump beams are not used for Zeeman slowing or MOT operation, but only for hyperfine state pumping prior to magnetic trap loading and low-field imaging of ^{23}Na in the science cell. The major part of SHG output is used for laser cooling in the 3D-MOT. A DP-AOM again compensates for the detuning induced by the frequency shift of the spectroscopy setup. We do not use a separate repump beam for MOT operation but instead use a resonantly driven electro-optical modulator

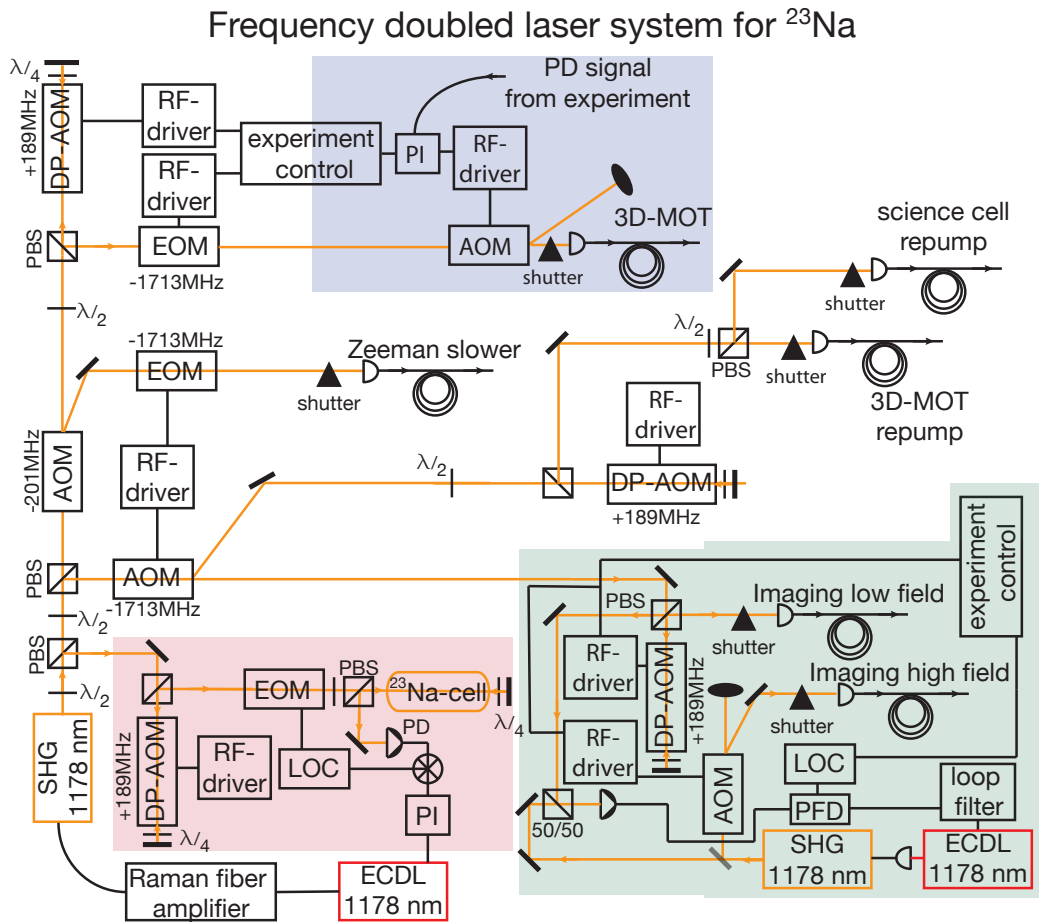


Figure 2.10 – Laser system for cooling, optical pumping and imaging of ^{23}Na atoms. A detailed description of all components is given in the main text.

(EOM) to produce sidebands at $\pm 1713\text{MHz}$ around the carrier frequency of the cooling laser. The sideband to carrier ratio is set to $\approx 10\%$. The same technique is also used to modulate sidebands onto the Zeeman slower beam. In order to keep the intensity in all six MOT beams as stable as possible, we use a single mode (SM), and polarization maintaining (PM) optical fiber to route the cooling light to the MOT setup. To compensate for common mode intensity drifts induced by residual polarization changes in the optical fiber, we use a power stabilization setup (blue shaded area) consisting of a photo diode at the MOT setup, a custom built PI controller and an AOM in front of the optical fiber. The imaging part of the ^{23}Na laser system (green shaded area) uses the zero order of the 1713MHz AOM for direct imaging on the cycling transition at low magnetic field. In this path a DP-AOM compensates the initial red detuning of the main laser and can be used for fine tuning of the imaging frequency. A second auxiliary imaging laser system based on an ECDL and a waveguide SHG module is used for imaging of in the science cell. This laser is offset locked to the main laser using an optical phase locked loop (OPLL) [50]. The large tuning range of the OPLL enables us to image ^{23}Na in a broad range of external magnetic fields for which the Zeeman shift of the imaging transition lies well outside of the tuning range of the low field imaging DP-AOM. Since AOM's do not extinguish a laser

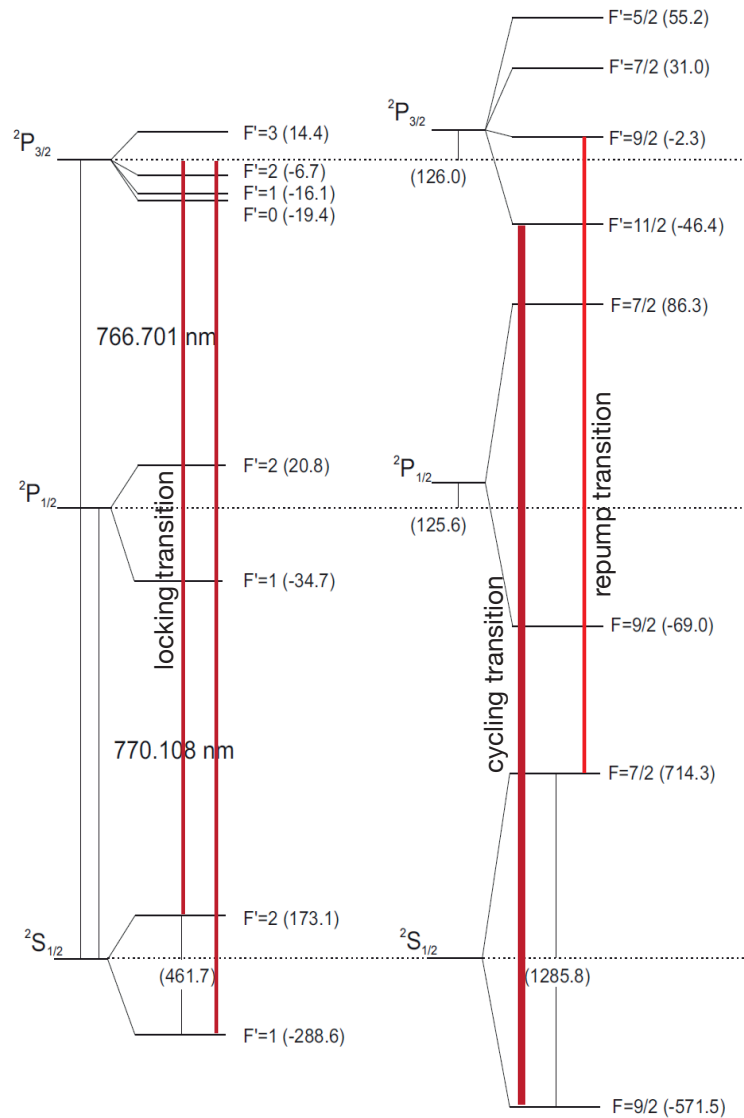
Atomic level scheme relevant for laser cooling of ^{40}K 

Figure 2.11 – Level scheme of ^{39}K and ^{40}K relevant for laser cooling of ^{40}K modified from [51]. Due to the low isotope concentration of ^{40}K , the D2-line of ^{39}K is used for frequency stabilization of an ECD master laser. The cooling, repump and imaging lasers for ^{40}K are offset locked via OPLL's. Note the inverted hyperfine structure of ^{40}K .

beam perfectly when they are switched off, we included custom-built laser beam shutters in front of every fiber coupling to block the light completely when needed. All relevant RF AOM and EOM drivers can be remote controlled (amplitude and frequency, on/off) by the experiment control system. The same applies for the beam shutters and the voltage controlled oscillator (VCO) that serves as frequency reference (i.e. local oscillators (LOC)) for the OPLL of the auxiliary imaging laser.

2.5.2 Laser system and 2D-MOT for ^{40}K

A beam of cold ^{40}K is generated in a standard 2D-MOT atom source [41] without on-axis cooling and pushing beams. The 2D-MOT vacuum chamber was loaded with 50mg of purified potassium. In this particular sample, the fraction of ^{40}K has been enriched to 3% compared to the natural isotope abundance of only $1.17 \cdot 10^{-4}$. The 2D-MOT assembly is constantly kept at a slightly elevated temperature of $\simeq 60^\circ\text{C}$, whereas the ^{40}K reservoir is held at $\simeq 100^\circ\text{C}$ to ensure that the ^{40}K atoms are accumulated in the vicinity of the 2D-MOT interaction region. A high power UV-LED can be used to increase ^{40}K vapor pressure during loading of the dual species 3D-MOT operated in the main vacuum chamber. The low pressure region of the 3D-MOT is separated from the 2D-MOT chamber by a $\simeq 1\text{cm}$ differential pumping tube with $\simeq 3\text{mm}$ diameter. It is imperative to overlap the 2D-MOT cooling region with the center of the differential pumping tube to ensure efficient loading of the 3D-MOT. The position of the 2D-MOT cooling region is monitored by fluorescence imaging along the axis of the atomic beam and can be precisely adjusted by independently changing the currents in all four 2D-MOT coils. The atomic level scheme relevant for lasers cooling, optical pumping and imaging is shown in Fig.2.11

Due to the low isotope abundance of ^{40}K saturated absorption spectroscopy for laser frequency stabilization is performed on the D2-line of ^{39}K . The laser system is therefore constructed in a master-slave configuration, where a single ECDL is locked to the $F = 1, F = 2$ groundstate crossover resonance of ^{39}K . The cooling, repumping and imaging lasers are offset locked with respect to the master laser via digital OPLL's. Fig. 2.12 displays the complete laser system. The local oscillators (LOC) are either VCO's or direct digital synthesizers (DDS).

The spectroscopy setup for frequency stabilization of the master laser is highlighted by the red shaded area. The master laser is distributed to four identical master oscillator power amplifier (MOPA) units based on a ECDL and a tapered amplifier (TA) chip and an additional ECDL that is used for absorption imaging. Five beat signals between the master and each slave laser generate the required RF signals that are compared to a tunable RF frequency reference by a digital phase-frequency discriminator (PFD). The error signal generated by the PFD is the fed back to the piezo and the laser diode current of each MOPA unit via a lead-lag compensating loop filter. A novel electronic phase-lock circuit has been developed for the ^{40}K laser system. The RF reference can be either supplied by a VCO that is adjusted by the experiment control system or by a direct digital synthesizer circuit. For fast switching of the slave lasers a single pass AOM is included in each beam path. Each pair of MOPA units is resonant with the $F = 9/2 \rightarrow F' = 11/2$ cycling transition and the $F = 7/2 \rightarrow F' = 9/2$ repump transition. The pair that is used for the 2D-MOT is operated with a cool to repump power ratio of 1/1, the 3D-MOT pair with a ratio of 10/1. The light for imaging and the 2D-MOT is directly routed to the vacuum setup via SM/PM fibers. For the 3D-MOT, an additional AOM has been built into the beam path after overlapping the repump with the cooling light in order to stabilize the total laser intensity that is routed to the experiment. To this end a photo-diode signal is recorded at the experiment and used for feedback onto the AOM driver via a custom built PI controller. The intensity stabilization setup is highlighted by the blue shaded area. For each optical

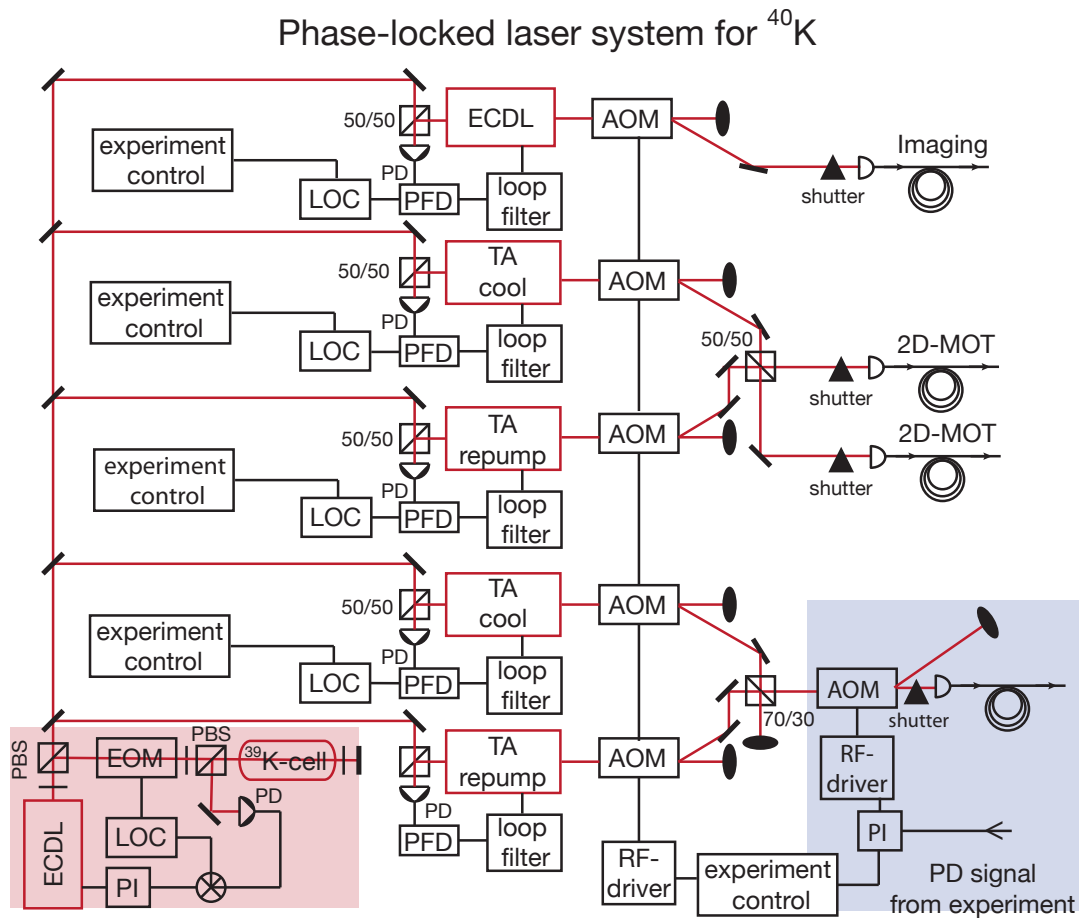


Figure 2.12 – Schematic of the ^{40}K laser system. Details are described in the main text.

fiber a mechanical beam shutter has been included. All laser frequencies and AOM drivers can be remotely set by the experiment control system. Since all laser frequencies and intensities can be remote controlled by the experiment control unit we can in principle change between both isotopes of potassium by just programming different values for the relevant parameters of the laser cooling sequence.

2.5.3 Dual-species MOT

As initial cooling step we operate a standard dual-species D2-line 3D-MOT [46] that captures atoms injected to the stainless steel chamber by the ^{23}Na Zeeman slower and the ^{40}K 2D-MOT. Fluctuations and long term drift of MOT performance is suppressed by transmitting the cooling light for each species in a single SM/PM optical fiber, using an intensity stabilization setup (see Fig. 2.12 and 2.10) and by employing a retro-MOT configuration. We overlap the cooling light for both species on a single dichroic mirror and distribute the light to all three MOT axes free-space. The repump light is either supplied by sideband generation with an resonant EOM (^{23}Na) or by combining the output of two separate MOPA units prior to the optical fiber (for details see Fig. 2.12 and 2.10). In this way we ensure intensity balance in each pair of MOT beams. The long-term stability of the

atom number for both species is $< \pm 5\%$. After initial MOT loading we employ the C-MOT technique to increase the density prior to loading a magnetic quadrupole trap. In order to suppress light-assisted inelastic collisions [52] of ^{23}Na and ^{40}K it is necessary to operate the dual species MOT with a slight mismatch of cloud position realized by not perfectly overlapping the MOT cooling light. All MOT parameters have been optimized after the MW evaporation in the plugged quadrupole trap down to $\simeq 6\mu\text{K}$ had been established. Since sympathetic cooling of fermionic ^{40}K requires an atom number ratio in the magnetic trap of $> 1000/1$, the dual species MOT, C-MOT and magnetic trap loading was first optimized for ^{23}Na alone.

2.6 Magnetic Trap and evaporative cooling

After compression in the C-MOT the $^{23}\text{Na}^{40}\text{K}$ mixture is optically pumped to the stretched low field seeking hyperfine states (i.e. $|F = 2, m_F = 2\rangle$ for ^{23}Na and $|F = 9/2, m_F = 9/2\rangle$ for ^{40}K) by a circular polarized laser beam. To this end, a $\simeq 1\text{G}$ guiding field is applied along the propagation direction of the optical pumping beam. Next, a magnetic quadrupole trap is switched on as fast as possible to minimize heating by mismatch in magnetic trap volume and the extension of the atomic cloud after C-MOT. To further optimize magnetic trap loading we use three pairs of compensation coils in Helmholtz configuration to match the position of the ^{23}Na C-MOT with the center of the quadrupole trap. Due to the large imbalance ($\simeq 10^3$) in atom numbers magnetic trap loading is optimized for ^{23}Na alone. Due to heating during trap loading and the temperature increase caused by adiabatic compression the temperature of the ^{23}Na cloud is $\simeq 1\text{mK}$ at the maximal magnetic field gradient of 250G/cm .

Spin purification

Since optical pumping does not produce a completely spin polarized sample, also atoms in non-stretched hyperfine states are trapped in the quadrupole trap. These have to be removed from the trap in order to suppress inelastic spin-exchange collisions that produce atoms in high field seeking states that are repelled from the magnetic trap. For a spin-polarized mixture two-body s-wave collisions which dominate at temperatures below 1mK can only be elastic due to conservation of angular momentum. For spin purification, we adiabatically reduce the magnetic trap gradient to 8.25G/cm and wait for $\simeq 2\text{s}$ until gravity has removed all atoms in a non-stretched low-field seeking state (see Fig. 2.15 below). The trap gradient is again increased to 250G/cm and the $^{23}\text{Na}^{40}\text{K}$ mixture is cooled from $\simeq 1\text{mK}$ to $\simeq 6\mu\text{K}$ by forced MW evaporation on the $F = 2 \rightarrow F' = 1$ hyperfine transition of ^{23}Na . The inter-species s-wave scattering length of $\simeq -690a_0$ facilitates efficient sympathetic cooling of fermionic ^{40}K atoms.

Plugged quadrupole trap

With spin-exchange collisions suppressed, two additional loss mechanisms have to be compensated for in order to reach a sufficiently large phase-space density to transfer the Bose-

Fermi mixture into an optical dipole trap. The first one originates from diabatic transitions to high-field seeking states that occur on trajectories that cross the center of the magnetic trap. Here the rate of change of the instantaneous magnetic field experienced by an atom moving along this trajectory can exceed the limit for adiabatic evolution set by the Larmor frequency. A detailed study of Majorana losses is presented in [43]. We focus a high intensity laser beam ($\lambda = 532\text{nm}$, $P = 5\text{W}$, $w_0 = 50\mu\text{m}$) that is blue detuned with respect to the D1 and the D2-line in ^{23}Na and ^{40}K to the center of the magnetic trap in order to prevent the atoms from following trajectories that lead to diabatic spin-flips. This so called *plug laser* is directed along the symmetry axis of the magnetic trap. For alignment of the plug focus position we overlap the the plug beam with a counter-propagating imaging beam by using a pair of dichroic mirrors. A remote controlled piezo driven steering mirror is used for fine tuning of the plug position with respect to the trap center. Fig. 2.13 illustrates the MW evaporation setup used in our experiment. This configuration allows us to directly

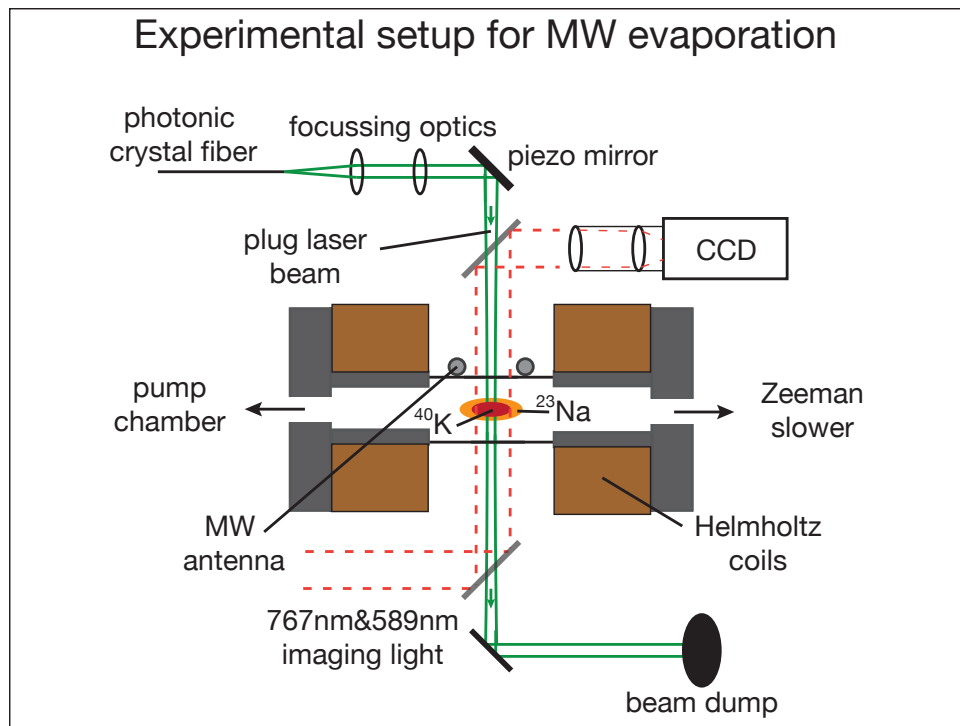


Figure 2.13 – Schematic illustration of the experimental setup used for evaporative cooling of ^{23}Na and ^{40}K . Both species are trapped in a plugged magnetic quadrupole trap generated by a pair of anti-Helmholtz coils. The high energy fraction of ^{23}Na is removed from the trap by MW radiation resonant with the Zeeman shifted $F = 2 \rightarrow F' = 1$ hyperfine transition. A plug laser is used to suppress Majorana losses. The plug position is detected by dual species absorption imaging along the plug axis and can be fine adjusted with a piezo driven steering mirror.

image the reduction of atomic cloud density that is caused by the repulsive dipole force of the plug laser. Fig. 2.14 shows an absorption picture of ^{23}Na that is taken at the end of evaporation, when the single beam dipole trap is in progress to be loaded. The hole in the center of the cloud is caused by the plug laser. The fact that the plug laser point in direction of gravity allows us to change the field gradient in the trap from its maximal value to almost zero without increasing the Majorana loss rate. In the plane perpendicular

Absorption image for plug alignment

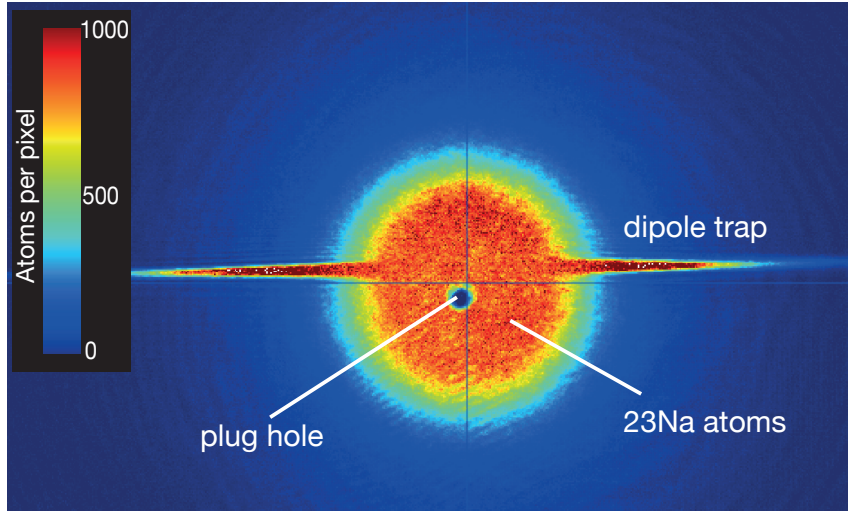
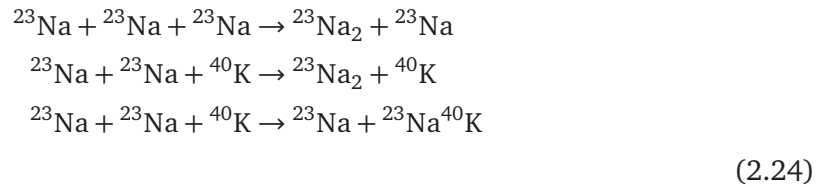


Figure 2.14 – Absorption image of ^{23}Na after MW evaporation has been completed. A single beam optical dipole trap is in progress of being loaded. Rotational symmetry is broken by pointing the plug slightly off center with respect to the magnetic trap.

to the plug axis we use two pairs of compensation coils to fine-tune the relative position of trap center and the plug beam.

Suppressing three-body loss

The final loss mechanism that has to be coped with is molecule formation caused by three-body collisions [53]. Due to the fermionic nature of ^{40}K , the collision cross-section for two-body and three-body collisions involving at least two ^{40}K atoms is strongly suppressed in a spin-polarized gas at low temperatures [54]. The dominant three-body loss channels during combined evaporation in the quadrupole trap are the following:



the corresponding loss equations are given by [54]:

$$\begin{aligned}
 \frac{dN_{\text{Na}}}{dt} &= -\beta_{\text{Na}} \int d\mathbf{r} n(\mathbf{r}, t)_{\text{Na}}^3 \\
 \frac{dN_{\text{Na}}}{dt} &= 2 \frac{dN_{\text{K}}}{dt} = -\beta_{\text{NaK}} \int d\mathbf{r} n(\mathbf{r}, t)_{\text{Na}}^2 n(\mathbf{r}, t)_{\text{K}}
 \end{aligned}
 \tag{2.25}$$

Here β is the three-body loss coefficient that depends non-trivially on the microscopic behavior of the scattering process [54] and $n(\mathbf{r}, t)_{Na/K}$ is the space and time dependent atomic density in the quadrupole trap. For a thermal ensemble the spacial variation of the density is given by:

$$n(\mathbf{r}) = n_0 \exp\left(-\frac{V(\mathbf{r})}{k_b T}\right) \quad (2.26)$$

where n_0 is the atomic density in the trap center and $V(\mathbf{r})$ the trapping potential given by:

$$V(\mathbf{r}) = \mu_{Na/K} \cdot \sqrt{(x^2 + y^2 + 4z^2)} dB_z, \quad (2.27)$$

where $\mu_{Na/K}$ is the magnetic moment of the trapped atoms and dB_z the magnetic field field gradient along the symmetry axis of the trap. In contrast to evaporation of a Bose-Fermi mixture in an optical dipole trap where the value of β can be adjusted by controlling the scattering length via a Feshbach resonance (see section 2.8.1 below), the only way to suppress three-body loss during evaporation in the magnetic trap is by controlling the density by reducing the trapping potential. Since combined evaporative cooling of the trapped atomic mixture relies on re-thermalization induced by $^{23}\text{Na} + ^{23}\text{Na}$ and $^{23}\text{Na} + ^{40}\text{K}$ collisions that scale with $n(\mathbf{r}, t)_{Na}^2$ and $n(\mathbf{r}, t)_{Na} \cdot n(\mathbf{r}, t)_K$ the magnetic field gradient can be dynamically reduced during an evaporation sequence in such a way that three-body loss is effectively suppressed while at the same time runaway evaporation defined by 2.4 can be sustained. The time course of the experimental parameters that are controlled during the evaporation sequence (i.e. the MW radiation frequency and the magnetic field gradient) is shown in Fig. 2.15

The exact shape of the magnetic field ramp was determined empirically by observing the ^{40}K atom number during the evaporation sequence and reducing the field gradient whenever strong losses appear. After a working evaporation sequence to a temperature of $\simeq 10\mu\text{K}$ was established all relevant experimental parameters for the 3D-MOT, the C-MOT, optical pumping, magnetic trap loading, spin purification and MW evaporation were optimized until we were satisfied with the attainable atom number and temperature for both species as well as with the experimental stability.

To summarize, the dual species MOT combined with subsequent evaporative cooling in the plugged quadrupole trap produces a spin polarized thermal ensemble of $\simeq 8 \cdot 10^7$ ^{23}Na and $\simeq 5 \cdot 10^6$ ^{40}K atoms at a temperature of $\simeq 6\mu\text{K}$. Shot to shot atom number fluctuations and long term atom number drift is below 10% of the average value. The experimental cycle time is $\simeq 27\text{s}$. In a next step the thermal $^{23}\text{Na}^{40}\text{K}$ sample is loaded to a single beam optical dipole trap.

2.7 Optical dipole trap

Addressing magnetic field controlled Feshbach resonances in ultracold gases [55] requires a precisely tuneable magnetic field. Since a magnetic quadrupole trap relies on a linearly increasing magnetic field it cannot serve as a tool to study Feshbach resonances and use them for molecule association. For this reason the $^{23}\text{Na}^{40}\text{K}$ mixture is transferred to a far detuned optical dipole trap [56] after pre-cooling to $\simeq 6\mu\text{K}$ by MW evaporation. In

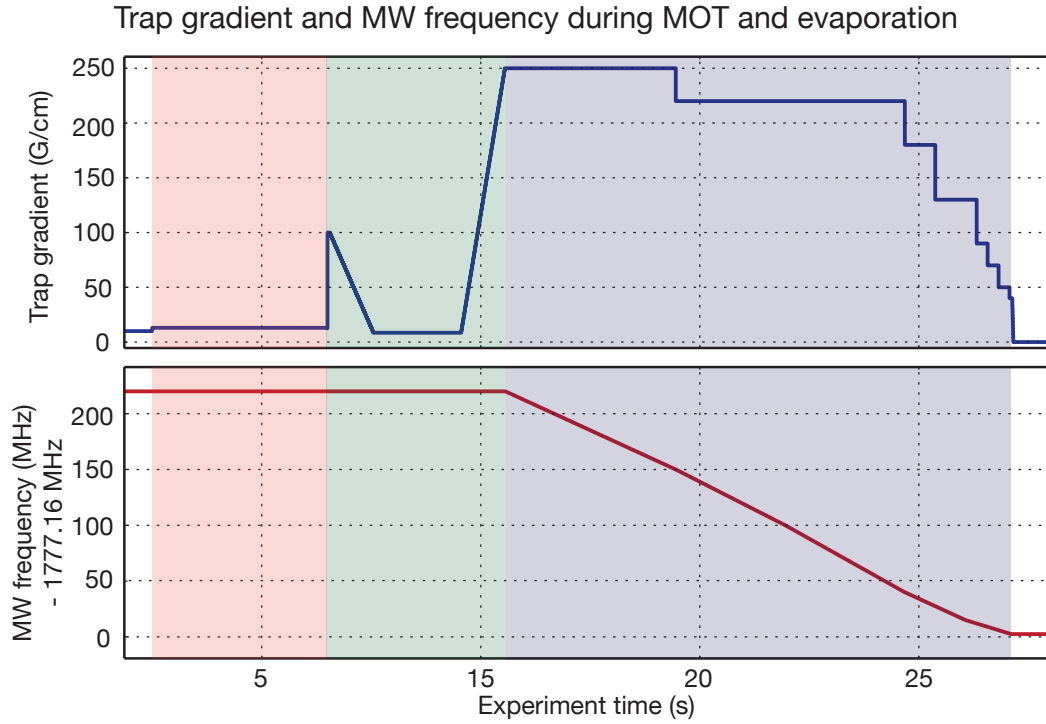


Figure 2.15 – Time course of the magnetic field gradient and the frequency of the MW radiation used for evaporation. The red shaded area indicates the MOT phase and optical pumping, the green shaded area magnetic trap loading and the spin-purification sequence. The blue shaded area highlights the evaporation sequence in the plugged quadrupole trap. Three-body loss is suppressed by reducing the initial gradient of 250G/cm in eight discrete steps to 40G/cm. The final step to 0.1G is used for loading the $^{23}\text{Na}^{40}\text{K}$ mixture into a single beam optical dipole trap.

a dipole trap the trapping potential is due to a spatially varying AC Stark shift caused by a focused high intensity laser beam that is far red-detuned with respect to all optical transitions of an alkali atom. For a single optical transition the trapping potential of an optical dipole trap is given by [56]:

$$U(r, z, \omega) = \frac{3\pi c^2}{2\omega_0^3} \left(\frac{\Gamma}{\omega_0 - \omega} + \frac{\Gamma}{\omega_0 + \omega} \right) \cdot I(r, z) \quad (2.28)$$

Here ω_0 and Γ are the angular transition frequency and natural linewidth of the nearest atomic transition, $\omega = \frac{2\pi c}{\lambda}$ the angular frequency of the trapping laser and $I(\mathbf{r})$ the spatial intensity distribution of the trapping lasers configuration. The *trap depth* U_0 of an optical dipole trap is defined by $U_0 = U(r = 0, z = 0)$. The spatial intensity of a single beam dipole trap is best expressed in cylindrical coordinates:

$$I(r, z) = \frac{2P}{\pi w(z)^2} \exp\left(-\frac{2r^2}{w(z)^2}\right), \quad (2.29)$$

with

$$w(z) = w_0 \sqrt{1 + \left(\frac{\lambda z}{\pi w_0}\right)^2} \quad (2.30)$$

Here P is the laser power in W, w_0 the beam waist and λ the wavelength of the laser. In our experiments we use optical dipole traps with two different wavelengths, 1064nm and

1550nm. The closest optical transitions in ^{23}Na and ^{40}K are the D1 and the D2-lines at 589.76nm and 589.16nm for ^{23}Na and 770.108nm and 766.70nm for ^{40}K . For this situation that differs from the ideal case of equation 2.7 the following formula approximates the combined trapping potential arising from both transitions [56]:

$$U(r, z, \omega) = \frac{\pi c^2}{2\omega_0^3} \left(\frac{2\Gamma}{\omega_{D2} - \omega} + \frac{\Gamma}{\omega_{D1} + \omega} \right) \cdot I(r, z) \quad (2.31)$$

For atomic or molecular samples with a temperature that is small compared to the trap depth the trapping potential can be approximated by an ideal harmonic trap. Expressed in cylinder coordinates the potential is:

$$U_h(r, z) = -U_0 + \frac{1}{2}m(\omega_r^2 r^2 + \omega_z^2 z^2) \quad (2.32)$$

With trap oscillation frequencies ω_r and ω_z given by:

$$\begin{aligned} \omega_r &= 2\sqrt{\frac{U_0}{mw_0^2}} \\ \omega_z &= \sqrt{\frac{2U_0}{m(\pi w_0^2/\lambda)^2}} \end{aligned} \quad (2.33)$$

The ratio $\frac{\omega_r}{\omega_z}$ is called the aspect ratio of the trap. For a single beam trap the aspect ratio is typically $\simeq 100 - 150$. The density of a trapped thermal gas of particles with mass m at a temperature T is then given by:

$$n(r, z) = n_0 \exp\left(-\frac{U_h(r, z)}{2k_b T}\right) = n_0 \exp\left(-\frac{m\omega_r^2 r^2}{2k_b T}\right) \cdot \exp\left(-\frac{m\omega_z^2 z^2}{2k_b T}\right) \quad (2.34)$$

The *effective volume* V_{eff} of the trap is defined as [45]:

$$V_{eff} = \int d\mathbf{r} \exp\left(-\frac{U_h(r, z)}{2k_b T}\right) = \left(\frac{2\pi k_b T}{m}\right)^{3/2} \cdot \frac{1}{\omega_r^2} \cdot \frac{1}{\omega_z} \quad (2.35)$$

The central density n_0 in the trap is related to the total number N of particles by:

$$n_0 = \frac{N}{V_{eff}} \quad (2.36)$$

Finally the so called *degeneracy parameter* D is defined as

$$D = n_0 \cdot \Lambda_{th} \quad (2.37)$$

where the thermal de Broglie wavelength Λ_{th} is defined as

$$\Lambda_{th} = \sqrt{\frac{2\pi\hbar}{mk_b T}} \quad (2.38)$$

For $D \geq 1$ particles in the center of the trap start to become indistinguishable and quantum statistics will determine system behavior.

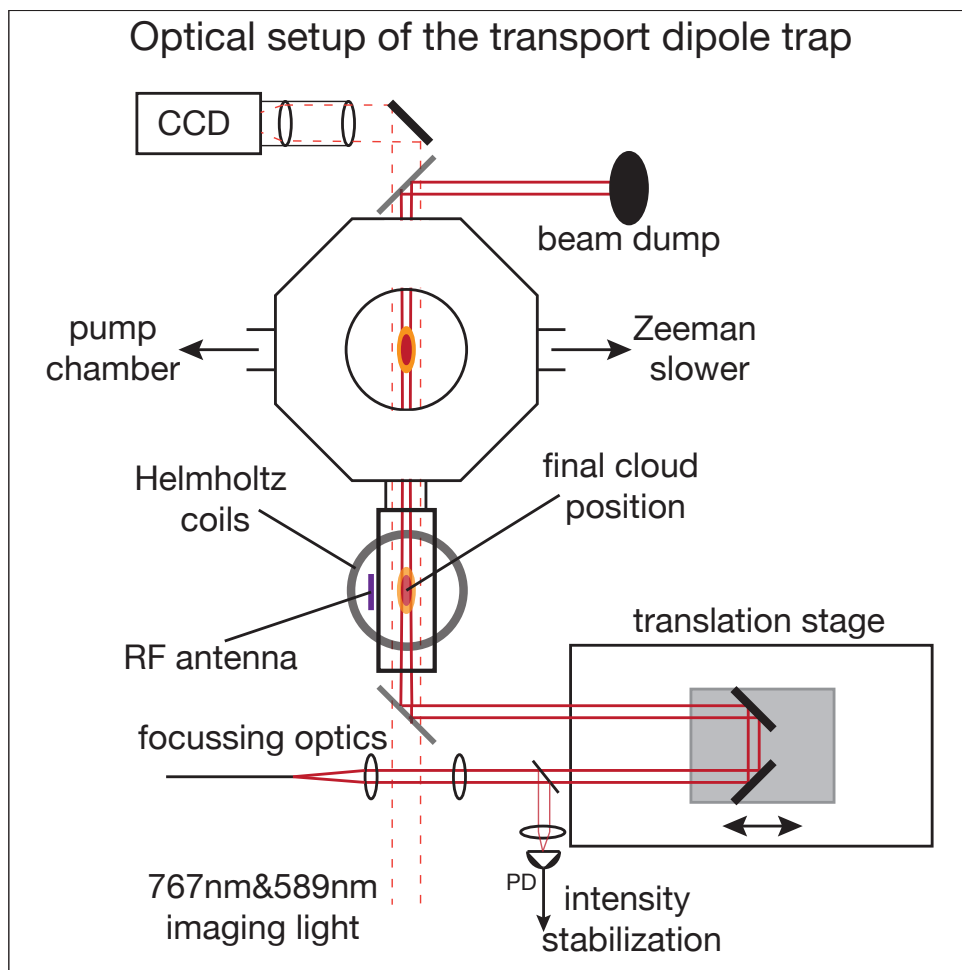


Figure 2.16 – Experimental setup of the 1064nm dipole trap that is used to capture the $^{23}\text{Na}^{40}\text{K}$ mixture after combined MW evaporation in the magnetic trap and for transporting it to the science cell. Absorption imaging along the dipole trap beam direction is used for fine adjustment of the focus position with respect to the center of the magnetic trap. Transport is executed by a air bearing translation stage. Around the science cell a RF antenna and water cooled Helmholtz coils are installed.

Fig. 2.16 displays a schematic of the 1064nm dipole trap setup that is used for capturing the $^{23}\text{Na}^{40}\text{K}$ mixture after combined MW evaporation in the magnetic trap.

This single beam dipole trap ($\lambda = 1064\text{nm}$, $P = 7.5\text{W}$, $w_0 = 40\mu\text{m}$) is also used for transporting the mixture from the stainless steel MOT chamber to the attached science cell. For this purpose a movable retro-reflector has been installed into the beam path. The movement is executed with an position encoded, air-bearing translation stage. To overlap the focus of the dipole trap with the potential minimum of the quadrupole trap in order to maximize loading efficiency we use a manual steering mirror and the programmable translation stage. For optimizing transfer to the dipole trap we installed a second absorption imaging system along the axis of the dipole trap. Together with the already existing imaging setup along the direction of the plug lasers we are able to focus the dipole trap precisely to the potential minimum of the quadrupole trap (see Fig. 2.14). For further

evaporative cooling in the science cell we also installed an additional 1550nm trapping laser forming a *crossed dipole trap* [56] together with the transport trap. The parameters of both traps are summarized in table 3.1. Note that trap frequencies scale as $\propto \sqrt{I/I_{max}}$

Parameter	transport trap	crossed trap
Power (W)	7.5	(7.5, 5)
Beam waist (μm)	40	(40, 100)
Trap depth ^{23}Na (μK)	78	78 + 6.7
Trap depth ^{40}K (μK)	200	200 + 13.5
ω_r for ^{23}Na (Hz)	1340	$\sqrt{1340^2 + 0.5^2}$
ω_r for ^{40}K (Hz)	1626	$\sqrt{1626^2 + 0.6^2}$
ω_z for ^{23}Na (Hz)	8.0	$\sqrt{8.0^2 + 154^2}$
ω_z for ^{40}K (Hz)	9.7	$\sqrt{9.7^2 + 176^2}$

Table 2.1 – Experimental parameters for both dipole traps that are currently operated in our setup. Trap depth and trapping frequencies are given for maximal available laser power. For the crossed trap the individual values are made transparent.

and the trap depth scales as $\propto I/I_{max}$. The exact loading sequence for the dipole trap is shown in Fig. 2.17.

The final step of MW evaporation is performed at a magnetic field gradient of 40G/cm. After the MW field is switched off we ramp down the gradient to 0.1G/cm in 30ms and simultaneously ramp up the dipole trap power to 90%. Fig. 2.18 shows an absorption image of taken a few ms after the dipole trap has been switched on. Almost 90% of the ^{23}Na that have been cooled in the magnetic trap are not captured by the dipole trap.

After the dipole trap has reached full power it is imperative to transfer ^{23}Na to its absolute hyperfine groundstate in order to suppress inelastic hyperfine changing collisions. For this purpose a $B \simeq 1.35\text{G}$ guiding field is applied in direction of gravity and a MW Landau-Zener sweep from $F = 2, m_F = 2$ to $F = 1, m_F = 1$ is performed during 5ms.

Transport to the science cell

We use the technique developed at MIT [57] to transport the ^{23}Na ^{40}K mixture from the stainless steel MOT chamber to the attached science cell where all further experimental steps take place (scattering channel preparation, addressing Feshbach resonances, molecule association, molecular spectroscopy etc.). Compared to transport experiments with ^{23}Na alone the large inter-species background scattering length of $a_{bg} = -690a_0$

In total there are three different mechanisms that contribute to atom loss during dipole transport:

1. Acceleration loss: mainly affects ^{23}Na due to weaker confinement. Ideally the acceleration of the translation stage should be small compared to the axial restoring force of the dipole trap i.e. $a_{stage} < F_z/m_{Na}$, where $F_z = -\partial_z U(r, z)$. High laser intensities allow for larger acceleration and shorter transport times.
2. Trap heating: mainly affects ^{23}Na due to weaker confinement. Pointing noise and

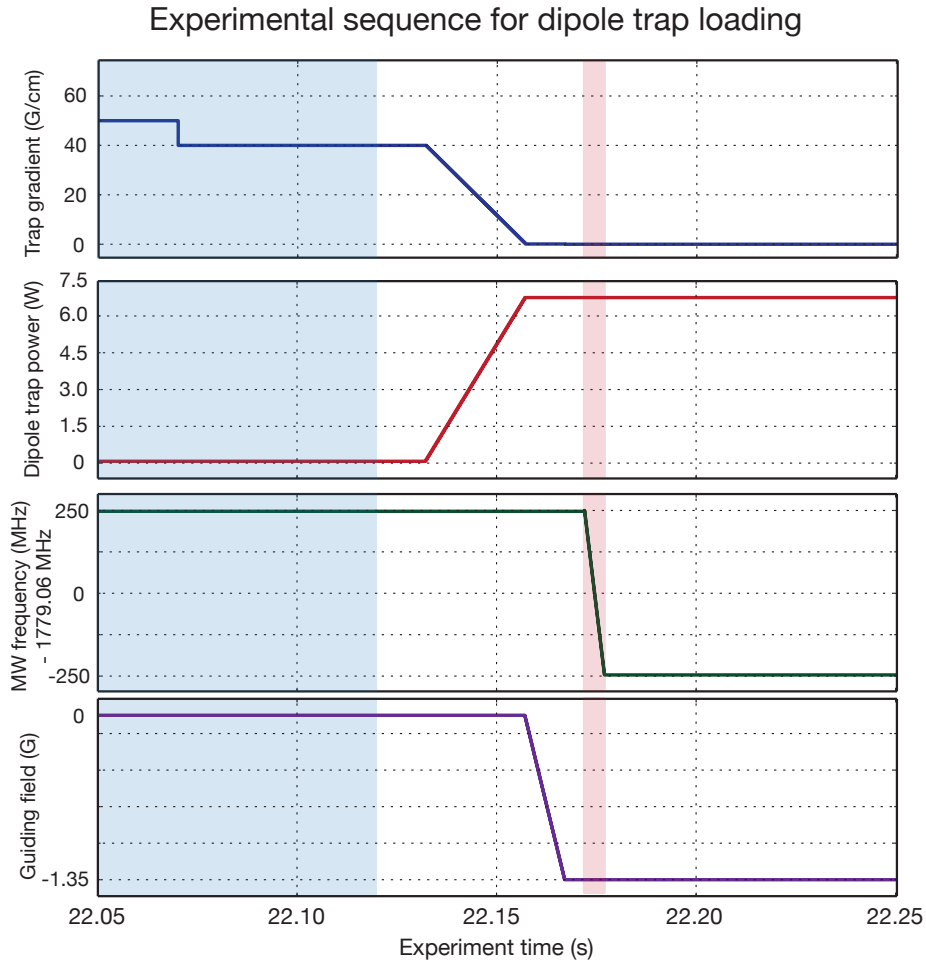


Figure 2.17 – Experimental sequence for loading the single beam dipole trap after MW evaporation in the quadrupole trap. In order to minimize exothermic hyperfine changing collisions for ^{23}Na a MW Landau Zener sweep from $F = 2, m_F = 2$ to the hyperfine groundstate $F = 1, m_F = 1$ is executed as fast as possible after the dipole trap has been loaded. For that purpose a guiding field of $\simeq 1.35\text{G}$ is applied in direction of gravity. The red shade area indicates the MW sweep.

intensity noise during the movement of the translation stage results in heating and consecutive evaporation of ^{23}Na .

3. Three body loss: mainly affects ^{40}K due to stronger confinement and much larger background scattering length (compare equation 2.25 and [54]).

For these reasons optimal transport is always a compromise between limiting acceleration loss by slow transport and high laser intensities as well as limiting trap heating and three-body loss by fast transport and working at low laser intensities. The fact that trap heating depends on the noise power convoluted with the energy spectrum of the trap can lead to resonant heating for certain values of the axial and radial trapping frequencies.

Empirically, we found that in our current setup (see Fig. 2.16) transfer efficiency for the ^{23}Na ^{40}K mixture with an atom number ratio of $\simeq 20/1$ is maximized by making transport as short as possible $\simeq 750\text{ms}$ without having to much acceleration loss. The current transport parameters are $\lambda = 1064\text{nm}$, $P = 0.9 \cdot 7.5\text{W}$, $w_0 = 40\mu\text{m}$, $t = 750\text{ms}$. The

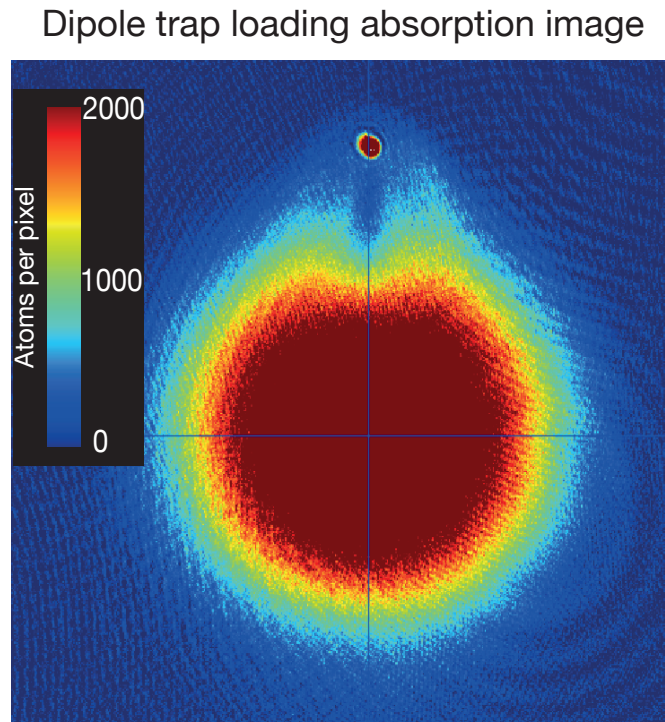


Figure 2.18 – Absorption image of ^{23}Na taken along the dipole trap a few ms after the dipole trap has been ramped to full power. Due to the much smaller trapping volume, almost 90% of the ^{23}Na atoms that have been cooled in the magnetic trap are not trapped in the dipole trap.

movement of the translation stage is programmed to have an trapezoid velocity profile. The transport efficiency is $\simeq 65\%$ for ^{23}Na and $\simeq 90\%$ for ^{40}K . We see that for transport, three-body loss is not a limitation. By varying the maximal acceleration we also made sure that we operate the transport in a configuration where acceleration loss is also not a limiting factor. We conclude that the losses we observe are dominated by trap heating. The temperature of the mixture after transport is $\simeq 12\mu\text{K}$. This is the same temperature as after dipole trap loading. We effectively use evaporation of excess ^{23}Na atoms as a cooling mechanism to compensate for trap heating. The increase from $6\mu\text{K}$ to $12\mu\text{K}$ during dipole trap loading is consistent with adiabatic heating at constant phase space density [45].

2.8 Attaining dual species degeneracy

To attain quantum degeneracy after transport to the science cell further evaporative cooling in the dipole trap has to be performed. In our current setup it is not possible to observe Bose-Einstein condensation of ^{23}Na in presence of ^{40}K , when evaporation is performed in the single beam dipole trap. For this reason we installed a second optical dipole trap ($\lambda = 1550\text{nm}$, $P = 5\text{W}$, $w_0 = 100\mu\text{m}$) that forms a crossed dipole trap together with the transport trap. In this way the density in the trap and therefore the thermalization rate

$$\gamma_{th}(r, z) \propto a_{Na}^2 n_{Na}(r, z) v_{av}(T) \quad (2.39)$$

can be increased by 3 orders of magnitude (compared equation 2.34 and table 3.1), making evaporative cooling much more efficient. Here v_{av} designates the average thermal velocity in the gas and $a_{Na} \simeq 58a_0$ the background scattering length for ^{23}Na in $F = 1$. For an ideal Bose gas in a harmonic trap the condensation temperature T_C is given by [45]:

$$T_C = \frac{\hbar}{k_B} \sqrt[3]{N_{Na} \omega_z \omega_r^2} \quad (2.40)$$

We can determine the fraction of condensed ^{23}Na atoms N_0/N_{Na} by fitting a parabolic Thomas-Fermi profile [58]

$$n_{TF}(x, y, z) = \frac{\mu_{TF}}{g} - \frac{1}{2g} m_{Na} (\omega_r^2 (x^2 + y^2) + \omega_z^2 z^2) \cdot \Theta(1 - ((x^2 + y^2)/R_r^2 + z^2/R_z^2))$$

$$\mu_{TF} = \frac{\hbar \sqrt[3]{\omega_z \omega_r^2}}{2} \left(\frac{15 N_{Na} a_{Na}}{a_{ho}} \right)^{2/5}$$

together with a Gaussian

$$n_{Th}(x, y, z) = \left(n_o - \frac{\mu_{TF}}{g} \right) \cdot \exp\left(\frac{-(x^2 + y^2)}{2\sigma_r^2}\right) \cdot \exp\left(\frac{-z^2}{2\sigma_z^2}\right) \quad (2.41)$$

to the observed line-density profile $n(x, z)$ after time of flight. The combined fitting function is given by:

$$n_{fit}(x, z) = \int dy n_{Th}(x, y, z) + n_{TF}(x, y, z) \quad (2.42)$$

Here the coupling constant $g = \frac{4\pi\hbar a_{Na}}{m_{Na}}$, Θ is the Heaviside function and

$$a_{ho} = \sqrt{\frac{\hbar}{m_{Na} \sqrt[3]{\omega_z \omega_r^2}}} \quad (2.43)$$

the averaged harmonic oscillator length. The Gaussian function accounts for non-condensed atoms in the thermal wings of the cloud and can also be used to estimate the temperature of the gas via

$$\sigma(t) = \sqrt{\sigma_0^2 + k_B T / m_{Na} \cdot t^2} \quad (2.44)$$

Fig. 2.19 illustrates how a Bose-Einstein condensate of $\simeq 5 \cdot 10^5$ ^{23}Na atoms forms in our crossed dipole trap when the end point of evaporation is varied from $2.04\mu\text{K}$ to $0.86\mu\text{K}$.

We take four absorption images after 7.5ms time of flight and fit the function of equation 2.42 to the observed density profiles. We then estimate the condensate fraction N_0/N_{Na} by calculating the ratio of the integrals of $n(x, z)_{TF}$ and $n(y, z)_{Th}$. Knowing the condensate fraction the ratio T/T_C can then be obtained using the following relation [45]:

$$\frac{T}{T_C} = 0.94 \cdot \sqrt[3]{1 - N_0/N_{Na}} \quad (2.45)$$

The values for T/T_C are given in Fig. 2.19. Note that we only determine the ratios N_0/N_{Na} and T/T_C and do not measure absolute values for the temperature, total atom number and condensate fraction. For the lowest evaporation endpoint we cannot detect the thermal fraction. We therefore assume a condensate fraction of 95% and obtain $T/T_C = 0.37$.

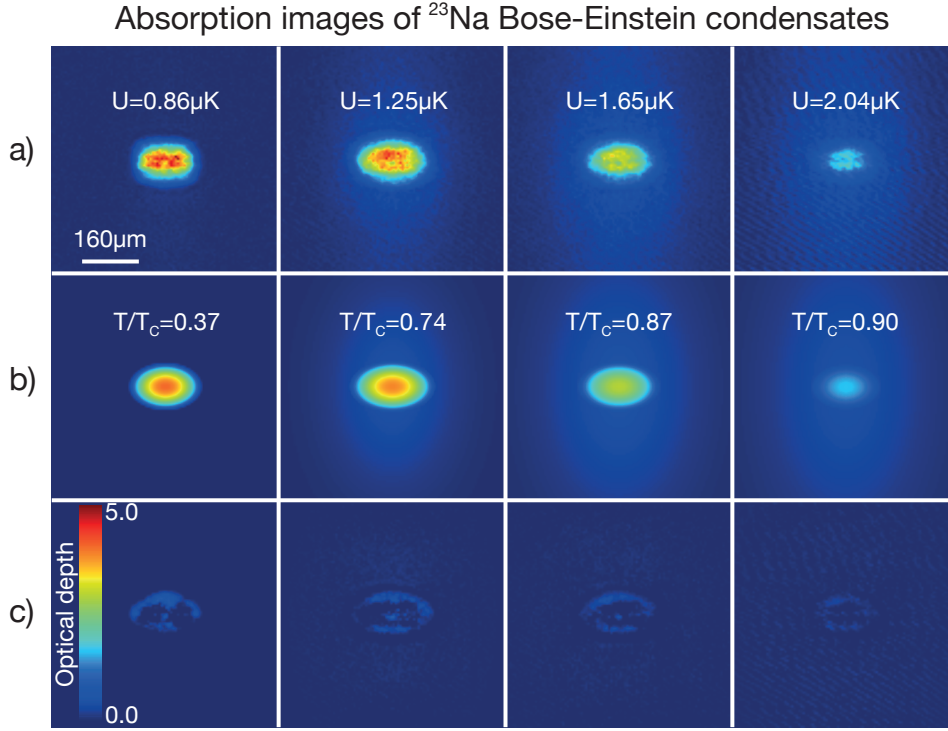


Figure 2.19 – a) Absorption images of a Bose-Einstein condensate ($N \simeq 10^5$) for decreasing trap depth. b) reconstruction of the density profile from a) obtained by a least square fit of equation 2.42. c) Residuals of the least square fit. The ratio T/T_C is obtained by numerical integration of the fitted line-densities for the Thomas-Fermi profile and the Gaussian thermal wing. For the lowest trap depth the thermal wing is not detectable and a condensate fraction of 95% is assumed.

For characterizing degenerate Bose-Fermi mixtures in our setup the following relations are useful: The Fermi temperature of ^{40}K in a harmonic trap is given by:

$$T_F = \frac{\hbar}{k_B} \sqrt[3]{6 \cdot N_K \omega_z \omega_r^2} \quad (2.46)$$

For our crossed dipole trap (see table 3.1), the ratio T_F/T_C is given by :

$$\frac{T_F}{T_C} = 2.21 \cdot \sqrt[3]{6 \cdot N_K/N_{Na}} \quad (2.47)$$

For a typical atom number ratio of $N_K/N_{Na} \simeq 0.1$ the Fermi temperature of ^{40}K and the condensation temperature of ^{23}Na are almost equal.

2.8.1 Feshbach optimized sympathetic cooling

Similar to the situation in the magnetic quadrupole trap (equation 2.25) inter-species three-body losses have to be suppressed in order to ensure efficient sympathetic cooling of ^{40}K by ^{23}Na . We use an inter-species Feshbach resonance to control the three-body loss coefficient $\beta_{NaK} = \beta(a_{NaK})$. In this way ^{40}K three-body loss can be minimized without decreasing the density in the trap ensuring efficient evaporative cooling of ^{23}Na . Note

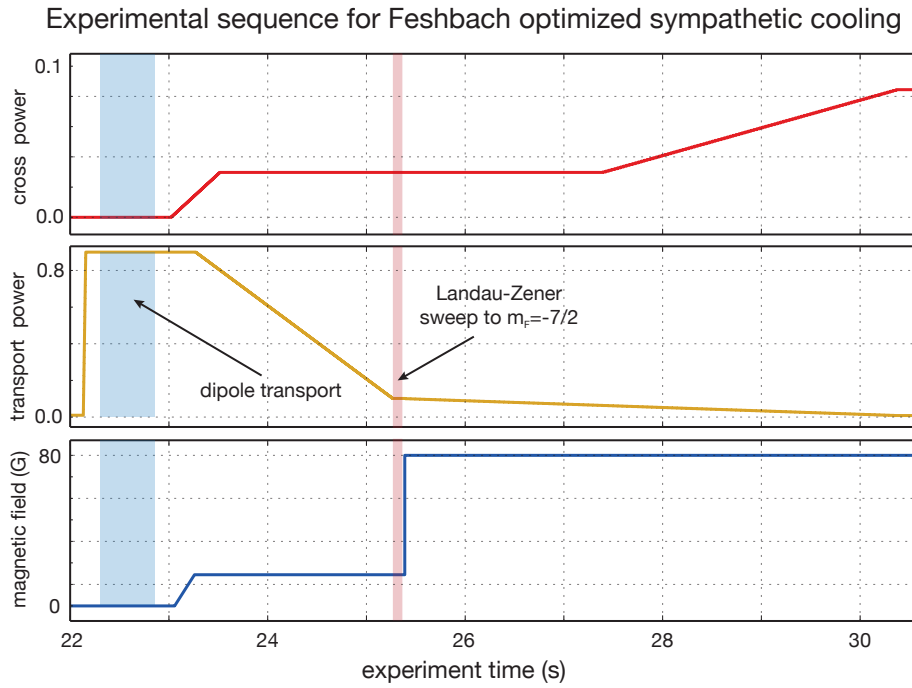


Figure 2.20 – Experimental sequence that was used to optimize sympathetic cooling of ^{40}K . The mixture is evaporated in $|F = 1, m_F = 1\rangle \otimes |F = 9/2, m_F = 9/2\rangle$ at 14.5G to a trap depth of $\simeq 8\mu\text{K}$. A multi-level Landau-Zener RF sweep then transfers ^{40}K to $|F = 9/2, m_F = -7/2\rangle$ and the magnetic field is adjusted to a value that lies in the vicinity of a Feshbach resonance. The mixture is then further evaporated until Bose-Einstein condensation of ^{23}Na appears.

that close to a Feshbach resonance β_{NaK} scales as $\beta_{NaK} \propto a_{NaK}^4$ [54]. With this in mind the evaporation sequence for sympathetic cooling of ^{40}K was optimized by the following procedure:

1. Evaporate the ^{40}K ^{23}Na mixture in the initially prepared collision channel $|F = 1, m_F = 1\rangle \otimes |F = 9/2, m_F = 9/2\rangle$ at a guiding field of $\simeq 14.5\text{G}$ until three-body loss of ^{40}K becomes significant.
2. Perform a multi-level Landau-Zener sweep at 14.5G to transfer the mixture to a Feshbach resonant collision channel (e.g. $|F = 1, m_F = 1\rangle \otimes |F = 9/2, m_F = -7/2\rangle$).
3. Ramp the magnetic field to a value where the inter-species scattering length is small enough to suppress three-body loss but still allows for thermalization between ^{23}Na and ^{40}K .

Fig. 2.20 shows the experimental sequence that was used to optimize the sympathetic cooling procedure.

The mixture is evaporated in the single beam dipole trap with only a weak crossed trap present until the 1064nm laser is at 10% of the total power of 7.5W. Then the resonant collision channel is prepared and the magnetic field is set to a value in the vicinity of a Feshbach resonance. The mixture is further evaporated until 1.75% of total power. We then measure both atom numbers after evaporation and observe when a ^{23}Na BEC

is prepared in presence of ^{40}K . Fig. 2.21 shows a scan of the magnetic field at which sympathetic cooling is performed.

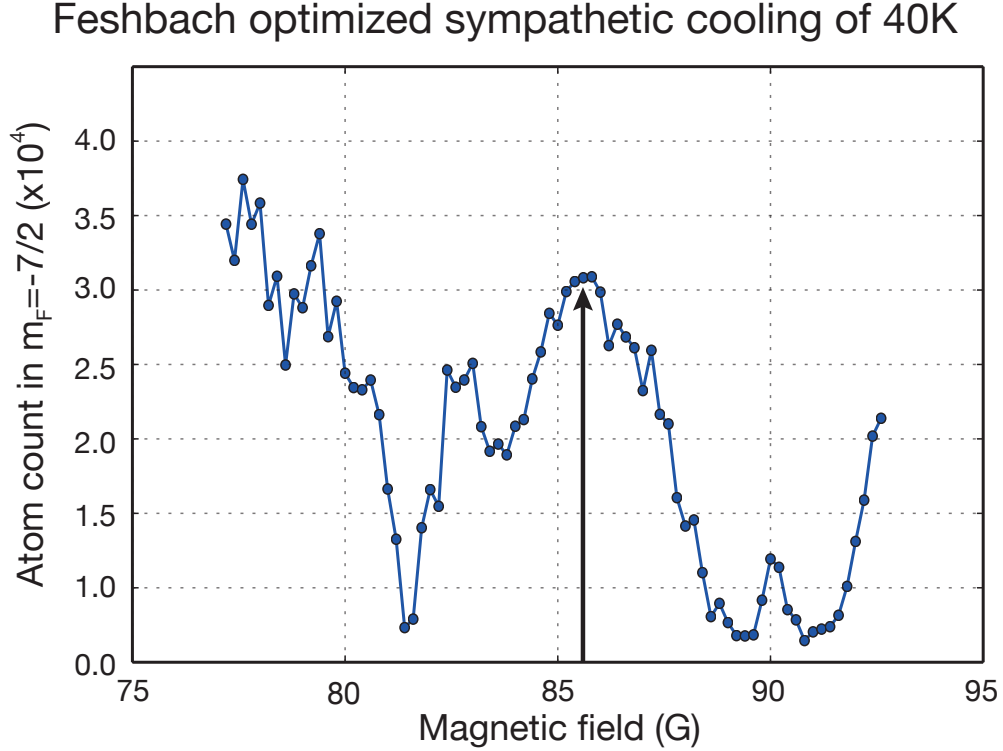


Figure 2.21 – ^{40}K atom number in $|F = 9/2, m_F = -7/2\rangle$ after combined evaporation in the crossed dipole trap as function of the applied magnetic field. Two Feshbach resonances at $\simeq 90\text{G}$ and $\simeq 81.5\text{G}$ result in strong loss of ^{40}K in their vicinity. The arrow indicates the field that gives best results for sympathetic cooling. Note the double peak structure of the 90G resonance feature, which is caused by a reduction in evaporation efficiency due to the large three-body loss rate.

We observe strong loss of ^{40}K caused by two Feshbach resonances at 81.5G and 90.2G . Evaporation works best close to the magnetic field value that corresponds to zero scattering length. The position and width of both Feshbach resonances can be determined more precisely by first evaporating the mixture at the optimal field of $B \simeq 85.5\text{G}$ and then measuring ^{40}K atom loss as a function of magnetic field. Fig. 2.22 shows the result of this measurement for two different hold times in the dipole trap after the magnetic field has been adjusted.

Unfortunately the magnetic field is not set arbitrarily fast. For this reason the shape of the loss features at 81.5G and 90.2G become asymmetric due to atom loss occurring when the magnetic field is swept from the value used for evaporation to a value that lies above (or below) the respective Feshbach resonance. From Fig. 2.22 we can determine the position of both resonances and estimate their widths (the width of the lower resonance is not accurate):

$$B_1 = 81.5\text{G}, \Delta B_1 \simeq -1\text{G} \quad B_2 = 90.2\text{G}, \Delta B_2 = -2.5\text{G} \quad (2.48)$$

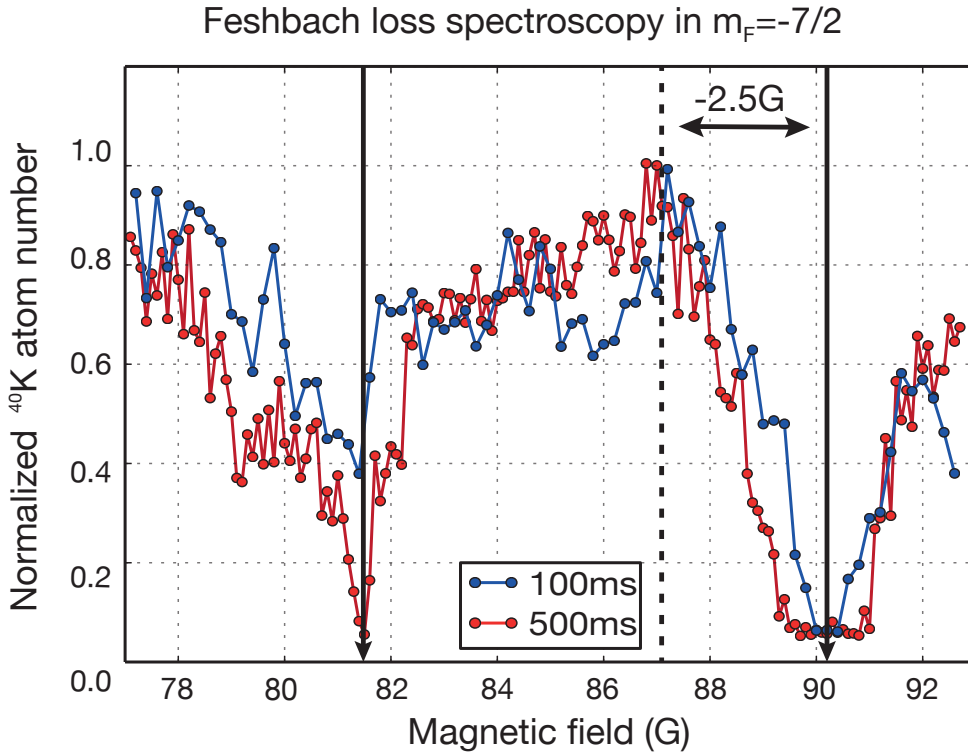


Figure 2.22 – Feshbach loss spectroscopy in the $|F = 1, m_F = 1\rangle \otimes |F = 9/2, m_F = 9/2\rangle$ collision channel. The mixture is evaporated in the crossed dipole trap at a magnetic field of 85.5G to suppress three-body loss. The field is then set to the value at which the loss is detected. ^{40}K atom number is the detected after a holding time of 100ms (500ms). The position of both Feshbach resonances can be clearly determined. For the resonance at 90.2G also the width can be clearly identified as the distance between the minimum and maximum of atom loss. For the resonance at 81.5G the identification of the width is less accurate.

Fig. 2.23 displays the inter-species scattering length a_{NaK} as function of magnetic field in the vicinity of both Feshbach resonances. The scattering length is calculated according to [55]:

$$a_{NaK}(B) = -690a_0 \cdot \left(1 + \frac{\Delta B_1}{B - B_1} + \frac{\Delta B_2}{B - B_2}\right) \quad (2.49)$$

With this technique at our disposal we can produce degenerate Bose-Fermi mixtures with varying atom number ratio. To do so, we set the magnetic field to 85.5G and evaporate to a final trap depth of $\simeq 0.9\mu\text{K}$. For ^{23}Na alone this evaporation sequence results in a condensate fraction of $> 95\%$ (compare Fig. 2.19). We then vary the atom number ratio of the mixture by changing the detuning of the ^{23}Na 3D-MOT cooling laser within $\pm 2\text{MHz}$. Although the total number of ^{23}Na is reduced by a factor of 2–3 compared to evaporation without loading ^{40}K we still produce almost pure Bose-Einstein condensates. Fig. 2.24 shows a series of dual species absorption images obtained after a time of flight of 7.5ms (8.25ms for ^{23}Na).

The moderately negative inter-species scattering length leads to an increase of density in the trap center for both species. This effect is still visible in the optical density of both atom clouds after a long time of flight (see row c) in Fig. 2.24). Since the intra-species scattering length of ^{23}Na is positive this configuration is ideal for sympathetic cooling;

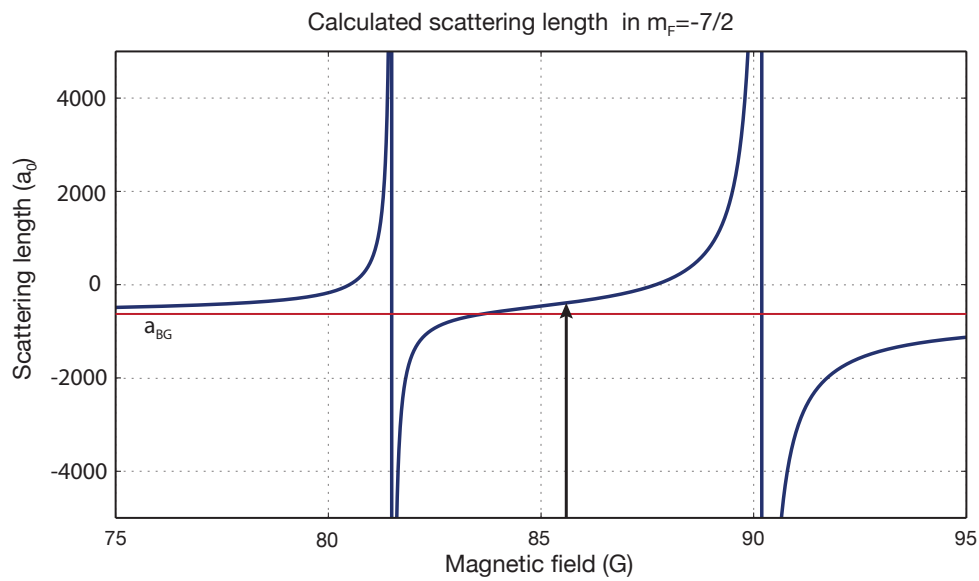


Figure 2.23 – ^{40}K ^{23}Na inter-species scattering length in the $|F = 1, m_F = 1\rangle \otimes |F = 9/2, m_F = 9/2\rangle$ collision channel as function of magnetic field (see equation 2.49). The horizontal red line indicates the background scattering length of $\simeq -690a_0$. The black arrow indicates the field at which sympathetic cooling works best.

Absorption images of degenerate ^{23}Na ^{40}K Bose-Fermi mixtures

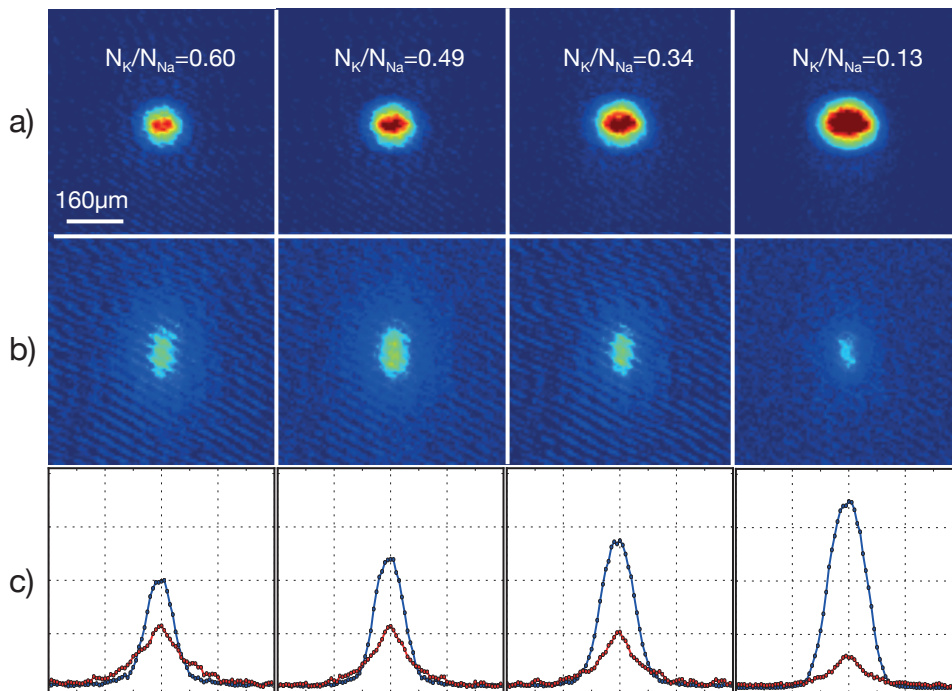


Figure 2.24 – Dual wavelength absorption images of deeply degenerate Bose-Fermi mixtures of ^{23}Na row a) and ^{40}K row b). Row c) shows a sum along the y-direction. The density distribution of the fermionic ^{40}K clearly is affected by attractive interaction with the ^{23}Na BEC.

we get high density in the overlap region whereas at the same time the mixture is stable against phases separation and collapse [59]. At the same time we can precisely adjust the three-body loss coefficient. When prepared in a quasi 1D geometry the ^{40}K ^{23}Na mixture could well be used to investigate stable bright dual species solitons predicted to exist in attractive Bose-Fermi mixtures [60] with repulsive Boson interaction. The increased density overlap in the center of the trap could also be used for efficient association of Feshbach molecules well below the critical temperature for Bose-Einstein condensation.

2.9 Summary

The presented experimental setup is capable of producing degenerate Bose-Fermi mixture of ^{40}K ^{23}Na at temperature as low as 40% of the Fermi temperature. In this configuration more than 95% of the ^{23}Na occupy the groundstate of the trapping potential. It was crucial to establish full control of the internal hyperfine state of both species in order to suppress inelastic spin-exchange and three-body losses. Precise control of the external magnetic field allows us to address inter-species Feshbach resonances and thereby adjust the effective low-temperature interaction potential between the atoms. In its current configuration our experimental setup is well suited for further experiments on association of weakly bound Feshbach molecules and high resolution molecular spectroscopy. Moreover the setup features in-vacuum field electrodes and a separate glass science with large optical access to facilitate future experiments on dipolar interacting quantum matter.

Feshbach molecules

This chapter treats the theoretical background and the experimental implementation of molecule association via magnetically tunable Feshbach resonances. Extensive review articles exist on the physics of Feshbach resonances in general [55] and molecule association in particular [61]. A Feshbach resonance appears in the low temperature multi-channel collision process of two atoms with internal hyperfine structure, when a bound state in an energetically not accessible (*closed*) collision channel is resonant (equal in energy) with the scattering state of the colliding unbound particles. For collisions of cold neutral atoms the closed channel and the scattering state are two different hyperfine state configurations of the atoms. The resonant closed channel can be populated (free atoms are associated to molecules) either by adiabatically transforming the scattering state into the bound state using magnetic field sweeps (*magneto-association*) [62] or by applying a suitable RF pulse that changes the hyperfine state configuration of the scattering channel to the configuration of the near-threshold bound state (*RF-association*) [63]. The difference in magnetic moment of the scattering state and the closed channel can be used to precisely adjust the binding energy of the bound state with respect to the total energy (*threshold*) of the colliding atoms.

Since the first observation of ultracold ^{85}Rb ^{87}Rb Feshbach molecules in 2006 [64], heteronuclear Feshbach molecules have been produced in Bose-Bose mixtures of ^{87}Rb ^{133}Cs [65], ^{87}Rb ^{41}K [66] and ^{87}Rb ^{23}Na [67] as well as in Bose-Fermi mixtures of ^{87}Rb ^{40}K [68], ^{23}Na ^6Li [69] and ^{23}Na ^{40}K [70]. For the subject of this thesis it is most relevant that Feshbach molecules of chemically different atoms can serve as a starting point for the production of polar groundstate molecules via STIRAP.

The following experimental requirements need to be fulfilled in order to successfully associate Feshbach molecules:

- A near degenerate mixture of the constituent elements.
- Coherent control over the internal hyperfine state of the atoms for clean preparation of collision channels that exhibit Feshbach resonances suitable for molecule association.
- Precise and fast magnetic field control to address Feshbach resonances and change the binding energy of the least-bound molecular state in the closed channel.

- Internal state sensitive detection methods for implementation of internal state control and direct observation of Feshbach molecules.

In this chapter, I will discuss the specialized equipment and experimental techniques that are required for collision channel preparation, magnetic field control, RF association of Feshbach molecules and internal state sensitive detection by absorption imaging.

3.1 Theoretical background: Feshbach resonances and molecule association

A complete theoretical description of Feshbach resonances can be found in the review article [55] and the references therein. In this section the presentation of the subject is limited to the mechanism that is responsible for the appearance of strong Feshbach resonances in s-wave collision of ultracold atoms. I therefore neglect relativistic spin-dependent inter-particle interactions [55] and do not consider partial waves with $l > 0$. We consider the scattering process of two particles with reduced mass μ in presence of a homogeneous external magnetic field \mathbf{B} . The internal structure of both particles is given by the groundstate hyperfine structure. The Hamiltonian of the total system is given by:

$$H = H_R + H_{int}. \quad (3.1)$$

Here H_R is the Hamiltonian that governs the relative motion of the two atoms and H_{int} describes their internal state. H_{int} comprises hyperfine interaction between the electron spins and the nuclear spins of the atoms as well as the Zeeman interaction between the atoms and the external magnetic field. The Hamiltonian of the relative motion is given by:

$$H_R = \frac{-\hbar^2}{2\mu} \frac{d^2}{dR^2} + V(R) \quad (3.2)$$

The molecular potential $V(R)$ that governs the collision process can be expressed in terms of projection operators on the spin-singlet ($J = 0$) and the spin-triplet ($J = 1$) subspace:

$$V(R) = V_1(R)|1\rangle\langle 1| + V_0(R)|0\rangle\langle 0|. \quad (3.3)$$

Here $V_0(R)$ is the singlet potential of the molecular groundstate i.e. $X^1\Sigma$ and $V_1(R)$ is the triplet potential i.e. $a^3\Sigma$. The scattering problem is analyzed in the Breit-Rabi pair basis:

$$|\alpha\rangle = |Fm_F\rangle_{Na}|F'm'_F\rangle_K, \quad (3.4)$$

which diagonalizes H_{int} . Here F and m_F just label the basis states and are only good quantum numbers if $B = 0$. The product state $|\alpha\rangle$ is called a *collision channel*. The *collision channel basis* that spans the complete Hilbert space corresponding to H is then given by:

$$\{|\alpha\rangle|\Psi_\alpha(R, E)\rangle\}_\alpha, \quad (3.5)$$

where $\Psi_\alpha(R, E)\rangle_\alpha$ are (depending on the energy E) either scattering wave functions or bound states of the scattering problem. Since in general, $|\alpha\rangle|\Psi_\alpha(R, E)\rangle$ is not an eigenstate

of the electron spin, the interaction potential (equation 3.3) mixes different collision channels (with the same value of m_F) when the atoms approach each other. In this sense, a general scattering process of cold atoms with internal hyperfine structure is a *coupled channel problem*. As a result, a spin-polarized ^{23}Na ^{40}K Bose-Fermi mixture that is not prepared in a state with maximal angular momentum projection can experience spin-exchange collisions. Since the interaction potential commutes with the total spin operator, for further analysis we express $|\alpha\rangle|\Psi_\alpha(R, E)\rangle$ in the *spin basis* [71]

$$|Jm_Jm_{Na}m_K\rangle = |Jm_JI_{Na}m_{Na}I_Km_K\rangle, \quad (3.6)$$

via

$$|\alpha\rangle|\Psi_\alpha(R, E)\rangle = \sum_{(Jm_Jm_{Na}m_K)} \langle Jm_Jm_{Na}m_K|\alpha\rangle |Jm_Jm_{Na}m_K\rangle \phi_J(R, E)/R. \quad (3.7)$$

The sum includes only spin basis states that have the same value for the projection of the total angular momentum as the collision channel $|\alpha\rangle$ i.e. $m_\alpha = m_J + m_{Na} + m_K$. The scattering wavefunction $\phi_J(R, E)$ is the solution to the time-independent radial Schrödinger equation:

$$\left(\frac{\hbar^2}{2\mu} \frac{d^2}{dR^2} + V_J(R) \right) \phi_J(R, E) = E_J \phi_J(R, E). \quad (3.8)$$

Here E is the total energy of the collision process, R the internuclear distance and the index $J = 0, 1$ indicates either spin-singlet or spin-triplet. In this basis the relative Hamiltonian H_R is now diagonal and the mixing between the basis states is caused by non-diagonal terms of the hyperfine interaction. The Hamiltonian for the internal structure is given by:

$$H_{int} = A_{Na} \mathbf{I}_{Na} \mathbf{J} + A_K \mathbf{I}_K \mathbf{J} + H_Z \quad (3.9)$$

The Zeeman Hamiltonian is diagonal in the spin-basis

$$E_z = \mu_B (g_J m_J + g_{I_{Na}} m_{Na} + g_{I_K} m_K) \cdot B \quad (3.10)$$

with electronic and nuclear g-factors $g_J, g_{I_{Na}}, g_{I_K}$. The hyperfine Hamiltonian

$$H_{hf} = A_{Na} \mathbf{I}_{Na} \mathbf{J} + A_K \mathbf{I}_K \mathbf{J} \quad (3.11)$$

ouples singlet and triplet spin-basis states. A complete diagonalization of the total Hamiltonian $H = H_R + H_{int}$ requires precise knowledge of the singlet and triplet groundstate Born-Oppenheimer potentials and involves a numerical integration of a system of coupled radial Schrödinger equations. The solutions of these coupled channel equations are all bound and scattering states of the interacting atoms.

In order to understand the appearance of Feshbach scattering resonances in the context of ultracold gases it is instructive to consider a simplification of the complete coupled channels problem. Assume that we can describe the scattering problem to a good approximation by just two scattering channels (see Fig. 1 of [55]). The system is prepared in the *entrance channel* $|\alpha\rangle$ with a total collision energy E that is close to zero and smaller than all other energy scales in the problem. The spatial part of the entrance channel therefore is an unbound scattering wavefunction $\Psi_\alpha(R, E)$. The second channel correspond to

a different hyperfine state configuration $|c\rangle$ that exhibits a different interaction potential and has an internal energy that is larger than the total energy of the entrance channel. For this reason the scattering continuum of this channel is energetically not accessible during the collision process and channel $|c\rangle$ is called the *closed channel* of the problem. A Feshbach scattering resonance can occur if one of the bound state solutions $|C\rangle = \Psi_C(R)|c\rangle$ of the closed channel (with eigenenergy E_C) is coupled to the entrance channel by a position dependent perturbation operator $W(R)$. For s-wave collisions this coupling is mediated by the spin-dependent molecular potential $V(R)$.

Without coupling to the closed channel the elastic scattering process in the entrance channel is solely characterized by a background phase shift $\eta_{bg}(E)$. For a s-wave collision the phase shift is related to the scattering wavefunction $\Psi_\alpha(R, E)$ at large internuclear distances via

$$\Psi_\alpha(R, E)/R \rightarrow c \frac{\sin(kR + \eta(E))}{\sqrt{k}} \cdot \exp(i\eta(E)) \text{ as } R \rightarrow \infty \quad (3.12)$$

The coupling operator $W(R)$ however mixes the open and the closed channels when the total energy of the entrance channel E approaches the energy of the bound state E_C in the closed channel. A resonance is associated with a π phase change of the scattering wavefunction in the entrance channel when the collision energy E is varied across a small energy interval around E_C . As we will see below, for observation and control of Feshbach resonances in ultracold gases the kinetic energy of the collision remains fixed and the energy difference $E - E_C$ is changed by an external magnetic field that affects the internal energy of each channel. It is also important to note that Feshbach resonances in ultracold gases appear always as threshold resonances i.e. at a point where the boundstate in the closed channel asymptotically approaches the scattering continuum [72] of the entrance channel. In this situation the scattering phase is modified by a resonant contribution[55]:

$$\eta_0(E) = \eta_{bg}(E) + \eta_{res}(E), \quad (3.13)$$

where $\eta_{res}(E)$ is given by a Breit-Wigner function [73]:

$$\eta_{res}(E) = -\tan^{-1} \left(\frac{\frac{1}{2}\Gamma(E)}{E - E_C - \delta E(E)} \right) \quad (3.14)$$

The energy dependent resonance parameters *width* $\Gamma(E)$ and *shift* $\delta E(E)$ are determined by the inter-channel coupling operator $W(E)$ via:

$$\begin{aligned} \Gamma(E) &= 2\pi |\langle C|W(R)|\alpha\rangle|^2 \\ \delta E(E) &= P \int_{-\infty}^{+\infty} \frac{|\langle C|W(R)|\alpha\rangle|^2}{E - E'} dE', \end{aligned} \quad (3.15)$$

where P indicates a Cauchy principal value integration.

Since the scattering potential in the entrance channel is of van der Waals type (i.e. $V(R) \propto 1/R^6$), the s-wave scattering phase shift is given by the *effective range* expansion [12]:

$$k \cot[\eta_0(E)] = \frac{1}{a} + \frac{1}{2}r_0k^2 + o(k^3), \quad (3.16)$$

where the constants a and r_0 have the dimension of length and are called *scattering length* and *effective range*. For s-wave collisions at ultracold temperatures (i.e. in a situation where $k \rightarrow 0$) it is a good approximation to only retain the first term of the expansion:

$$\tan[\eta_0(E)] \simeq \eta_0(E) \rightarrow -ka. \quad (3.17)$$

In particular we have for the background phase-shift:

$$\tan[\eta_{bg}(E)] \simeq \eta_{bg}(E) \rightarrow -ka_{bg}. \quad (3.18)$$

For collision that only involve a single open channel and are therefore purely elastic the scattering length a is related to the energy dependent elastic scattering cross section $\sigma_{el}(E)$ via [55]

$$\sigma_{el}(E) = \frac{\pi}{k^2} |1 - \exp(-i2ka)|^2 \rightarrow 4\pi a^2, \text{ as } k \rightarrow 0 \quad (3.19)$$

By taking the limit of low collision energy $k \rightarrow 0$ of equations 3.13, 3.14 and 3.18:

$$\frac{1}{2}\Gamma(E) \rightarrow ka_{bg}\Gamma_0, \quad (3.20)$$

$$\delta E(E) \rightarrow \delta E_0, \quad (3.21)$$

$$\tan[\eta_{res}(E)] \rightarrow \frac{-ka_{bg}\Gamma_0}{-E_C - \delta E_0},$$

we finally arrive at a relation between the scattering length and the energy of the bound state in the closed channel:

$$a(E_C) = a_{bg} + \frac{a_{bg}\Gamma_0}{-E_C - \delta E_0}. \quad (3.22)$$

Note that the zero of energy or *scattering threshold* is always defined as the internal energy (hyperfine + Zeeman) of the entrance channel and therefore $E \rightarrow 0$ as $k \rightarrow 0$. The energy of the bound state relative to threshold can be changed by adjusting the external magnetic field:

$$E_C(B) = \delta\mu(B - B_C), \quad (3.23)$$

where $\delta\mu$ is the difference in magnetic moment of open and closed channel and B_C the value of the magnetic field where $E_C = 0$. In this way we finally obtain the well-known formula for the s-wave scattering length as function of magnetic field for an isolated Feshbach resonance:

$$a(B) = a_{bg} \left(1 - \frac{\Delta B}{B - B_0} \right) \quad (3.24)$$

The phenomenological width of a magnetic field controlled Feshbach resonance is given by:

$$\Delta B = \frac{\Gamma_0}{\delta\mu} \quad (3.25)$$

The position of the Feshbach resonance is shifted by the interaction between the closed and the open channel:

$$B_0 = B_C + \delta B, \quad (3.26)$$

where the magnitude of this shift is given by:

$$\delta B = -\frac{\delta E_0}{\delta \mu}. \quad (3.27)$$

Since the scattering length is directly related to the collision cross section, Feshbach resonances are generally detected in ultracold gases by observing a strong increases of the three-body loss rate. This method is conventionally termed *Feshbach loss spectroscopy*. Experimentally the resonance position is identified with the point of maximal three-body loss rate and the width with the distance between the position and a magnetic field at which the loss is minimal (see Fig. 2.22). Depending on the sign of a_{bg} and $\delta\mu$ the point where the scattering length becomes zero is either below or above the resonance position. For the $^{23}\text{Na}^{40}\text{K}$ mixture 21 Feshbach resonances have been identified and characterized by loss spectroscopy [44]. Table 3.1 lists the collision channel, resonance position and resonance width for the 11 s-wave resonances from [44]:

Collision channel	Position B_0	Width ΔB
$ F = 1m_F = 1\rangle_{Na} F = 9/2m_F = -3/2\rangle_K$	116.9	0.5
$ F = 1m_F = 1\rangle_{Na} F = 9/2m_F = -3/2\rangle_K$	129.5	4.6
$ F = 1m_F = 1\rangle_{Na} F = 9/2m_F = -5/2\rangle_K$	175	20.0
$ F = 1m_F = 1\rangle_{Na} F = 9/2m_F = -5/2\rangle_K$	96.5	0.5
$ F = 1m_F = 1\rangle_{Na} F = 9/2m_F = -5/2\rangle_K$	106.9	1.8
$ F = 1m_F = 1\rangle_{Na} F = 9/2m_F = -5/2\rangle_K$	138	30
$ F = 1m_F = 1\rangle_{Na} F = 9/2m_F = -7/2\rangle_K$	81.6	0.2
$ F = 1m_F = 1\rangle_{Na} F = 9/2m_F = -7/2\rangle_K$	89.8	1.1 (2.5)
$ F = 1m_F = 1\rangle_{Na} F = 9/2m_F = -7/2\rangle_K$	108.6	6.6
$ F = 1m_F = 1\rangle_{Na} F = 9/2m_F = -9/2\rangle_K$	78.3	1.1
$ F = 1m_F = 1\rangle_{Na} F = 9/2m_F = -9/2\rangle_K$	88.2	4.3 (12)

Table 3.1 – Collision channels, resonance positions and resonance widths for all 11 s-wave Feshbach resonances that have been identified in [44]. Values in brackets indicate the results of our measurements.

At a magnetic field that is close to the resonance position B_0 the molecular bound state is strongly affected by mixing with the scattering state. Close to threshold the binding energy depends quadratically on the scattering length [55]:

$$E_b(B) = \frac{\hbar^2}{2M\alpha(B)^2}, \quad (3.28)$$

where M is the reduced mass of the colliding atom pair. Since the bound state crosses the threshold to the scattering continuum at $B = B_0$ and due to the fact that it is resonantly dressed by the scattering state it is possible to transfer the initial scattering state to the molecular boundstate by adiabatically changing the magnetic field from a value above the resonance, where the bare bound state energy $E_c > 0$ to a value below the resonance where $E_c < 0$. It is also possible to associate Feshbach molecules by RF association [63] when the magnetic field is adjusted to a value that is slightly below resonance.

3.2 RF association of $^{23}\text{Na}^{40}\text{K}$ Feshbach molecules

In our experiment we associate Feshbach molecules with a binding energy of $E_b \simeq h83\text{kHz}$ using the s-wave resonance at $B_0 \simeq 89.8\text{G}$ in the

$|F = 1, m_F = 1\rangle_{\text{Na}}|F = 9/2, m_F = -9/2\rangle_{\text{K}}$ collision channel. This particular resonance has been chosen deliberately. Starting from a Feshbach molecule in this hyperfine state configuration it is possible to populate the absolute hyperfine groundstate of the $^{23}\text{Na}^{40}\text{K}$ molecule and thereby to suppress spin-exchange collisions. This statement will become clear when STIRAP is discussed below in section 4.6.1. Fig. 3.1 illustrates how weakly bound molecules can be associated starting from a near degenerate Bose-Fermi mixture. The $^{23}\text{Na}^{40}\text{K}$ mixture is prepared in the non-resonant

$|F = 1, m_F = 1\rangle_{\text{Na}}|F = 9/2, m_F = -7/2\rangle_{\text{K}}$ channel at a magnetic field that is set slightly below 85.5G a resonance in the neighboring $|F = 1, m_F = 1\rangle_{\text{Na}}|F = 9/2, m_F = -9/2\rangle_{\text{K}}$ channel.

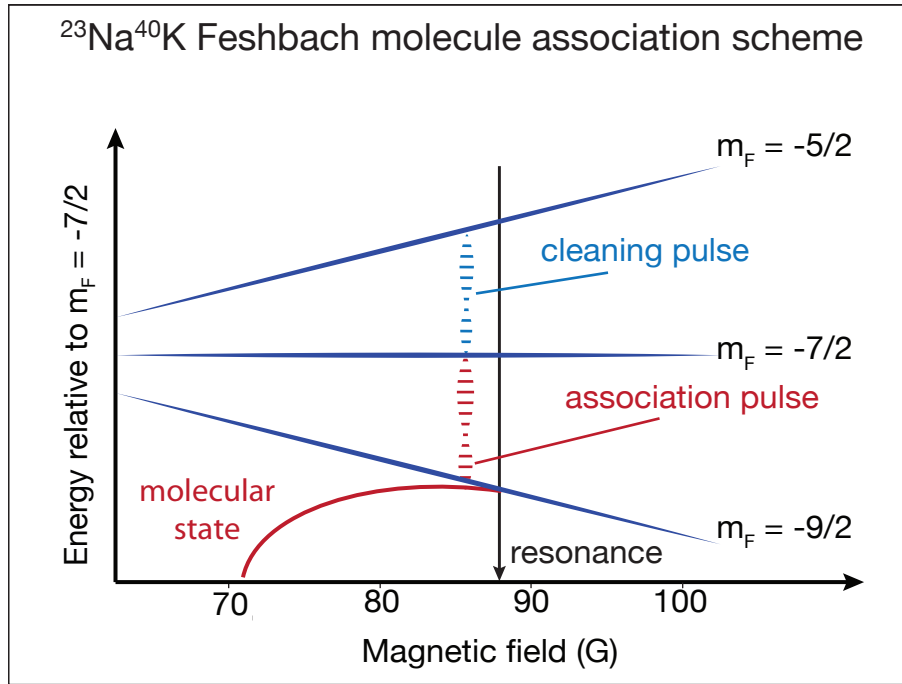


Figure 3.1 – Experimental scheme for RF association of $^{23}\text{Na}^{40}\text{K}$ Feshbach molecules. The $^{23}\text{Na}^{40}\text{K}$ mixture is prepared in the non-resonant collision channel $|F = 1, m_F = 1\rangle_{\text{Na}}|F = 9/2, m_F = -7/2\rangle_{\text{K}}$ at a magnetic field that is set just below the Feshbach resonance in the neighboring $|F = 1, m_F = 1\rangle_{\text{Na}}|F = 9/2, m_F = -9/2\rangle_{\text{K}}$ channel. A RF pulse drives the transition from the non-resonant channel to the resonant one. Depending on the frequency of the RF pulse either the hyperfine state of free ^{40}K atoms is changed or weakly bound molecules are associated (see Fig. 3.4). A second RF pulse transfers non-associated ^{40}K atoms to the $|F = 1, m_F = 1\rangle_{\text{Na}}|F = 9/2, m_F = -5/2\rangle_{\text{K}}$ channel in order to reduce the background signal during absorption imaging of Feshbach molecules.

Close to resonance the binding energy E_b of the dressed molecular bound state approaches the scattering continuum quadratically according to equation 3.28. The molecular bound state can now be directly populated by a suitable RF pulse that transfers ^{40}K atoms from the $|F = 9/2, m_F = -9/2\rangle_{\text{K}}$ hyperfine state to the adjacent $|F = 9/2, m_F =$

$-9/2\rangle_K$ state. In this way the $^{23}\text{Na}^{40}\text{K}$ mixture is transferred to the Feshbach resonant channel. If the frequency of the RF photon equals the difference in Zeeman energy i.e. $\omega_{RF} = \delta\mu \cdot B/\hbar$ the mixture is transferred to the open channel. By increasing the RF frequency to $\omega_{RF} = \delta\mu \cdot B/\hbar + E_b$ the bound state in the closed channel is populated. In the experiment we apply an additional RF cleaning pulse on the $|F = 9/2, m_F = -7/2\rangle \rightarrow |F = 9/2, m_F = -5/2\rangle$ transition in order to remove ^{40}K atoms from the $|F = 9/2, m_F = -7/2\rangle$ state that have not been transferred to the $|F = 9/2, m_F = -7/2\rangle$ state. The purpose of this cleaning pulse is to suppress non-resonant absorption when we directly detect Feshbach molecules at the given magnetic field by absorption imaging on the $|F = 9/2, m_F = -9/2\rangle \rightarrow |F' = 11/2, m_F = -11/2\rangle$ cycling transition.

In order to estimate the RF coupling we can achieve in the experiment we measure the Rabi frequency for the bare $|F = 9/2, m_F = -7/2\rangle \rightarrow |F = 9/2, m_F = -9/2\rangle$ transition. For this measurement the ^{40}K atoms are detected simultaneously in both hyperfine states by internal state selective absorption imaging. Fig. 3.2 shows the result of two different measurements of the Rabi frequency. We measure the normalized difference in atom count

$$N = \frac{N_{-9/2} - \alpha N_{-7/2}}{N_{-9/2} + \alpha N_{-7/2}} \quad (3.29)$$

as function of the RF pulse length and perform a least square fit to obtain the Rabi oscillation period. We also include an exponential decay and an additional fit parameter α to account for the different absorption cross sections of both imaging transitions. The number $N_{-9/2}$ and $N_{-7/2}$ are derived from the absorption images by assuming the maximal absorption cross-section for a cycling transition [47].

$$\sigma_{sc} = \frac{3\lambda^2}{2\pi} \quad (3.30)$$

In panel a) the Rabi frequency is measured with ^{40}K alone and in panel b) in presence of ^{23}Na . Since the measurement is performed close to a Feshbach resonance the interaction between the two species results in an increased decoherence rate. In both cases the Rabi frequency is determined to $\Omega_{RF} \simeq 2\pi \cdot 14\text{kHz}$ and $\alpha = 0.32$.

For generating the RF signal we use custom build direct digital synthesizer (DDS) circuits that also allow us to perform continuous frequency sweeps for Landau-Zener transfers as well as to generate amplitude modulated RF pulses. The output of the DDS circuits are combined by RF switches and are then amplified by a 25W power amplifier. Finally a custom build RF coil antenna ($\simeq 10$ windings, $\simeq 4\text{cm}$ diameter) is placed as close as possible to the glass science cell. We monitor the transmitted RF signals by an amplified pick up antenna.

Precise and fast magnetic field control is established by a custom build current control loop. Fig. 3.3 shows a schematic of the current magnetic field setup.

Water-cooled Helmholtz coils are placed around the glass science cell. The electrical current is controlled by two different actuators based on metal oxide semiconductor field effect transistors (MOSFETs). The major part of the total current is controlled by 4 identical high power MOSFET's (Semikron SKM111AR) that are mounted on a water cooled copper base plate. The gate-source voltage is supplied by a custom build PI controller. The

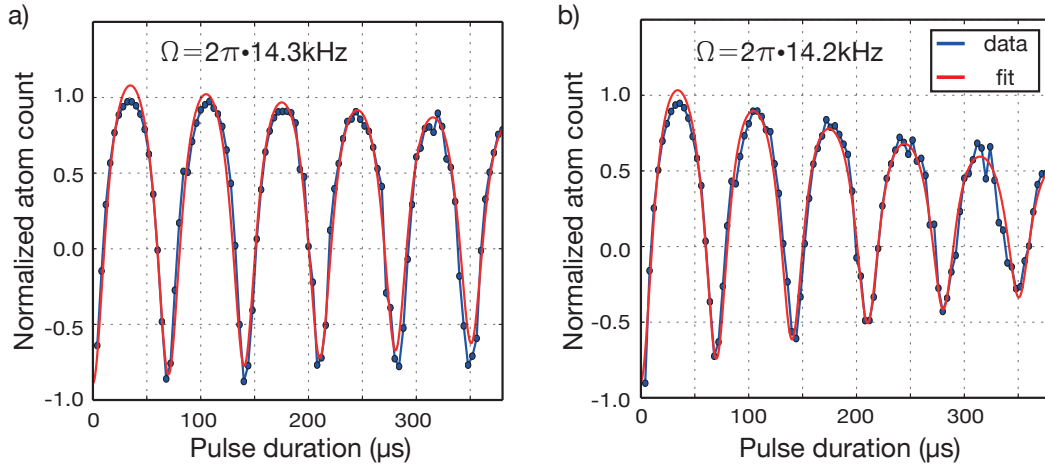
Measurement of the ^{40}K $m_F = -7/2$ to $m_F = -9/2$ Rabi frequency

Figure 3.2 – Measurement of the peak Rabi frequency for the bare $|F = 9/2, m_F = -7/2\rangle \rightarrow |F = 9/2, m_F = -9/2\rangle$ transition for ^{40}K alone **a)** and in the presence of ^{23}Na **b)**. In presence of ^{23}Na the decoherence rate is significantly increased.

current is measured directly after the MOSFETS via a high precision current transducer (LEM IT 700-SB Ultrastab). The bandwidth $\simeq 1\text{kHz}$ of this control loop is limited by the large gate capacitance of the high power MOSFETs. For this reason we upgraded the current control setup by a fast bypass that can control a maximal current of 15A. For this bypass we use a different type of MOSFET with significantly smaller gate capacitance (International Rectifiers IRL-88721). To charge and discharge the gate as fast as possible we drive the bypass MOSFET by a specialized current feedback amplifier (Linear technologies LT1210). With these modifications we increase the loop bandwidth by one order of magnitude. In its current configuration we can execute magnetic field changes of $\simeq \pm 10\text{G}$ with a $1/e$ settling time of $< 2\text{ms}$. For fast switch off of the magnetic field we use a high power insulated gate bi-polar transistor (IGBT) (Semikron SKM800GA176D) and connect a $30\mu\text{F}$ high voltage capacitor in parallel with the Feshbach coils. When the IGBT is switched to non-conducting, the Feshbach coils and the capacitor form a LC-circuit. A high power fast recovery diode (FRD) (ABB 5SDF 12F3005) ensure that the oscillation in the LC-circuit is stopped after one quarter of a period. This configuration ensures that the magnetic field generated by the Feshbach coils decays with a $1/e$ time constant of $\tau < 150\mu\text{s}$ after switch off. This decay time is currently limited by eddy currents. The high voltage capacitor is discharged on a much longer timescale using a shunt resistor.

The experimental sequence that is used for RF association of Feshbach molecules is the following: The mixture is evaporated in collision channel $|F = 1, m_F = 1\rangle_{\text{Na}} |F = 9/2, m_F = -7/2\rangle_{\text{K}}$ at a magnetic field of 85.5G (see section 2.8.1 for details). At a trap depth of $\simeq 1\mu\text{K}$ evaporation is stopped and the mixture is irradiated by an amplitude modulated Blackman RF pulse. In order to record a molecule association spectrum the frequency of the RF pulse is varied in an interval of $\pm 125\text{kHz}$ around the the bare $|F = 9/2, m_F = -7/2\rangle \rightarrow |F = 9/2, m_F = -9/2\rangle$ transition. The pulse area is adjusted to $\simeq 10 \cdot \pi$ for the atomic

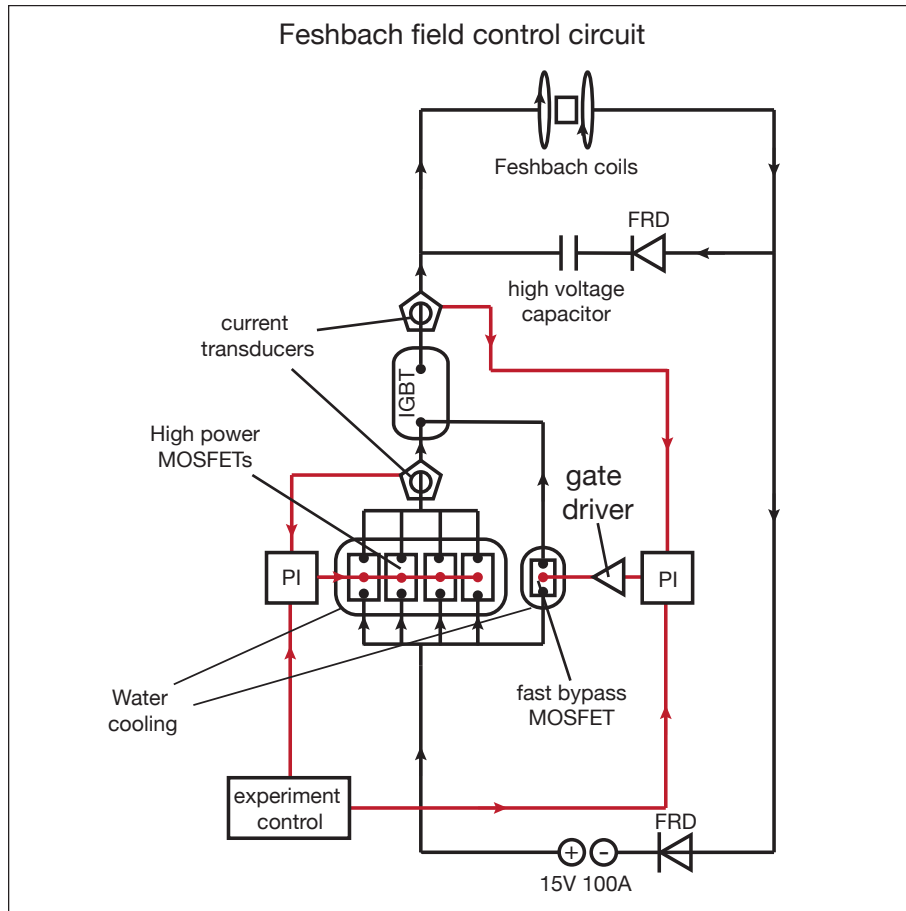


Figure 3.3 – Magnetic field control setup based on 4 high power MOSFETs and a fast bypass MOSFET. Two separate control loops are used to stabilize the total current that runs through the coils by feedback to the gate-source Voltage of the MOSFETs. A high voltage capacitor ensures in combination with two fast recovery diodes that the current can be switched off in less then $150\mu\text{s}$. More details are given in the main text.

transition. Directly after the spectroscopy/association pulse a second RF π -pulse is used to transfer all ^{40}K atoms that have not been transferred to $m_F = -9/2$ from $m_F = -7/2$ to $m_F = -5/2$. Atoms or weakly bound molecules in the $m_F = -9/2$ state are detected by direct absorption imaging at 85.5G. The Zeeman splitting between the $m_F = -9/2$ and the $m_F = -5/2$ state allows us to selectively only image atoms or molecules in the target state. We image the atoms and Feshbach molecules with σ_- polarized light along the direction of the magnetic field.

In this way we can address the $|F = 9/2, m_F = -9/2\rangle \rightarrow |F' = 11/2, m_F = -11/2\rangle$ cycling transition for best signal to noise and most reliable atom/molecule number estimation. In order to not overestimate the molecule number we assume unity Clebsch-Gordon coefficient and carefully determine the magnification of our imaging system by shifting the atomic cloud using the position encoded translation stage.

Fig. 3.4 shows a typical RF association spectrum at a magnetic field of 85.5G. We observe a power broadened atomic peak at a RF frequency of 22.801MHz. A second peak that is offset by the binding energy of the Feshbach molecule at this magnetic field $E_b(85.5\text{G}) = h \cdot 83\text{kHz}$ is clearly visible. Assuming an equal absorption cross section for

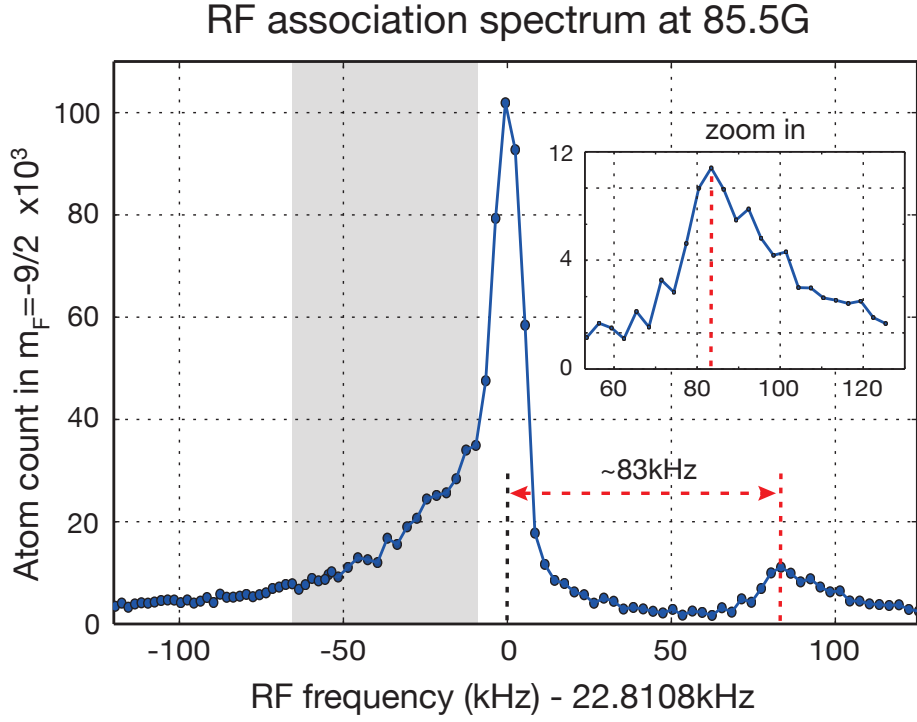


Figure 3.4 – RF association spectrum of $^{23}\text{Na}^{40}\text{K}$ Feshbach molecules at a magnetic field of $B = 85.5\text{G}$. The binding energy of the molecule is given by the distance between the atomic resonance at 22.8108MHz and the molecular resonance at $\simeq +83\text{kHz}$. The grey shaded area indicates highlights the effect of the inter-species interaction in the target collision channel.

absorption imaging of Feshbach molecules and the bare ^{40}K atoms we get a lower bound of $\simeq 10^4$ on the molecule number. Fig. 3.4 deliberately displays non-averaged measurements that were recorded in individual experimental runs in order to illustrate the exceptional shot to shot stability and almost background free detection we can achieve with our experimental sequence. The asymmetry of the atomic peak highlighted by the grey shaded-area in Fig. 3.4 is caused by the strong dressing of the ^{40}K atoms in presence of the near-degenerate ^{23}Na cloud. The binding energy as function of magnetic field can also be measured by *RF loss spectroscopy*. Fig. 3.5 shows the result of these measurements together with a least square fit of equation 3.28. In this way we determine the position $B_0 \simeq 88\text{G}$ and width $\delta B \simeq 12\text{G}$ of the underlying Feshbach resonance. As a final measurement in Fig. 3.6 we determine the temperature of the Feshbach molecules via a time of flight (TOF) measurement and compare the expansion dynamics to the one of ^{40}K atoms. The temperature of the cloud is obtained by fitting a Gaussian function to the density distribution at varying time of flight (TOF) and in second step by a least square fit of the measured cloud widths to the TOF formula

$$\sigma(t_{\text{TOF}}) = \sqrt{\sigma_0^2 + \frac{k_b T}{m} t_{\text{TOF}}^2} \quad (3.31)$$

Here m is either the mass of the atoms or the Feshbach molecule, T the temperature, σ_0 the initial cloud size in the dipole trap and t_{TOF} the time after release from the trap.

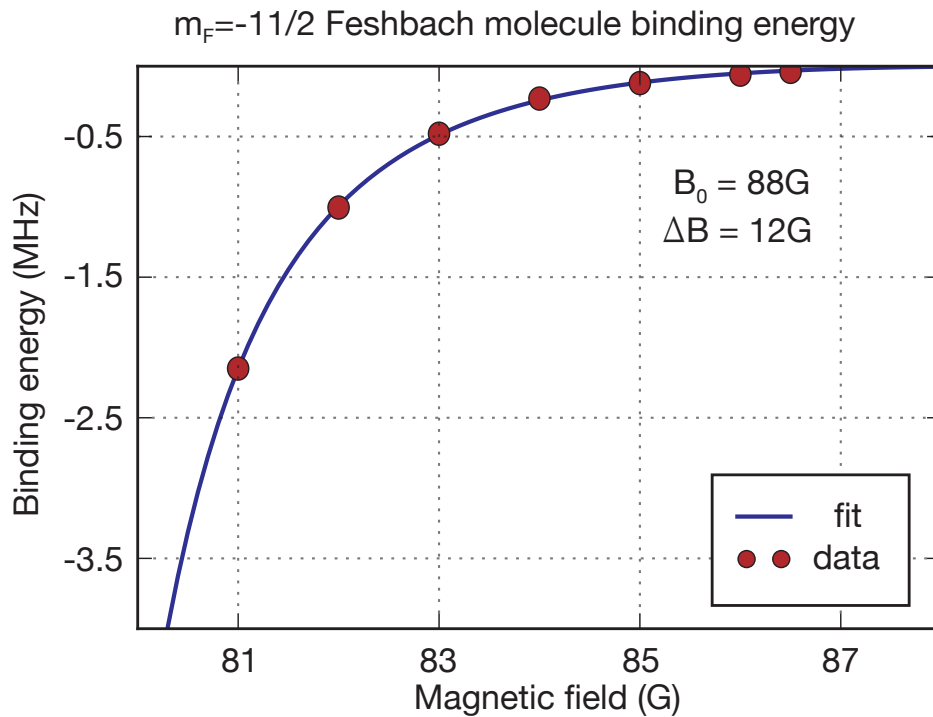


Figure 3.5 – Binding energy of the $^{23}\text{Na}^{40}\text{K}$ Feshbach molecule in vicinity of the s-wave resonance at 88G in collision channel $|F = 1 m_F = 1\rangle_{\text{Na}} |F = 9/2 m_F = -9/2\rangle_{\text{K}}$ measured by RF spectroscopy. The resonance parameters are determined by a least square fit of equation 3.28 to the data.

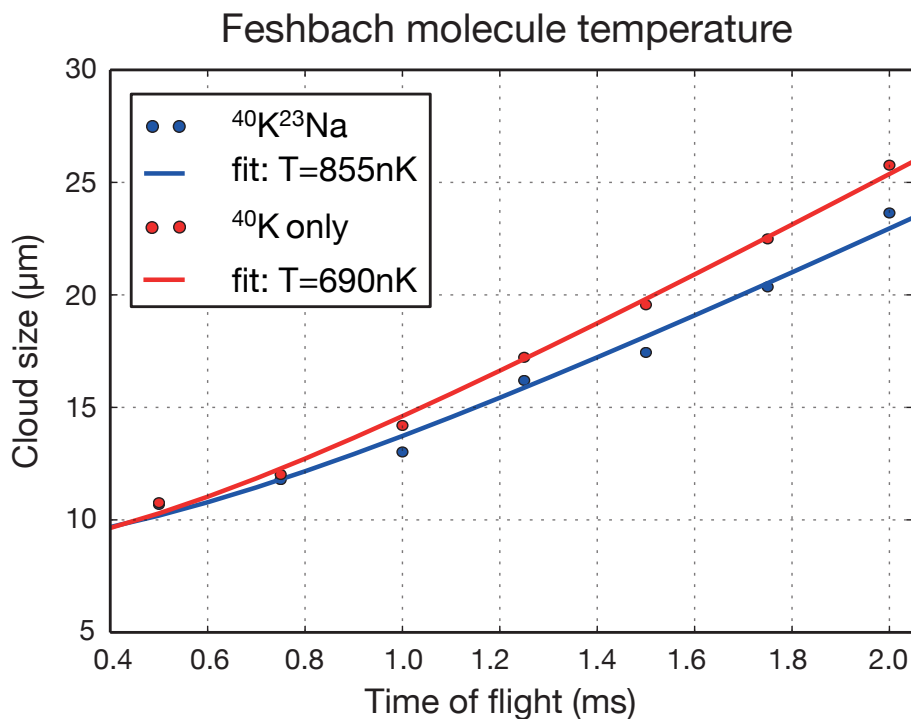


Figure 3.6 – Time of Flight measurement of $^{23}\text{Na}^{40}\text{K}$ Feshbach molecule and bare ^{40}K atoms. A least square fit of equation 3.31 yields a temperature for the Feshbach molecules of $T = 855\text{nK}$.

3.2.1 Improved Feshbach association starting from a deeply degenerate Bose-Fermi mixture

While writing this report we succeeded in using the Feshbach optimized evaporation technique from section 2.8.1 to reduce the temperature of the Feshbach molecules by a factor of 2.7 to 330nK while keeping the total number of molecules constant. Moreover, the lifetime of the Feshbach molecules increased by almost one order of magnitude to 13.5ms. Fig. 3.7 shows a time of flight measurement for $^{23}\text{Na}^{40}\text{K}$ Feshbach molecules. A least square fit of equation 3.31 yields an initial cloud size of $10\mu\text{m}$ and assuming a thermal cloud a temperature of $T = 330\text{nK}$. Fig. 3.8 shows a lifetime measurement of Feshbach molecules. A least square fit of a single exponential decay curve yields a $1/e$ lifetime of $\tau = 13.5\text{ms}$. Fig. 3.9 shows how the total number of associated Feshbach molecules depends on the pulse length of the RF pulse. Finally Fig. 3.10 gain shows an Feshbach molecule association spectrum measured with a pulse area of $\Omega_{RF} \cdot \tau_{RF} \simeq 10$, where τ_{RF} is the pulse duration of the Blackman pulse. By comparing the spectrum of Fig. 3.10 to the spectrum of Fig. 3.4 we observe that the molecule association peak is significantly narrowed at lower temperatures. This observation is in good agreement with results obtained by time-dependent perturbation theory [63] where the shape of the molecular peak reflects the energy distribution of the trapped Bose-Fermi mixture. In addition, also the bare atomic resonance appears to be more narrow at lower temperatures. In contrast the long tail on the low energy side of the atomic resonance (grey shaded area) did not change while going to lower temperatures. As already mentioned in the introduction of this

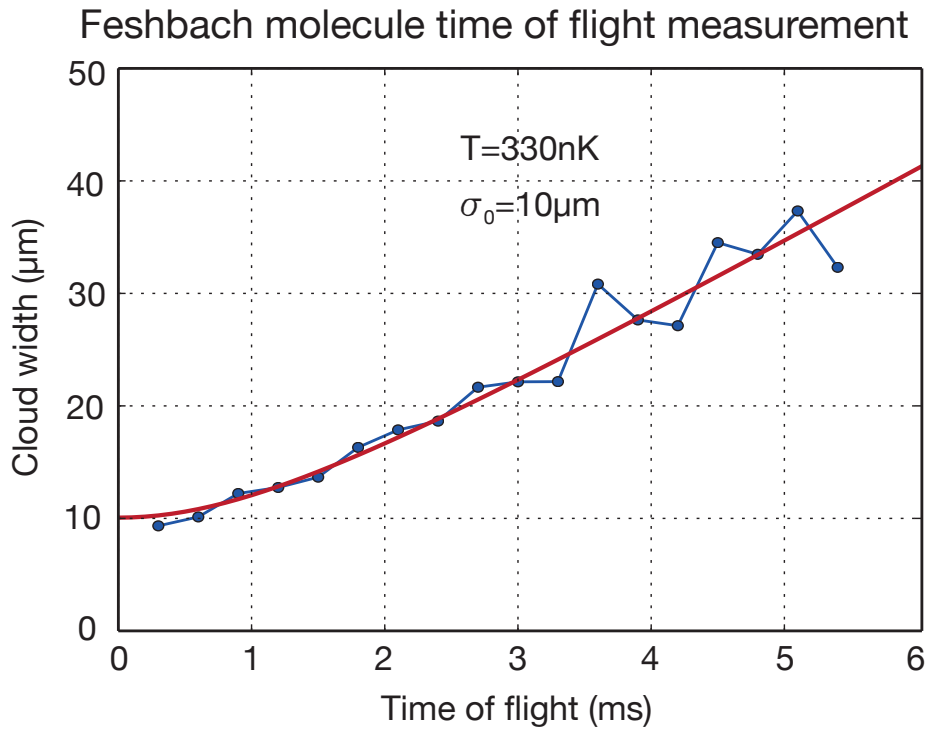


Figure 3.7 – Time of Flight measurement of $^{23}\text{Na}^{40}\text{K}$ Feshbach molecules after RF association. A least square fit of equation 3.31 yields a temperature of $T = 330\text{nK}$ and an initial cloud size of $\sigma_0 = 10\mu\text{m}$.

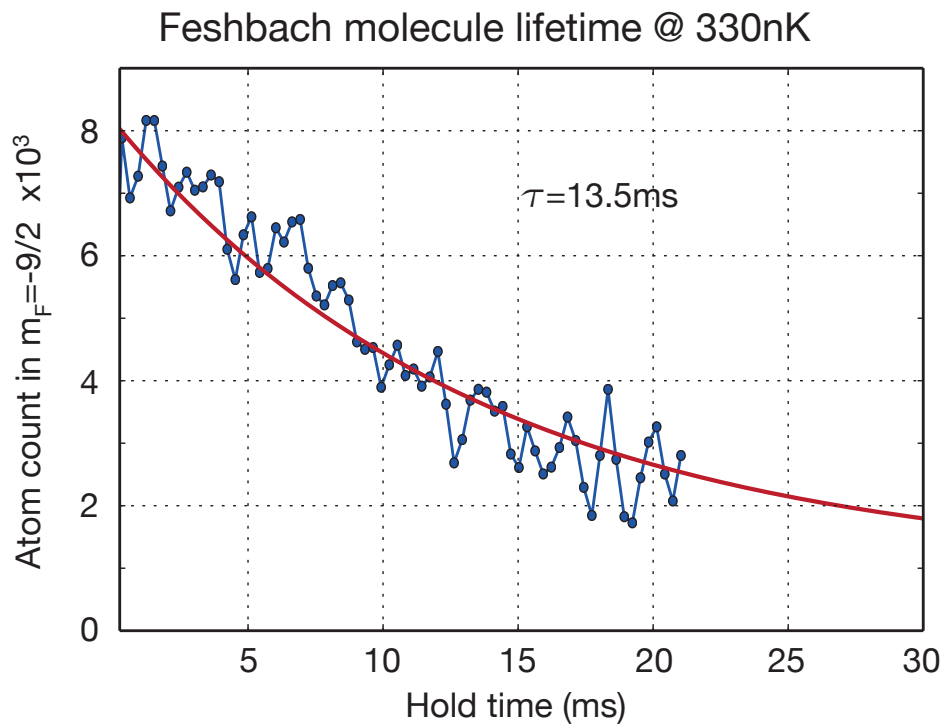


Figure 3.8 – Lifetime measurement of $^{23}\text{Na}^{40}\text{K}$ Feshbach molecules with a binding energy of $E_b = h \cdot 81\text{kHz}$ and a temperature of $T = 330\text{nK}$. A least square fit of a single exponential decay gives a $1/e$ -lifetime of $\tau = 13.5\text{ms}$.

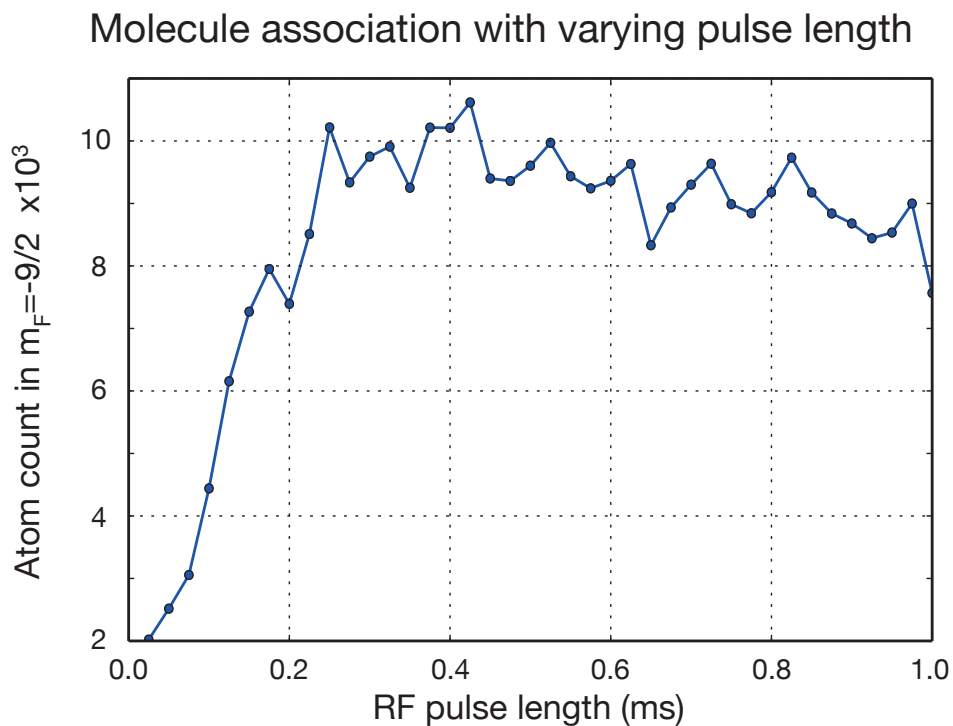


Figure 3.9 – Feshbach molecule number as a function of the RF pulse length. The molecule number saturates at $\approx 10^4$ for a pulse length of $\tau_{RF} \geq 0.4\text{ms}$.

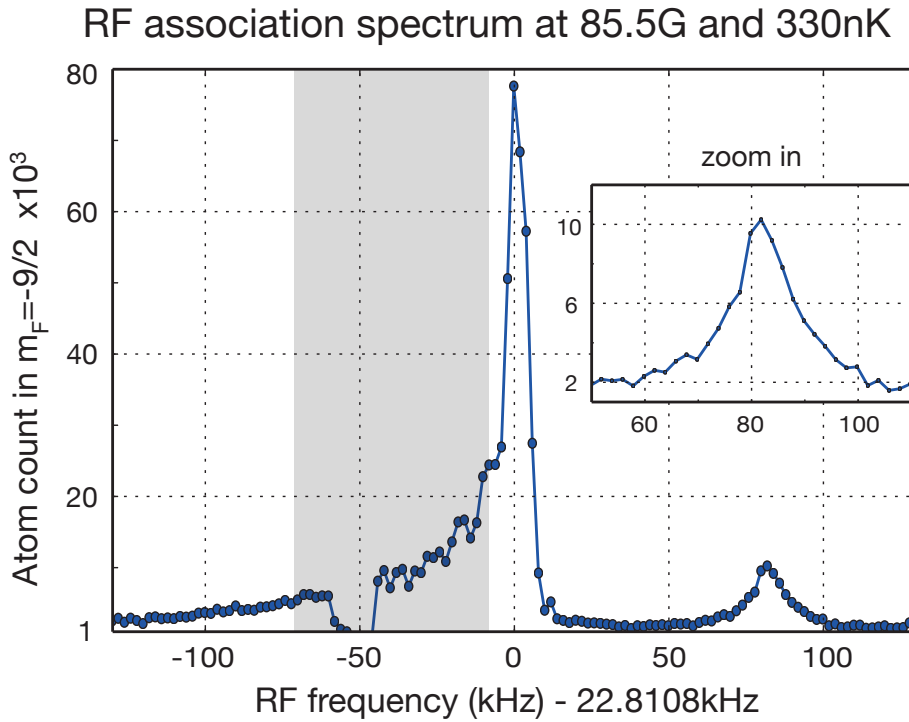


Figure 3.10 – RF association spectrum of $^{23}\text{Na}^{40}\text{K}$ Feshbach molecules at a magnetic field of $B = 85.5\text{G}$ and a temperature of $T = 330\text{nK}$. The binding energy of the molecule is given by the distance between the atomic resonance at 22.8108MHz and the molecular resonance at $\simeq +81\text{kHz}$. The more narrow molecular resonance compared to Fig. 3.4 reflects the decrease in temperature. The grey shaded area again highlights the effect of the inter-species interaction in the target collision channel. The drop in signal around -50kHz is an artifact caused by wrong programming of the MW evaporation driver.

report the favorable mass ratio between the light bosonic species and the heavy fermionic one, combined with stronger confinement of ^{40}K in the 1064nm dipole trap results in a good density overlap between both species even in the degenerate regime, where Fermi pressure results in a reduction of phase-space overlap. The slightly negative inter-species interaction in the collision channel that is used for evaporation increases density overlap even further [59]. As a result we do not have to perform Feshbach association above the critical temperature for Bose-Einstein condensation of ^{23}Na and chances are good to create heteronuclear fermionic groundstate molecules at unprecedented phase-space density.

In future experiments we will try whether molecule association via magnetic field sweeps can improve the low association efficiency of only $\simeq 10\%$.

3.3 Summary and discussion

Starting from near-degenerate Bose-Fermi mixture of $^{23}\text{Na}^{40}\text{K}$ we produce $\simeq 10^4$ Feshbach molecule via RF association. Molecule association is performed at a magnetic field that is $\simeq 2.5\text{G}$ below a 12G broad s-wave Feshbach resonance in the $|F = 1m_F = 1\rangle_{\text{Na}}|F = 9/2m_F = -9/2\rangle_{\text{K}}$ collision channel at 88G . The temperature of those weakly bound

molecules is $< 350\text{nK}$ and they live long enough to perform high resolution molecular spectroscopy and groundstate transfer via STIRAP. The hyperfine state configuration of the Feshbach molecules with total projection of angular momentum $m_F = -7/2$ allows to couple them directly to the absolute hyperfine groundstate of the $^{23}\text{Na}^{40}\text{K}$ molecule. Rovibronic groundstate molecules should be therefore not susceptible to spin-exchange collisions [19]. Due to the favorable mass imbalance between the bosonic species and the fermionic one the density overlap between the two clouds is not significantly decreased as the mixture becomes more degenerate. Moreover the attractive effective interaction between the two clouds at 85.5G increases density overlap even further and facilitates efficient sympathetic cooling prior to molecule association. In this respect the $^{23}\text{Na}^{40}\text{K}$ mixture offers a significant advantage over the $^{40}\text{K}^{87}\text{Rb}$ mixture for which Feshbach association works optimal just above the critical temperature for Bose-Einstein condensation of ^{87}Rb [74].

Molecular spectroscopy

Coherent population transfer of Feshbach molecules (see section 3.2) to the rovibronic groundstate $|X^1\Sigma, \nu = 0, J = 0\rangle$ relies on the identification of a suitable molecular level that serves as intermediate state in the STIRAP process. This level has to offer a large transition dipole moment (TDM) to both the Feshbach state and the $|X^1\Sigma, \nu = 0, J = 0\rangle$ state. For this purpose, significant singlet-triplet mixing is required in order to facilitate a two-photon coupling between Feshbach molecules and the $|X^1\Sigma, \nu = 0, J = 0\rangle$ state. In diatomic alkali molecules singlet-triplet mixing is primarily mediated by spin-orbit interaction of near degenerate vibrational levels of different spin-character (multiplicity). In order to find a two-photon transition that can be used for efficient groundstate transfer one first relies on ab initio calculations of the molecular level structure or preexisting measurements to identify a pair of excited electronic states with overlapping vibrational substructure. Suitable candidate states are then selected on basis of favorable Frank-Condon factors [75] and by searching for accidental resonances between two vibrational levels of different spin character. In a second step high resolution molecular spectroscopy is performed in order to determine the exact transition frequencies as well as the fine and hyperfine structure of the candidate state. The present chapter introduces the level structure of the $^{23}\text{Na}^{40}\text{K}$ molecule relevant for our choice of intermediate state. I then present results obtained by photoassociation (PA) spectroscopy of ultracold ^{23}Na and ^{40}K atoms as well as high resolution molecular spectroscopy on ultracold $^{23}\text{Na}^{40}\text{K}$ Feshbach molecules. These measurements are used to identify a candidate state for STIRAP that belongs to the spin-orbit coupled $d^3\Pi/D^1\Pi$ complex (see Fig. 4.1). A molecular perturbation model is introduced that is used to assign quantum numbers to all observed resonances and extract the model parameters from our data. We then perform coherent two-photon spectroscopy that allows us to measure the binding energy of the $|X^1\Sigma, \nu = 0, J = 0\rangle$ state. Finally I will discuss the adequacy of the identified intermediate state for coherent population transfer.

4.1 Overview

We only consider vibrational levels belonging to the lowest eight electronic states of the $^{23}\text{Na}^{40}\text{K}$ molecule as potential intermediate states for STIRAP, since suitable laser sources in the UV range of the electromagnetic spectrum are not available. These states correlate at large internuclear distance to the atomic $3^2S + 4^2P$ and $3^2P + 4^2S$ asymptotes. The relevant potential curves are shown in Fig. 4.1.

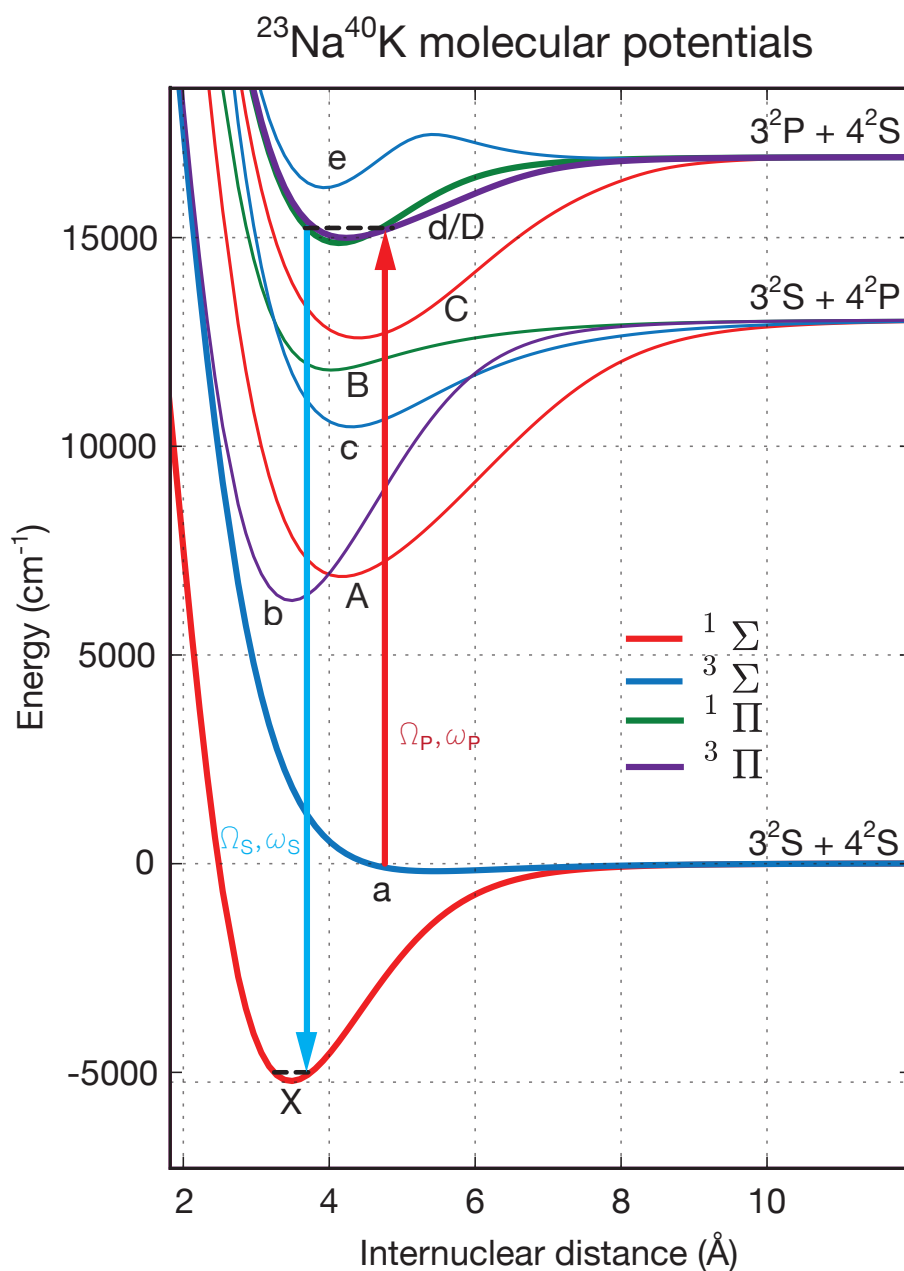


Figure 4.1 – Potential energy curves of the electronic ground state and the lower electronic excited states. Raman lasers (pump: $\sim 652\text{nm}$, Stokes: $\sim 487\text{nm}$) with frequencies $\omega_{P/S}$ and Rabi frequencies $\Omega_{P/S}$ couple a pair of vibrational states in the spin-orbit coupled $d^3\Pi/D^1\Pi$ complex to weakly bound $a^3\Sigma$ Feshbach molecules and the rovibronic groundstate in $X^1\Sigma$. Excited state molecular spectroscopy is performed on the pump transition.

Candidate levels are located in a range of binding energies where the vibrational structure of two electronic states with different spin character overlap. The possible combinations are therefore b/A , c/B , d/C and d/D . Due to a high degree of similarity of the potential curves the d/D manifold seems to be the most promising choice for finding accidental resonances between spin-singlet and spin-triplet vibrational levels. This manifold

has been studied intensively in molecular beam experiments [76] and indeed significant spin-orbit induced singlet-triplet mixing was identified [77, 78]. A more detailed calculation [79] that also takes into account the Frank-Condon factors for the involved transitions allows us to aim for a specific pair of vibrational states that simultaneously optimizes the transition dipole moment for both transitions. The result of this calculation is shown in Fig. 4.2.

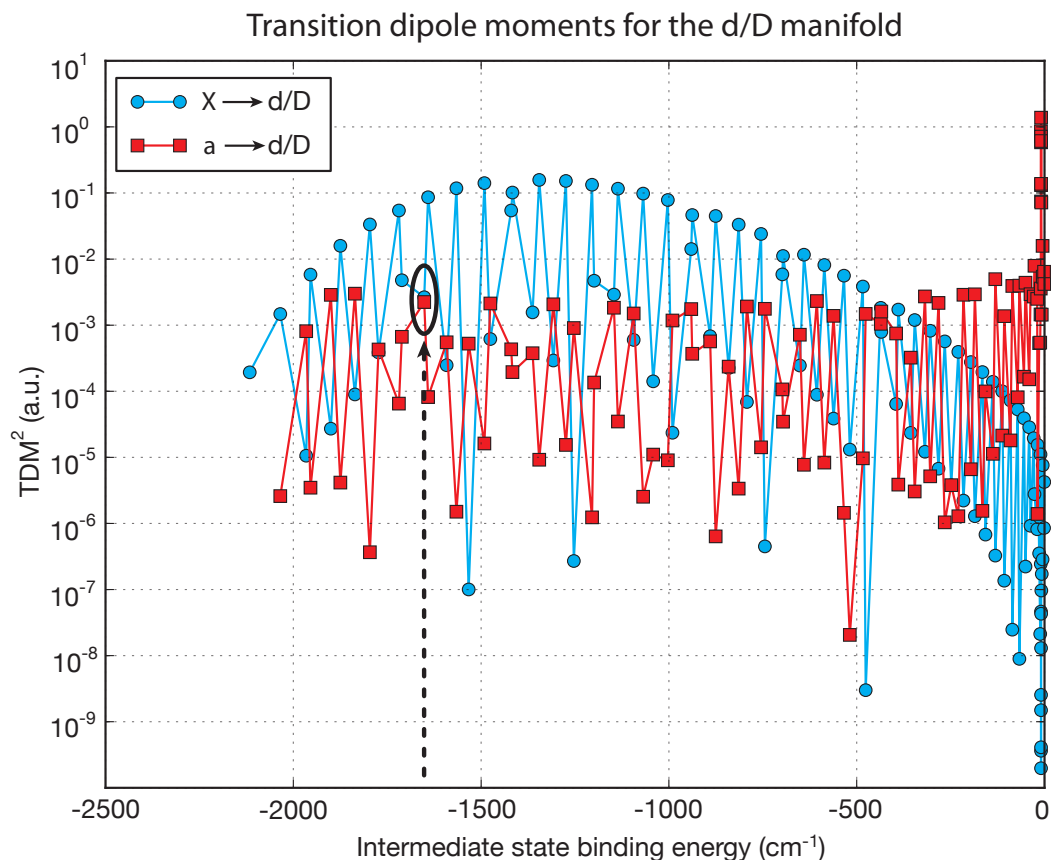


Figure 4.2 – Modulus squared transition dipole moments [79] from the Feshbach molecule state and the $|X^1\Sigma^v = 0J = 0\rangle$ state to the vibrational levels of the spin-orbit coupled $d^3\Pi/D^1\Pi$ complex are given in atomic units. Accidental resonances between $d^3\Pi$ and $D^1\Pi$ vibrational states lead to large values of the TDM for both transitions to a given level. The candidate level with a binding energy of $\sim 1350\text{cm}^{-1}$ is highlighted. Binding energies are measured with respect to the atomic $3^2P + 4^2S$ asymptote.

4.2 Background: Molecular structure of $^{23}\text{Na}^{40}\text{K}$

The quantitative interpretation of high resolution molecular spectroscopy requires a detailed model of the electronic, vibrational, rotational, fine and hyperfine structure of the molecule under study. This section reviews relevant aspects of the theory of diatomic molecules including the Born-Oppenheimer approximation, perturbation mechanisms and the theory of molecular fine and hyperfine structure. I will then present a molecular perturbation model of the $d^3\Pi/D^1\Pi$ complex that is used to explain the observed resonances. The treatment of the next section is primarily based on [80, 75].

A diatomic molecule is a stable bound state of two atoms. The molecular bond is caused by Coulomb forces between the electrons and the nuclei. The exact non-relativistic Hamiltonian \mathbf{H} can be approximated by a sum of three operators [80]:

$$\mathbf{H} = \mathbf{H}_{\text{kin}}^{\text{N}}(R, \theta, \phi) + \mathbf{H}_{\text{kin}}^{\text{el}}(\mathbf{r}_1, \dots, \mathbf{r}_n) + V_C(r_1, \dots, r_n, R). \quad (4.1)$$

Here $\mathbf{H}_{\text{kin}}^{\text{N}}$ is the kinetic energy operator of the nuclear motion, $\mathbf{H}_{\text{kin}}^{\text{el}}$ the kinetic energy of the electrons and V_C the coulomb interaction between all particles. \mathbf{r}_i are the coordinates of the electrons with respect to a molecule-fixed coordinate system, R is the internuclear distance and ϕ, θ specify the orientation of this rotating coordinate system with respect to the laboratory frame of reference.

Analogous to the treatment of the hydrogen atom the kinetic energy of the nuclei $\mathbf{H}_{\text{kin}}^{\text{N}}$ can be written as:

$$\mathbf{H}_{\text{kin}}^{\text{N}} = \mathbf{H}_{\text{kin}}^{\text{N}}(R) + \frac{\mathbf{N}^2}{2\mu R^2} \quad (4.2)$$

with reduced nuclear mass

$$\mu = \frac{m_A m_B}{m_A + m_B}, \quad (4.3)$$

radial kinetic energy operator

$$\mathbf{H}_{\text{kin}}^{\text{N}}(R) = \frac{-\hbar^2}{2\mu} \left(\partial_R^2 + \frac{2}{R} \partial_R \right) \quad (4.4)$$

and the angular momentum operator of rotation

$$\mathbf{N}^2 = -\hbar^2 \left(\frac{1}{\sin(\theta)} \partial_\theta \sin(\theta) \partial_\theta + \frac{1}{\sin(\theta)^2} \partial_\phi^2 \right). \quad (4.5)$$

The kinetic energy of the electrons is given by:

$$\mathbf{H}_{\text{kin}}^{\text{el}} = \frac{-\hbar^2}{2m_e} \sum_{i=1}^n \nabla_i^2 \quad (4.6)$$

In addition to the Coulomb forces between the nuclei and the electrons also magnetic interactions between the different angular momenta within a molecule have to be included in order to explain spectroscopic measurements. These relativistic corrections are phenomenologically accounted for by an operator \mathbf{H}_{spin} .

4.2.1 The Born-Oppenheimer approximation

The Born-Oppenheimer approximation (BOA) tries to find an approximate solution to the eigenvalue problem of the total Hamiltonian $\mathbf{H}_{\text{tot}} = \mathbf{H} + \mathbf{H}_{\text{spin}}$ by assuming that the motion of the electrons is adiabatic with respect to the nuclear motion. This is justified by considering that the large mass ratio of $\frac{m_e}{\mu} \ll 1$ results in a separation of time scales for nuclear and electronic motion; the electrons adjust their positions quasi-instantaneously to a change in nuclear position. The exact solution to the Schrödinger equation

$$\mathbf{H}_{\text{tot}} \psi_{\alpha}^{\text{tot}} = E_{\alpha} \psi_{\alpha}^{\text{tot}}, \quad (4.7)$$

where α is a composite index that includes labels for the electronic orbital, molecular vibration, spin, molecular rotation, etc. is approximated in the BOA by a product of two wavefunctions:

$$\psi_{i,\nu}^{\text{BO}} = \phi_i^{\text{el}}(\mathbf{r}_1, \dots, \mathbf{r}_n, R) \cdot \xi_{\nu,i}(R, \theta, \phi), \quad (4.8)$$

where $\phi_i^{\text{el}}(\mathbf{r}_1, \dots, \mathbf{r}_n, R)$ is the electronic wavefunction and $\xi_{\nu,i}(R, \theta, \phi)$ the vibration-rotation wavefunction. The index i labels different electron configurations, and ν the vibrational quantum number. The approximate solution $\psi_{i,\nu}^{\text{BO}}$ is called a *Born-Oppenheimer (BO) product function* and precisely corresponds to the situation where \mathbf{H}_{spin} is neglected and the electronic motion is adiabatic in the nuclear coordinates. In particular the BOA entails that:

$$\langle \phi_i^{\text{el}} | \mathbf{H}_{\text{kin}}^{\text{N}} | \phi_i^{\text{el}} \rangle = \langle \phi_i^{\text{el}} | \phi_i^{\text{el}} \rangle \mathbf{H}_{\text{kin}}^{\text{N}} \quad (4.9)$$

The internuclear distance R is not considered as a dynamical variable for the electronic motion, but appears as a slowly time-dependent (adiabatic) parameter in the electronic Hamiltonian.

The electronic wavefunction ϕ_i^{el} is a solution to the electronic Schrödinger equation for fixed internuclear distance R :

$$\mathbf{H}^{\text{el}} \phi_i^{\text{el}}(\mathbf{r}_1, \dots, \mathbf{r}_n, R) = E_i^{\text{el}}(R) \phi_i^{\text{el}}(\mathbf{r}_1, \dots, \mathbf{r}_n, R), \quad (4.10)$$

where \mathbf{H}^{el} is given by

$$\mathbf{H}^{\text{el}} = \mathbf{H}_{\text{kin}}^{\text{el}} + V_{\text{C}}(r_1, \dots, r_n, R) \quad (4.11)$$

For every electron configuration ϕ_i^{el} an effective Hamiltonian for the nuclear motion can be derived by averaging $\mathbf{H} = \mathbf{H}_{\text{kin}}^{\text{N}} + \mathbf{H}_{\text{kin}}^{\text{el}} + V_{\text{C}}$ over the electron coordinates:

$$\mathbf{H}^{\text{N}}(R, \theta, \phi) = \langle \phi_i^{\text{el}} | \mathbf{H}_{\text{kin}}^{\text{N}} + \mathbf{H}_{\text{kin}}^{\text{el}} + V | \phi_i^{\text{el}} \rangle_r = \mathbf{H}_{\text{kin}}^{\text{N}} + E_i^{\text{el}}(R), \quad (4.12)$$

with

$$E_i^{\text{el}} = \langle \phi_i^{\text{el}} | \mathbf{H}_{\text{kin}}^{\text{el}} + V | \phi_i^{\text{el}} \rangle_r \quad (4.13)$$

Note that this corresponds to taking only the diagonal elements of \mathbf{H} into account. The result is an approximate Schrödinger equation for the nuclear motion:

$$[\mathbf{H}_{\text{kin}}^{\text{N}}(R, \theta, \phi) + E_i^{\text{el}}(R)] \xi_{\nu,i}(R, \theta, \phi) = E_{\nu,i} \xi_{\nu,i}(R, \theta, \phi). \quad (4.14)$$

Separating the motion into angular and radial part,

$$\xi_{\nu,i}(R, \theta, \phi) = \mathfrak{R}_{\nu,i}(R) \xi_{\mathbf{N}}(\theta, \phi) \quad (4.15)$$

and knowing the spectrum

$$\mathbf{N}^2 \xi_{\mathbf{N}}(\theta, \phi) = \hbar^2 \mathbf{N}(\mathbf{N} + 1) \xi_{\mathbf{N}}(\theta, \phi) \quad (4.16)$$

of the angular part of the nuclear kinetic energy, finally gives the radial equation for molecular vibration:

$$[\mathbf{H}_{\text{kin}}^{\mathbf{N}}(R) + \frac{\hbar^2}{2\mu R^2} \mathbf{N}(\mathbf{N} + 1) + E_i^{\text{el}}(R)] \mathfrak{R}_{\nu,i,\mathbf{N}}(R) = E_{i,\nu} \mathfrak{R}_{\nu,i,\mathbf{N}}(R, \theta, \phi). \quad (4.17)$$

In terms of the total angular momentum $\mathbf{J} = \mathbf{N} + \mathbf{\Omega}$, where $\mathbf{\Omega}$ is the projection of the total electronic angular momentum onto the internuclear axis, the radial equation becomes:

$$[\mathbf{H}_{\text{kin}}^{\mathbf{N}}(R) + \frac{\hbar^2}{2\mu R^2} [J(J + 1) - \mathbf{\Omega}^2] + E_i^{\text{el}}(R)] \mathfrak{R}_{\nu,i,\mathbf{J}}(R) = E_{i,\nu} \mathfrak{R}_{\nu,i,\mathbf{J}}(R, \theta, \phi). \quad (4.18)$$

The effective potential energy $E_i^{\text{el}}(R)$ for the nuclear motion is called Born-Oppenheimer potential (BOP). Given a BOP the radial Schrödinger equation can then be solved numerically to obtain vibrational wavefunctions and the corresponding eigenenergies. The BOA approximates the total energy of the molecule by a sum of three independent contributions originating from the electronic energy E_{el} , the vibrational energy $G(\nu)$ and the rotational energy $F(J)$:

$$E_{\text{tot}} \simeq E_{\text{el}} + G(\nu) + F(J). \quad (4.19)$$

It is of course never possible to express the total energy E_{tot} exactly as in equation 4.19. Deviations from the BOA are either caused by off-diagonal matrix elements of \mathbf{H} or by diagonal and off-diagonal matrix elements of \mathbf{H}_{spin} . In principle, however the exact solution $\psi_{\alpha}^{\text{tot}}$ that completely diagonalizes \mathbf{H}_{tot} can be expressed as an infinite expansion of BO product functions:

$$\psi_{\alpha}^{\text{tot}} = \sum_{i,\nu} c_{i,\nu} \psi_{i,\nu}^{\text{BO}}. \quad (4.20)$$

The complete set of basis functions $\psi_{i,\nu}^{\text{BO}}$ is called the BO *representation*.

4.2.2 Basis functions and perturbations

The starting point for treating deviations from the Born-Oppenheimer approximation and for incorporating magnetic interactions is a Born-Oppenheimer representation, i.e. a complete set of basis vectors:

$$\{|\psi_{\alpha}^{\text{BO}}\rangle\} = \{|i \nu S \Lambda \Sigma \Omega J M_J\rangle\} \quad (4.21)$$

Here i indicates the principal quantum number of the electronic orbital, ν the vibrational quantum number and S the total electronic spin. The remaining labels are the signed eigenvalues of the following operators:

- Λ , the projection of the orbital angular momentum onto the internuclear axis
- Σ , the projection of the spin angular momentum onto the internuclear axis
- $\Omega = \Lambda + \Sigma$, projection of the total electronic angular momentum onto the internuclear axis
- $\mathbf{J} = \Omega + \mathbf{N}$, the total angular momentum, where \mathbf{N} designates the angular momentum of rotation of the nuclei
- \mathbf{J}_z , the z -component of the total angular momentum in the laboratory frame (i.e. $J_z|i\nu S\Lambda\Sigma\Omega JM_J\rangle = M_J|i\nu S\Lambda\Sigma\Omega JM_J\rangle$)

A structural model for a situation that significantly deviates from the BOA (as it will be the case for the spin-orbit coupled $d^3\Pi/D^1\Pi$ complex) is constructed according to the following procedure:

1. By using the Born-Oppenheimer approximation (BOA) and taking into account symmetry properties of the system find a complete set of basis functions $\{\psi_\alpha^{\text{BO}}\}$.
2. Partition the full Hamiltonian into two parts $\mathbf{H}_{\text{tot}} = \mathbf{H}_0 + \mathbf{H}_{\text{pert}}$, where \mathbf{H}_0 is diagonal in the chosen BO basis $\{\psi_\alpha^{\text{BO}}\}$. The partitioning should be done such that off-diagonal matrix elements of \mathbf{H}_{pert} are much smaller than the diagonal elements of \mathbf{H}_{pert} .
3. Derive a matrix representation of the total microscopic Hamiltonian \mathbf{H}_{tot} in the chosen basis set $\{\psi_\alpha^{\text{BO}}\}$.
4. Approximate the real eigenstates of \mathbf{H}_{tot} by a perturbation series in \mathbf{H}_{pert} or diagonalize exactly if possible.

The partitioning of \mathbf{H}_{tot} into $\mathbf{H}_0 + \mathbf{H}_{\text{pert}}$ determines which of the labels ($i, \nu, S, \Lambda, \Sigma, \Omega, J, M_J$) are good quantum numbers (i.e. eigenvalues of commuting observables) with respect to \mathbf{H}_0 . The most commonly used partitions of \mathbf{H}_{tot} are called *Hund's cases a)- d)* (see [75]). For the the spin-orbit coupled $d^3\Pi/D^1\Pi$ complex and low values of J , the appropriate choice of basis functions is *Hund's case a)* [80, 77]:

$$\begin{aligned} \mathbf{H}_0 &= \mathbf{H}_{\text{kin}}^{\text{N}} + \mathbf{H}_{\text{kin}}^{\text{el}} + V_C(r_1, \dots, r_n, R) + B_\nu \mathbf{J}^2 \\ \{|\psi_\alpha^{\text{BO}}\rangle\} &= \{|i\nu S\Lambda\Sigma JM_J\rangle\} \end{aligned} \quad (4.22)$$

Here B_ν is the rotational constant for a given vibrational state with vibrational quantum number ν :

$$B_\nu = \frac{\hbar^2}{2\langle\mu R^2\rangle_\nu}. \quad (4.23)$$

In molecular spectroscopy one observes transitions between eigenstates of the parity operator \hat{P}_ν , which commutes with the Hamiltonian of the molecule. These eigenstates can be formed by a superposition of BO basis states. The total parity is a product operator of

rotational and electronic parity. I use the phase-convention of [80] where the eigenstates are labeled by either e (even electronic parity) or f (odd electronic parity):

$$|^{2S+1}\Lambda_{\Omega}^{e/f} \nu J m_J\rangle = \frac{1}{\sqrt{2}}(|S\Lambda\Sigma\Omega \nu J m_J\rangle \pm |S - \Lambda - \Sigma - \Omega \nu J m_J\rangle) \quad (4.24)$$

For these eigenstates the action of the parity operator is given by:

$$\hat{P}_{\nu}|^{2S+1}\Lambda_{\Omega}^{e/f} \nu J m_J\rangle = \pm 1^{J-S}|^{2S+1}\Lambda_{\Omega}^{e/f} \nu J m_J\rangle. \quad (4.25)$$

For example, the closed channel of the Feshbach molecule has $\Lambda = 0, S = 1, J = 1$. Therefore the parity of the Feshbach molecule is positive and only excited molecular levels with negative parity can be accessed in a dipole transition when performing spectroscopy.

We are now in the position to construct a restricted basis set that can be used to analyze the candidate levels for STIRAP belonging to the spin-orbit coupled $d^3\Pi/D^1\Pi$ complex.

4.2.3 Fine structure model for the $d^3\Pi/D^1\Pi$ complex

The Hund's case a) basis states (see equation 4.24) that are used to analyze the $d^3\Pi/D^1\Pi$ complex are given by:

$$\begin{aligned} |^3\Pi_0^{e/f} \nu J m_J\rangle &= \frac{1}{\sqrt{2}}(|11 - 10 \nu J m_J\rangle \pm |1 - 110 \nu J m_J\rangle), \\ |^3\Pi_1^{e/f} \nu J m_J\rangle &= \frac{1}{\sqrt{2}}(|1101 \nu J m_J\rangle \pm |1 - 10 - 1 \nu J m_J\rangle), \\ |^3\Pi_2^{e/f} \nu J m_J\rangle &= \frac{1}{\sqrt{2}}(|1112 \nu J m_J\rangle \pm |1 - 1 - 1 - 2 \nu J m_J\rangle), \\ |^1\Pi_1^{e/f} \nu' J m_J\rangle &= \frac{1}{\sqrt{2}}(|0101 \nu' J m_J\rangle \pm |0 - 10 - 1 \nu' J m_J\rangle). \end{aligned} \quad (4.26)$$

The generic Hamiltonian for a diatomic molecule can be written as [80]:

$$H = H_e + H_v + H_R + H_S, \quad (4.27)$$

where H_e is the electronic, H_v the vibrational and H_R the rotational part. H_S designates the spin part of the Hamiltonian that includes the spin-spin H_{SS} , the spin-orbit H_{SO} and the spin-rotation H_{SR} operator.

The diagonal matrix elements of H in the Hund's case a) basis (labels for parity and m_J omitted) are given by [81]

$$\begin{aligned} \langle ^3\Pi_0 \nu J | H | ^3\Pi_0 \nu J \rangle &= E_{\nu} - A_{\nu} + B_{\nu} [J(J+1) + 1] + \frac{2}{3} \lambda_{\nu}, \\ \langle ^3\Pi_1 \nu J | H | ^3\Pi_1 \nu J \rangle &= E_{\nu} + B_{\nu} [J(J+1) + 1] - \frac{4}{3} \lambda_{\nu}, \\ \langle ^3\Pi_2 \nu J | H | ^3\Pi_2 \nu J \rangle &= E_{\nu} + A_{\nu} + B_{\nu} [J(J+1) - 3] + \frac{2}{3} \lambda_{\nu}, \\ \langle ^1\Pi_1 \nu' J | H | ^1\Pi_1 \nu' J \rangle &= E_{\nu'} + B_{\nu'} [J(J+1) + 1]. \end{aligned} \quad (4.28)$$

Here E_ν are the unperturbed energies of the vibrational levels, B_ν the corresponding rotational constants, A_ν the diagonal part of the spin-orbit interaction and λ_ν the coupling constants of the spin-spin interaction.

Non-diagonal elements of H_R are due to the S- and L-uncoupling operators H_{SL} and H_{JL} . The selection rules for these perturbation operators are given by [80]:

$$H_{JL}: \Delta\Lambda = \pm 1 = \Delta\Omega, \Delta S = 0 \quad (4.29)$$

and

$$H_{JL}: \Delta\Sigma = \pm 1 = \Delta\Omega, \Delta S = 0, \Delta\Lambda = 0 \quad (4.30)$$

Therefore non-zero elements occur for the $d^3\Pi$ levels and H_{SJ} only:

$$\begin{aligned} \langle {}^3\Pi_0 \nu J | H_{SJ} | {}^3\Pi_1 \nu J \rangle &= -B_\nu \sqrt{2} [J(J+1)]^{1/2}, \\ \langle {}^3\Pi_1 \nu J | H_{SJ} | {}^3\Pi_2 \nu J \rangle &= -B_\nu \sqrt{2} [J(J+1) - 2]^{1/2}. \end{aligned} \quad (4.31)$$

The spin part of H has non-diagonal matrix elements due to spin-orbit interaction H_{SO} and the spin-rotation operator H_{SR} :

$$\begin{aligned} \langle {}^3\Pi_0 \nu J | H_{SR} | {}^3\Pi_1 \nu J \rangle &= \frac{\gamma_\nu}{2} [J(J+1)]^{1/2}, \\ \langle {}^3\Pi_1 \nu J | H_{SR} | {}^3\Pi_2 \nu J \rangle &= \frac{\gamma_\nu}{2} [J(J+1) - 2]^{1/2}, \\ \langle {}^3\Pi_1 \nu J | H_{SO} | {}^1\Pi_1 \nu' J \rangle &= \xi_{\nu\nu'}. \end{aligned} \quad (4.32)$$

Note that since H commutes with \mathbf{J} the matrix representation of H is block-diagonal and can be diagonalized for each value of J independently. The analysis is further simplified by considering that at ultracold temperatures it is only possible to observe single photon transitions to states with $J = 0, 1, 2$. I construct this block diagonal matrix from the diagonal and off-diagonal matrix elements given above. To analyze the observed photoassociation spectra that are presented in the next section, I numerically diagonalize H for $J = 0, 1, 2$ and then determine all coupling parameters of H via a least-square fit of the obtained eigenenergies to the observed resonance positions (see section 4.3.3 below).

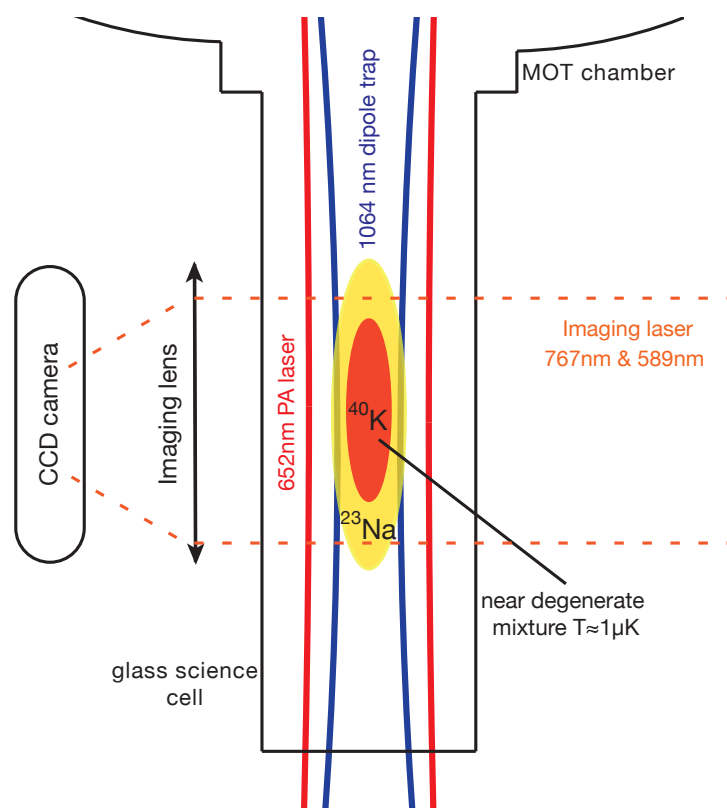


Figure 4.3 – Schematic of the experimental configuration for PA spectroscopy. The near degenerate $^{23}\text{Na}^{40}\text{K}$ mixture is levitated against gravity in a single beam dipole trap ($\lambda = 1064\text{nm}$, $P = 7\text{W}$, $w_0 = 45\mu\text{m}$). PA is performed using a ring dye laser ($\lambda \sim 652\text{nm}$, $P = 100\text{mW}$, $w_0 = 50\mu\text{m}$). Prior to PA spectroscopy the mixture is transported from the stainless steel MOT chamber to the attached glass science cell and spin polarized to $|1, 1\rangle_{^{23}\text{Na}} \otimes |9/2, -9/2\rangle_{^{40}\text{K}}$. PA induced atom loss is detected via simultaneous absorption imaging for both species.

4.3 Photoassociation spectroscopy

Deeply bound electronically excited molecules are associated starting from a near-degenerate $^{23}\text{Na}^{40}\text{K}$ mixture using a Coherent 899 ring dye laser operated with DCM dye. 100mW of the dye laser output are focused to a waist of $50\mu\text{m}$ and superimposed with the dipole trap. The laser frequency is stabilized to a low finesse cavity and can be tuned within several tens of THz. The laser frequency is monitored by a wavemeter (High Fines WS7, resolution 10MHz, accuracy 300MHz). For coarse spectroscopy the mixture is illuminated for 10s while the dye laser frequency is swept across several GHz. PA induced atom loss is detected by simultaneous absorption imaging of both species (see Fig. 4.3). Detected resonances were verified with 10MHz frequency resolution. Fig. 4.3 shows a schematic of the experimental configuration. The $^{23}\text{Na}^{40}\text{K}$ mixture is levitated against gravity in a single beam dipole trap ($\lambda = 1064\text{nm}$, $P = 7\text{W}$, $w_0 = 45\mu\text{m}$). Prior to PA spectroscopy the mixture is transported from the stainless steel MOT chamber to the attached glass science cell, evaporatively cooled to $\sim 1\mu\text{K}$ and spin polarized to $|1, 1\rangle_{^{23}\text{Na}} \otimes |9/2, -9/2\rangle_{^{40}\text{K}}$.

4.3.1 Spin Character and wave function of the initial state

To analyze the spin character of the initial state, we use the *spin basis* $|J, m_J, m_{Na}, m_K\rangle$ from section 3.1, where $\mathbf{J} = \mathbf{S}_{Na} + \mathbf{S}_K$ is the total electronic spin ($J = 1$ is the triplet state, and $J = 0$ is the singlet), m_J is the projection of the total electronic spin on the quantization axis, and $m_{Na}(m_K)$ is the nuclear spin projection of Na (K). PA spectroscopy is performed on unbound atoms in the collision channel $|1, 1\rangle_{23Na} \otimes |9/2, -9/2\rangle_{40K}$ at a magnetic field of 85.5 G. This state can be expressed in the spin basis as:

$$|1, 1\rangle_{23Na} \otimes |9/2, -9/2\rangle_{40K} = 0.32|0, 0, 1/2, -4\rangle - 0.89|1, -1, 3/2, -4\rangle + 0.32|1, 0, 1/2, -4\rangle$$

This is simply obtained by a Clebsch-Gordon transformation of the coupled hyperfine basis states into the spin basis. PA spectroscopy is performed in a collision channel and at a magnetic field where no scattering resonances occur and coupling to closed channels can be neglected.

4.3.2 Vibrational structure of the $d^3\Pi/D^1\Pi$ complex

In order to become familiar with molecular spectroscopy we have measured the resonance position of the seven most deeply bound $|^3\Pi_{\Omega=2} J = 2\rangle$ vibrational levels via PA spectroscopy starting from an ultracold $^{23}\text{Na}^{40}\text{K}$ mixture prepared in the collision channel $|1, 1\rangle_{Na} \otimes |9/2, 9/2\rangle_{K_{40}}$ (see Fig. 4.4). We compare the measured transition frequencies to predictions based on mass scaled potentials from [82, 79]. Measurements and predictions agree within $\pm 20\text{GHz}$. Note that due to spin-orbit coupling between the $d^3\Pi$ and the $D^1\Pi$ state we can directly observe the $\nu = 6$ level of the $D^1\Pi$ state already in PA spectroscopy. When spin-orbit coupling is absent, the Frank-Condon factor between the singlet component of the multi-channel wave function of the initial state and a deeply bound vibrational level in the $D^1\Pi$ state is almost vanishing. The reason for that is, that the singlet component of scattering wavefunction of the initial state oscillates very rapidly in the range of internuclear distances for which the $D^1\Pi$ vibrational states extend. The overlap integral therefore averages almost to zero. The same behavior is encountered when transitions between a Feshbach molecule and the $D^1\Pi$ manifold are considered. Even for a large spin-singlet admixture in the Feshbach state - as it is realized for broad Feshbach resonances [70] - does not allow for an efficient coupling to a general $D^1\Pi$ level, since the least bound state of the groundstate singlet potential behaves almost identical to the singlet scattering wave function at the relevant internuclear distances. A detailed analysis of this phenomenon is given in [83].

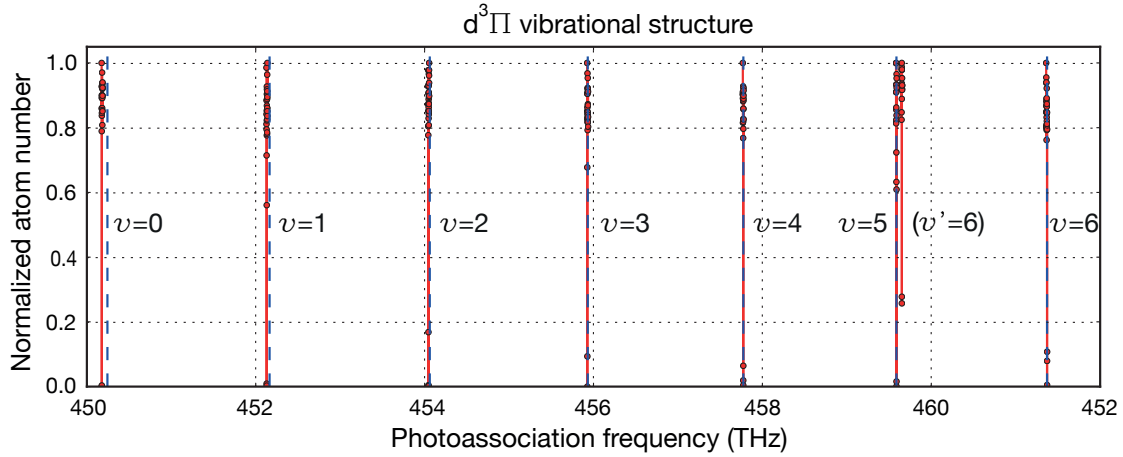


Figure 4.4 – Photoassociation resonances for the seven lowest most deeply bound $|\ ^3\Pi_{\Omega=2} J = 2 \rangle$ vibrational levels. Predictions based on mass scaled potentials from [82, 79] are indicated by the blue dashed lines. They agree within ± 20 GHz. For the $\nu = 5$ candidate level the near resonant $\nu' = 6$ $|\ ^1\Pi_{\Omega=1} J = 1 \rangle$ level can be also observed.

4.3.3 Molecular fine structure of the $d^3\Pi/D^1\Pi$ complex

For further analysis we observe all fine structure components for the $\nu = 2$ level in PA spectroscopy (see Fig. 4.5). Since spin-orbit coupling to the $D^1\Pi$ state can be neglected for this level [77] due to non-overlapping vibrational level structure, it serves as a benchmark for the fine structure model of section 4.2.3 For this purpose I numerically diagonalize the molecular perturbation Hamiltonian given by equation 4.28-4.33 and perform a least-square fit of the obtained eigenenergies to the observed resonance positions. For the $\nu = 2$ level I restrict the Hilbert space on which the diagonalization algorithm operates to the accessible fine structure components of the $d^3\Pi$ state:

$$\begin{aligned}
 &|\ ^3\Pi_0^f \nu = 2J = 0 \rangle, |\ ^3\Pi_0^e \nu = 2J = 1 \rangle, |\ ^3\Pi_0^f \nu = 2J = 2 \rangle \\
 &|\ ^3\Pi_1^e \nu = 2J = 1 \rangle, |\ ^3\Pi_1^f \nu = 2J = 2 \rangle \\
 &|\ ^3\Pi_2^f \nu = 2J = 2 \rangle.
 \end{aligned} \tag{4.34}$$

The model and the measurements agree within ± 300 MHz. The deviation is largest for the three $\Omega = 0$ components. For the $\Omega = 1, 2$ components model and data agree within ± 50 MHz. The model parameters that resulted from the least-square fitting routine are given in table 4.1. These values are in good agreement with the results reported in [77, 78].

Due to most favorable predictions for the TDM's [79] to both the Feshbach molecular state and the $|X^1\Sigma \nu = 0J = 0\rangle$ state (see Fig. 4.2) we chose the $\Omega = 1, J = 1$ component of the $|\ ^3\Pi \nu = 5 \rangle$ level as candidate state for STIRAP. We therefore determine all fine structure components for this level and fit the molecular perturbation model of section 1.2.4 (equation 4.28 - 4.33) including off-diagonal spin-orbit coupling. The necessary singlet-triplet mixing is mediated by the near resonant $|\ ^1\Pi_{\Omega=1} \nu = 6J = 1 \rangle$ level. The

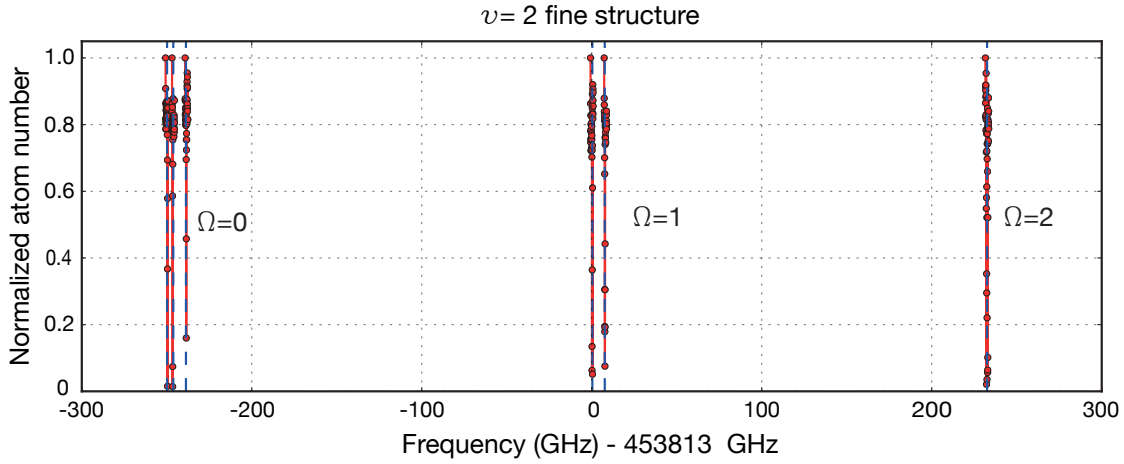


Figure 4.5 – Fine structure components of the $d^3\Pi\nu = 2$ vibrational level. The fine structure model of section 4.2.3 (equation 4.28 - 4.33) excluding off-diagonal spin-orbit coupling is used to fit the observed resonances. Fit and data agree within ± 300 MHz. The predicted transition frequencies are indicated by the blue dashed lines.

Parameter	Value (GHz)
E_2	453802.937
B_2	1.862
A_2	1.862
λ_2	-0.009
γ_2	-3.557

Table 4.1 – Molecular perturbation model parameters (bare vibrational energies and coupling constants) obtained from a least square fit of equation 4.28 - 4.33 to the observed resonance positions (see Fig. 4.5) for the $d^3\Pi, \nu = 2$ fine structure multiplet. Spin-orbit coupling to the $D^1\Pi$ state was not considered. The model reproduces the observed resonances within 300 MHz.

measured fine structure is shown in Fig. 4.6. I again numerically diagonalize the molecular perturbation Hamiltonian given by equation 4.28-4.33 and perform a least-square fit of the obtained eigenenergies to the observed resonance positions. For the $\nu = 5$ level the restricted Hilbert space is spanned by:

$$\begin{aligned}
 &|{}^3\Pi_0^f \nu = 5J = 0\rangle, |{}^3\Pi_0^e \nu = 5J = 1\rangle, |{}^3\Pi_0^f \nu = 5J = 2\rangle, \\
 &|{}^3\Pi_1^e \nu = 5J = 1\rangle, |{}^3\Pi_1^f \nu = 5J = 2\rangle, \\
 &|{}^3\Pi_2^f \nu = 5J = 2\rangle, \\
 &|{}^1\Pi_1^e \nu = 5J = 1\rangle, |{}^1\Pi_1^e \nu = 5J = 2\rangle.
 \end{aligned} \tag{4.35}$$

The predictions of the fine structure model and the measurements agree within ± 300 MHz. The deviation is again largest for the three $\Omega = 0$ components of the $d^3\Pi$ state. For the $\Omega = 1, 2$ components model and data agree within ± 50 MHz. The model parameters that resulted from the least-square fitting routine are given in table 4.2. Again these values are in good agreement with the results of [77, 78]. Since we identified the desired spin-orbit

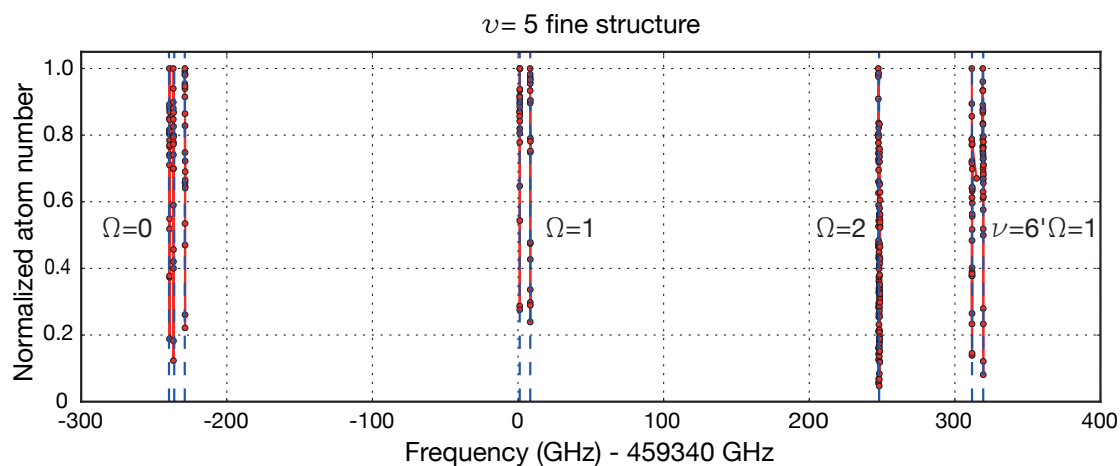


Figure 4.6 – Fine structure components of the ${}^3d\Pi\nu = 2$ vibrational level. The fine structure model of section 4.2.3 (equation 4.28 - 4.33) including off-diagonal spin-orbit coupling is used to fit the observed resonances. Fit and data agree within ± 300 MHz. The predicted transition frequencies are indicated by the blue dashed lines.

coupled intermediate state and verified that sufficient singlet-triplet mixing is present, we did not try to improve our model further but proceeded with finding a two photon transition to the rovibronic groundstate.

Parameter	Value (GHz)
E_5	459337.520
B_5	1.895
E_6	459641.838
B_6	1.920
A_5	241.784
$\xi_{5,6}$	49.270
λ_5	-0.182
γ_5	-2.778

Table 4.2 – Molecular perturbation model parameters (bare vibrational energies and coupling constants) obtained from a least square fit of equation 4.28 - 4.33 to the observed resonance positions (see Fig. 4.5) for the $d^3\Pi, \nu = 5$ fine structure multiplet. The model reproduces the observed resonances within 300 MHz.

4.4 High resolution molecular spectroscopy

High resolution molecular spectroscopy of the candidate level was performed with a narrow linewidth diode laser system frequency stabilized to a dual wavelength high finesse (≈ 200000 for 652 nm and ≈ 37000 for 487 nm) ULE cavity (Advanced thin films, Stable Lasers) via the Pound-Drever-Hall technique [84]. Frequency tuning over > 1 GHz is achieved by using a phase-locked master-slave configuration. A schematic of the complete

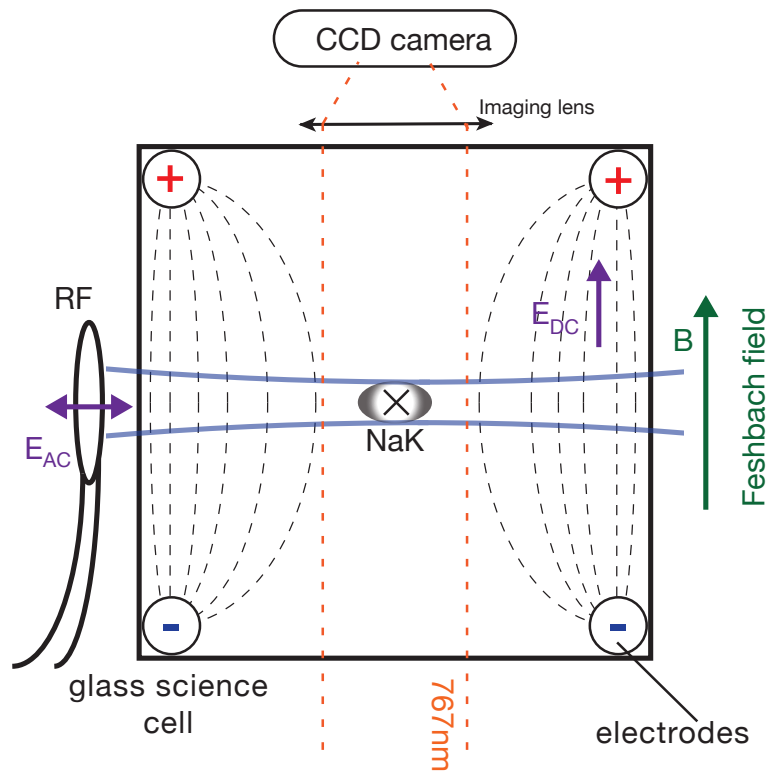


Figure 4.7 – Schematic of the experimental configuration for high resolution spectroscopy of $^{23}\text{Na}^{40}\text{K}$ Feshbach molecules. Feshbach molecules with a binding energy of 83kHz are RF associated in a crossed dipole trap in the glass science cell at a magnetic field of 85.5G . Spectroscopy is performed with a narrow linewidth diode laser system. 10mW of the diode laser output is focused to a waist of $50\mu\text{m}$ and superimposed with one of the beams forming the dipole trap. The cross in the center of the molecule sample indicates the direction of the dipole trap laser and of the diode laser used for spectroscopy. Loss of molecules that is induced by the spectroscopy laser is detected via direct absorption imaging of Feshbach molecules.

Raman laser setup is shown in Fig. 4.8 and details can be found in [85]. Starting from a sample of $\approx 1.0 \cdot 10^4$ $^{23}\text{Na}^{40}\text{K}$ Feshbach molecules with a binding energy of $\sim 83\text{kHz}$ we observe hyperfine and Zeeman substructure for the $\Omega = 1, J = 1$ and the $\Omega = 2, J = 2$ components of the $|d^3\Pi_{\Omega=1} \nu = 5\rangle$ level at a magnetic field of 85.5G . Fig. 4.7 shows a schematic of the experimental configuration. Weakly bound Feshbach molecules are associated in a crossed dipole trap from a near-degenerate and spin polarized mixture of ^{23}Na and ^{40}K atoms via RF association (for details see section 3.2). For spectroscopy, 10mW of the diode laser output is focused to a waist of $50\mu\text{m}$ and superimposed with the dipole trap. Illumination times varied between $1 - 100\mu\text{s}$. To ensure optimal overlap between dipole trap and the spectroscopy laser we modulate the power of the spectroscopy laser at twice the trap frequency ($\sim 180\text{Hz}$) and maximize parametric trap heating of a pure ^{23}Na BEC.

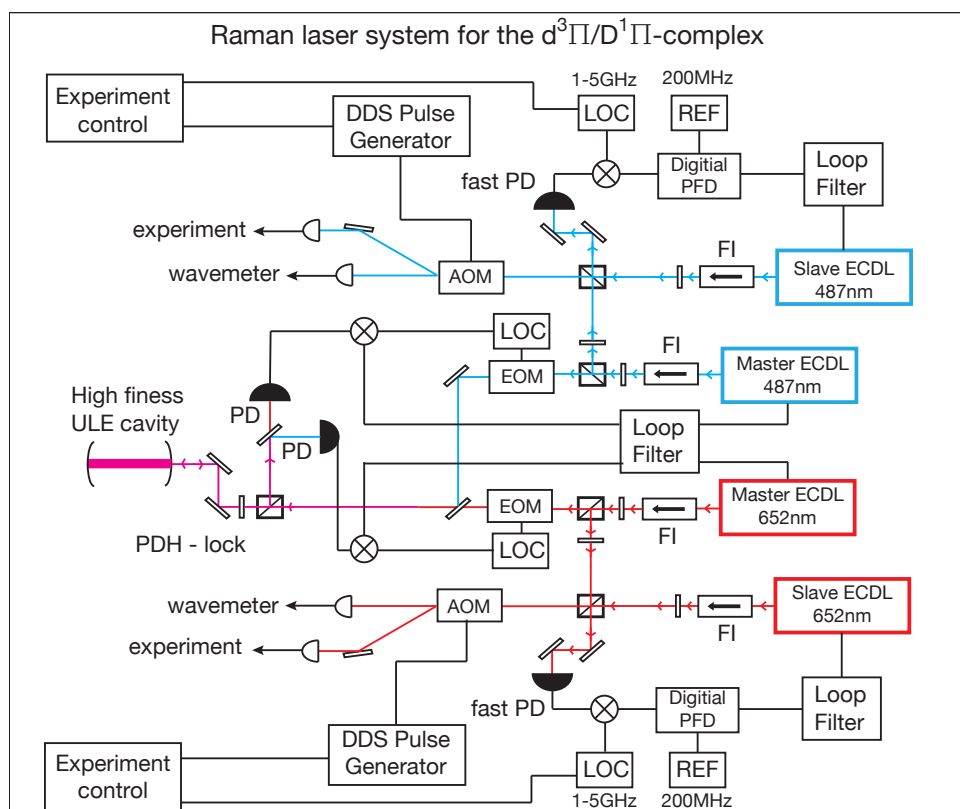


Figure 4.8 – Schematic of the narrow linewidth laser system that is used for high resolution and coherent molecular spectroscopy. For both wavelength a master ECDL is PDH-locked to the high finesse cavity. The phase-locked master-slave configuration ensures continuous frequency tunability over more than the free spectral range of the cavity.

4.4.1 Wave function and spin-character of the initial state

The interpretation and quantitative analysis of the observed molecular excitation spectra require a detailed knowledge of the initial state that we use for spectroscopy. As reported in section 3.2 we use Feshbach molecules with a binding energy of $\approx 83\text{kHz}$ that are RF associated close to a Feshbach resonance in the $|1, 1\rangle_{Na} \otimes |9/2, -9/2\rangle_{K_{40}}$ channel. In order to analyze the spin-character and hyperfine state composition of the Feshbach molecule, we use the *asymptotic bound state model* (ABM) [71]. The Feshbach molecule state is a superposition of the scattering state of the *entrance channel* and the resonant boundstate of the *closed channel*. The channels are coupled via the spin-dependent molecular interaction potential and the hyperfine interaction (for details see section 3.1. The Feshbach molecule state can be written as [55]):

$$|FB\rangle = \sqrt{Z(B)}\phi_C(R)|close\rangle + \sqrt{1-Z(B)}\phi_{bg}(R)|open\rangle \quad (4.36)$$

Here $Z(B)$ and $1-Z(B)$ indicate the *closed* and *open channel fraction*, which depend on the distance in magnetic field with respect to the Feshbach resonance located at $B_0 = 88\text{G}$. The closed channel bound state wavefunction $\phi_C(R)$ in general has to be obtained by a *coupled channels* calculation [13]. For weakly bound Feshbach molecules, where the

binding energy is given by

$$E_b(B) = -\frac{\hbar^2}{ma(B)}, \quad (4.37)$$

the long range part of the closed channel wavefunction can be approximated by a *halo*-state that does not depend on the details of interaction potential but solely on the s-wave scattering length $a(B)$. The halo-wavefunction is given by [13]:

$$\phi_h(R) = \frac{e^{-R/a}}{\sqrt{2\pi a(B_0 - B)R}} \quad (4.38)$$

For molecular spectroscopy however, it is the short range part of the bound state wave function that determines the Frank-Condon factor with the bound state in the $D^1\Pi/d^3\Pi$ complex which is not altered by the coupling to the entrance channel. We determine the close/open channel fraction of the Feshbach molecule following the definition from [55]. Based on the ABM model, we then find that at 85.5G and 80kHz binding energy, the open channel fraction is 98.4% (amplitude square) and the close channel fraction is 1.6%. Due to admixture of the least bound state of the closed channel, the Frank-Condon factor [75] between the Feshbach molecule and the target level in the $D^1\Pi/d^3\Pi$ complex is significantly enhanced compared to the situation of PA spectroscopy of free atoms. By increasing the distance in magnetic field to the Feshbach resonance not only the binding energy can be therefore increased but also the Frank-Condon factor.

The main purpose of the ABM model however is to identify the closed channel hyperfine state composition (the open channel is given in section 4.3.1). Expressed in the spin basis the Feshbach molecule is a superposition of the basis states listed in table 4.3. This

J	m_J	μ_{Na}	μ_K	closed channel (amplitude)	open channel (amplitude)
0	0	-3/2	-2	0.017	0.0
0	0	-1/2	-3	-0.036	0.0
0	0	1/2	-4	-0.045	0.0
1	-1	-3/2	-1	0.129	0.319
1	-1	-1/2	-2	-0.377	0.0
1	-1	1/2	-3	0.077	0.0
1	-1	3/2	-4	0.148	-0.893
1	0	-3/2	-2	0.151	0.0
1	0	-1/2	-3	0.323	0.0
1	0	1/2	-4	0.457	0.319
1	1	-3/2	-3	-0.632	0.0
1	1	-1/2	-4	-0.273	0.0

Table 4.3 – Spin components of the Feshbach molecular state at 85.5G calculated with the asymptotic bound state model of [71]

hyperfine state composition of the Feshbach molecules has to be considered when high resolution molecular spectra are analyzed in detail. By just considering the spin composition of the Feshbach molecule one could argue (as it is done in [70]) that due to the

significant singlet admixture it could be possible to establish a direct two-photon coupling to the rovibronic groundstate via a spin-singlet intermediate state without the need to rely on spin-orbit coupling. However, this reasoning does not take into account, that the wave function of the singlet components only offers a very weak Frank-Condon overlap to the intermediate state manifold. A detailed coupled channels analysis of this problem can be found in [83].

4.4.2 Hyperfine and Zeeman substructure of the candidate level

Starting from Feshbach molecules prepared at a magnetic field of 85.5G, we perform high resolution spectroscopy of the $\Omega = 1, J = 1$ fine structure component of the already identified $|d^3\Pi v = 5\rangle$ candidate level. Fig. 4.9 shows a high resolution spectrum. The polarization of the excitation laser is chosen such, that all possible $(\sigma_+, \sigma_-, \Pi)$ transitions are simultaneously addressed. We observe a Zeeman triplet of energy levels with magnetic quantum numbers $m_J = -1, 0, +1$. The Zeeman splitting between the three m_J components amounts to ~ 70 MHz.

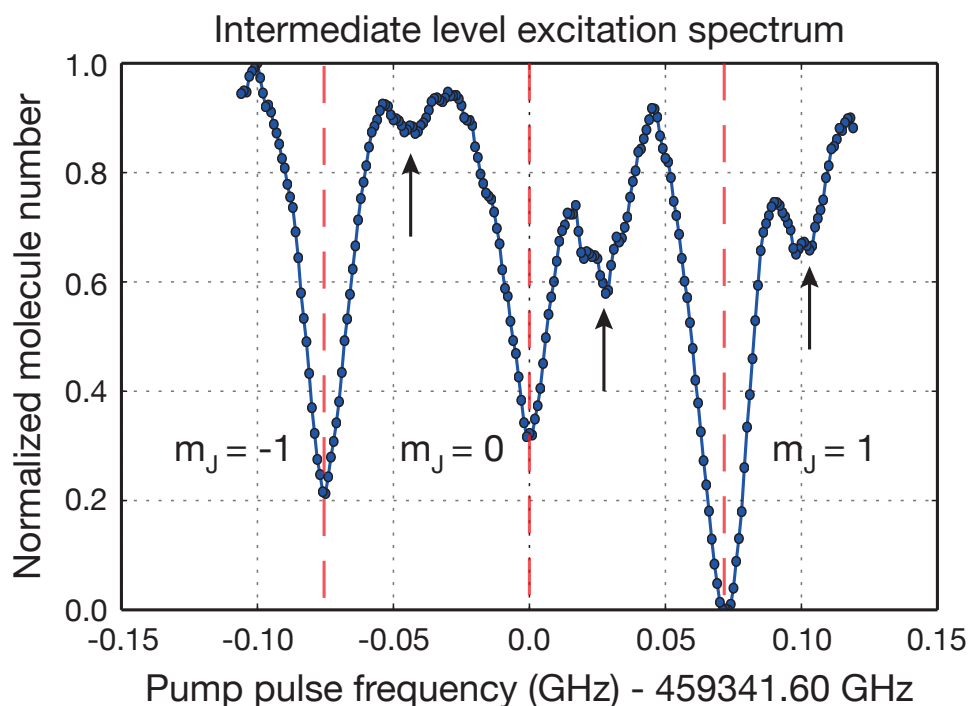


Figure 4.9 – Excitation spectrum of Feshbach molecules to the $J = 1, \Omega = 1$ intermediate level. Polarization of the excitation laser was adjusted to an angle of 45° with respect to the magnetic field direction. A Zeeman triplet $m_J = -1, 0, 1$ is clearly observable. The molecular hyperfine structure is not resolved. The additional features indicated by the black arrows could be caused by the molecular spin-orbit interaction (compare Fig. 5. of [86]) or weak hyperfine interaction. Note that a running average with a bin-size of 12 has been applied to the raw data.

This result is in good agreement with the Zeeman Hamiltonian for pure Hund's case a) molecules [87]:

$$E_Z = \frac{m_J(\Sigma + \Omega)\Omega}{J(J+1)}\mu_B \cdot B. \quad (4.39)$$

The additional features indicated by the black arrows could be caused by the molecular spin-orbit interaction (compare Fig. 5. of [86]). Since the molecular hyperfine structure is not resolved for the $\Omega = 1, J = 1$ fine structure component, I assume that each m_J component of the Zeeman triplet can consist of several molecular hyperfine states. Starting from Feshbach molecules with total projection of angular momentum $m_F = -7/2$ along the direction of the magnetic field only hyperfine components with $m_F = -5/2, -7/2, -9/2$ can be accessed in a single photon transition. To understand which states those are, I work in the spin basis $|Jm_Jm_{Na}m_K\rangle$ and consider which of these basis states can be accessed for each m_J component of the Zeeman triplet starting from a Feshbach molecule with hyperfine state composition given in table 4.3. The tables 4.4, 4.5 and 4.6 summarize the result.

$m_F = -9/2$	$m_F = -7/2$	$m_F = -5/2$
$m_{Na} = 0.5, m_K = -4$	$m_{Na} = 1.5, m_K = -4$	$m_{Na} = 1.5, m_K = -3$
$m_{Na} = -0.5, m_K = -3$	$m_{Na} = 0.5, m_K = -3$	$m_{Na} = 0.5, m_K = -2$
$m_{Na} = -1.5, m_K = -2$	$m_{Na} = -0.5, m_K = -2$	$m_{Na} = -0.5, m_K = -1$
	$m_{Na} = -1.5, m_K = -1$	$m_{Na} = -1.5, m_K = 0$

Table 4.4 – Hyperfine states contributing to the $m_J = -1$ component of the $|d^3\Pi_{\Omega=1}\nu = 5\rangle$ Zeeman triplet expressed in the nuclear spin decoupled basis.

$m_F = -9/2$	$m_F = -7/2$	$m_F = -5/2$
$m_{Na} = -0.5, m_K = -4$	$m_{Na} = 0.5, m_K = -4$	$m_{Na} = 1.5, m_K = -4$
$m_{Na} = -1.5, m_K = -3$	$m_{Na} = -0.5, m_K = -3$	$m_{Na} = 0.5, m_K = -3$
	$m_{Na} = -1.5, m_K = -2$	$m_{Na} = -0.5, m_K = -2$
		$m_{Na} = -1.5, m_K = -1$

Table 4.5 – Hyperfine states contributing to the $m_J = 0$ component of the $|d^3\Pi_{\Omega=1}\nu = 5\rangle$ Zeeman triplet expressed in the nuclear spin decoupled basis.

$m_F = -9/2$	$m_F = -7/2$	$m_F = -5/2$
$m_{Na} = -1.5, m_K = -4$	$m_{Na} = -0.5, m_K = -4$	$m_{Na} = 0.5, m_K = -4$
	$m_{Na} = -1.5, m_K = -3$	$m_{Na} = -0.5, m_K = -3$
		$m_{Na} = -1.5, m_K = -2$

Table 4.6 – Hyperfine states contributing to the $m_J = 1$ component of the $|d^3\Pi_{\Omega=1}\nu = 5\rangle$ Zeeman triplet expressed in the nuclear spin decoupled basis.

Next I estimate the relative line strength for a transition from the Feshbach molecule (with hyperfine state composition given by table 4.3) to a given hyperfine component of the $|d^3\Pi_{\Omega=1}\nu=5\rangle$ Zeeman triplet given by table 4.4,4.5,4.6. The relative line strength can be obtained from the matrix elements of the dipole operator expressed in the spin basis:

$$\begin{aligned} \langle Jm_J | \otimes \langle m_K m_{Na} | e \cdot r_q | m'_K m'_{Na} \rangle \otimes | J' m'_J \rangle &= \langle Jm_J | e \cdot r_q | J' m'_J \rangle \cdot \langle m_K m_{Na} | m'_K m'_{Na} \rangle = \\ &= \langle J || e \cdot r || J' \rangle \cdot \langle Jm_J | J' 1 q m'_J \rangle \cdot \langle m_K m_{Na} | m'_K m'_{Na} \rangle, \end{aligned} \quad (4.40)$$

where I use the Wigner-Eckart theorem [88] to reduce the dipole operator. Here $\langle J || e \cdot r || J' \rangle$ indicates the reduced matrix element and $\langle Jm_J | J' 1 q m'_J \rangle$ the corresponding Clebsch-Gordon factor with q indexing the polarization of the excitation laser via $q = -1 \rightarrow \sigma_-$, $q = 0 \rightarrow \pi$, $q = 1 \rightarrow \sigma_+$. Due to the much larger Frank-Condon factor only the closed channel fraction of the Feshbach molecule has to be considered. The relative line strength for a transition from the Feshbach molecule to a hyperfine component $|J = 1m_J I_{Na} m_{Na} I_K m_K\rangle$ is then given by multiplying the closed channel amplitude for given values of m_{Na} and m_K (see table 4.3) by the corresponding Clebsch-Gordon factor $\langle J = 1m_J | J' = 1 1 q m'_J \rangle$ for a single photon transition. Since $\langle J = 1m_J | J' = 1 1 q m'_J \rangle$ is either 0 or 1, the relative line strengths are given by the squared modulus of the values given in table 4.3. The results are listed in tables 4.7, 4.8 and 4.9.

m_F	m_{Na}	m_K	line strength
-5/2	-1.5	0	0.000
-5/2	-0.5	-1	0.000
-5/2	0.5	-2	0.000
-5/2	1.5	-3	0.000
-7/2	-1.5	-1	0.017
-7/2	-0.5	-2	0.142
-7/2	0.5	-3	0.006
-7/2	1.5	-4	0.022
-9/2	-1.5	-2	0.023
-9/2	-0.5	-3	0.104
-9/2	0.5	-4	0.209

Table 4.7 – Relative line strengths for the $m_J = -1$ component of the $|d^3\Pi_{\Omega=1}\nu=5\rangle$ Zeeman triplet, given in multiples of the reduced matrix element $\langle J || e \cdot r || J' \rangle^2$

Since the hyperfine structure of the $\Omega = 1, J = 1$ fine structure component is clearly not resolved it makes no difference whether we calculate transition matrix elements in the nuclear spin coupled (i.e $\langle F m_F \rangle$) basis or the spin basis $\langle m_J m_K m_{Na} \rangle$. The non-resolved hyperfine structure however makes the identification of a suitable two-photon pathway to the $|X^1\Sigma\nu=0J=0\rangle$ state more involved, since we have to take into account multiple near-degenerate transitions that are addressed simultaneously by the excitation laser.

m_F	m_{Na}	m_K	line strength
-5/2	-1.5	-1	0.017
-5/2	-0.5	-2	0.142
-5/2	0.5	-3	0.006
-5/2	1.5	-4	0.022
-7/2	-1.5	-2	0
-7/2	-0.5	-3	0
-7/2	0.5	-4	0
-9/2	-1.5	-3	0.399
-9/2	-0.5	-4	0.074

Table 4.8 – Relative line strengths for the $m_J = 0$ component of the $|d^3\Pi_{\Omega=1}\nu = 5\rangle$ Zeeman triplet, given in multiples of the reduced matrix element $\langle J||e \cdot r||J'\rangle^2$

m_F	m_{Na}	m_K	line strength
-5/2	-1.5	-2	0.023
-5/2	-0.5	-3	0.104
-5/2	0.5	-4	0.209
-7/2	-1.5	-3	0.399
-7/2	-0.5	-4	0.074
-9/2	-1.5	-4	0.0

Table 4.9 – Relative line strengths for the $m_J = 1$ component of the $|d^3\Pi_{\Omega=1}\nu = 5\rangle$ Zeeman triplet, given in multiples of the reduced matrix element $\langle J||e \cdot r||J'\rangle^2$

4.4.3 Origin of the non-resolved hyperfine structure of the $\Omega = 1, J = 1$ component

In order to understand why the excited state hyperfine structure is not resolved for the $d^3\Pi/D^1\Pi$ complex consider the following:

First, note that the the spin-singlet $D^1\Pi$ state only exhibits nuclear-nuclear hyperfine coupling, which is below the kHz level even for the $|X^1\Sigma\nu = 0, J = 0\rangle$ state [21]. Therefore the hyperfine structure of the spin-orbit coupled $d^3/D^1\Pi$ complex will be completely dominated by the $d^3\Pi$ state.

The Hamiltonian governing the hyperfine structure of the $d^3\Pi$ state is given by [89]:

$$H_{HF} = d_{Na} \mathbf{I}_{Na} \cdot \mathbf{k}' + d_K \mathbf{I}_K \cdot \mathbf{k}', \quad (4.41)$$

where

$$d = a\Lambda + (b + c)\Sigma \quad (4.42)$$

and \mathbf{k}' is a unit vector pointing in the direction of the internuclear axis. The hyperfine coupling constants a , b and c correspond to various magnetic dipole interactions averaged over the electron orbital [89]. Only in b there is a term that includes the operator $\frac{\delta(r)}{r^2}$

giving rise to *Fermi contact interaction*. H_{HF} is diagonal in the coupled basis $|I_K I_{Na} J F m_F\rangle$ and matrix elements are given by:

$$E_{HF} = \Omega \frac{F(F+1) - J(J+1) - I(I+1)}{2J(J+1)} \quad (4.43)$$

From equations (4.41) and (4.43) one directly sees that only levels with $\Sigma = 1, \Omega = 2$ will exhibit Fermi contact interaction. Due to the nuclear shielding effect [90, 91] the molecule hyperfine structure of NaK can only be resolved for electronic states that exhibit Fermi contact interaction [81, 92, 93]. As expected from this reasoning the $\Omega = 2, J = 2$ component of the $\nu = 5$ fine structure multiplet shows complex hyperfine structure (see Fig. 4.10). In general, it is strongly desired to identify a hyperfine state resolved molecular level as intermediate state for STIRAP [94, 95, 96, 97]. Unfortunately, the $\Omega = 2$ component is not suited for this purpose since first, parity selection excludes a two-photon transition to the $|X^1\Sigma \nu = 0, J = 0\rangle$ state. Second, even parity allowed transitions to excited rotational levels ($J = 2n + 1$) of the groundstate manifold will be strongly suppressed by a factor $\propto \frac{B_5^2}{A_5^2}$. This can be understood on the basis of equations 4.28 - 4.33. In contrast to the singlet admixture for the $J = 1$ component which is due to spin-orbit interaction with coupling constant $\xi_{5,6}$ the singlet admixture to the $J = 2$ component is a second order effect that is mediated by the S-uncoupling operator with a coupling constant proportional to B_5 . The resulting Rabi frequency for the Stokes transition would be orders of magnitude (2–3) smaller than the natural linewidth Γ of the intermediate state - effectively excluding STIRAP success (see section 4.5.1 and 4.5.3 below). For these reasons the hyperfine structure of the $\Omega = 2$ component was not investigated further and quantum numbers have not been assigned.

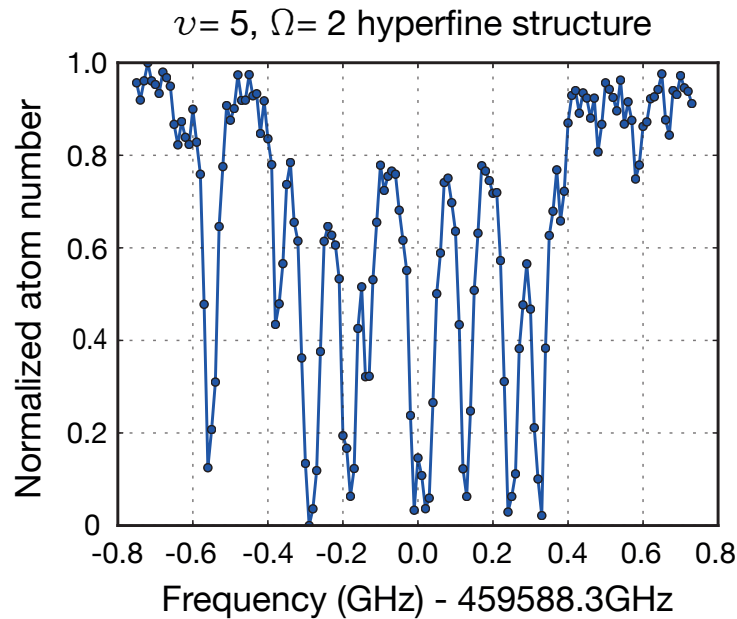


Figure 4.10 – High resolution spectrum of the $|d^3\Pi_{\Omega=2} \nu = 5, J = 2\rangle$ state. The molecular hyperfine structure is clearly resolved due to presence of Fermi contact interaction.

4.5 Groundstate spectroscopy

Having identified a suitable singlet-triplet mixing intermediate state in the $d^3\Pi/D^1\Pi$ complex, the next step is to measure the transition frequency and determine the coupling strength from this level to the $|X^1\Sigma\nu=0J=0\rangle$ state. Due to the short lifetime ($< 15\text{ns}$) of the intermediate state conventional pump-probe spectroscopy is not feasible. Instead we employ coherent Raman spectroscopy (see section 4.5.1 below). In order to be able to observe coherent excitation phenomena both spectroscopy lasers need to be simultaneously locked to the same high finesse ULE cavity via the PDH technique. Continuous frequency tuning over $> 1\text{GHz}$ was implemented by a phase-locked master-slave configuration (see Fig. 4.8). For spectroscopy we focus $\sim 10\text{mW}$ of each laser to a waist of $50\mu\text{m}$ and overlap it with Feshbach molecules prepared in a crossed optical dipole trap (see Fig. 4.7).

4.5.1 Coherent population trapping, STIRAP and EIT

Before we present and discuss our results on coherent two-photon spectroscopy, we briefly review the phenomena that can be observed in a coherently coupled three level lambda system. This section is primarily based on the review articles [98, 99, 100, 14].

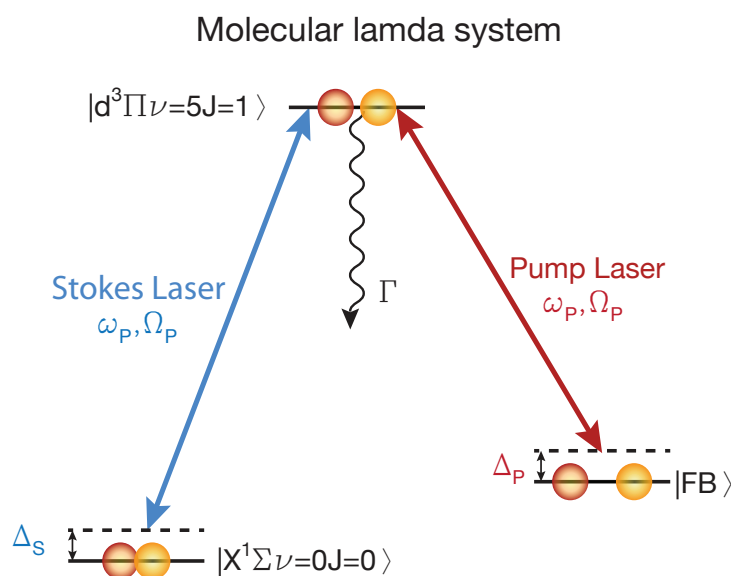


Figure 4.11 – Schematic for the molecular lambda system formed by the Feshbach molecule, the $d^3\Pi/D^1\Pi$ intermediate level and the $|X^1\Sigma\nu=0J=0\rangle$ state. States are coherently coupled by a pair of Raman lasers with frequencies $\omega_{P/S}$, Rabi frequencies $\Omega_{P/S}$ and single photon detunings with respect to the molecular transition frequencies $\Delta_{P/S}$. The lasers are said to be in Raman resonance for $\Delta_P = \Delta_S = \Delta$.

Consider the molecular three level system shown in Fig. 4.11. The initially populated Feshbach molecular level is coupled via the *pump* laser to the intermediate level in the $d^3\Pi/D^1\Pi$ complex with single photon Rabi frequency $2\pi \cdot \Omega_P$ and single photon detuning $2\pi \cdot \Delta_P = 2\pi(\omega_1 - \omega_P)$ with respect to the molecular transition frequency $2\pi \cdot \omega_1$. The intermediate level will predominantly decay to lower lying rovibronic states of the $^{23}\text{Na}^{40}\text{K}$

molecule that are not coupled by the Raman lasers. The effect of these various decay channels is parametrized by a single effective decay rate $2\pi \cdot \Gamma$. Finally the intermediate level is coupled by the so called *Stokes* laser to the rovibronic groundstate $|X^1\Sigma v = 0, J = 0\rangle$ with Rabi frequency $2\pi \cdot \Omega_S$ and detuning $2\pi \cdot \Delta_S = 2\pi(\omega_2 - \omega_S)$. Both lasers are said to be in Raman resonance when $\Delta_S = \Delta_P = \Delta$. In the rotating wave approximation [98] (which is justified for near resonant pump and Stokes lasers) the non-hermitian evolution matrix is given by:

$$W(t) = \frac{1}{2} \begin{pmatrix} 2\Delta_P & \Omega_P(t) & 0 \\ \Omega_P(t) & -i\Gamma & \Omega_S(t) \\ 0 & \Omega_S(t) & 2\Delta_S \end{pmatrix}, \quad (4.44)$$

where we made a potential time dependence of the Rabi frequencies (as required for STIRAP) explicit. The detunings as well as the decay rate are assumed to be constant. The time evolution of the amplitudes $C_i(t)$ of the three level state vector

$$|\Phi\rangle = e^{-iE_2 t/\hbar} [C_1(t)e^{-i\omega_P/\hbar}|1\rangle + C_2(t)|2\rangle + C_3(t)e^{-i\omega_S/\hbar}|3\rangle] \quad (4.45)$$

is then given by the following equation of motion:

$$\frac{d}{dt}\mathbf{C}(t) = -iW(t) \cdot \mathbf{C}(t), \quad \text{With } \mathbf{C}(t) = \begin{pmatrix} C_1(t) \\ C_2(t) \\ C_3(t) \end{pmatrix}. \quad (4.46)$$

In single photon resonance i.e. $\Delta_S = 0 = \Delta_P$ the eigenvalues of the evolution matrix are computed as:

$$\begin{aligned} \lambda_0 &= 0 \\ \lambda_{1/2} &= \frac{1}{4} \left(-i\Gamma \pm \sqrt{-\Gamma^2 + 4\Omega_2^2 + 4\Omega_P^2} \right). \end{aligned} \quad (4.47)$$

The zero eigenvalue λ_0 of $W(t)$ signals the existence of a non-evolving and non-decaying eigenmode of the three-level lambda system. To make this statement more concrete we perform the following basis transformation:

$$\begin{pmatrix} C_1 \\ C_2 \\ C_3 \end{pmatrix} \rightarrow \begin{pmatrix} C_+ \\ C_2 \\ C_- \end{pmatrix} = T \begin{pmatrix} C_1 \\ C_2 \\ C_3 \end{pmatrix} = \begin{pmatrix} \frac{1}{\Omega}(\Omega_P C_1 + \Omega_S C_3) \\ C_2 \\ \frac{1}{\Omega}(\Omega_S C_1 - \Omega_P C_3) \end{pmatrix}, \quad (4.48)$$

and

$$W \rightarrow W' = TWT^{-1}, \quad (4.49)$$

where we omitted the labels for time dependence. The transformation matrix is:

$$T = \begin{pmatrix} \frac{\Omega_P}{\Omega} & 0 & \frac{\Omega_S}{\Omega} \\ 0 & 1 & 0 \\ \frac{\Omega_S}{\Omega} & 0 & -\frac{\Omega_P}{\Omega} \end{pmatrix}, \quad (4.50)$$

with the RMS two-photon Rabi frequency given as $\bar{\Omega} = \sqrt{\Omega_p^2 + \Omega_s^2}$. On Raman resonance ($\Delta_p = \Delta_s = \Delta$) the evolution of the coupled system can now be expressed as:

$$\begin{aligned}\frac{d}{dt}C_+(t) &= -i\Delta C_+(t) - \frac{i\bar{\Omega}}{2}C_2(t) \\ \frac{d}{dt}C_2(t) &= -\frac{i\bar{\Omega}}{2}C_+(t) - \frac{i\Gamma}{2}C_2(t) \\ \frac{d}{dt}C_-(t) &= -i\Delta C_-(t)\end{aligned}$$

These equations show that the decaying state $|2\rangle$ is only coupled to the superposition state $|+\rangle$, while the other superposition state $|-\rangle$ evolves freely without being subjected to loss. Since the system does not absorb and scatter any photons from both Raman lasers once it is prepared in or has evolved into state $|-\rangle$, this state is called a *dark state*. Due to the existence of a dark state in a coupled three level system several closely related physical phenomena can be observed:

Coherent population trapping

Consider the lambda system of Fig. 4.11 with parameters **a**) : $\Delta_s = 0 = \Delta_p, \Gamma = \Omega_p = \Omega_s$ and **b**) : $\Delta_s = 0 = \Delta_p, \Gamma = 5 \cdot \Omega_p = 5 \cdot \Omega_s$. Numerical integration of 4.46 gives the temporal evolution for the state populations of the lambda system (see Fig. 4.12). We observe that even for significant decay of the intermediate state half of the population becomes trapped in the dark state.

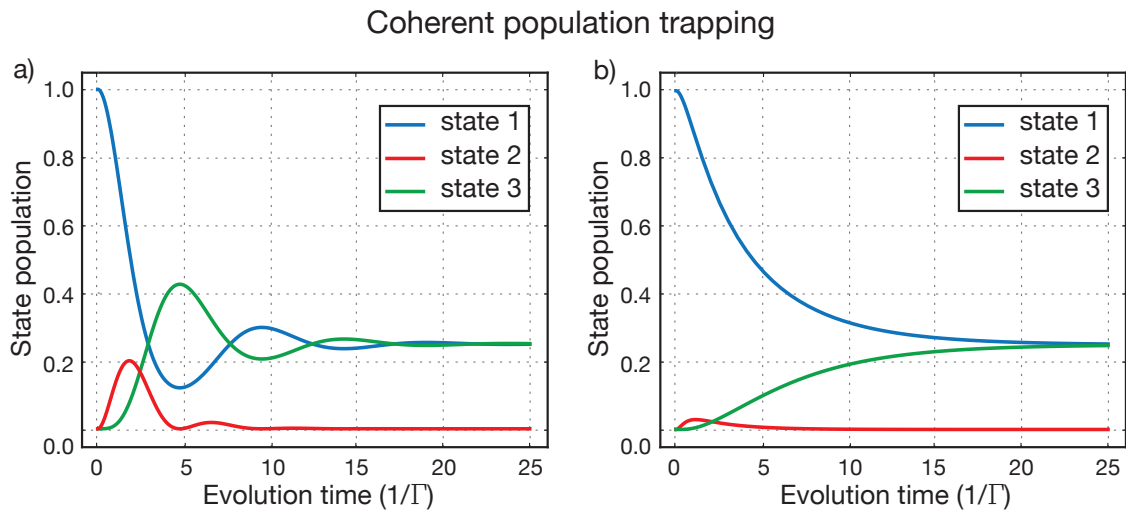


Figure 4.12 – Population evolution for a coherently coupled three level lambda system obtained by numerical integration of equation 4.46. Parameters are given by **a**) : $\Delta_s = 0 = \Delta_p, \Gamma = \Omega_p = \Omega_s$, **b**) : $\Delta_s = 0 = \Delta_p, \Gamma = 5 \cdot \Omega_p = 5 \cdot \Omega_s$.

Electromagnetically induced transparency

In the situation when $\Omega_s \gg \Omega_p$ (called *strong coupling regime*), the Stokes laser can be used to render an ensemble of particles with the internal level structure of Fig. 4.11

completely transparent for the pump laser beam. In the strong coupling regime and on Stokes resonance ($\Delta_S = 0$) the absorption spectrum for the pump laser is given by the following equation[99]

$$N(t, \Delta_P) = N_0 \cdot \exp\left(-t \cdot \Omega_P^2 \frac{4\Gamma\Delta_P^2 + \Gamma_{eff}(\Omega_S^2 + \Gamma_{eff} \cdot \Gamma)}{(\Omega_S^2 + \Gamma \cdot \Gamma_{eff} - 4\Delta_P^2)^2 + 4\Delta_P^2(\Gamma + \Gamma_{eff})^2}\right), \quad (4.51)$$

here N designates the number of Feshbach molecules. In contrast to the treatment of coherent population trapping - an additional effective loss rate Γ_{eff} has been introduced that phenomenologically accounts for decoherence between the Feshbach state and the $|X^1\Sigma v = 0J = 0\rangle$ state. In a real experiment potential sources of decoherence include relative linewidth fluctuations of the Raman lasers, external magnetic or electric field fluctuations, external field gradients, etc. Even when both Raman lasers are in single photon resonance ($\Delta_P = \Delta_S = 0$) the dark state (EIT peak) does decay due to decoherence.

$$N(t) = N_0 \cdot \exp\left(-t \frac{\Omega_P^2 \Gamma_{eff}}{\Omega_S^2 + \Gamma_{eff} \Gamma}\right) \quad (4.52)$$

The associated decay constant is given by:

$$\tau_{EIT} = \frac{\Omega_S^2 + \Gamma_{eff} \cdot \Gamma}{\Omega_P^2 \cdot \Gamma_{eff}} \quad (4.53)$$

By measuring the Rabi frequencies Ω_S , Ω_P and the EIT decay with both Raman lasers on resonance one is therefore able to determine Γ_{eff} experimentally. Fig. 4.13 a) shows a typical EIT spectrum for a pump irradiation time of $t = \Omega_P^2/\Gamma$ and $t = 5 \cdot \Omega_P^2/\Gamma$. Fig. 4.13 b) illustrates the effect of different values for Γ_{eff} on EIT decay.

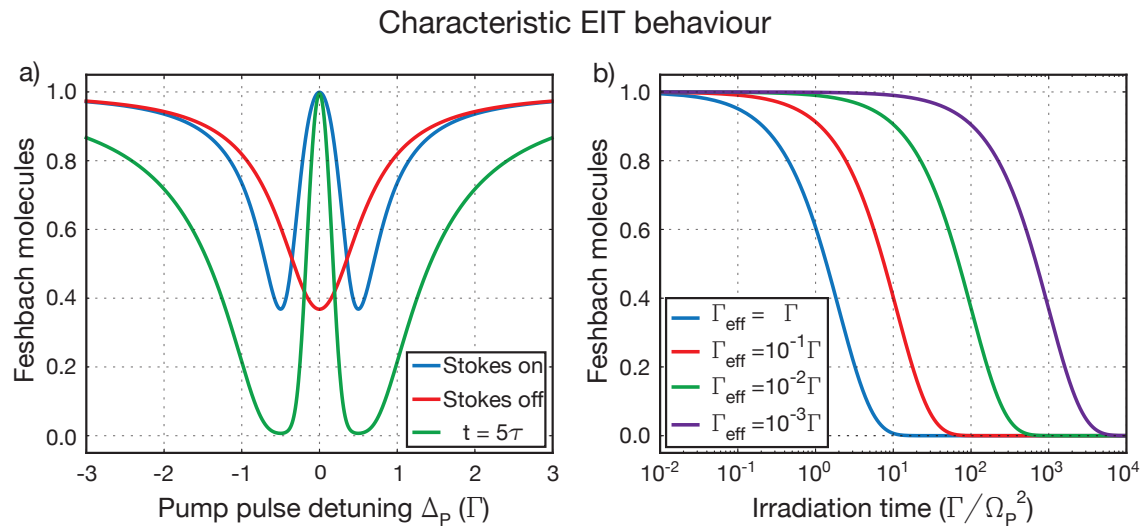


Figure 4.13 – a) EIT spectra as calculated by equation 4.51. Parameters are given by: $\Omega_S = \Gamma = 100 \cdot \Omega_P$, $\Gamma_{eff} = 0.001 \cdot \Gamma$ and $\tau = \Omega_P^2/\Gamma$. **b)** Decay of the EIT peak on resonance ($\Delta_P = \Delta_S = 0$) for different values of the phenomenological decoherence rate Γ_{eff} . Parameters are given by: $\Omega_S = \Gamma = 100 \cdot \Omega_P$.

Note that in a real experiment the Stokes pulse is switched on (off) $\sim 1000 \cdot 1/\Gamma$ earlier (later) than the pump pulse. Since $\Omega_S \sim \Gamma \gg \Omega_P$ the system then adiabatically evolves from a state with all population in the Feshbach state into the dark state [99].

STIRAP - Stimulated Raman Adiabatic passage

The coherent dark superposition state can be used for adiabatic population transfer from the Feshbach state into the $|X^1\Sigma^+\nu=0, J=0\rangle$ state. By controlling the ratio of the pump and Stokes laser Rabi frequencies $r(t) = \frac{\Omega_S(t)}{\Omega_P(t)}$ the RWA Hamiltonian becomes time dependent. According to the adiabatic theorem of quantum mechanics [101] the molecular three level system will remain in an instantaneous eigenstate of the time dependent Hamiltonian, given the change in $r(t)$ happens slowly compared to the rate of unitary evolution. Recall that the eigenstates of the coupled three level system can be expressed as:

$$\begin{aligned} |\Phi_+\rangle &= \frac{\Omega_P(t)}{\Omega(t)}|1\rangle + \frac{\Omega_S(t)}{\Omega(t)}|3\rangle \\ |\Phi_2\rangle &= |2\rangle \\ |\Phi_-\rangle &= \frac{\Omega_S(t)}{\Omega(t)}|1\rangle - \frac{\Omega_P(t)}{\Omega(t)}|3\rangle, \end{aligned} \quad (4.54)$$

The corresponding eigenvalues are given by:

$$\begin{aligned} \lambda_+ &= \frac{1}{2}\sqrt{\Omega_P^2 + \Omega_S^2} \\ \lambda_2 &= -\frac{1}{2}\sqrt{\Omega_P^2 + \Omega_S^2} \\ \lambda_- &= 0 \end{aligned} \quad (4.55)$$

Decay-free population transfer can now be achieved by ensuring that the system adiabatically follows the zero eigenvalue eigenstate $|\Phi_-\rangle$. The adiabaticity criterium for STIRAP is given by [14]:

$$\left| \left\langle \frac{d}{dt} \Phi_- | \Phi_{+/2} \right\rangle \right| \ll |\lambda_{+/2} - \lambda_-|, \quad \forall t \in [0, \tau] \quad (4.56)$$

For population transfer of Feshbach molecules one has to ensure spatial overlap between both Raman lasers and the trapped molecular sample and then uses amplitude modulated laser pulses that partially overlap in time. A convenient choice for the STIRAP pulse sequence is based on a Cos^2 pulse:

$$\begin{aligned} f(t, \tau) &= \text{Cos}^2(\pi/2 \cdot \frac{t}{\tau}) \\ \Omega_P(t) &= \Omega_0 \cdot f(t - \tau, \tau), \quad \text{for } t \in [0, \tau] \\ \Omega_S(t) &= \Omega_0 \cdot f(t, \tau), \quad \text{for } t \in [0, \tau] \end{aligned} \quad (4.57)$$

Fig. 4.14 a) shows this pulse sequence. For this pulse sequence the adiabaticity criterium (equation 4.56) becomes $\Omega_0 \cdot \tau \gg 1$. Note that the Cos^2 pulse gives $\frac{d}{dt} \Omega_{P/S}(t)|_{t=0/\tau} = 0$ as required by the adiabatic theorem. Numerical integration of equation 4.46 illustrates the effect of the STIRAP pulse sequence of equation 4.57 on the populations of an exemplary molecular three level system (see Fig. 4.14 b)).

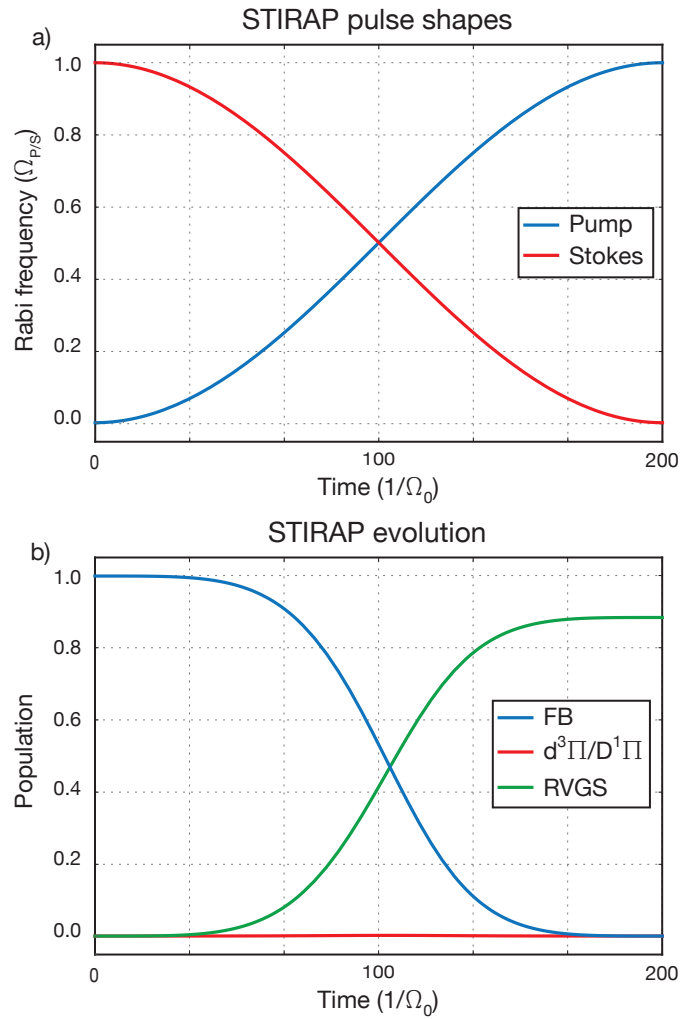


Figure 4.14 – a) Cos^2 shaped pulse sequence for STIRAP. b) Temporal evolution of the populations in the molecular three level system of Fig. 4.11 obtained by numerical integration of equation 4.46. Parameters are given by: $\Omega_0 = \Gamma, \Delta_P = \Delta_S = 0, \tau = 200 \cdot 1/\Omega_0$.

We observe that for an ideal three level system (no decoherence due to external fields, laser linewidth fluctuations etc.) STIRAP results in efficient population transfer $> 80\%$ from the Feshbach state to the rovibronic groundstate even in presence of strong intermediate state decay $\Gamma \sim \Omega_0$ if the adiabaticity criterium is fulfilled. To investigate the importance of adiabaticity further, Fig. 4.15 shows how STIRAP efficiency depends on the total pulse duration.

Fig. 4.16 shows how STIRAP efficiency depends on the detuning of the Stokes pulse for two different values of Ω_0/Γ .

For the pulse sequence of equation 4.57 it is also possible to derive an analytic result for the functional dependence of STIRAP efficiency on pulse duration τ and Stokes detuning Δ_S [102]:

$$P(\tau, \Delta_S) = \exp\left(-\frac{\Gamma\tau^2}{\Omega_0^2\tau} - \frac{\Delta_S^2\Gamma\tau}{2\Omega_0^2}\right) \quad (4.58)$$

Including the detrimental effects of uncorrelated broadband laser frequency noise origi-

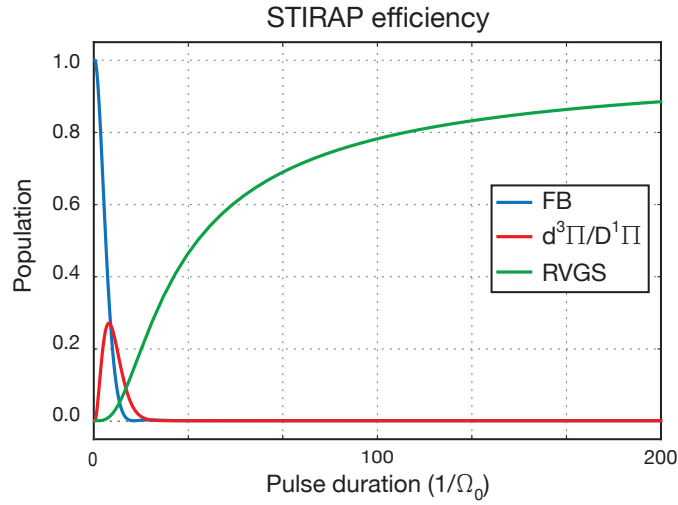


Figure 4.15 – STIRAP efficiency as function of total pulse duration for the pulse shape of equation 4.57 obtained by numerical integration of equation 4.46. Parameters are given by: $\Omega_0 = \Gamma, \Delta_P = \Delta_S = 0$

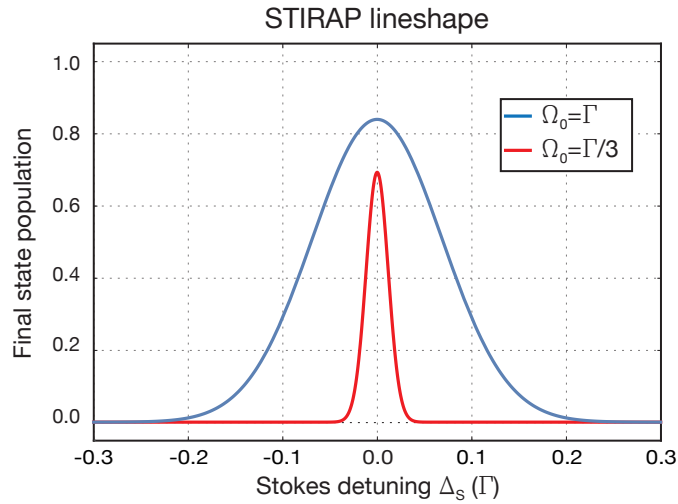


Figure 4.16 – STIRAP efficiency as function of Stokes pulse detuning for two different values of Γ/Ω_0 . Parameters are given by: $\Delta_P = 0, \tau = 200 \cdot \frac{1}{\Omega_0}$

nating from spontaneous emission of the gain medium results in the following expression for STIRAP efficiency on resonance ($\Delta_P = \Delta_S = 0$) [102]:

$$P(\tau, D) = \text{Exp}\left(-\frac{\Gamma\pi^2}{\Omega_0^2\tau} - \frac{D\tau}{2}\right), \quad (4.59)$$

where D is the linewidth of the frequency difference of the Raman lasers. Details on the physical origin of laser noise are discussed in [102] and [103]. Fig. 4.17 illustrates how the STIRAP efficiency depends on total pulse duration for realistic values of D and Ω_0 .

In general STIRAP will be efficient for groundstate transfer of Feshbach molecules, if

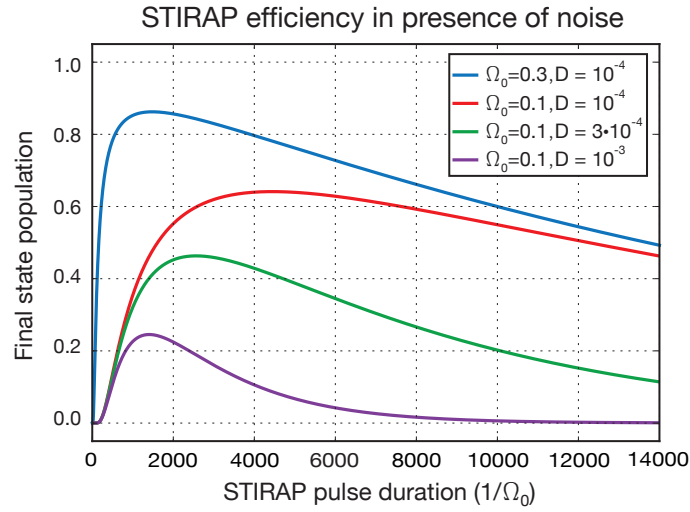


Figure 4.17 – STIRAP efficiency as function of pulse duration in presence of white frequency noise leading to a relative laser linewidth D [102]. Parameter values are given in units of Γ : $\Delta_P = \Delta_S = 0$.

the following inequality is fulfilled:

$$D \ll \frac{1}{\tau} \ll \frac{\Omega_0^2}{\pi^2 \Gamma}. \quad (4.60)$$

Therefore one should look for a *STIRAP scheme* (intermediate state, laser system) that:

- Minimizes Γ by reducing the number of potential decay channels.
- Maximizes Ω_0 by choosing a strong transition and high power lasers.
- Minimizes D by working with narrow linewidth lasers. In particular one should avoid, if it is possible, to work with short cavity semiconductor lasers due to a inferior noise performance [104, 105, 106, 107].

Unfortunately we only considered to look for a strong transition and did not take into account the other criteria when we decided for an intermediate state in the $d^3\Pi/D^1\Pi$ complex and a low output power semiconductor based Raman laser system.

4.5.2 Results of EIT spectroscopy

For measuring the transition frequency from the $d^3\Pi/D^1\Pi$ intermediate state to the $|X^1\Sigma v = 0 J = 0\rangle$ state we make use of the coherent population trapping phenomenon discussed in section 4.5.1. The general idea is to prepare a molecular three level system as shown in Fig. 4.11 in the strong coupling regime and eventually detect an EIT signal when both Raman lasers are in resonance. Fortunately we could build on measurements of the binding energy of the $|X^1\Sigma v = 0 J = 0\rangle$ state in $^{23}\text{Na}^{39}\text{K}$ that were performed at a molecular beam experiment [108]. The mass scaled result for the binding energy of the rovibronic groundstate of $^{23}\text{Na}^{40}\text{K}$ is: 5212.05cm^{-1} . The starting point for dark state spectroscopy is calculated by adding the measured transition frequency from the Feshbach

molecule to the $m_J = 0$ component of the $J = 1, \Omega = 1$ Zeeman triplet and subtracting the hyperfine and Zeeman energy of the Feshbach molecule:

$$\begin{aligned} f_{start} &= f_{RVGS} - f_{pump} - f_{Hf/Zee} = \\ &= 5212.05 \text{cm}^{-1} \cdot c + 459.34160 \text{THz} - 1.86 \text{GHz} = \end{aligned} \quad (4.61)$$

$$= 615.59306 \text{THz}. \quad (4.62)$$

The experimental sequence for the detection of coherent population trapping is the following:

1. A sample of $^{23}\text{Na}^{40}\text{K}$ Feshbach molecules is prepared in the crossed dipole trap.
2. The sample is simultaneously illuminated with two square pulses from both Raman lasers that are locked to the ULE cavity.
3. The pump pulse is adjusted to one-photon resonance with the $m_J = 0$ component of the $J = 1, \Omega = 1$ Zeeman triplet.
4. The polarization for the pump pulse is $\frac{1}{\sqrt{2}}(\sigma_- + \sigma_+)$, for the Stokes pulse it is Π , such that the angular momentum of the molecule is changed by \hbar .
5. The frequency of the Stokes pulse is varied in steps of 5% of the expected Rabi frequency $\Omega_S \sim 2\pi \cdot 10 \text{MHz}$ for the $|X^1\Sigma \nu = 0, J = 0\rangle \rightarrow |D^3\Pi_{\Omega=1} \nu = 5, J = 1\rangle$ transition.
6. The Stokes pulse predates the pump pulse by $20\mu\text{s}$. The pulse length ($\sim 30\mu\text{s}$) is chosen such that away from two-photon resonance Feshbach molecule number drops to 20% above the detection noise level due to resonant excitation by the 652nm laser. The exact timing for both spectroscopy pulses can be seen in Fig. 4.18.
7. Remaining Feshbach molecules are detected via direct absorption imaging on the cycling transition of ^{40}K at 85.5G.

This experimental sequence was repeated until a reduction of resonant Feshbach molecule loss due to coherent population trapping [98, 99, 100] could be detected. Fig.4.19 shows the final scan of the Stokes laser frequency that exhibited the dark-resonance feature. Fig. 4.20 shows the reciprocal experiment where the frequency of the Stokes laser is kept in one-photon resonance and the frequency of the pump laser is scanned across the $m_J = 0$ absorption feature. Absorption of the pump laser is blocked when both lasers are in Raman resonance and a typical EIT (electromagnetically induced transparency) spectrum can be observed (compare Fig. 4.13). With these measurements we determine the binding energy of the $|X^1\Sigma \nu = 0, J = 0\rangle$ state by measuring the frequency of both Raman lasers using a commercial wavemeter (Toptica, WS7) with 10MHz resolution and an accuracy of 300MHz. Our result, 156.25319THz agrees well with the more precise measurement of [21] where the laser frequencies have been measured with reference to an iodine spectroscopy and a self-referenced frequency comb.

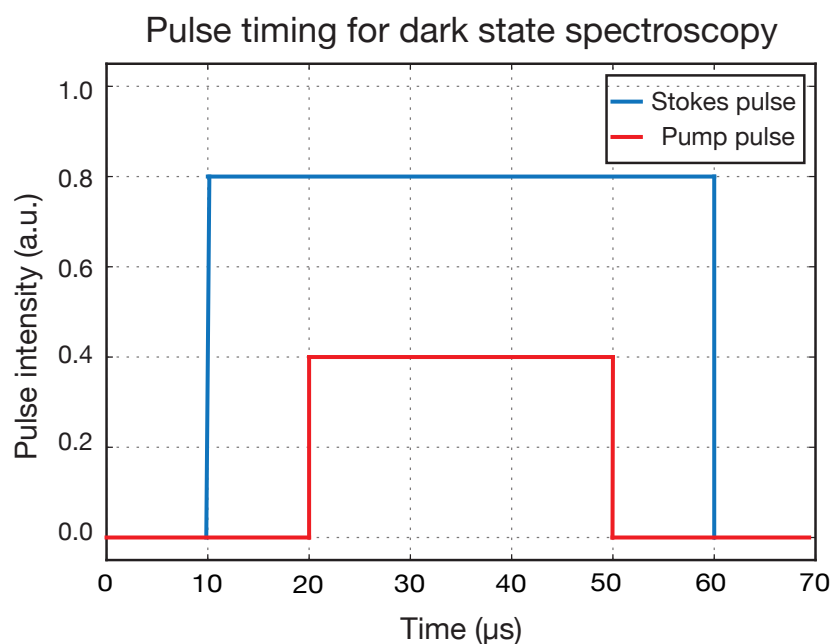


Figure 4.18 – Pulse timing diagram for dark state spectroscopy. The Stokes pulse operates at full laser power (i.e. $\sim 10\text{mW}$) and predates the pump pulse by $20\mu\text{s}$ in order to allow the system to evolve into a potential dark state. The power and irradiation time for the pump pulse is chosen such that the Feshbach molecule number drops to $1/e$ without the Stokes pulse present.

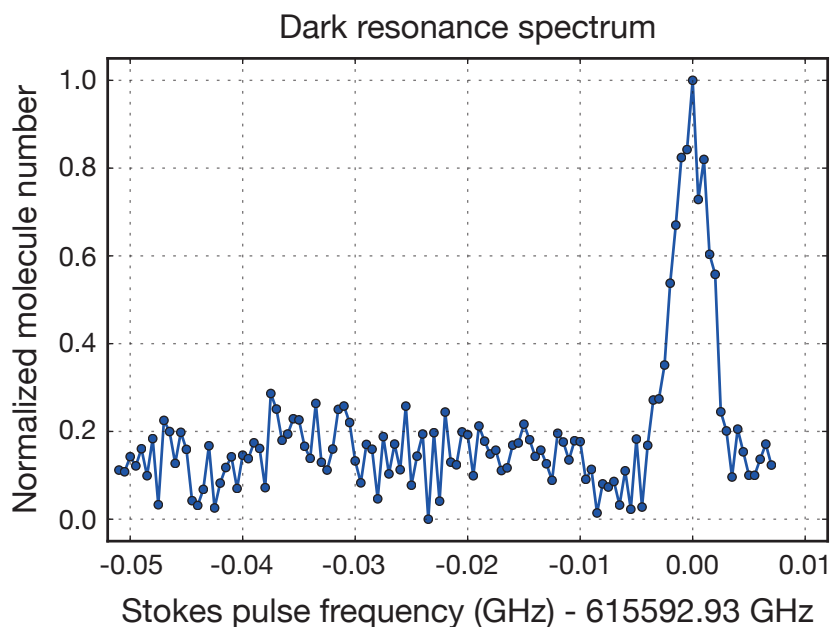


Figure 4.19 – Dark resonance spectrum involving the Feshbach molecule and the $|X^1\Sigma^v = 0, J = 0\rangle$ state via the intermediate $|d^3\Pi_{\Omega=1^v} = 5, J = 1\rangle$ state. When both Raman lasers fulfill their respective one-photon and the combined two-photon resonance condition absorption of the 652nm pump pulse is blocked by coherent population trapping [98, 99, 100].

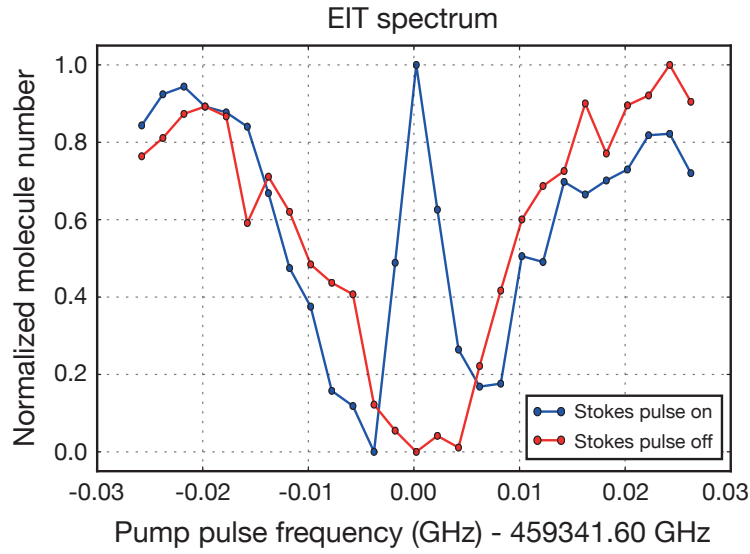


Figure 4.20 – EIT (electromagnetically induced transparency) spectrum from the $m_J = 0$ component of the $|d^3\Pi_{\Omega=1}\nu = 5, J = 1\rangle$ Zeeman triplet. Without the Stokes pulse Feshbach molecules are almost completely lost on resonance. The presence of the Stokes laser pulse completely blocks absorption of the pump pulse when both lasers fulfill the two-photon resonance condition.

4.5.3 Characterization of the $d^3\Pi/D^1\Pi$ - STIRAP scheme

The observation of EIT enabled us to investigate the suitability of the chosen STIRAP scheme for groundstate transfer.

Determination of STIRAP parameters from EIT spectroscopy

In order to estimate the feasibility of the chosen STIRAP scheme, we determine the experimental accessible parameters Ω_p , Ω_S , $\frac{\Omega_p^2}{\Gamma}$ and Γ_{eff} by the following procedure:

1. Measure the on resonant excitation rate of Feshbach molecules for the $m_J = 0$ component of the $\Omega = 1, J = 1$ Zeeman triplet and determine $\tau_{res} = \frac{\Gamma}{\Omega_p^2}$ by fitting a single exponential decay.
2. Measure the decay rate of Feshbach molecules in a strong coupling (i.e. $\Omega_S \gg \Omega_p$) EIT configuration when both Raman lasers fulfill the single photon resonance condition $\Delta_p = \Delta_S = 0$. Fitting a single exponential decay determines the $1/e$ lifetime τ_{EIT} of the dark state .
3. Substitute $\Gamma = \frac{\Omega_p^2}{\tau_{res}}$ and τ_{EIT} in equation 4.51 for the EIT lineshape. A two parameter fit of equation 4.51 for a given irradiation time $t = t_{irr}$ then yields estimates for Ω_p and Ω_S

Fig. 4.21 shows the measurement that is used to determine $\tau_{res} = \frac{\Gamma}{\Omega_p^2}$ and $\tau_{EIT} \simeq \frac{\Omega_S^2}{\Omega_p^2 \cdot \Gamma_{eff}}$. Both quantities are obtained via a least square fit of a single exponential decay.

Fig. 4.22 shows a two-parameter (Ω_p and Ω_S) least square fit of equation 4.51 to an EIT spectrum measured with an irradiation time of $t_{irr} = 30\mu s$. The results of the complete

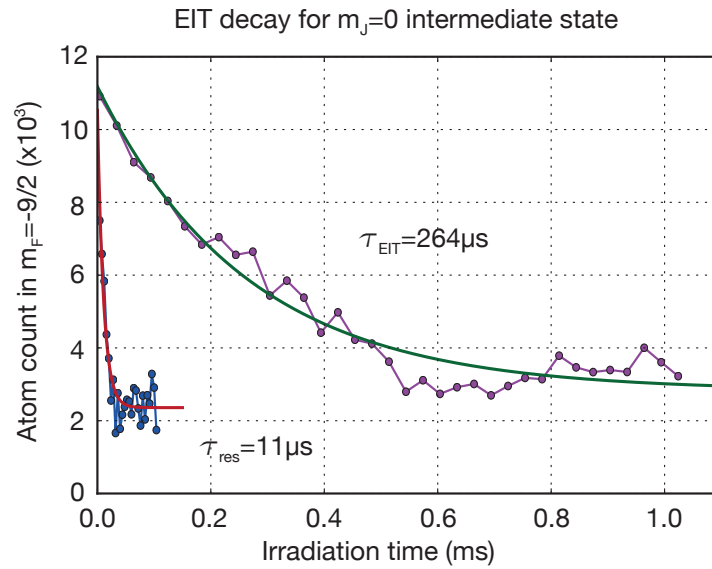


Figure 4.21 – Resonant decay of Feshbach molecules induced by the pump laser with and without the Stokes laser present. Both Raman lasers are adjusted to single photon resonance $\Delta_P = \Delta_S = 0$. In the EIT configuration the on resonant decay rate is reduced by a factor of $\simeq 26$.

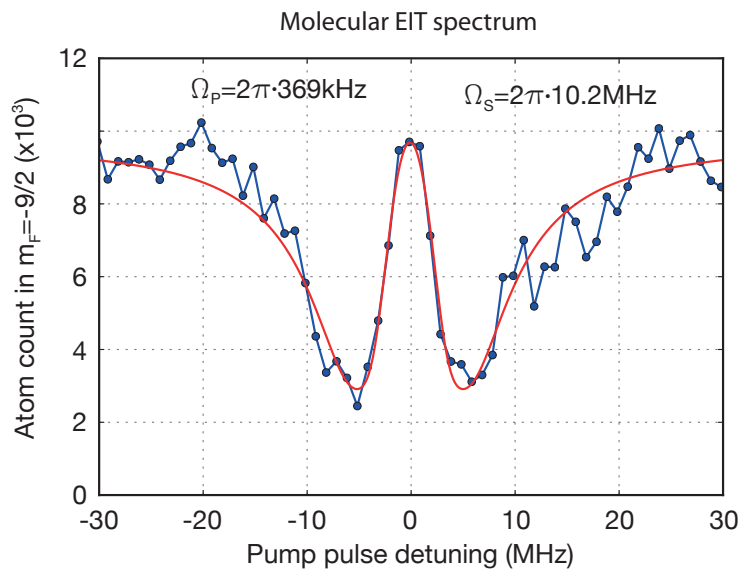


Figure 4.22 – High resolution EIT spectrum that is used for a two parameter least square fit of equation 4.51 in order to estimate the values of Ω_P and Ω_S .

fitting procedure are listed in table 4.10.

We obtain reasonable and self-consistent values for Ω_P , Ω_S and Γ . The phenomenological decoherence rate Γ_{eff} however is much larger than one would expect for external sources of decoherence in a standard laboratory environment. Since STIRAP and EIT both depend on the coherent nature of the darkstate, this large phenomenological decoherence rate could pose a significant limitation on STIRAP efficiency. Moreover, it does not allow us to measure the hyperfine structure of the groundstate in EIT spectroscopy. Note that EIT lifetime cannot be used to draw quantitative conclusions on STIRAP performance. All

Parameter	Value
τ_{res}	$11\mu s$
τ_{EIT}	$264\mu s$
Ω_P	$2\pi \cdot 369\text{MHz}$
Ω_S	$2\pi \cdot 10.2\text{MHz}$
Γ	$2\pi \cdot 9.4\text{MHz}$
Γ_{eff}	$2\pi \cdot 461\text{kHz}$

Table 4.10 – Experimental parameters of the chosen molecular STIRAP scheme determined by EIT spectroscopy. The large value of Γ_{eff} signals a fundamental problem either with the laser system or the molecular level structure.

attempts to perform STIRAP with the current Raman laser setup have been futile. As a first step in diagnostics we could identify the phase noise pedestal of the 652nm Raman laser system as the dominating cause for EIT decay. To quantify this observation we measured the EIT lifetime τ_{EIT} as function of the noise power fraction outside of the center region of the phase locked beat signal. We then change the noise power fraction by adjusting the feedback gain of the analog control electronics and observe (as in Fig. 4.21) how EIT lifetime is affected.

Power spectra of the phase locked beat signal of the pump laser system

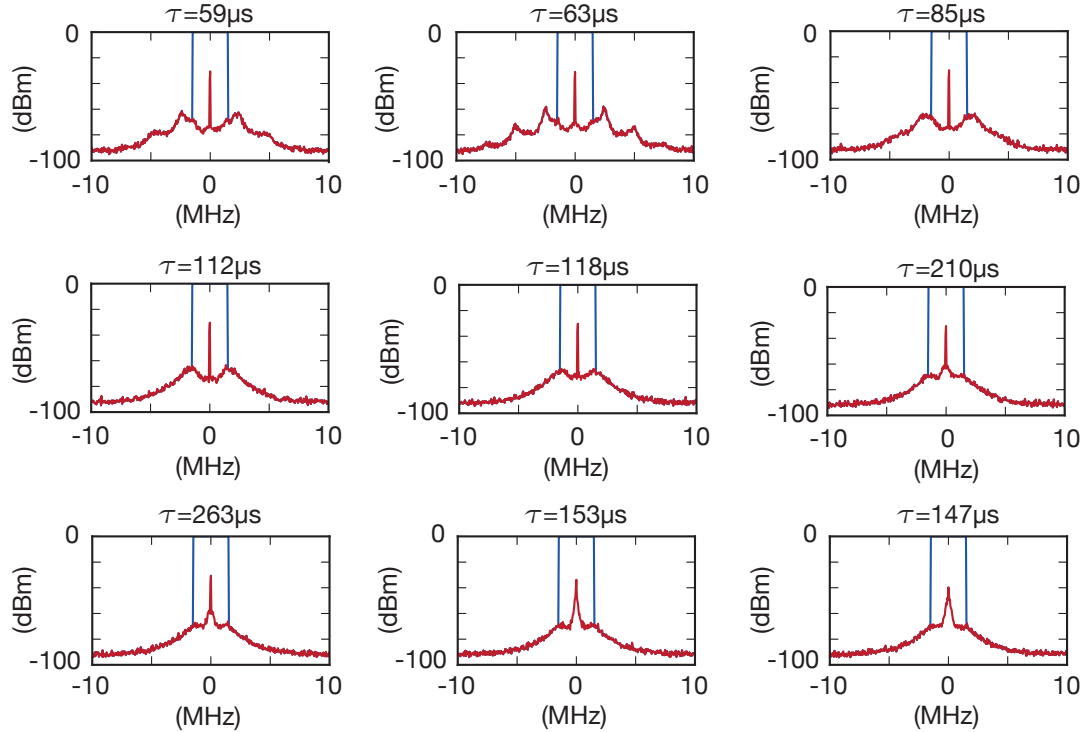


Figure 4.23 – Power spectra of the beat signal between the master and the slave laser of the pump laser system (see Fig. 4.8). For each power spectrum the corresponding EIT lifetime τ_{EIT} is indicated. The blue lines indicate the central region of the power spectrum that is excluded for calculation the noise power fraction.

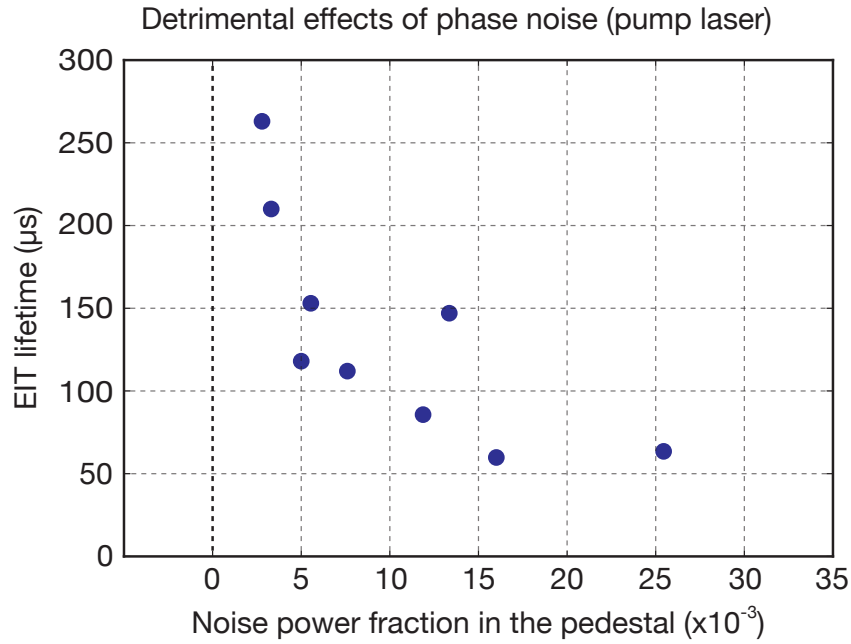


Figure 4.24 – Scatter plot of the results from the series of measurements listed in Fig. 4.23. The EIT lifetime significantly increases for noise power fraction below 0.5%. Unfortunately conventional diode lasers do not allow to decrease the noise pedestal much further.

The result of this measurement is shown in Fig. 4.23 and summarized in Fig. 4.24. With this measurement we have a clear indication that EIT lifetime is currently limited by the phase noise performance of the pump laser system. Since typical semiconductor lasers always exhibit a significant phase noise pedestal, we need to replace the pump laser system by a different technology if we want to further investigate whether STIRAP via the $d^3\Pi/D^1\Pi$ complex is possible. During writing this report we managed to directly lock a Coherent 899 Dye laser to the high finesse cavity via the PDH technique that replaces the 652nm pump laser system. Although we have seen some first indication that this indeed decreased the effective decoherence rate for EIT as compared to the previous diode laser system, we do not have a final result.

Since the current laser system excludes me from doing further experimental diagnostics I numerically simulate the STIRAP process for the currently chosen intermediate level to get more insight into the effects of the non-resolved hyperfine structure of the intermediate level.

4.6 Numerical model for groundstate transfer via the $d^3\Pi/D^1\Pi$ complex

The RWA (rotating wave approximation) treatment of a coherently coupled, dissipative three-level lambda system can be found in [98]. The main result is, that regardless of the exact values of Ω_S , Ω_p and Γ for zero detuning $\Delta_S = 0$ and in Raman resonance $\Delta_p = \Delta_S$ a dark-state always exist, that can be used for dissipation free coherent population transfer

via STIRAP.

This situation changes for multiple quasi-degenerate intermediate states and non degenerate final states. The problem of multiple intermediate states for STIRAP was analyzed in detail in a series of publications by the Bergmann group [94, 95, 96, 97]. Their main result can be summarized as follows: For a dissipation free multilevel lambda system successful STIRAP is not guaranteed but relies on fine-tuning of the experimental parameters. Decay of the intermediate states will always be detrimental and when spontaneous emission becomes significant can ruin STIRAP efficiency. Note also that, all groups that were successful in preparing ground state molecules via STIRAP were using hyperfine state resolved three-level systems. Due to the non-resolved hyperfine structure it is impossible to single out a true three-level system for our choice of intermediate state and the question whether STIRAP could work efficiently is far from trivial to answer. In the final two sections of this report I therefore apply the RWA approach of Shore and Bergmann [98] to the near-degenerate multi-level lambda system that is formed by the Feshbach molecule, the rovibronic groundstate and the non-resolved hyperfine manifold of the $|d^3\Pi_{\Omega=1} \nu = 5J = 1\rangle$ level.

4.6.1 Hyperfine structure of the rovibronic groundstate

To identify a suitable STIRAP pathway to the $|X^1\Sigma \nu = 0J = 0\rangle$ state not only the hyperfine structure/state composition of the Feshbach molecule and the $d^3\Pi/D^1\Pi$ intermediate state has to be considered (see table 4.3 and section 4.4.2) but also the hyperfine structure of the target $|X^1\Sigma \nu = 0J = 0\rangle$ state itself. Since the $|X^1\Sigma \nu = 0J = 0\rangle$ state is the electronic groundstate $\Lambda = 0$, is of pure spin-singlet character $\Sigma = 0$ and is non-rotating ($J = 0$), the hyperfine structure is just given by the interaction between the electric and magnetic moments of the nuclei alone. The dominant contribution is due to the scalar spin-spin interaction [109]:

$$H_{Sc} = c_4 \cdot \mathbf{I}_K \cdot \mathbf{I}_{Na} \quad (4.63)$$

Note that this interaction is not caused by direct magnetic dipole forces between the nuclei but is mediated by the electron distribution of the $X^1\Sigma$ state [109]. Since we produce the initial state for STIRAP (i.e. the Feshbach molecule) by RF association at a magnetic field of 85.5G, we also have to take into account the Zeeman interaction between the external field and the magnetic moments $|\mu_{K/Na}| = gI_{K/Na} \cdot m_{K/Na} \cdot \mu_B$ of both nuclei. The total Hamiltonian that governs the groundstate hyperfine structure is the given by:

$$H_{HF} = c_4 \cdot \mathbf{I}_K \cdot \mathbf{I}_{Na} + \mu_B(gI_K \mathbf{I}_K + gI_{Na} \mathbf{I}_{Na}) \cdot \mathbf{B} \quad (4.64)$$

Here $\mu_B = h \cdot 1.3996 \cdot \text{MHz/G}$ is the Bohr magneton, $gI_{K/Na}$ are the nuclear g-factors for each species [51, 47] and \mathbf{I} the nuclear spin operators. Since at a magnetic field of 85.5G the scalar spin-spin coupling constant $c_4 \simeq -466\text{Hz}$ [21] is smaller than 1% of the Zeeman interaction, we can treat H_{Sc} as a perturbation (Paschen-Back regime). The energy eigenvalues E_{HF} of H_{HF} are then approximately given by

$$E_{HF} = \mu_B(gI_{Na}m_{Na} + gI_Km_K)B + c_4m_Km_{Na} \cdot \quad (4.65)$$

STIRAP starting from Feshbach molecules with projection $m_F = -7/2$ along the magnetic field direction of the total angular momentum $\mathbf{F} = \mathbf{J} + \mathbf{I}_{\text{Na}} + \mathbf{I}_{\text{K}}$ can only populate groundstate hyperfine components with $m_F = m_K + m_{\text{Na}} = -11/2, -9/2, -7/2, -3/2$ - in a two photon transition the angular momentum of the molecule can only change by $2h$ at most. Fig. 4.25 lists the energy eigenvalues for all groundstate hyperfine components. The red dots indicate the components that are accessible by STIRAP. We find that the expected energy splitting between two adjacent hyperfine components with the same value of m_F is on the order of $\sim 100\text{kHz}$.

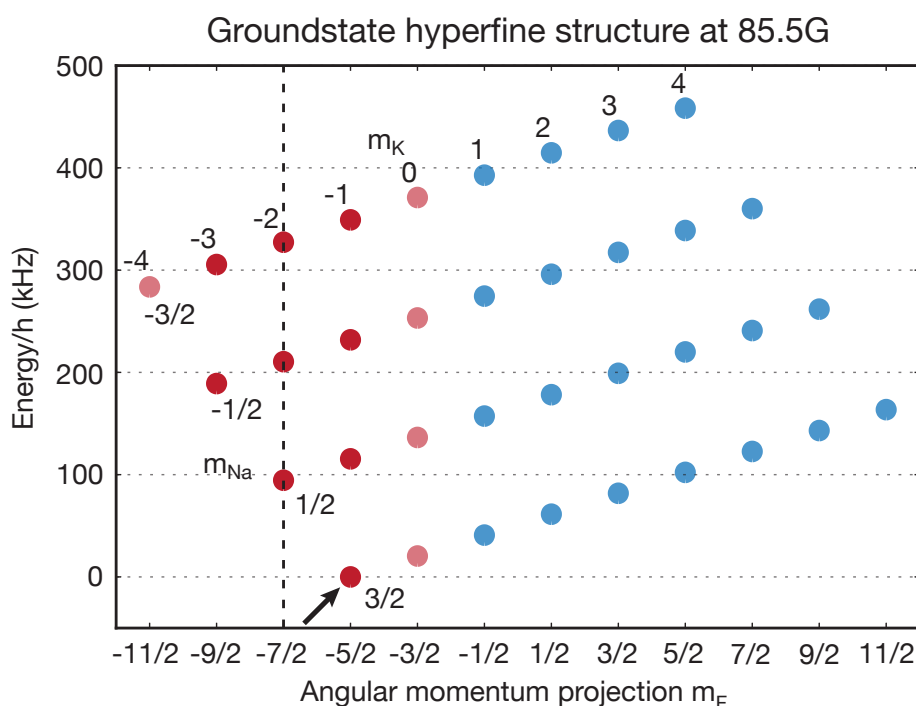


Figure 4.25 – Hyperfine structure of the rovibronic groundstate at 85.5G obtained by equation 4.65. The red dots indicate hyperfine components that can be accessed by STIRAP starting from Feshbach molecules with $m_F = -7/2$ (dashed black line). The light red dots indicate hyperfine components that are not present in the Feshbach molecule and therefore can only be accessed via mixing of hyperfine states in the excited state. The expected energy splitting between two adjacent hyperfine components with the same value of m_F is on the order of $\sim 100\text{kHz}$. The hyperfine component with total lowest energy is indicated by the black arrow. The value for the scalar nuclear spin-spin interaction parameter c_4 was taken from [21].

The absolute groundstate $|X^1\Sigma v = 0J = 0\rangle \otimes |m_K = -4m_{\text{Na}} = 3/2\rangle$ (the state of lowest electronic, vibrational, rotational and hyperfine energy) of the $^{23}\text{Na}^{40}\text{K}$ molecule at a magnetic field of 85.5G is indicated by the black arrow. Since spin changing two-body collisions are suppressed for this hyperfine component at ultra-cold temperatures [19], it is the desired target state for groundstate transfer. Using the results of the asymptotic bound state model and the analysis of the intermediate hyperfine structure (see table 4.7 - 4.9) we are now in the position to identify two different two-photon pathways to the desired target state.

Two photon pathways to the hyperfine groundstate of the $|X^1\Sigma^v = 0J = 0\rangle$ state

Since the excited state hyperfine structure is not resolved for the $d^3\Pi/D^1\Pi$ complex, the projection of the total angular momentum excluding nuclear spin m_J stays a good quantum number for describing possible two-photon transitions to the rovibronic groundstate. The Feshbach molecule is expressed as a superposition of spin basis states $|Jm_Jm_Km_{Na}\rangle$ i.e.

$$|FB\rangle = \sum_{\alpha} \alpha |Jm_Jm_Km_{Na}\rangle \quad (4.66)$$

with ABM coefficients α and quantum numbers J , m_J , m_K and m_{Na} given in table 4.3. The accessible hyperfine components of the intermediate state are as well expressed in the spin basis:

$$|Jm_Jm_Km_{Na}\rangle \text{ with } J = 1, m_J = -1, 0, 1, m_K = -4, \dots, 4 \text{ and } m_{Na} = -1.5, \dots, 1.5 \quad (4.67)$$

The final state of STIRAP i.e. a single hyperfine component of the $|X^1\Sigma^v = 0J = 0\rangle$ state is also expressed in the nuclear spin decoupled basis as $|J = 0m_J = 0m_Km_{Na}\rangle$. Since STIRAP involves two electric dipole transitions of the form

$$\langle J'm'_Jm'_Km'_{Na} | \hat{d} \cdot \mathbf{E}_{P/S}(t) | Jm_Jm_Km_{Na} \rangle = \langle J'm'_J | \hat{d} \cdot \mathbf{E}_{P/S}(t) | Jm_J \rangle \cdot \langle m'_Km'_{Na} | m_Km_{Na} \rangle, \quad (4.68)$$

the projections of the nuclear spins are conserved in a two-photon transition. In the last equation \hat{d} is the electric dipole operator and $\mathbf{E}_{P/S}$ the electric field vector of the pump or Stokes Raman laser. Since the Feshbach molecule is a superposition of ABM basis states, multiple hyperfine components of the $|X^1\Sigma^v = 0J = 0\rangle$ state are simultaneously addressed in STIRAP for a given combination of Raman laser polarizations. Table 4.11 list all possible combinations of Raman laser polarizations that allow to couple the rovibronic groundstate (with $J = 0, m_J = 0$) to the Feshbach molecule via a given m_J component of the $J = 1, \Omega = 1$ Zeeman triplet. Transitions that allow to access the hyperfine groundstate $|J = 0m_J = 0m_K = -4m_{Na} = -3/2\rangle$ are highlighted in bold face.

$ FB\rangle$	$ J = 1, \Omega = 1\rangle$	Pump	Stokes
$m_J = 0$	$m_J = -1$	σ_-	σ_+
$m_J = -1$	$m_J = -1$	Π	σ_+
$m_J = 1$	$m_J = 0$	σ_-	Π
$m_J = 0$	$m_J = 0$	Π	Π
$m_J = -1$	$m_J = 0$	σ_+	Π
$m_J = 1$	$m_J = 1$	Π	σ_-
$m_J = 0$	$m_J = 1$	σ_+	σ_-

Table 4.11 – Possible combinations of Raman laser polarization and m_J component of the $J = 1, \Omega = 1$ Zeeman triplet that exhibit a non-vanishing two-photon coupling from the Feshbach molecule to the rovibronic groundstate $|X^1\Sigma^v = 0J = 0m_J = 0\rangle$. Transitions that allow to access the hyperfine groundstate $|J = 0m_J = 0m_K = -4m_{Na} = -3/2\rangle$ are highlighted in bold face.

Fig. 4.26 and 4.27 illustrate the only two STIRAP configurations that allow to access the $|J = 0, m_J = 0, m_K = -4, m_{Na} = -3/2\rangle$ hyperfine groundstate. Both are near-resonant multilevel STIRAP schemes. The pump laser couples four different ABM basis states with amplitudes α_i to the either the $m_J = -1$ or the $m_J = 0$ Zeeman component of the $|d^3\Pi_{\Omega=1}, \nu = 5, J = 1\rangle$ intermediate level. The relevant Zeeman component ($m_J = 0$ or $m_J = -1$) of the intermediate level is then coupled via the Stokes laser to the hyperfine manifold (see Fig. 4.25) of the rovibronic groundstate. For both combinations we therefore get four near degenerate STIRAP paths to four different groundstate hyperfine components that are offset in frequency by the groundstate hyperfine splitting.

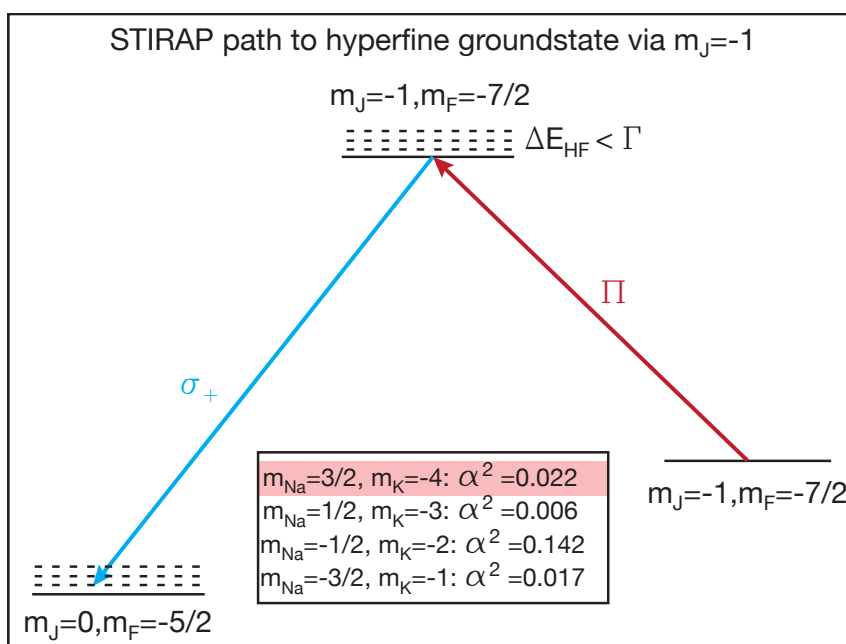


Figure 4.26 – Possible STIRAP pathway to the hyperfine groundstate of $|X^1\Sigma, \nu = 0, J = 0\rangle$ using the $m_J = -1$ component of the $\Omega = 1, J = 1$ Zeeman triplet. Four different hyperfine components contribute. The transition to the desired $|m_K = -4, m_{Na} = 3/2\rangle$ component is highlighted in light red. The values for the relative transition strength α^2 are obtained from the amplitudes of the ABM basis states of the Feshbach molecule at a magnetic field of 85.5G (see table 4.7).

With these considerations in mind it is now possible to setup a realistic RWA Hamiltonian (see section 4.5.1 above) that can be used to simulate the effect of multiple near-degenerate two-photon transitions on STIRAP success. To ensure that the simulation is as realistic as possible and does give an upper bound on STIRAP efficiency, the following assumptions are made:

1. The initial state for STIRAP is the Feshbach molecule at 85.5G. It can be expressed as a superposition of ABM basis states with amplitudes α_i given in table 4.3.
2. The Feshbach molecule is assumed to have an infinite lifetime.
3. The natural linewidth of the intermediate state is given by $\Gamma \simeq 2\pi \cdot 10\text{MHz}$
4. The hyperfine splitting δ_p for the different components in the the $|d^3\Pi_{\Omega=1}, \nu = 5, J = 1\rangle$ intermediate level is assumed to be $\delta_p \simeq 0.1 \cdot \Gamma$.

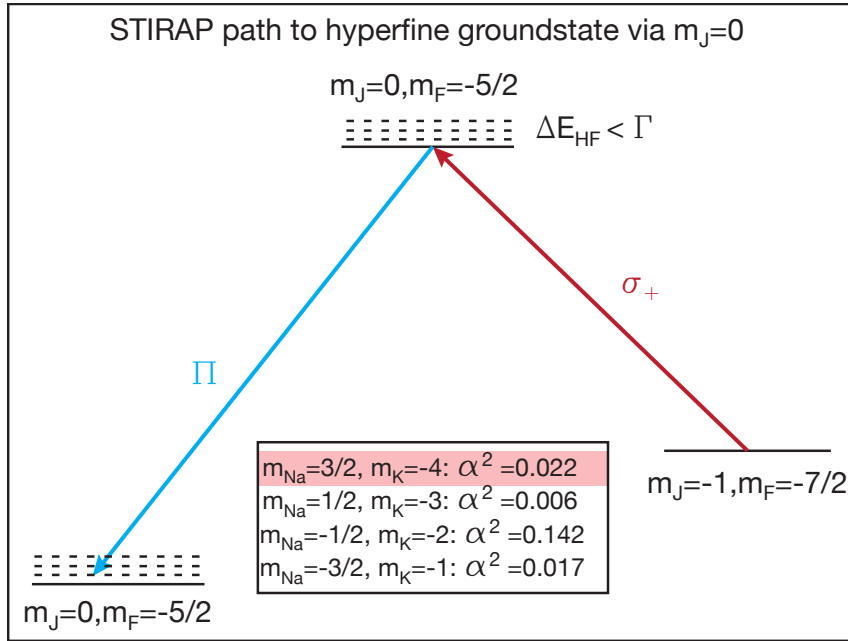


Figure 4.27 – Possible STIRAP pathway to the hyperfine groundstate of $|X^1\Sigma\nu = 0J = 0\rangle$ using the $m_J = 0$ component of the $\Omega = 1, J = 1$ Zeeman triplet. Four different hyperfine components contribute. The transition to the desired $|m_K = -4m_{Na} = 3/2\rangle$ component is highlighted in light red. The values for the relative transition strength α^2 are obtained from the amplitudes of the ABM basis states of the Feshbach molecule at a magnetic field of 85.5G (see table 4.8).

5. The hyperfine splitting δ_S between the groundstate components (see Fig. 4.25) is calculated with equation 4.65.
6. Peak Rabi frequencies are assumed to be $\Omega_P = \Omega_S = 0.1 \cdot \Gamma$. For the different pump transitions to the various hyperfine components Ω_P is multiplied by the relative line strength of the transition $s_i = \frac{|\alpha_i|}{\sum_j |\alpha_j|}$.
7. Raman laser polarizations are assumed to be perfect.
8. Laser frequency noise and phase noise is not included as well as external sources of decoherence.

The RWA hamiltonian is then given by the 9x9 matrix of equation 4.69:

$$\begin{pmatrix}
 2\Delta & s_1\Omega_P(t) & s_2\Omega_P(t) & s_3\Omega_P(t) & s_4\Omega_P(t) & 0 & 0 & 0 & 0 \\
 s_1\Omega_P(t) & -i\Gamma - 6\delta_P & 0 & 0 & 0 & \Omega_S(t) & 0 & 0 & 0 \\
 s_2\Omega_P(t) & 0 & -i\Gamma - 4\delta_P & 0 & 0 & 0 & \Omega_S(t) & 0 & 0 \\
 s_3\Omega_P(t) & 0 & 0 & -i\Gamma - 2\delta_P & 0 & 0 & 0 & \Omega_S(t) & 0 \\
 s_4\Omega_P(t) & 0 & 0 & 0 & -i\Gamma & 0 & 0 & 0 & \Omega_S(t) \\
 0 & \Omega_S(t) & 0 & 0 & 0 & 2\Delta - 2\delta_{S3} & 0 & 0 & 0 \\
 0 & 0 & \Omega_S(t) & 0 & 0 & 0 & 2\Delta - 2\delta_{S2} & 0 & 0 \\
 0 & 0 & 0 & \Omega_S(t) & 0 & 0 & 0 & 2\Delta - 2\delta_{S1} & 0 \\
 0 & 0 & 0 & 0 & \Omega_S(t) & 0 & 0 & 0 & 2\Delta
 \end{pmatrix}
 \quad (4.69)$$

In order to investigate STIRAP efficiency in a situation that is fundamentally different from the usual three level case, we solve the RWA evolution equation 4.46 for the matrix 4.69 and try to find parameter were STIRAP transfers population to the desired target state. Since the the values for Γ , s_i , δ_P and δ_{Si} are fixed and since decreasing the peak Rabi frequency does not enhance STIRAP performance the only parameter that seems sensible to vary is the one-photon detuning Δ . As a starting point we investigate STIRAP in one photon resonance $\Delta = 0$ using the pulse sequence of equation 4.57 and a STIRAP pulse area of $\Omega_0 \cdot \tau = 200$ that should allow for efficient adiabatic transfer in the corresponding three level scheme (see Fig. 4.15) with otherwise equal parameters. Note that the exact order of energy levels for the excited state can not be determined without knowing the hyperfine coupling constants of the excited state. The temporal evolution of the Feshbach molecule and the population in the $|m_K = -4m_{Na} = 3/2\rangle$ component of the rovibronic groundstate is shown in Fig. 4.28. Fig. 4.29 shows how the situation changes when Raman lasers are resonant not with the $|m_K = -4m_{Na} = 3/2\rangle$ component but with the component of strongest weight i.e. $|m_K = -2m_{Na} = -1/2\rangle$. For both configurations STIRAP efficiency is below 25%.

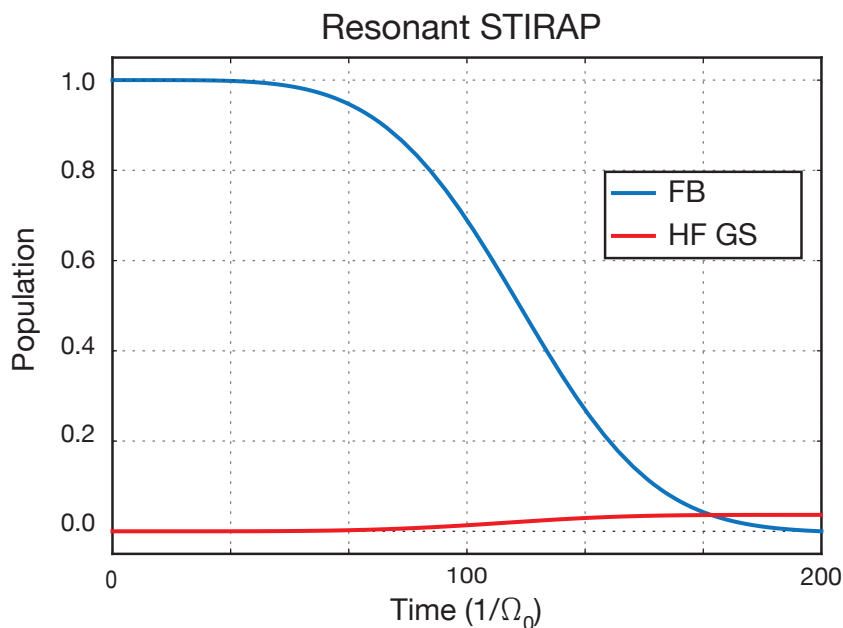


Figure 4.28 – Temporal evolution of the populations for the Feshbach molecule and the target hyperfine component ($|m_K = -4m_{Na} = 3/2\rangle$) in the rovibronic groundstate during resonant ($\Delta = \Gamma$) STIRAP obtained by numerical integration of the RWA evolution equation 4.46 using the Hamiltonian of equation 4.69.

I then tested whether a detuned ($\Delta = 2\Gamma$) configuration as proposed in [94, 96] improves STIRAP efficiency. Fig. 4.30 and 4.31 show the result. For both final states STIRAP efficiency increases compared to the resonant configuration. However only the $|m_K = -2m_{Na} = -1/2\rangle$ hyperfine component can be populated with an efficiency of $\simeq 65\%$. Note that for detection of groundstate molecules the STIRAP process has to be reversed to allow for direct absorption imaging of Feshbach molecules. Detection

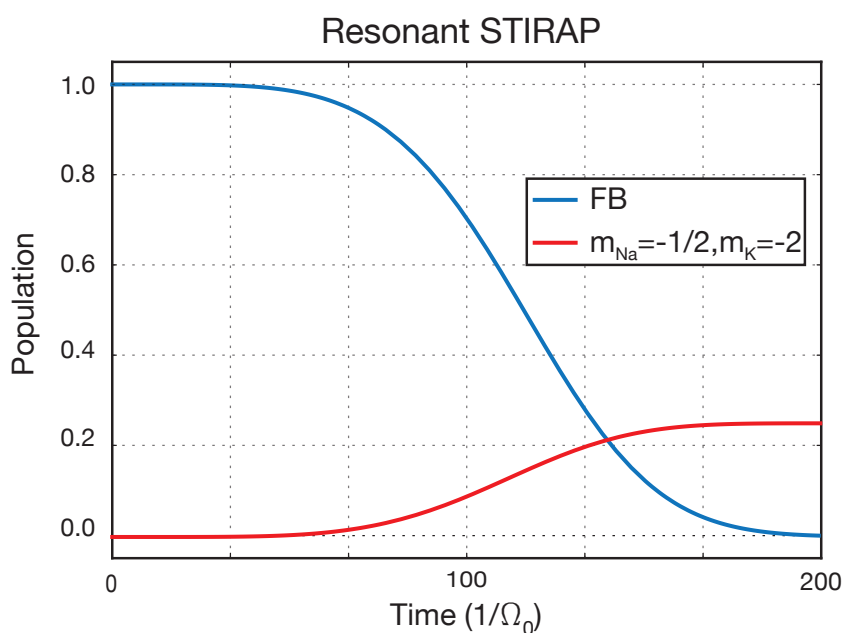


Figure 4.29 – Temporal evolution of the populations for the Feshbach molecule and the hyperfine component with largest spectroscopic weight ($|m_K = -2m_{Na} = -1/2\rangle$) in the rovibronic groundstate during resonant ($\Delta = \Gamma$) STIRAP obtained by numerical integration of the RWA evolution equation 4.46 using the Hamiltonian of equation 4.69.

efficiency therefore would be decreased to 42%. Moreover the required pulse duration for STIRAP has to be increased by a factor of ≥ 7.5 in order to fulfill the adiabaticity criterium. The increased STIRAP pulse duration increases the susceptibility to external sources of decoherence (e.g. ambient magnetic field noise) which are completely neglected in the present analysis.

The main results from the numerical simulation of the multilevel $d^3\Pi/D^1\Pi$ STIRAP scheme can be summarized as follows:

1. A dark state i.e. a state with no amplitude of the decaying intermediate levels does not exist.
2. Therefore STIRAP could only work efficiently in a detuned configuration, where the single photon detuning in Raman resonance is larger than the natural linewidth of the excited state (i.e. $\Delta > \Gamma$).
3. Even in the detuned configuration it is only possible to transfer significant population ($> 50\%$) to the hyperfine component with strongest spectroscopic weight.
4. A STIRAP efficiency above 60% requires a pulse duration that is $> 200\mu s$ - a time scale that is 10 – 50 times longer than all successful groundstate transfers for ultra-cold alkali-alkali molecule [21, 18, 20, 19, 15].
5. The effects of imperfect polarization, external decoherence and laser phases noise, that obviously (compare Fig. 4.24) has a significant influence on the coherence

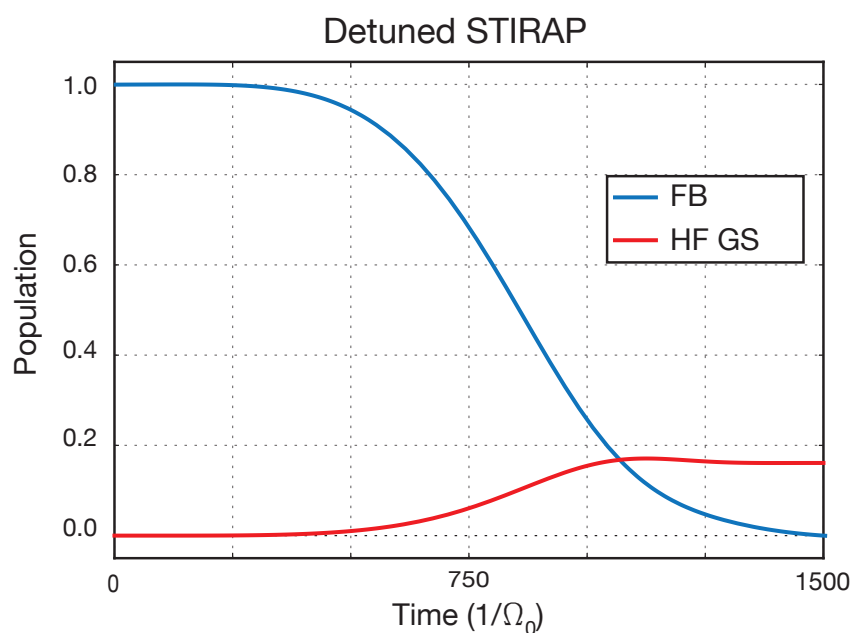


Figure 4.30 – Temporal evolution of the populations for the Feshbach molecule and the target hyperfine component ($|m_K = -4m_{Na} = 3/2\rangle$) in the rovibronic groundstate during resonant ($\Delta = 2 \cdot \Gamma$) STIRAP obtained by numerical integration of the RWA evolution equation 4.46 using the Hamiltonian of equation 4.69.

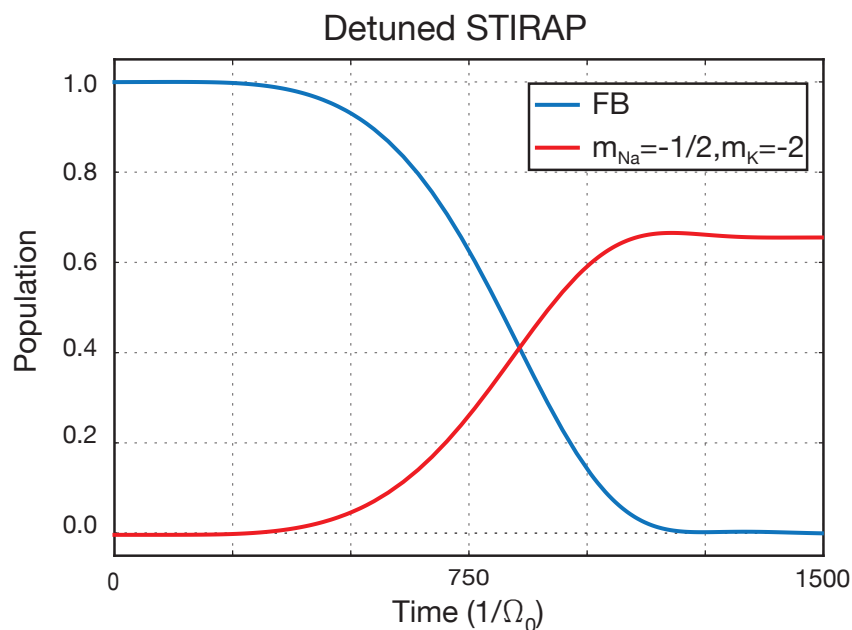


Figure 4.31 – Temporal evolution of the populations for the Feshbach molecule and the hyperfine component with largest spectroscopic weight ($|m_K = -2m_{Na} = -1/2\rangle$) in the rovibronic groundstate during detuned ($\Delta = 2 \cdot \Gamma$) STIRAP obtained by numerical integration of the RWA evolution equation 4.46 using the Hamiltonian of equation 4.69.

properties of the darkstate are neglected in the presented model.

For these reasons I am highly skeptical whether efficient groundstate transfer of $^{23}\text{Na}^{40}\text{K}$

molecules can be established via an intermediate level the $d^3\Pi/D^1\Pi$ complex.

4.6.2 Conclusions

Due to the non-resolved hyperfine structure in the $d^3\Pi/D^1\Pi$ complex it will be not possible to single out a true three-level system for STIRAP. Therefore the effects of multiple non-resolved intermediate levels have to be considered. Even for a dissipation-free multilevel lambda system successful STIRAP is not guaranteed but relies on fine tuning of the experimental parameters [94, 95, 96, 97]. Decay of the intermediate states will be always detrimental for STIRAP success. For our choice of intermediate state the decay rate of the intermediate states $\Gamma > 2\pi \cdot 10\text{MHz}$ is ten times larger than the Rabi frequency $\Omega_0 = \sqrt{\Omega_S^2 + \Omega_P^2}$. So even neglecting all possible technical problems (see Fig. 4.24) ground-state transfer via the current intermediate state could well be impossible and will certainly not be optimal.

With regard to our ambitious primary objective - the observation of strongly correlated many-body effects in a dipolar quantum gas of molecules - STIRAP efficiency should be as high as possible in order to conserve phase-space density and to allow for efficient molecule detection. We should be therefore prepared to change the STIRAP scheme to an intermediate state manifold that exhibits Fermi contact interaction and allows for hyperfine state resolved STIRAP. The scheme characterized in [86] and successfully used in [21] would be the natural choice. For the laser system, we should aim for technologies with intrinsically narrow linewidth and enough output power that allow for Rabi frequencies that are at least $\geq 0.3 \cdot \Gamma$ (compare the parameters given in [21]).

Summary and outlook

During the course of this PhD project a novel experimental setup was constructed that should allow to study dipolar interacting quantum many-body systems of ultracold $^{23}\text{Na}^{40}\text{K}$ molecules. Among all possible fermionic alkali-alkali combinations that are chemically stable in a two-body reaction the $^{23}\text{Na}^{40}\text{K}$ molecule offers the largest intrinsic dipole moment. In the current configuration this experiment creates deeply degenerate Bose-Fermi mixtures of the constituent atoms. Full hyperfine state control for both elements and precise magnetic field control allow us to address various inter-species Feshbach resonances. In the vicinity of a particular Feshbach resonance weakly bound $^{23}\text{Na}^{40}\text{K}$ halo dimers are created by radio frequency association. These molecules serve as a potential starting point for the adiabatic preparation of rovibronic groundstate molecules via the STIRAP technique. The implementation of STIRAP requires to identify a suitable electronically excited molecular level, that facilitates significant two-photon Raman coupling between the halo dimer and the rovibronic groundstate. To this end we have performed high resolution molecular spectroscopy and have identified a near-resonant pair of vibrational levels in $d^3\Pi/D^1\Pi$ electronic state complex. Molecular spin-orbit coupling results in the required mixing of spin singlet and spin triplet levels. By using a narrow linewidth Raman laser system we have measured the binding energy of the rovibronic groundstate in coherent dark-state spectroscopy. In addition EIT experiments in the molecular three-level system formed by the halo dimer, the $d^3\Pi/D^1\Pi$ intermediate state and the rovibronic groundstate allow us to estimate the Rabi frequencies of both transitions. We observe a very large effective dark state decoherence rate that indicates a fundamental shortcoming of the current STIRAP scheme and prevents us from achieving ground state transfer. We have identified the phase noise performance of the short cavity semiconductor lasers that are used in the Raman laser system as the current limiting parameter. Therefore we will try to replace the semiconductor lasers with intrinsically narrow laser sources (dye lasers, titanium sapphire lasers) in future experiments. Unfortunately the absence of Fermi contact interaction for the intermediate level results in a non-resolved molecular hyperfine structure resulting in a dissipative multi-level STIRAP scheme. In this configuration STIRAP will only result in efficient groundstate transfer for a single photon detuning that is larger than the natural linewidth Γ of the intermediate state. With the current Rabi frequencies limited to well below 10% of Γ STIRAP will fail in the detuned configuration even in absence of phase noise and all other sources of decoherence.

5.1 Outlook

Recently $^{23}\text{Na}^{40}\text{K}$ groundstate molecules have been prepared at MIT by using a different STIRAP scheme (resolved hyperfine structure, no semiconductor lasers) relying on a spin-orbit coupled level pair in the $c^3\Sigma/B^1\Pi$ complex. The natural solution would be to also use this STIRAP scheme for groundstate transfer. However, changing the current STIRAP scheme constitutes a major investment in terms of preparation time and technical equipment. We therefore intend to investigate whether the current STIRAP scheme could indeed work efficiently in a detuned configuration. To this end we decided not to target the absolute hyperfine groundstate but instead aim for the hyperfine state that has the largest weight in the Feshbach molecule. In addition we have replaced the semiconductor lasers of one part of the Raman laser system by a dye laser, which features much less phase noise and increases the Rabi frequency for STIRAP to $\simeq 0.1\Gamma$. A numerical integration of the optical master equations for this STIRAP scheme results in $> 80\%$ STIRAP efficiency for a detuning of $\simeq 3\Gamma$ and a STIRAP pulse duration of $\simeq 250\mu\text{s}$. This promising prediction will be tested in near future experiments.

Bibliography

- [1] C.J. Pethick and H. Smith. *Bose-Einstein Condensation in Dilute Gases*. Cambridge University Press, 2001 (cit. on pp. 1, 22).
- [2] A.J. Leggett. *Quantum Liquids - Bose Condensation and Cooper Pairing in Condensed-Matter Systems*. 2006 (cit. on pp. 1, 10, 11).
- [3] Wilhelm Zwerger. *The BCS-BEC Crossover and the Unitary Fermi Gas*. 2012 (cit. on p. 1).
- [4] Markus Greiner, Olaf Mandel, Tilman Esslinger, Theodor W. Haensch, and Immanuel Bloch. “Quantum phase transition from a superfluid to a Mott insulator in a gas of ultracold atoms”. In: *Nature* 415 (2002), pp. 39–40 (cit. on p. 1).
- [5] Immanuel Bloch, Jean Dalibard, and Wilhelm Zwerger. “Many-body physics with ultracold gases”. In: *Rev. Mod. Phys.* 80 (3 2008), pp. 885–964 (cit. on pp. 1, 2).
- [6] Jean Dalibard, Fabrice Gerbier, Gediminas Juzelinis, and Patrik Oehberg. “Artificial gauge potentials for neutral atoms”. In: *Rev. Mod. Phys.* 83 (4 2011), pp. 1523–1543 (cit. on p. 1).
- [7] Jean Dalibard. “Introduction to the physics of artificial gauge fields”. In: *arXiv:1504.05520* (2015) (cit. on p. 1).
- [8] Waseem S. Bakr, Jonathon I. Gillen, Amy Peng, Simon Foelling, and Markus Greiner. “A quantum gas microscope for detecting single atoms in a Hubbard-regime optical lattice”. In: *Nature* 462 (2009), pp. 74–77 (cit. on p. 1).
- [9] Jacob F. Sherson, Christof Weitenberg, Manuel Endres, Marc Cheneau, Immanuel Bloch, and Stefan Kuhr. “Single-atom-resolved fluorescence imaging of an atomic Mott insulator”. In: *Nature* 467 (2010), pp. 68–72 (cit. on p. 1).
- [10] Patrick A. Lee, Naoto Nagaosa, and Xiao-Gang Wen. “Doping a Mott insulator: Physics of high-temperature superconductivity”. In: *Rev. Mod. Phys.* 78 (1 2006), pp. 17–85 (cit. on pp. 2, 14).
- [11] L.D. Carr, D. DeMille, KREMS R. V., and J. Ye. “Cold and ultracold molecules: science, technology and applications”. In: *New Journal of Physics* (11 2009) (cit. on p. 2).
- [12] Lev Davidovich Landau and Evgenii Mikhailovich Lifshits. *Quantum Mechanics (non-relativistic Theory)*. 1958 (cit. on pp. 2, 58).
- [13] Thorsten Koehler, Krzysztof Goral, and Paul S. Julienne. “Production of cold molecules via magnetically tunable Feshbach resonances”. In: *Rev. Mod. Phys.* 78 (4 2006), pp. 1311–1361 (cit. on pp. 2, 86, 87).

- [14] K. Bergmann, H. Theuer, and B. W. Shore. “Coherent population transfer among quantum states of atoms and molecules”. In: *Rev. Mod. Phys.* 70 (3 1998), pp. 1003–1025 (cit. on pp. 2, 93, 97).
- [15] Johann G. Danzl, Elmar Haller, Mattias Gustavsson, Manfred J. Mark, Russell Hart, Nadia Bouloufa, Olivier Dulieu, Helmut Ritsch, and Hanns-Christoph Naegerl. “Quantum Gas of Deeply Bound Ground State Molecules”. In: *Science* 321.5892 (2008), pp. 1062–1066. eprint: <http://www.sciencemag.org/content/321/5892/1062.full.pdf> (cit. on pp. 2, 113).
- [16] Simon Stellmer, Benjamin Pasquiou, Rudolf Grimm, and Florian Schreck. “Creation of Ultracold Sr_2 Molecules in the Electronic Ground State”. In: *Phys. Rev. Lett.* 109 (11 2012), p. 115302 (cit. on p. 2).
- [17] G. Reinaudi, C. B. Osborn, M. McDonald, S. Kotochigova, and T. Zelevinsky. “Optical Production of Stable Ultracold $^{88}\text{Sr}_2$ Molecules”. In: *Phys. Rev. Lett.* 109 (11 2012), p. 115303 (cit. on p. 2).
- [18] K.-K. Ni, S. Ospelkaus, M. H. G. de Miranda, A. Peer, B. Neyenhuis, J. J. Zirbel, S. Kotochigova, P. S. Julienne, D. S. Jin, and J. Ye. “A High Phase-Space-Density Gas of Polar Molecules”. In: *Science* 322.5899 (2008), pp. 231–235. eprint: <http://www.sciencemag.org/content/322/5899/231.full.pdf> (cit. on pp. 2, 18, 113).
- [19] Tetsu Takekoshi, Lukas Reichsoellner, Andreas Schindewolf, Jeremy M. Hutson, C. Ruth Le Sueur, Olivier Dulieu, Francesca Ferlaino, Rudolf Grimm, and Hanns-Christoph Naegerl. “Ultracold Dense Samples of Dipolar RbCs Molecules in the Rovibrational and Hyperfine Ground State”. In: *Phys. Rev. Lett.* 113 (20 2014), p. 205301 (cit. on pp. 2, 3, 70, 108, 113).
- [20] Peter K. Molony, Philip D. Gregory, Zhonghua Ji, Bo Lu, Michael P. Koeppinger, C. Ruth Le Sueur, Caroline L. Blackley, Jeremy M. Hutson, and Simon L. Cornish. “Creation of Ultracold $^{87}\text{Rb}^{133}\text{Cs}$ Molecules in the Rovibrational Ground State”. In: *Phys. Rev. Lett.* 113 (25 2014), p. 255301 (cit. on pp. 2, 113).
- [21] Jee Woo Park, Sebastian A. Will, and Martin W. Zwierlein. “Ultracold Dipolar Gas of Fermionic $^{23}\text{Na}^{40}\text{K}$ Molecules in Their Absolute Ground State”. In: *Phys. Rev. Lett.* 114 (20 2015), p. 205302 (cit. on pp. 2, 3, 91, 101, 107, 108, 113, 115).
- [22] Bo Yan, Steven A. Moses, Bryce Gadway, Jacob P. Covey, Kaden R. A. Hazzard, Ana Maria Rey, Deborah S. Jin, and Jun Ye. “Observation of dipolar spin-exchange interactions with lattice-confined polar molecules”. In: *Nature* 501 (2013), pp. 521–525 (cit. on pp. 2, 14, 15).
- [23] Alexey V. Gorshkov, Salvatore R. Manmana, Gang Chen, Jun Ye, Eugene Demler, Mikhail D. Lukin, and Ana Maria Rey. “Tunable Superfluidity and Quantum Magnetism with Ultracold Polar Molecules”. In: *Phys. Rev. Lett.* 107 (11 2011), p. 115301 (cit. on pp. 2, 14, 15, 18).

- [24] S. Ospelkaus, K.-K. Ni, D. Wang, M. H. G. de Miranda, B. Neyenhuis, G. Quemener, P. S. Julienne, J. L. Bohn, D. S. Jin, and J. Ye. “Quantum-State Controlled Chemical Reactions of Ultracold Potassium-Rubidium Molecules”. In: *Science* 327.5967 (2010), pp. 853–857. eprint: <http://www.sciencemag.org/content/327/5967/853.full.pdf> (cit. on p. 3).
- [25] Piotr S. Zuchowski and Jeremy M. Hutson. “Reactions of ultracold alkali-metal dimers”. In: *Phys. Rev. A* 81 (6 2010), p. 060703 (cit. on p. 3).
- [26] M.A. Baranov, M. Dalmonte, Pupillo M., and Zoller P. “Condensed Matter Theory of Dipolar Quantum Gases”. In: *Chemical Reviews* 112 (9 2012) (cit. on pp. 4, 6, 9–11, 13, 14).
- [27] R. Feynman. *Lectures on physics 2, Electromagnetism*. Boston: Addison-Wesley, 1964 (cit. on p. 4).
- [28] E.M. Lifshitz and L.P. Pitaevskii. *Statistical Physics Part 2: Theory of the Condensed State*. London: Butterworth Heinemann, 1980 (cit. on pp. 9, 10).
- [29] G. Veeravalli, E. Kuhnle, P. Dyke, and C. J. Vale. “Bragg Spectroscopy of a Strongly Interacting Fermi Gas”. In: *Phys. Rev. Lett.* 101 (25 2008), p. 250403 (cit. on pp. 10, 11).
- [30] Zhen-Kai Lu, S. I. Matveenko, and G. V. Shlyapnikov. “Zero sound in a two-dimensional dipolar Fermi gas”. In: *Phys. Rev. A* 88 (3 2013), p. 033625 (cit. on p. 10).
- [31] A. Micheli, G. Pupillo, H. P. Büchler, and P. Zoller. “Cold polar molecules in two-dimensional traps: Tailoring interactions with external fields for novel quantum phases”. In: *Phys. Rev. A* 76 (4 2007), p. 043604 (cit. on pp. 12–14).
- [32] Andrea Micheli, Zbigniew Idziaszek, Guido Pupillo, Mikhail A. Baranov, Peter Zoller, and Paul S. Julienne. “Universal Rates for Reactive Ultracold Polar Molecules in Reduced Dimensions”. In: *Phys. Rev. Lett.* 105 (7 2010), p. 073202 (cit. on pp. 12, 13).
- [33] Bloch Immanuel. *Ecole de Physique des Houches: Many-Body Physics with Ultracold Gases*. Oxford University Press, 2010 (cit. on p. 12).
- [34] N. Matveeva and S. Giorgini. “Liquid and Crystal Phases of Dipolar Fermions in Two Dimensions”. In: *Phys. Rev. Lett.* 109 (20 2012), p. 200401 (cit. on pp. 13, 14).
- [35] A. V. Gorshkov, S. R. Manmana, G. Chen, J. Ye, E. Demler, M. D. Lukin, and A. M. Rey. “Tunable Superfluidity and Quantum Magnetism with Ultracold Polar Molecules”. In: *Phys. Rev. Lett.* 107 (11 2011) (cit. on pp. 14, 15).
- [36] D. Jaksch, C. Bruder, J. I. Cirac, C. W. Gardiner, and P. Zoller. “Cold Bosonic Atoms in Optical Lattices”. In: *Phys. Rev. Lett.* 81 (15 1998), pp. 3108–3111 (cit. on p. 14).
- [37] N.W. Ashcroft and D. Mermin. *Solid State Physics*. Brooks Cole, 1976 (cit. on p. 14).

- [38] Takeshi Fukuhara, Peter Schauss, Manuel Endres, Sebastian Hild, Marc. Cheneau, Immanuel Bloch, and Christian Gross. “Microscopic observation of magnon bound states and their dynamics”. In: *Nature* 502 (2013), pp. 76–79 (cit. on p. 15).
- [39] H. P. Buechler, E. Demler, M. Lukin, A. Micheli, N. Prokofiev, G. Pupillo, and P. Zoller. “Strongly Correlated 2D Quantum Phases with Cold Polar Molecules: Controlling the Shape of the Interaction Potential”. In: *Phys. Rev. Lett.* 98 (6 2007) (cit. on p. 18).
- [40] William D. Phillips and Harold Metcalf. “Laser Deceleration of an Atomic Beam”. In: *Phys. Rev. Lett.* 48 (9 1982), pp. 596–599 (cit. on pp. 21, 27).
- [41] K. Dieckmann, R. J. C. Spreeuw, M. Weidemüller, and J. T. M. Walraven. “Two-dimensional magneto-optical trap as a source of slow atoms”. In: *Phys. Rev. A* 58 (5 1998), pp. 3891–3895 (cit. on pp. 21, 35).
- [42] “Transient compression of a MOT and high intensity fluorescent imaging of optically thick clouds of atoms”. In: *Optics Communications* 180 (2000) (cit. on p. 21).
- [43] D. M. Brink and C. V. Sukumar. “Majorana spin-flip transitions in a magnetic trap”. In: *Phys. Rev. A* 74 (3 2006), p. 035401 (cit. on pp. 22, 38).
- [44] Jee Woo Park, Cheng-Hsun Wu, Ibon Santiago, Tobias G. Tiecke, Sebastian Will, Peyman Ahmadi, and Martin W. Zwierlein. “Quantum degenerate Bose-Fermi mixture of chemically different atomic species with widely tunable interactions”. In: *Phys. Rev. A* 85 (5 2012), p. 051602 (cit. on pp. 22, 24, 60).
- [45] J.T.M Walraven. *Elements of Quantum Gases: Thermodynamic and Collisional Properties of Trapped Atomic Gases*. 2010 (cit. on pp. 23, 42, 46, 47).
- [46] Harold J. Metcalf and Peter van der Straten. *Laser Cooling and Trapping*. 1999 (cit. on pp. 24, 25, 36).
- [47] Daniel A. Steck. “Sodium D Line Data”. In: <http://steck.us/alkalidata> (2010) (cit. on pp. 25–27, 62, 107).
- [48] Norman Ramsey. *Molecular beams*. 1956 (cit. on p. 27).
- [49] Kenneth J. Guenther. “Design and implementation of a Zeeman slower for 87Rb”. Diploma thesis. Ecole Normale Supérieure, Paris, 2004 (cit. on p. 27).
- [50] M. Prevedelli, T. Freearge, and T.W. Hänsch. “Phase locking of grating tuned diode lasers”. In: *Appl. Phys. B* 60 (1995) (cit. on p. 33).
- [51] T.G. Tiecke. “Properties of Potassium”. In: (2010) (cit. on pp. 34, 107).
- [52] M. H. Anderson, W. Petrich, J. R. Ensher, and E. A. Cornell. “Reduction of light-assisted collisional loss rate from a low-pressure vapor-cell trap”. In: *Phys. Rev. A* 50 (5 1994), R3597–R3600 (cit. on p. 37).
- [53] A. J. Moerdijk, H. M. J. M. Boesten, and B. J. Verhaar. “Decay of trapped ultracold alkali atoms by recombination”. In: *Phys. Rev. A* 53 (2 1996), pp. 916–920 (cit. on p. 39).

- [54] Ruth S. Bloom, Ming-Guang Hu, Tyler D. Cumby, and Deborah S. Jin. “Tests of Universal Three-Body Physics in an Ultracold Bose-Fermi Mixture”. In: *Phys. Rev. Lett.* 111 (10 2013), p. 105301 (cit. on pp. 39, 40, 45, 49).
- [55] Cheng Chin, Rudolf Grimm, Paul Julienne, and Eite Tiesinga. “Feshbach resonances in ultracold gases”. In: *Rev. Mod. Phys.* 82 (2 2010), pp. 1225–1286 (cit. on pp. 40, 51, 55–60, 86, 87).
- [56] Rudolf Grimm, Matthias Weidemueller, and Yurii B Ovchinnikov. “Optical dipole traps for neutral atoms”. In: *arXiv:physics/9902072* (1999) (cit. on pp. 40–42, 44).
- [57] T. L. Gustavson, A. P. Chikkatur, A. E. Leanhardt, A. Görlitz, S. Gupta, D. E. Pritchard, and W. Ketterle. “Transport of Bose-Einstein Condensates with Optical Tweezers”. In: *Phys. Rev. Lett.* 88 (2 2001), p. 020401 (cit. on p. 44).
- [58] Franco Dalfovo, Stefano Giorgini, Lev P. Pitaevskii, and Sandro Stringari. “Theory of Bose-Einstein condensation in trapped gases”. In: *Rev. Mod. Phys.* 71 (3 1999), pp. 463–512 (cit. on p. 47).
- [59] Robert Roth. “Structure and stability of trapped atomic boson-fermion mixtures”. In: *Phys. Rev. A* 66 (1 2002), p. 013614 (cit. on pp. 53, 69).
- [60] Tomasz Karpiuk, Mirosław Brewczyk, and Kazimierz Rzążewski. “Bright solitons in Bose-Fermi mixtures”. In: *Phys. Rev. A* 73 (5 2006), p. 053602 (cit. on p. 53).
- [61] Thorsten Köhler, Krzysztof Góral, and Paul S. Julienne. “Production of cold molecules via magnetically tunable Feshbach resonances”. In: *Rev. Mod. Phys.* 78 (4 2006), pp. 1311–1361 (cit. on p. 55).
- [62] F. H. Mies, E. Tiesinga, and P. S. Julienne. “Manipulation of Feshbach resonances in ultracold atomic collisions using time-dependent magnetic fields”. In: *Phys. Rev. A* 61 (2 2000), p. 022721 (cit. on p. 55).
- [63] C. Klempt, T. Henninger, O. Topic, M. Scherer, L. Kattner, E. Tiemann, W. Ertmer, and J. J. Arlt. “Radio-frequency association of heteronuclear Feshbach molecules”. In: *Phys. Rev. A* 78 (6 2008), p. 061602 (cit. on pp. 55, 60, 67).
- [64] S. B. Papp and C. E. Wieman. “Observation of Heteronuclear Feshbach Molecules from a ^{85}Rb - ^{87}Rb Gas”. In: *Phys. Rev. Lett.* 97 (18 2006), p. 180404 (cit. on p. 55).
- [65] Michael P. Koeppinger, Daniel J. McCarron, Daniel L. Jenkin, Peter K. Molony, Hung-Wen Cho, Simon L. Cornish, C. Ruth Le Sueur, Caroline L. Blackley, and Jeremy M. Hutson. “Production of optically trapped $^{87}\text{RbCs}$ Feshbach molecules”. In: *Phys. Rev. A* 89 (3 2014), p. 033604 (cit. on p. 55).
- [66] C. Weber, G. Barontini, J. Catani, G. Thalhammer, M. Inguscio, and F. Minardi. “Association of ultracold double-species bosonic molecules”. In: *Phys. Rev. A* 78 (6 2008), p. 061601 (cit. on p. 55).
- [67] Fudong Wang, Xiaodong He, Xiaoke Li, Bing Zhu, Jun Chen, and Dajun Wang. “Formation of ultracold NaRb Feshbach molecules”. In: *New Journal of Physics* 17.3 (2015), p. 035003 (cit. on p. 55).

- [68] C. Ospelkaus, S. Ospelkaus, L. Humbert, P. Ernst, K. Sengstock, and K. Bongs. “Ultracold Heteronuclear Molecules in a 3D Optical Lattice”. In: *Phys. Rev. Lett.* 97 (12 2006), p. 120402 (cit. on p. 55).
- [69] Myoung-Sun Heo, Tout T. Wang, Caleb A. Christensen, Timur M. Rvachov, Dylan A. Cotta, Jae-Hoon Choi, Ye-Ryoung Lee, and Wolfgang Ketterle. “Formation of ultracold fermionic NaLi Feshbach molecules”. In: *Phys. Rev. A* 86 (2 2012), p. 021602 (cit. on p. 55).
- [70] Cheng-Hsun Wu, Jee Woo Park, Peyman Ahmadi, Sebastian Will, and Martin W. Zwierlein. “Ultracold Fermionic Feshbach Molecules of $^{23}\text{Na}^{40}\text{K}$ ”. In: *Phys. Rev. Lett.* 109 (8 2012), p. 085301 (cit. on pp. 55, 81, 87).
- [71] T. G. Tiecke, M. R. Goosen, J. T. M. Walraven, and S. J. J. M. F. Kokkelmans. “Asymptotic-bound-state model for Feshbach resonances”. In: *Phys. Rev. A* 82 (4 2010), p. 042712 (cit. on pp. 57, 86, 87).
- [72] Paul S. Julienne and Bo Gao. “Simple Theoretical Models for Resonant Cold Atom Interactions”. In: *AIP Conference Proceedings* 869.1 (2006) (cit. on p. 58).
- [73] G. Breit and E. Wigner. “Capture of Slow Neutrons”. In: *Phys. Rev.* 49 (7 1936), pp. 519–531 (cit. on p. 58).
- [74] Tyler D. Cumby, Ruth A. Shewmon, Ming-Guang Hu, John D. Perreault, and Deborah S. Jin. “Feshbach-molecule formation in a Bose-Fermi mixture”. In: *Phys. Rev. A* 87 (1 2013), p. 012703 (cit. on p. 70).
- [75] Gerhard Herzberg. *Molecular Spectra and Molecular Structure. Volume 1 - Spectra of Diatomic Molecules*. 1950 (cit. on pp. 71, 74, 77, 87).
- [76] Walter J. Stevens, Daniel D. Konowalow, and Lyn B. Ratcliff. “Electronic structure and spectra of the lowest five $^1\Sigma^+$ and $^3\Sigma^+$ states, and the three $^1\Pi$, $^3\Pi$, $^1\Delta$, and $^3\Delta$ states of NaK”. In: *The Journal of Chemical Physics* 80.3 (1984), pp. 1215–1224 (cit. on p. 73).
- [77] P. Kowalczyk. “Perturbation facilitated observation of the $d^3\Pi$ state in NaK”. In: *Journal of Molecular Spectroscopy* 136.1 (1989), pp. 1–11 (cit. on pp. 73, 77, 82, 83).
- [78] E. A. Pazyuk, A. V. Stolyarov, A. Zaitsevskii, R. Ferber, P. Kowalczyk, and C. Teichteil. “Spin-orbit coupling in the $d^3\Pi/D^1\Pi$ complex of $^{23}\text{Na}^{39}\text{K}$ ”. In: *Molecular Physics* 96.6 (1999), pp. 955–961 (cit. on pp. 73, 82, 83).
- [79] Nadia Bouloufa, Romain Vexieu, and Olivier Dulieu. *Private communication* (cit. on pp. 73, 81, 82).
- [80] Helen Lefebvre-Brion and Robert W. Field. *Perturbations in the Spectra of Diatomic Molecules*. 1986 (cit. on pp. 74, 77–79).
- [81] Kiyoshi Ishikawa, Takahiro Kumauchi, Masaaki Baba, and Hajime Katô. “Hyperfine structure of the NaK $c^3\Sigma^+$ state and the effects of perturbation”. In: *The Journal of Chemical Physics* 96.9 (1992), pp. 6423–6432 (cit. on pp. 78, 92).

- [82] Anastasia Drozdova. “Study of spin-orbit coupled electronic states of Rb₂, NaCs and NaK molecules. Laser spectroscopy and accurate coupled-channel deperturbation analysis”. PhD thesis. University of Lyon, 2013 (cit. on pp. 81, 82).
- [83] T. A. Schulze, I. I. Temelkov, M. W. Gempel, T. Hartmann, H. Knöckel, S. Ospelkaus, and E. Tiemann. “Multichannel modeling and two-photon coherent transfer paths in NaK”. In: *Phys. Rev. A* 88 (2 2013), p. 023401 (cit. on pp. 81, 88).
- [84] Eric D. Black. “An introduction to Pound-Drever-Hall laser frequency stabilization”. In: *American Journal of Physics* 69.1 (2001), pp. 79–87 (cit. on p. 84).
- [85] Diana Amaro. “A Raman Laser System for Groundstate transfer of NaK”. Master thesis. Universidade de Coimbra, 2013 (cit. on p. 85).
- [86] Jee Woo Park, Sebastian A. Will, and Martin Zwierlein. *Two-Photon Pathway to Ultracold Ground State Molecules of ²³Na⁴⁰K*. 2015. url: arXiv:1505.01835 (cit. on pp. 88, 89, 115).
- [87] F. H. Crawford. “Zeeman Effect in Diatomic Molecular Spectra”. In: *Rev. Mod. Phys.* 6 (2 1934) (cit. on p. 88).
- [88] D. M. Brink and G. R. Satchler. *Angular Momentum*. 1962 (cit. on p. 90).
- [89] R. A. Frosch and H. M. Foley. “Magnetic Hyperfine Structure in Diatomic Molecules”. In: *Phys. Rev.* 88 (6 1952) (cit. on p. 91).
- [90] J. C. Slater. “Atomic Shielding Constants”. In: *Phys. Rev.* 36 (1 1930), pp. 57–64 (cit. on p. 92).
- [91] H. Geisen, D. Neuschaefer, and Ch. Ottinger. “Hyperfine structure of N₂ from LIF measurements on a beam of metastable N₂ molecules”. English. In: *Zeitschrift fuer Physik D Atoms, Molecules and Clusters* 4.3 (1987), pp. 263–290 (cit. on p. 92).
- [92] Kiyoshi Ishikawa. “Hyperfine structure of the NaK $a^3\Sigma^+$ state: Interaction of an electron spin with the sodium and potassium nuclear spins”. In: *The Journal of Chemical Physics* 98.3 (1993), pp. 1916–1924 (cit. on p. 92).
- [93] P. Burns, A. D. Wilkins, A. P. Hickman, and J. Huennekens. “The NaK 1(b) $\Pi_{\Omega=0}$ state hyperfine structure”. In: *The Journal of Chemical Physics* 122.7 (2005) (cit. on p. 92).
- [94] B. W. Shore, J. Martin, M. P. Fewell, and K. Bergmann. “Coherent population transfer in multilevel systems with magnetic sublevels. I. Numerical studies”. In: *Phys. Rev. A* 52 (1 1995), pp. 566–582 (cit. on pp. 92, 107, 112, 115).
- [95] J. Martin, B. W. Shore, and K. Bergmann. “Coherent population transfer in multilevel systems with magnetic sublevels. II. Algebraic analysis”. In: *Phys. Rev. A* 52 (1 1995), pp. 583–593 (cit. on pp. 92, 107, 115).
- [96] J. Martin, B. W. Shore, and K. Bergmann. “Coherent population transfer in multilevel systems with magnetic sublevels. III. Experimental results”. In: *Phys. Rev. A* 54 (2 1996), pp. 1556–1569 (cit. on pp. 92, 107, 112, 115).

- [97] N. V. Vitanov and S. Stenholm. “Adiabatic population transfer via multiple intermediate states”. In: *Phys. Rev. A* 60 (5 1999), pp. 3820–3832 (cit. on pp. 92, 107, 115).
- [98] Bruce W. Shore. *The Theory Of Coherent Atomic Excitation*. 1990 (cit. on pp. 93, 94, 101, 102, 106, 107).
- [99] Michael Fleischhauer, Atac Imamoglu, and Jonathan P. Marangos. “Electromagnetically induced transparency: Optics in coherent media”. In: *Rev. Mod. Phys.* 77 (2 2005), pp. 633–673 (cit. on pp. 93, 96, 97, 101, 102).
- [100] E. Arimondo. “Electromagnetically induced transparency: Optics in coherent media”. In: *Prog. Opt.* 35 (259 1996) (cit. on pp. 93, 101, 102).
- [101] M. Born and V. Fock. “Beweis des Adiabatensatzes”. German. In: *Zeitschrift für Physik* 51.3-4 (1928), pp. 165–180 (cit. on p. 97).
- [102] L. P. Yatsenko, V. I. Romanenko, B. W. Shore, and K. Bergmann. “Stimulated Raman adiabatic passage with partially coherent laser fields”. In: *Phys. Rev. A* 65 (4 2002), p. 043409 (cit. on pp. 98–100).
- [103] L. P. Yatsenko, B. W. Shore, and K. Bergmann. “Detrimental consequences of small rapid laser fluctuations on stimulated Raman adiabatic passage”. In: *Phys. Rev. A* 89 (1 2014), p. 013831 (cit. on p. 99).
- [104] T. Heil, I. Fischer, and W. Elsässer. “Influence of amplitude-phase coupling on the dynamics of semiconductor lasers subject to optical feedback”. In: *Phys. Rev. A* 60 (1 1999), pp. 634–641 (cit. on p. 100).
- [105] C.H. Henry. “Theory of the linewidth of semiconductor lasers”. In: *Quantum Electronics, IEEE Journal of* 18.2 (1982), pp. 259–264 (cit. on p. 100).
- [106] J. Alnis, A. Matveev, N. Kolachevsky, Th. Udem, and T. W. Hänsch. “Subhertz linewidth diode lasers by stabilization to vibrationally and thermally compensated ultralow-expansion glass Fabry-Pérot cavities”. In: *Phys. Rev. A* 77 (5 2008), p. 053809 (cit. on p. 100).
- [107] N. Kolachevsky, J. Alnis, S. D. Bergeson, and T. W. Hänsch. “Compact solid-state laser source for 1S-2S spectroscopy in atomic hydrogen”. In: *Phys. Rev. A* 73 (2 2006), p. 021801 (cit. on p. 100).
- [108] A. Gerdes, M. Hobein, H. Knoeckel, and E. Tiemann. “Ground state potentials of the NaK molecule”. English. In: *The European Physical Journal D* 49.1 (2008), pp. 67–73 (cit. on p. 100).
- [109] J. Aldegunde, Ben A. Rivington, Piotr S. Żuchowski, and Jeremy M. Hutson. “Hyperfine energy levels of alkali-metal dimers: Ground-state polar molecules in electric and magnetic fields”. In: *Phys. Rev. A* 78 (3 2008), p. 033434 (cit. on p. 107).

Danksagung

Ich möchte mich vielmals bei meinem Doktorvater, Professor Immanuel Bloch dafür bedanken, dass er mir vor genau fünf Jahren - damals aus der Gehirnforschung kommend - die Möglichkeit gab, bei ihm an vorderster 'Front' der Atom- und Molekülphysik zu promovieren. Das Forschungsumfeld am MPQ, aber vor allem der Teamgeist, die aussergewöhnlichen Fähigkeiten und die Hingabe aller Mitglieder seiner Arbeitsgruppe waren und sind mir eine starke Motivation stets Neues zu lernen und nie aufzugeben. Auch dafür, dass er mir die Teilnahme an der Sommerschule in Les Houches und an vielen anderer Konferenzen (Beijing, Stuttgart, Venedig, Innsbruck, etc.) ermöglicht hat, möchte ich mich hier nochmal bedanken.

Bei meinem Teamleiter und Freund, Dr. Christoph Gohle möchte ich mich vor allem dafür bedanken, dass er aus mir einen richtigen Physiker gemacht hat. All das aufzuzählen, was er mir während der letzten Jahre beigebracht hat, würde bei weitem den Rahmen sprengen. Gerne erinnere ich mich an unsere gemeinsamen Geburtstagsfeiern im Haus seiner Familie in Nymphenburg, die mit Livemusik, Lagerfeuer (bei Eis und Schnee) und allem was sonst noch dazu gehört jedes Mal einmalig waren.

Meinem guten Freund und Co-Doktoranden Zhenkai Lu möchte ich sagen, dass er einer der vielschichtigsten und empathischsten Menschen ist, die ich kenne und ich sehr froh darüber bin, sein Freund zu sein. Es hat mich wirklich beeindruckt, wie ungezwungen und herzlich mich seine Familie in Ningbo aufgenommen hat. Auch mein begrenztes Wissen um Landau'sche Fermi-Flüssigkeiten, Streuresonanzen und natürlich um die kulinarischen Vorzüge der besten Küche der Welt, verdanke ich ihm.

Bei meinem guten Freund und Co-Doktoranden Martin Boll möchte ich mich für die vielen gemeinsamen Abenteuer im Gebirge, perfekten italienischen *caffè* und seine virtuose Kochkunst bedanken. Die Zeit in unserer gemeinsamen Wohnung am englischen Garten, zählt zu den fröhlichsten Erinnerungen meiner Promotion.

Meinen ehemaligen und aktuellen Kollegen, Dr. Tobias Schneider, Diana Amaro, Frauke Seeßelberg und Roman Bause möchte ich für die gemeinsam geleistete Arbeit danken. Ohne Frauke wüsste ich nicht, wie viel Freude Molekülspektroskopie mit einem Farbstoff-Laser macht.

Meinen Eltern, meiner Familie und meinen Freunden danke ich für Ihre Unterstützung und dafür, dass sie immer an das Gelingen meiner Promotion geglaubt haben. Zuletzt möchte ich meiner Lebensgefährtin Judith danken. Für alles. Du bist die Liebe meines Lebens.